Experimental approaches in studying polyelectrolytes inside a porous matrix : the case of nanoporous alumina membranes

Anastasia Christoulaki

Sorbonne Université

École doctorale de Chimie Physique et Chimie Analytique de Paris Centre
Laboratoire Physicochimie des Electrolytes et Nanosystèmes InterfaciauX

Experimental approaches in studying polyelectrolytes inside a porous matrix: The case of nanoporous alumina membranes

Anastasia CHRISTOULAKI

Directrice de thèse : Emmanuelle DUBOIS

Présentée et soutenue publiquement le *5 Octobre 2018* devant un jury composé de :

M.Jean-Marc ZANOTTI (Laboratoire Léon Brillouin / CRG SHARP) ... *Rapporteur*
M.Jörg SCHNEIDER (Technische Universität Darmstadt) ..... *Rapporteur*
Mme Marie-Claude CLOCHARD (École Polytechnique) ..... *Examinatrice*
M.Alessandro SIRIA (École Normale Supérieure) ..... *Examinateur*
Mme Sophie CASSAIGNON (Sorbonne-Université) ..... *Examinatrice*
Mme Emmanuelle DUBOIS (Sorbonne Université) ..... *Directrice de thèse*

Acknowledgements

This thesis wouldn't have been accomplished without the presence and help of some people to whom I acknowledge in the following lines.

My professors, Emmanuelle Dubois and Nicolas Jouault offered me this opportunity to come in France and be involved in a very interesting scientific project while getting hands on the unique experimental technique of Small Angle Neutron scattering (SANS). I am grateful for the knowledge they passed on, their advices and experimental freedom they gave me. I appreciate that this independence was encompassed by sincere discussions and critical examination of the results and ideas throughout the project. Above all, I appreciate that they set conditions such that I could work as a researcher while learning how to make research.

My recognition and appreciation is expressed to Jean Marc Zanotti and Jörg Schneider for accepting to report on the thesis and to Marie-Claude Clochard, Alessandro Siria and Sophie Cassaignon for accepting to be members of the jury.

I am grateful to the director of the laboratory Pierre Levitz for accepting me to work in PHENIX laboratory and for his remarks and ideas on the project.

It was a pleasure to have worked with Alexis Chennevière whose time, scientific experience and creativity was given to me in abundance whenever I had questions, ideas or difficulties during experiments. His pedagogic style of passing knowledge and persistence to understand the underlying physics would always be an example for me. I want to thank him specifically for the nice collaboration in the SANS experiments, the development of the SEM image processing software tools and the materials and scientific support for the neutron reflectivity measurements. His active and constant contribution is reflected in this project.

I express my gratitude to Didier Lairez and the members of Laboratoire des Solides Irradiés (LSI) at École Polytechnique for the warm host there. More precisely I am grateful to Didier Lairez for giving me the opportunity to use the device he developed for the streaming potential and conductivity measurements of the membranes. Apart from the materials, processing tools and scientific support he offered me, I thank him for the time he took to explain me the the streaming potential measurements as well as certain aspects of small angle neutron scattering technique. At LSI I found an environment where I could discuss on my project, learn from previous experience and explore new possibilities for the implementation of the membranes in other scientific studies.

Parts of this thesis were understood and completed due to the hard work of interns who were committed and showed remarkable maturity during their internship. Léopold Remy focused on the synthesis of membranes in the less explored selenic acid electrolyte and was enrolled in testing protocols for the detachment of the membranes. Chiara Moretti, worked on the synthesis of membranes with deuterated electrolytes, their characterisation by SEM

and titration experiments with ICP. I praise them for their character and motivation, I am sure that they will reach even higher!

I am happy to have worked Erigene Bakangura, post-doc at LLB, for sharing beam time, the nice collaboration and interesting discussions during the project.

Many thanks to Guillaume Mériguet. In certain moments, he appeared out of the blue as a *deus ex machina*, coming up with a helpful idea or a useful equipment. Moreoever, I would like to thank Amandine Anfry for the help with density measurements, the ordering of materials and the proper organisation in the laboratory.

Numerous hours were spent for the characterisation of the membranes by SEM in the platform of the Institut des Matériaux de Paris Centre with the scientific support of David Montero whom I praise for his expertise on the SEM, EDX characterisation of the samples as well as for the interest and curiosity he showed on my project.

I acknowledge Emmanuel Briot for his support in the XRD and specific surface characterisation.

The specific surface characterization came in the very end of the thesis project and I am thankful to Laurent Michot for sharing the details of the technique, shedding light the experimental results and discussing ideas for future work.

I thank Serge Durand-Vidal for measuring the membranes by the Atomic Force Microscopy, these measurements helped in the understanding of certain points of the flow measurements.

I would like to acknowledge some people for their contribution in the experimental set up: Jean Chevalet for building and providing the electronic elements of the anodization set-up as well as for the help in the establishment of the pc interface of the multimeter. I promise that he will get back the kilometers of solder wire which he generously offered to me; José Gomes, for the construction of different pieces needed for the experiments.

Thanks to the members of the neutron sources, Isabelle Grillo and Lionel Porcar from Insitute Laue Langevin (ILL), for the help in the SANS experiments at D11 and Frédéric Ott for the support during the neutron imaging measurements at the instrument IMAGINE in Laboratoire Léon Brillouin (LLB).

I am thankful to the members of the administration of PHENIX, Lise Michelot, Brigitte Carrez, Stéphanie Grison, Gérard Guillard for their kind assistance.

A special thanks to Marie Jardat for her leading role and initiations in keeping the MEM team an active group with a collective spirit.

I sincerely thank the Ph.D students, post-docs and the permanent members of PHENIX who kept with their attitude a pleasant environment to work in. Among them: Caterina, Stéphane, Wilfried, Pauline S., Pauline B., Sébastien, Vivien, Lizbeth, Cintia, Alessandra, Adelchi, Xudong, Mario, Nathaly, Kyle, Chérazade, Seong Koo, Ana, Nadia, Antonin, Jesse, Mitradeep, Thomas, Sam, Laura, Claire, Nidhal, Sofia, Yasine, Esther, Maria, Stella, Rania, Blandine, Jamoowantee, Jean-Baptiste, Mesut, Clément, Agathe, Karol, Charlotte, Emilie..

All my gratitude and respect to my friends, who helped me integrate in France, I admire their effort to accomplish their studies and follow their dream while having to deal with a very difficult reality. (Άλεξ, Ρόιλα, Τεό, Αναστάση...)

Finally, I express my love to my parents and family in Paris for their support during the thesis and for all of these years.. Σταυρούλα, Δημήτρη, Ρούλα, Τίνα, Ραχήλ, *Theodore*, Μιχάλη, Έλενα, Λέων...Ευχαριστώ!

Contents

Introduction **3**

1 Synthesis and characterisation of nanoporous alumina membranes **9**

1.1 Introduction 9

1.1.1 Description and application of nanoporous alumina membrane (nPAAMs) 9

1.1.2 Anodization process 11

1.2 Synthesis of nPAAMs 13

1.2.1 Anodization set up 13

1.2.2 Pretreatments 14

1.2.3 Structural characterisation of nPAAMs synthesized under different electrolytes 15

1.2.4 Growth mechanism and anodization efficiency 26

1.2.5 Influence of deuterium on pore organisation and growth rate 31

1.2.6 Post treatments of as prepared nPAAMs 40

1.3 Nanoporous alumina membranes on silicon wafers for neutron reflectivity measurements 48

1.3.1 Synthesis of nPAAM on silicon wafer 49

1.3.2 nPAAMs characterization by Neutron Reflectivity (NR) 58

1.4 General conclusions of Chapter 1 62

2 Structure and composition of nanoporous alumina membranes **65**

2.1 Introduction 65

2.1.1 Chemical composition of nPAAMs 65

2.1.2 Probing the composition by Small Angle Scattering techniques 67

2.2 Experimental aspects 68

2.2.1 Sample preparation 68

2.2.2 SANS measurements and nPAAMs alignment 69

2.2.3 Multiple Scattering and optimal SANS conditions 70

2.3 Results . . . 72
2.3.1 nPAAMs prepared in oxalic acid . . . 72
2.3.2 nPAAMs prepared in sulfuric acid . . . 101
2.3.3 nPAAM prepared in selenic acid . . . 106
2.4 Discussion on data fitting . . . 108
2.5 General conclusions of Chapter 2 . . . 113

3 Surface charge of nanoporous alumina membrane 115
3.1 Origin of the surface charge in metal oxides and its measurement by streaming potential . . . 115
3.2 Surface charge of nanoporous alumina membranes . . . 118
3.2.1 Experimental setup . . . 119
3.2.2 Sample preparation . . . 121
3.2.3 Effect of buffer solutions on the ζ -potential . . . 125
3.2.4 Transformation of nPAAMs and effect on the ζ -potential . . . 129
3.2.5 ζ- potential of commercial Anodisc membranes . . . 130
3.3 General Conclusions of Chapter 3 . . . 132

4 Experimental approaches in studying polyelectrolyte confinement 133
4.1 Introduction . . . 133
4.2 Characterisation of the polyelectrolyte . . . 133
4.2.1 Indroduction . . . 133
4.2.2 Experimental part: NaPSS characterisation . . . 135
4.3 NaPSS inside nanoporous anodic alumina . . . 139
4.3.1 Loading NaPSS on nPAAMs . . . 139
4.3.2 Kinetics of adsorption of NaPSS probed by streaming potential measurements . . . 141
4.4 Description of the flow measurements . . . 147
4.4.1 Implementation of flow measurements on nPAAMs for examining the adsorption of nPAAMs . . . 147
4.4.2 SANS measurements on nPAAMs with NaPSS . . . 159
4.5 Conclusions on Chapter 4 . . . 166

Conclusions 169

Annexes 177

A Structure characterisation by SEM 179

B Small Angle neutron Scattering **185**

C Neutron Reflectivity **191**

D Emission Spectroscopy **195**

References **197**

Introduction

The confinement of condensed matter in nanoporous medium can induce at the nanoscale drastic structural or dynamical changes that ultimately lead to original properties that are not achievable under bulk condition [1]. Such behaviors can be then exploited to design new devices or materials with enhanced properties [2]. While many works dealt with the confinement of liquid crystals [3], liquid mixtures [4] , [5] or polymer melts [6, 7, 8, 9, 10] few experimental studies focus on the confinement of charged polymers, i.e. polyelectrolytes (PEs), in solution. Better understanding of PE behavior (conformation, dynamics and transport properties) under confinement is relevant for nanofluidic or biological applications as sequencing of DNA strands, designing pores for biosensors, filtration or chemical separation or for more fundamental aspects such as the understanding of protein insertion [11] and translocation into biological membranes. The geometrical constraints imposed by the nanopore and the existence of charges inside the pore might modify the static and dynamics properties of PEs.

As mentioned previously few studies focused on conformation and dynamics of PE under confinement. For example, the conformation in confined geometries might be modified by the size of the nanopores and by charges at the pore wall surface. So far, one work addressed the conformation of PE solution under confinement by Small Angle Neutron Scattering (SANS) using the Zero Average Contrast (ZAC) method. Gilbert et al.[12] studied the permeation of aqueous solution of polystyrene sulfonate due to osmotic pressure inside Vycor porous glass and its dependence on the polyelectrolyte's concentration. In the same study, the authors showed that the confined polyelectrolyte chain is stretched inside the pore. The possible electrostatic origin of such stretching is proposed but needs to be clearly elucidated. However, more studies can be found on the transport of PE by, for example, measuring the concentration of PE flowing through nanopores [13, 14]. Oukhaled and coworkers [15] studied the translocation of dextran through hemolysin channels (2 nm in diameter) and showed that the chain penetration is slowed down when the Debye length is similar to the pore sizes; small pores being more sensitive to ionic strength. In a different approach, layer-by-layer PE assemblies were used to modify the surface of nanopores in order to control the

transport of chemical species[16]. The kinetic of PE penetration is not discussed in this work but Lazarra et al. studied in more details the deposition process of charged dendrimers as a function of pore sizes and ionic strength by optical waveguide measurements [17]. They found that PE deposition inside the pores saturates whatever the pore diameter and that the penetration is inhibited at low ionic strength. They also observed that the deposition occurs first at the pore entrance and might slow the diffusion of PE inside the pore.

What drives the penetration of PE into a confining medium? How the conformation is affected by the charges and the geometrical constrains? Moreover the fact that only few experimental works can be found in the literature can be related to some experimental limitations: how can we directly access the behavior of PE in a confining medium? What conditions are required to have reliable data? Should we design specific experiments to study the PE confinement? In this context, the impact of charges and sizes of nanopores on PE penetration and conformation is still an open question we want to address here and is still challenging in term of experimental approaches.

To answer these different questions a model confining medium is necessary to control and adjust the pore morphology. Among various nanoporous materials that can be used as a confining medium (clays, mesoporous silica, Vycor glass, nanotubes ...) nanoporous anodic alumina oxide (nPAAMs) are very promising host systems for confinement studies. nPAAMs are obtained through the controlled anodization of aluminium in acidic electrolytes and are composed of high-ratio parallel cylindrical channels with perfectly tunable pore diameters (D_p from 10 nm to 100 nm), interpore distances (D_{int} from 50 nm to 200 nm), lengths (L_p up to 500 µm) and porosity. Since the pioneering work of Masuda and Fukuda in 1995 who proposed a two-step anodization process to produce very ordered nanopores [18], several studies have explored the potential applications of nPAAMs such as biosensors[19], templates for the growth of functional materials[20], [21], ion selective membranes [22], filtration or chemical separation devices or batteries [23], making nPAAMs interesting materials for many purposes and in particular to study the confinement of PE, which will be here sodium polystyrene sulfonate (NaPSS), a well described PE in solution [24, 25, 26, 27, 28, 29].

In this context, this thesis has several objectives:

i) Synthesize nPAAMs with different pore morphologies and gain understanding on the mechanism of nPAAM formation to propose innovative synthesis that improve the self-organized growth of ordered pores, i.e widen the window of anodizing conditions (voltage, time, temperature, electrolyte nature...) and that lead to large range of pore diameters. Here we will study in particular the influence of deuterium on the synthesis by using heavy water as a solvent. The synthesis of open membrane is also necessary for further characterization (surface charge) or to study the PE behavior (see below).

ii) Fully characterize the nPAAMs, i.e. study the pore organization, determine the composition and the surface charge behaviour. Before studying the behavior of confined PE one has to completely characterize the confining medium. Indeed, a still challenging issue is to find an experimental strategy to fully described the nPAAMs. Pore size distribution and porosity of porous materials can be investigated from the nanometer to hundreds of micrometers by different methods. Most of the previous works done on nPAAMs used direct imaging techniques (Scanning or Transmission Electron Microscopy (SEM or TEM) and Atomic Force Microscopy (AFM)) to characterize the surface structure of nPAAMs. These techniques have some limitations such as the restricted number of studied pores inducing a lack of statistic and the impossibility to have access to the composition in the whole sample. Small-Angle Scattering techniques can overcome this issue by giving access to averaged structural information over a larger volume. Small-Angle X-rays Scattering has been used to characterize the pore arrangement and long range ordering. However internal composition is still non available. To that end, we decided to use Small-Angle Neutron Scattering (SANS) technique, which is a powerful tool to characterize both the pore organization and the chemical composition by determining the different scattering length density (SLD) of the material using the contrast variation method. The charge will be determined by streaming potential technique that gives the ζ- potential of the nPAAMs under different pH and buffer conditions. This aspect will form an important part of this thesis.

iii) Develop experimental approaches to access the PE behaviour in confining medium. Can we use different techniques to study the kinetic of penetration and conformation of PE under confinement? Should we adapt the nPAAMs geometry (bulk or on Si wafer) to the experimental devices? The characterization of PE solution under confinement is challenging and experimental strategy has to be proposed to extract information. Here we combined SANS, ζ-potential and flow measurements to detect the presence of PE, to know whether it adsorbs and to quantify it.

The thesis will be divided into 4 Chapters that covers the three previous objectives. **Chapter 1** described the general synthesis of nPAAMs starting from aluminum foil. Three different electrolytes will be used (oxalic, sulfuric and selenic acid) to vary the pore diameter and ordering. The nPAAMs will be characterized by Scanning Electron Microscopy from which the structure factor (S(q)) can be extracted. Membrane post treatments such as pore widening, annealing or detachment will also be described. In this Chapter we also propose to discuss the mechanism of pore formation by titrating the amount of Al cations produced during the process. The last part of this Chapter will present the synthesis of nPAAMs on silicon wafers and its characterization by Neutron Reflectivity. **Chapter 2** is dedicated to

the structural characterization of the nPAAMs by Small-Angle Neutron Scattering (SANS). We will present some issues (such as multiple scattering) that have to be overcome to measure nPAAMs with this technique and determine the best experimental conditions and discuss a fitting method, combining SEM analysis and SANS contrast variation, that leads to a description of the SANS data with an open discussion about a critical fitting parameter. We will discuss the effect of different parameters (electrolyte nature, synthesis time, aging or solvents) on structure and composition of nPAAMs and a specific discussion will be made on one criticial fitting parameter. **Chapter 3** focuses on the determination of the surface charge on nPAAMs by streaming potential experiments. This technique will be described and the influence of the pH and nature of the buffers will be shown as well as some kinetic effects on the zeta potential. **Chapter 4** deals with the characterisation of the NaPSS inside the nPAAM. The adsorption of NaPSS is probed by streaming potential and the technique is used for in-situ adsorption kinetic study under positive and negative surface charge. The results are combined with flow measurements through detached nPAAMs. By this technique the permeation of NaPSS can be studied in-situ or ex-situ and the different phenomena such as adsorption, pore plugging are discussed. The measurements are completed by Small Angle Neutron Scattering (SANS) of the nPAAM with NaPSS.

Finally a general conclusion will summarize the important results of this thesis and some perspectives will be provided.

Chapter 1

Synthesis and characterisation of nanoporous alumina membranes

In this chapter the electrochemical synthesis of the confining medium, the nanoporous alumina membranes, will be described. The experimental set up and protocol for producing membranes on aluminum substrate, self-standing and on silicon wafer will be presented. It will be shown that the structure and organisation, extracted from SEM analysis can be tuned by the synthesis conditions.

1.1 Introduction

1.1.1 Description and application of nanoporous alumina membrane (nPAAMs)

Self-ordered nPAAMs are a laboratory synthesized membranes made from aluminum oxide. The distinctiveness of the membrane is its hexagonal symmetry of the pore arrangement which emerges under specific synthesis conditions. The pore diameter is found in the nanometric scale and range from 10 to 800nm, thus making them a very popular material in the field of nanotechnology [30, 31].

More precisely, the membrane consists of parallel monodispersed pores that are packed in an hexagonal structure. The pores grow on an aluminum substrate and are parallel to each other. Each pore is enclosed by an hexagonal cell made from aluminum oxide and ends into a barrier type oxide which is called the "barrier layer". A schematic representation is given in Figure 1.1.

The membranes are characterised by their :

1) D_p: pore diameter

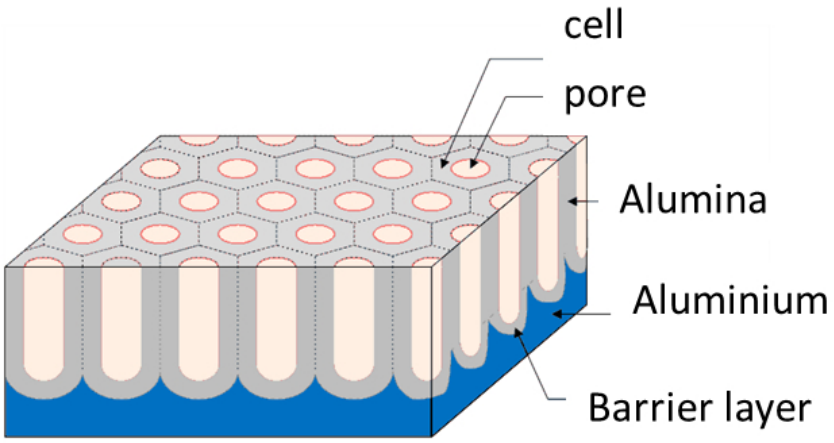

[Image courtesy:Nikolaos Spiliopoulos]

Figure 1.1: Schematic view of a porous alumina membrane grown on aluminum substrate .

2) D_{int}: interpore distance, that is the distance beetween the centers of two adjacent pores.

3) D_c: cell diameter , which is the diameter of the hexagonal cell

4) L_p: length

5) L_b: thickness of the barrier layer

6) n: pore density, which is the number of pores per unit surface

7) P: porosity , which is the volume fraction of the pores to the total membrane surface.

All these structural parameters can be tuned through the synthesis conditions, making nPAAMs interesting nanomaterials for many purposes. Indeed, the versatility of the nanoporous alumina membrane becomes apparent if one examines the vast number of applications in which it is implemented. The low cost synthesis of the ordered structure on large surfaces makes them appropriate templates for the synthesis of other nanomaterials such as nanowires and nanodots [32, 33]. Furthermore, their high surface to volume ratio intensifies the recorded signal when the membranes are implemented in different types of nanosensors [34, 35].

The nPAAMs have been also used for the confinement of condensed matter such as polymers since their pore diameters can be tuned to some nanometers, a length scale that is comparable to certain size parameters of polymers such as the radius of gyration R_g. In general, the restriction on the available space for the polymer chain to explore brings new physics in the conformation, thermodynamics and dynamics of the polymers. More precisely

the membranes are appropriate templates for addressing the problem of the conformation of polymer brushes or polyelectrolytes in concave geometry [36, 37]. In terms of the thermodynamic properties it has been experimentally observed a depression of the melting point of polyethylene oxide (PEO) of about 20K when it is confined in a nPAAM [38] . Moreover the membranes have been used for observing dynamics of confined polymer melts [39, **?**, 40].

1.1.2 Anodization process

The nPAAMs are synthesised by an electrochemical process known as anodization. The process involves the immersion of a metal, which serves as the anode, inside an electrolyte, usually acidic, such as oxalic, sulfuric or phosphoric acid and the application of a constant voltage or current.

Anodization results in the oxidation of the metal and the growth of an oxide layer. Historically, anodization was a process that was introduced during the early 20^{th} century in the industry for producing protective and decorative coatings. In the case of self ordered porous films, the first ordered hexagonal arrangement of the pores was observed in the 1950s by means of an electronic microscope [41]. At the beginning of the anodization the pores don't hold ordered positions. As the anodization proceeds in deeper layers the pores experience compressive forces which force them to arrange in a more ordered close packed hexagonal structure. In order to obtain membranes with high ordering the method of "two-step" anodization method was proposed [42]. A schematic of the two-step anodization process is depicted in Figure 1.2. The method involves the synthesis of an anodic film of several microns which is subsequently dissolved in an aqueous solution consisting of 6 wt.% H_3PO_4 and 1.8 wt.% CrO_3 at 50 ℃. The use of chromic acid has been verified to leave the aluminum substrate intact. After the dissolution of the oxide, ordered dimples appear on the aluminum that are the imprints of the pores formed at the first anodization step. Then, a second anodization step is applied at the same conditions as the first one. Now the pores will start to form from much more ordered positions.

The hexagonal structure appears under anodizing in a narrow window of electrochemical conditions and stretches out on the whole anodized surface. Since then different models have been proposed to explain the mechanism of nPAAMs formation which will be discussed later in the chapter. The basic conditions of anodization are:

1) the electrolyte nature and concentration C

2) the applied voltage, V or current, I

3) temperature, T

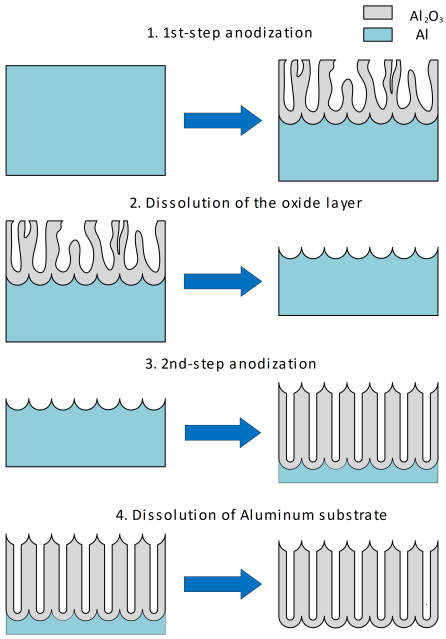

Figure 1.2: Schematic representation of the "two-step" anodization process.

4) duration of the anodization, T

Throughout the years different experimental protocols, using various anodization conditions, gave oxide coatings with different structural characteristics. In particular, anodization conditions are divided in two categories, mild (MA) and hard (HA). The exploration of different anodization regimes provides scaling laws that relate the applied voltage with the interpore distance D_{int}, the barrier layer thickness L_b, the pore diameter and the pore density. Mild anodization involves the application of relatively higher temperatures and lower voltages whereas in hard anodization the application of high voltages requires the use of very low temperatures to avoid burning phenomena. The application of hard anodization conditions produce anodic coatings at a higher growth rate and with slightly different geometrical characteristics and composition [43]. The Figure 1.3 shows the evolution of D_{int} with applied voltage in mild and hard anodization conditions, leading to different scaling laws (2.5 and 2 nm/V respectively).

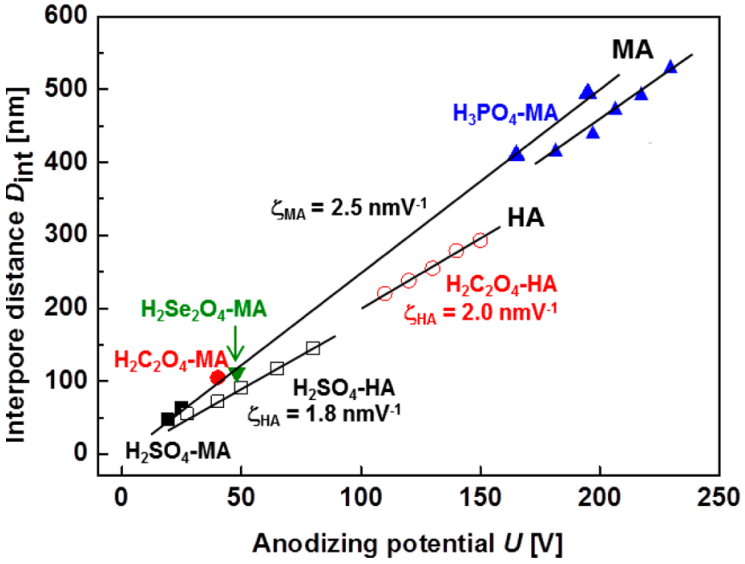

Figure 1.3: Dependency of the interpore distance on the applied anodization voltage for mild (MA) and hard anodization conditions (HA) [44].

1.2 Synthesis of nPAAMs

1.2.1 Anodization set up

A scheme of the experimental set up is represented in Figure 1.4. The core of the anodization set up is the electrochemical cell which is a jacketed glass beaker with double walls. A cooling liquid is circulated by a cryostat between the beaker's walls and ensures a constant electrolyte temperature. Inside the cell, the desired electrolyte is poured and constantly stirred by a cross shape magnetic stirrer. Stirring helps to homogenize the solution's temperature and composition. The stirrer is rotating by a stirring plate placed under the electrochemical cell. In this thesis the anodization is made under the application of constant voltage (potentiostatic conditions) and two electrodes are immersed inside the cell, the aluminum foil that serves as the anode and a platinum foil as the cathode. Two types of Pt electrodes were used, one with rectangular geometry and dimensions 2x4(cm^2),which was attached to a Pt wire of thickness 2 mm and the second electrode consisted of a Pt cylindrical mesh basket. In the case of the platinum foil, the two electrodes were placed opposite to each other, next to the cell walls while for the cylindrical one the aluminum electrode was placed in the middle of the cell. Although the geometry of the two electrodes differs and in the case of the cylindrical electrode there is divergence of the electric field while for the rectangular one there is not, no differences though were noticed on the characteristics of the membranes that were synthesized. On the contrary, after the pretreatment process of electropolishing,

the reflectivity of the surface is higher in the case of the Pt cylindical mesh. The electrodes are connected to a constant voltage power supply and a multimeter with a PC interface in order to record the current throughout the anodization. The solutions' temperature is measured by an electronic thermometer.

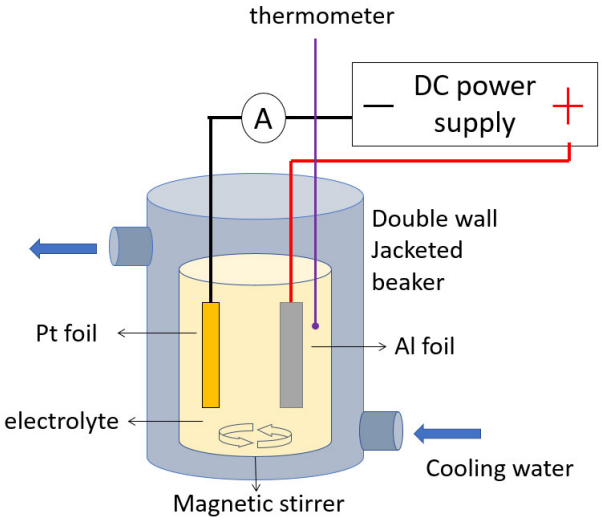

Figure 1.4: Schematic representation of the anodization set-up

1.2.2 Pretreatments

High purity aluminum foil 99.999 % with thickness 0.32 mm was cut in rectangular shape with dimensions 2.5x4 cm^2. The foils were cleansed in acetone and placed in ultrasonic bath for 5 minutes in order to degrease the surface. Before proceeding to anodization, an electropolishing step is necessary to reduce the surface irregularities of aluminum and avoid burning effects. The solution in use was a mixture of ethanol/perchloric acid 37 wt.% at a volume ratio of 75/25. The applied voltage was 20 V and the temperature set at T=10 ℃. The duration of the electropolishing was adjusted by observing the surface of the aluminum electrode. After some seconds from the initiation of the electropolishing a black membrane covering the electrode surface was peeled off by the stirring. After several seconds the aluminum acquired a mirror like appearance and the voltage tension was switched off. The foil was cleansed with water and let to dry. In the case where the platinum foil was used as electrode, the two sides of the electropolished foil were different: The side facing the platinum electrode and was closer to the convection vortex was more reflective than the other side. This was not the case for the foils electropolished with the cylindrical basket electrode, both showing the same reflectance.

1.2.3 Structural characterisation of nPAAMs synthesized under different electrolytes

The nPAAMs were synthesized by the two-step process in mild anodization conditions using three different types of electrolytes at concentrations and voltages that are given in Table 1.1. The time of the first step anodization ranged between 2-4 hours. Apart from electrolytes already explored in literature like oxalic, sulfuric and the recent selenic acid we also chose to study the effect of deuteration of the water solvent with the view to study the effect of water contamination during synthesis. The choice of these electrolytes was made to have access to the wide range of pore diameters from 10 to 60 nm. In the following we will present the current density evolution and structural characterisation of nPAAMs, synthesized in hydrogenated aqueous electrolytes. The effect of deuteration will be discussed in a different section.

Electrolyte	concentration (M)	Voltage (V)	Temperature ℃)
Oxalic acid	0.3	40	18
Sulfuric/deuterated-sulfuric acid	0.3	20	10
Selenic acid	0.3	45	0

Table 1.1: Anodization conditions used in this thesis.

1.2.3.1 Pore diameter D_p, Porosity P and specific surface S_{spe}

Scanning Electron Microscopy (SEM) images of the top surface of nPAAMs prepared in the different electrolytes are shown in Figure 1.5. As we pass to different electrolyte conditions, the size and the ordering of the pores change.

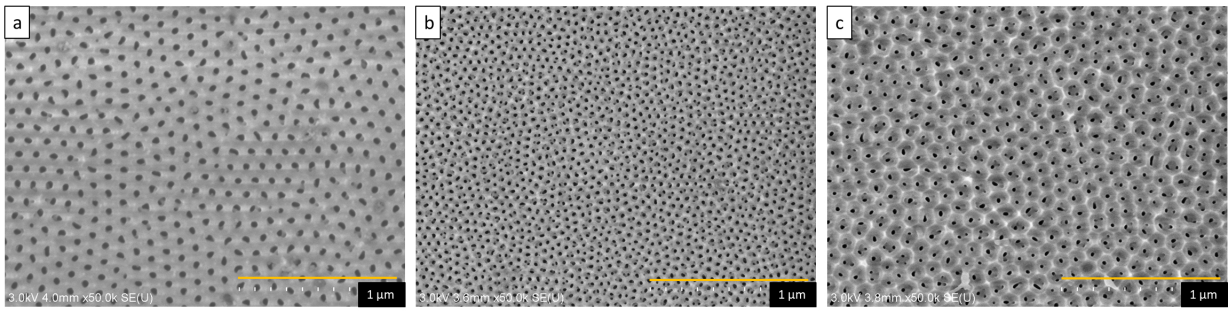

Figure 1.5: a: oxalic acid 0.3 M, 40 V, T=18 ℃ . b) sulfuric acid 0.3 M , 20 V, T=10 ℃ c) selenic acid 0.3 M, 45 V, T=0 ℃.

Through image analysis, pore diameters and porosity can be determined. The pore diameter decreases in the order oxalic>sulfuric>selenic as seen in Table 1.2. The anodization time affects also the pore diameter as the sample is gradually dissolved with time by the acidic electrolyte. Figure 1.6 shows SEM images of nPAAMs prepared in oxalic and selenic acid with different anodization time. The pore enlargement is clearly observed in the SEM images for short and long anodization times t_{an} in oxalic and selenic acid. The evolution of the pore diameter as a function of the anodization time for these samples prepared with oxalic acid is presented in Figure 1.7.

electrolyte	t (hours)	D_p (nm)	Porosity (%)	n $*10^{10}$ cm^{-2}	Specific surface m^2/g
oxalic	4	41	14.3	1.07	5.7
sulfuric	8	23	16.1	4.2	11.6
selenic	6.5	15	1.8	0.97	1.7

Table 1.2: Structural characteristics of nPAAMs prepared in different electrolytes.

It has been shown that enlargement should decrease towards the bottom of the membrane as the later formed oxide has been in contact for less time with the electrolyte. As a consequence for long anodization times, the pores diameters at the top surface are enlarged and might not be representative of the whole membrane's body. For such case, complementary to the SEM, other experimental techniques must be used, such as Small Angle Neutron Scattering (Chapter 2) or permeability measurements (see Chapter 4).

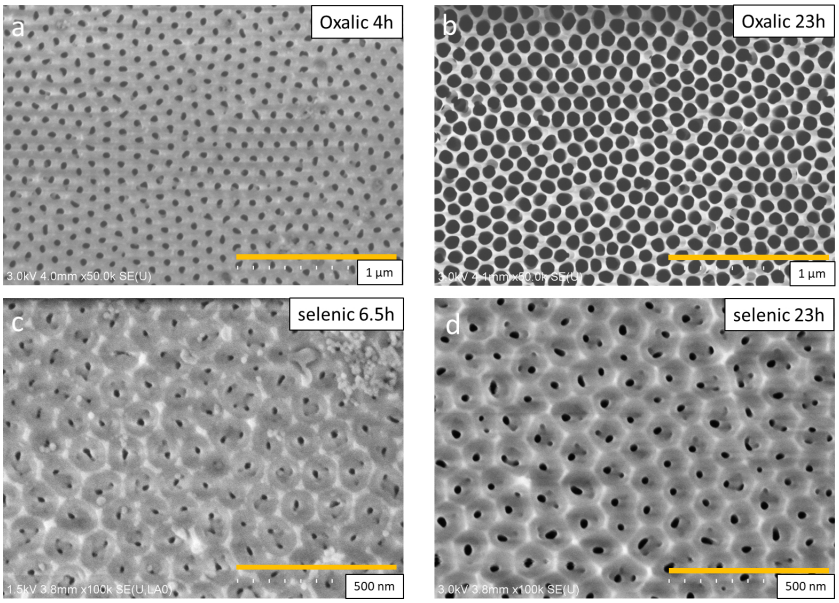

Figure 1.6: Top: oxalic acid 0.3 M, 40 V, T=18 ℃ . a) t_{an}=4 hours, D_p=42 nm b) t_{an}=23 hours, D_p=87 nm. Bottom: selenic acid 0.3 M 45 V, T=0 ℃s . c) t_{an}=6.5 hours, D_p=15 nm , d) t_{an}=23 hours, D_p=19 (nm).

From the pore diameter and porosity one can then calculate the geometrical specific surface S_{spe} of nPAAMs with the following expression:

$$S_{spe} = \frac{4}{(\frac{1}{P} - 1)D_p d} \tag{1.1}$$

with

1. P: Porosity
2. D_p: pore diameter
3. d: AAO density (here 2.88 g/cm^3 [45])

The corresponding values for the different electrolytes are shown in Table 1.2.

The specific surface has also been measured by BET measurements on oxalic nPAAMa and a value of 11.4 m^2/g by using Krypton gas has been obtained. This value is different from the expected one ($\approx 6\ m^2$ suggesting the existence of an extra porosity or roughness in nPAAMs.

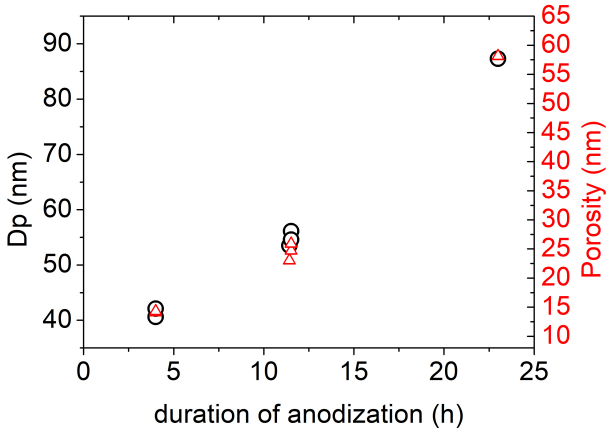

Figure 1.7: Pore diameter D_p and porosity as a function of the anodization time for membranes with no post treatments ("as prepared").

1.2.3.2 Degree of pores ordering: a structure factor analysis

In order to characterize the degree of ordering in our samples the Structure factor *S(q)* will be derived from the SEM image.

This approach has been used to characterise nPAAMs by K.Lagrené [46]. By applying an image processing method as described in the Annex (image software developed by Alexis Chennevière, LLB) the corresponding *S(q)* can be extracted for hexagonal arrangement as follows [47]:

$$S(q) = 1 - G(q) + G(q)\frac{2c_L}{\sqrt{3}a^2 q}\sum m_{hk}L_{hk}(q) \tag{1.2}$$

with

$$G(q) = e^{-\sigma_{int}^2 a^2 q^2} \tag{1.3}$$

And L_{hk}(q) is the normalized peak shape function:

$$L_{hk}(q) = \frac{1}{\delta\sqrt{\pi}}e^{-\frac{(q-q_{hk})^2}{2\delta^2}} \tag{1.4}$$

where

a: is the lattice constant which corresponds to the interpore distance D_{int} in our case.

δ: the peak width

σ_{int} :the relative standard deviation of the D_{int} distribution

Electrolyte	Voltage(V)	D_{int}(nm)	σ_{int}	G (nm)	ξ nm V^{-1}
0.3M oxalic	40	106	0.06	785	2.65
0.3M sulfuric	20	55	0.106	286	2.75
0.3M selenic	45	107	0.524	524	2.38

Table 1.3: Comparative table with the fitting parameters of the *S(q)* for membranes prepared under different electrolytes and voltage

G: the extent of the ordered domains (called here grain size

$$G = \frac{2\pi}{\delta}$$

) can also be extracted from the S(q) fitting.

m_{hk} is the multiplicity factor (here fixed to 3) and c_L is a correction factor for the Porod invariant [48].

The first term 1-G(q) of equation 1.2 takes into account the diffuse scattering induced by the disorder in the lattice positions while the second term accounts for the corresponding decrease in the intensity of the Braag peaks.

In Figure 1.8 the experimental structure factors derived from SEM images are presented for the three types of membranes (oxalic, sulfuric and selenic) and the fit using an hexagonal structure factor provides the values presented in Table 1.3.

The S(q) of the different nPAAMs show similar general features with the presence of peaks whose positions and amplitude give information about the degree of pore ordering. Note that we chose the same hexagonal model to fit the three S(q). It is clear that sulfuric and selenic are not hexagonally ordered and the S(q) can be fitted with a hard sphere model [46].

By comparing both σ_{int} and the average grain size G we can conclude that the best ordering is observed for the sample prepared in oxalic acid. It is known that the highest ordering occurs at a specific voltage value for each electrolyte. Samples prepared in 0.3 M oxalic are best ordered at 40 V while sulfuric and selenic under 25 V and 48 V respectively [49, 50, 51]. In the case of sulfuric acid lowering the applied voltage was chosen in order to shift the pore diameter to lower values at an expense of the ordering, while for selenic sample, the applied tension was the highest voltage where no burning occurred during the synthesis. Through the S(q) analysis one can quantify the structural organisation and degree of ordering nPAAM. The structural parameters will be then used for the complete fitting of SANS curves (see Chapter 2).

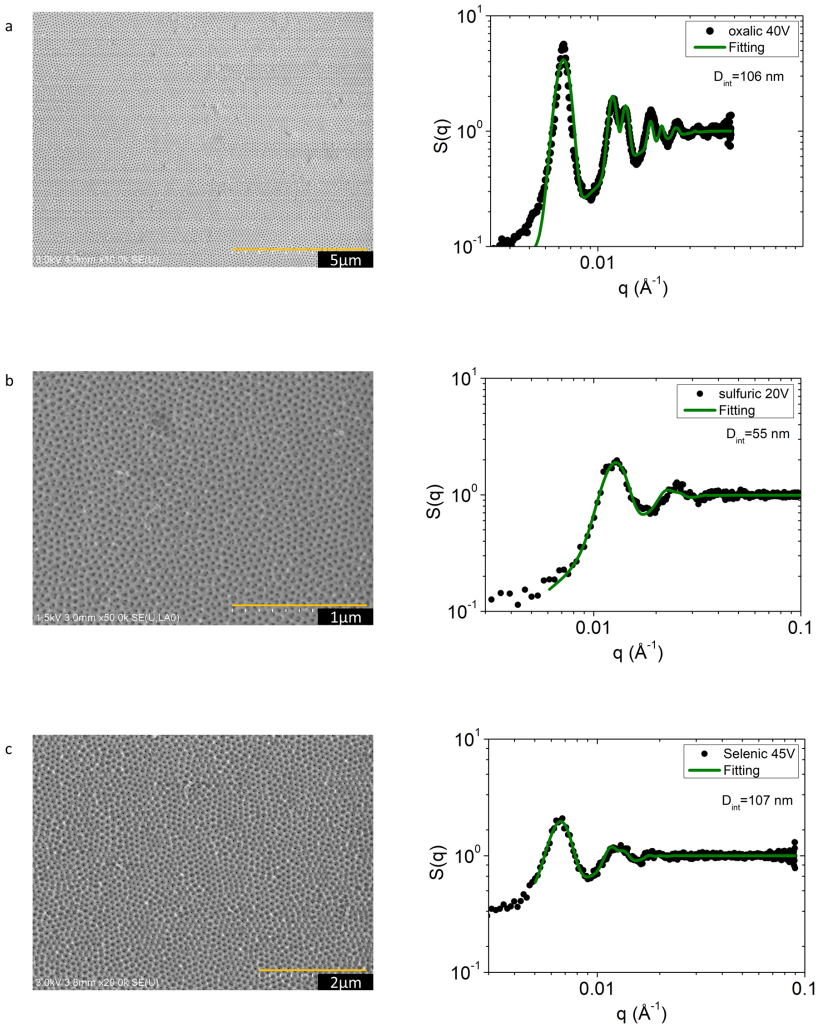

Figure 1.8: SEM images of top surface of nPAAMs prepared by two-step anodization under different conditions. a) Oxalic acid 0.3 M, 40 V, T=18 ℃, t=4 hours. b) Sulfuric acid 0.3 M, 20 V, T=10 ℃ t=8 hours. c) Selenic acid 0.3 M, 45 V, T=0 ℃, t=6.5 hours.

1.2.3.3 Oxide thickness

The enlargement in the pore diameter sets a limit on the maximum thickness of oxide that can be synthesized in these mild anodization conditions. The thickness of the porous alumina membrane h depends linearly on duration of the anodization time t as seen in Figure 1.9 for oxalic nPAAMs for which we can attribute an average growth rate R_{ox} of 7.0 μm/h, for the membranes prepared at these anodization conditions (40 V, T=18 ℃).

As the anodization time increases the wall of the pores dissolves and the porous network is destroyed. The pore cell can be assumed to be hexagonal and in this case the wall w thickness is defined by:

$$w = \frac{D_{int} - D_p}{2} \tag{1.5}$$

It can be seen that the maximum thickness to be reached before the collapse of the wall is obtained before 30 hours of anodization for nPAAMs synthesized in oxalic acid.

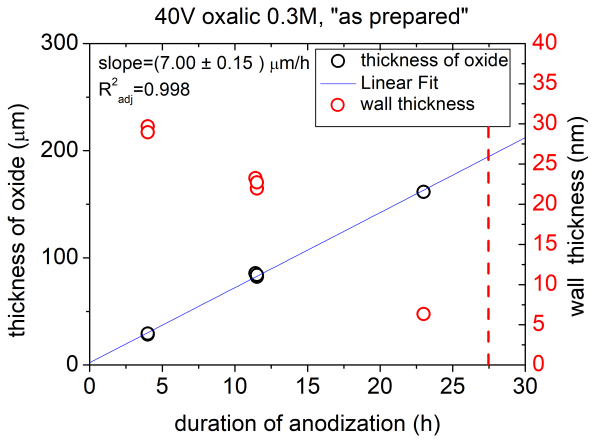

Figure 1.9: Pore wall thickness w and oxide thickness h a function of the anodization time for membranes prepared in oxalic acid (0.3 M, 40 V and T=18 ℃). The vertical dash line corresponds to the wall collapse.

1.2.3.4 Relation between anodization current density and growth rate

During mild anodization, the recorded current evolves typically as presented in Figure 1.10. The behaviour of current with time at the first seconds of the anodization is connected to the pore initiation, growth and ordering as shown by recent ex-situ study of the oxide morphology by SEM and in-situ by Grazing Transmission X-ray Scattering (GI-SAXS)[52, 53] .

The current curve is characteristic of a porous oxide formation and is usually separated in three stages. Initially the current falls exponentially until a certain minimum is reached (zone 1 in Figure 1.10). This stage is related to the oxidation of the aluminum surface and the formation of a barrier type oxide. Then, the current increases (zone 2) which is related to the pores nucleation on the oxide surface and as a consequence the increase of the anodization surface. The pores finalize their positions at the maximum distance and this corresponds to the overshoot in the current versus time graph. Finally, the current slightly decreases and reaches a constant value (zone 3). At this point the anodization reaches a steady state and the pores grow at a constant growth rate.

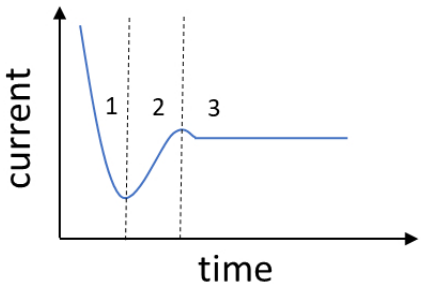

Figure 1.10: Schematic depiction of the typical current versus time graph for mild anodization.

Figure 1.11 shows the current density j versus time for the three different electrolytes for both 1^{st} and 2^{nd} anodization step. The current density is calculated as the ratio of the current I to the surface S exposed to the electrolyte during anodization. All curent density curves present the same overall behaviour depicted in Figure 1.11. However, differences are observed between the 1^{st} and the 2^{nd} anodization curves. The minimum is larger for the 1^{st}, the constant value is reached earlier at the 2^{nd} step and there is no overshoot of the current density j at the 2^{nd} step. These differences can be explained by the morphology of the aluminum surface prior to anodization. After the dissolution of the oxide formed in the 1^{st} step, the aluminum substrate is patterned with ordered concave imprints of the pores formed during the 1^{st} step. As a consequence, during the 2^{nd} anodization the substrate possess a higher surface available for the electrochemical reactions at the interface. The

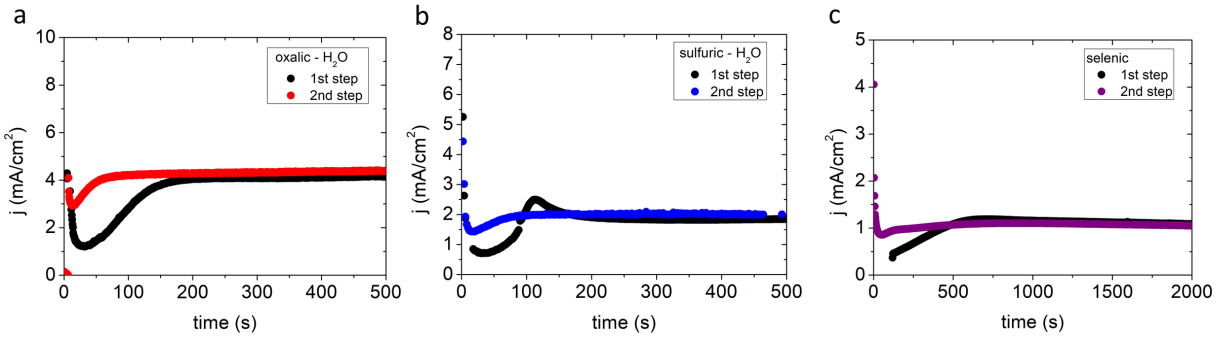

Figure 1.11: Typical behaviour of current density versus time for 1^{st} and 2^{nd} anodization in a) oxalic acid 0.3 M b) sulfuric acid 0.3 M c) selenic acid .

ordered pattern of the surface facilitates the pores to reach their equilibrium positions at an earlier time.

It should be mentioned that the appearance of an overshoot point in the current density versus time graph is more pronounced at voltages just below the breakdown voltages. This explains the presence of the overshoot only for the sulfuric acid nPAAMs and not for the others.

The current is proportional to the rate of the electrochemical reaction for the oxidation of aluminum. If we assume that there are no other faradaic reactions that contribute to the total charge then the area under the current versus time graph equals the total charge that comes from the oxidation of aluminum according to equation 1.6.

$$Al \rightarrow Al^{3+} + 3e^{-} \tag{1.6}$$

The mass of aluminum cations that have been produced is given by law in equation 1.7.

$$m_{Al^{3+}} = \frac{M_{Al} Q_{tot}}{3F} = \frac{M_{Al} \int_0^t I dt}{3F} \tag{1.7}$$

where

- Q_{tot} : the total charge produced by the oxidation
- I: current
- t : time
- z: the number of electrons associated with the oxidation, in the case of aluminum z=3
- F: Faraday constant, the charge of one mole of electrons (96485.33 C/mol)
- M_{Al} : Molar mass of Aluminum = 27 g/mol

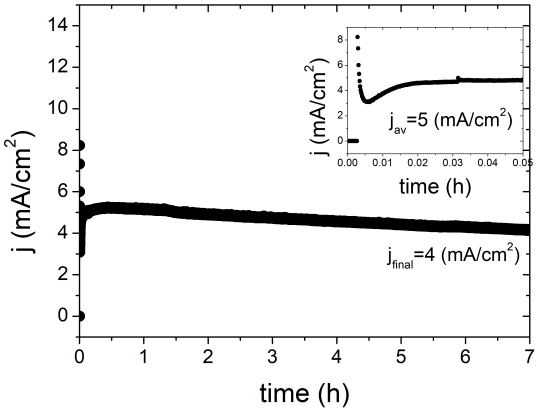

Figure 1.12: Current versus time graph for long anodization of sample prepared in oxalic acid 0.3 M under 40 V and T=18 ℃.

In the next paragraphs a quantitative study will be made on the moles of aluminum cations that have been produced and the total charge that we record during the experiment (see next section).

For now, it is not clear, what is the rate determining step for the formation of alumina (e.g oxidation of aluminum, reaction with oxygen, oxide displacement rate, ionic migration through the barrier layer, dissociation of water) and consequently which interface or region involves (e.g metal/oxide, bulk oxide, oxide/electrolyte). Nevertheless, in these mild anodization conditions where the current attains a constant value, the reaction rate is controlled by processes at the bottom of the pores. In terms of kinetics this is called the "migration controlled" region [49] . As the pores increase in thickness, the reaction rate starts to be limited by the diffusion of oxygen carrying species (O^{2-},OH^{-}) from the bulk electrolyte to the pore bottoms. The oxygen anions are depleted at a certain rate at the pore bottoms. If the diffusion rate of fresh electrolyte is slower that its depletion rate at the pore bottoms, the reaction rate will response by a decrease until the two rates equilibrate. Long term equilibrium cannot be reached because the pore channel is continuously growing. For this reason during long anodization times the current continuously decreases as seen in Figure 1.12 up to 10 % in 7 hours. This effect is a similar, but less pronounced, (due to the lower applied voltages) than in "hard anodization" conditions where the current decreases exponentially with time [43] .

Another useful relation that emerges from the structural analysis is the dependency of the thickness growth rate G_r with the average current density j_{av} as seen in Figure 1.13. The thickness growth rate is calculated using SEM section images and is equal to:

$$G_r = \frac{h}{t} \tag{1.8}$$

where,

h: thickness of the nPAAMs

t: anodization time

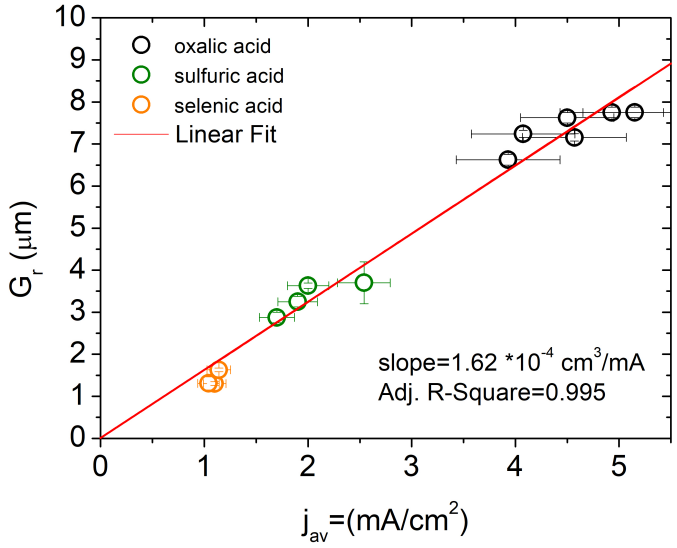

Figure 1.13: Thickness growth rate G_r as a function of average current density j_{av}.

It is observed that independently of the electrolyte in use, the growth rate G_r varies linearly with the current density with the proportionality constant of $1.6 * 10^{-4}(cm^3/(\text{mA}))$. Moreover, the variability in the achieved current density for each electrolyte can be explained in terms of error in the surface calculation, temperature measurement and agitation speed. The current density appears to be a global parameter through which different anodization conditions can be compared.

1.2.4 Growth mechanism and anodization efficiency

In this section, a brief description of the proposed models for growth mechanism of nPAAM will be given and an experimental quantity, the total amount of Al^{3+} produced, will be measured by titration and compared to the value calculated from the recorded charge at the external circuit. The results will be discussed in comparison to one of the proposed models for the porous alumina formation mechanism.

Since the discovery of the porous structure obtained by electrochemical anodization of aluminum, the different scientific groups tried to explain:

1. What initiates the formation of pores?
2. What is the growth mechanism of the porous oxide ?

Several models have been proposed throughout the years and a big part of this vast bibliography has been recently organized by J.M. Runge [54]. The basic models are:

1. field assisted dissolution
2. viscous flow
3. oxygen evolution
4. Electrohydrodynamic convection

Electrohydrodynamic convection has been recently proposed by certain researchers as the mechanism of formation of porous alumina [55, 56]. Inspired by the self ordering behaviour in other systems like in the case of Rayleigh-Bénard cells, it is proposed that in a similar way cells of nanoconvective flow of the electrolyte just above the pores controls the deposition of alumina colloids on the electrode. In an attempt to predict new experimental conditions for the appearance of porous oxide, a semi-empirical parameter that depends on physical chemical parameters (pH, C, Voltage, viscosity, conductivity) is proposed [57, 58].

The model of field assisted dissolution (F.A.D) is one of the oldest model and has been partially rejected. It states that the pores result from oxide dissolution at surface irregularities of the oxide (such defects, hillocks etc.) and that the chemical dissolution is enhanced by the electric field. The pore growth is realised through equilibrium process of oxide dissolution and oxide growth at these points. This model has been rejected as a possible mechanism for the growth by J.Siejka and C.Ortega, showing that there is no dissolution of oxygen from the oxide into the electrolyte [59]. Furthermore, by comparing the anodization efficiency to the amount of the oxygen in the oxide they deduced that, instead of a decomposition of the

oxide, an ejection of Al^{3+} into the electrolyte takes place [60]. Nevertheless, the role of the electric field seems to play an important role and field assisted dissolution has been proposed to take place at low current densities and to be responsible for the appearance of incipient pores at the onset of the anodizaton while the appearance of major pores is attributed to mechanical deformation (plastic flow of the oxide) [61, 62].

Indeed the displacement of oxide material from the base of the pores towards the pore wall has been experimentally observed. A number of studies have studied this oxide movement by following tracers (such as W, Xe) that have been implanted inside the aluminum substrate prior to the anodization [63]. Garcia-Vergara et al. followed the movement of tungsten implants after the anodization of the aluminum by means of TEM section images and Rutherford Backscattering Spectroscopy (RBS) [64]. They proposed that the pore develops due to volume expansion of the oxide and electrostriction. The idea of stress driven flow of the oxide has been modeled and it was suggested that the compressive stress arises due to electrolyte anion incorporation and adsorption on the oxide rather than to the volume expansion during conversion of the metal to the oxide [65]. The residual stress in the oxide was measured in open circuit dissolution and related to the electrolyte anions incorporated in the oxide by X-Ray Photoelectron Spectroscopy (XPS) [66, 67].

Finally, the oxygen evolution model proposes that the continuous generation of oxygen bubbles inside the oxide acts as a mould that create the characteristic pore shape [68, 69]. The basis of this model is the formation of oxygen gas at the electrolyte/oxide interface according to [70]:

$$2O^{2-} \rightarrow O_2 \uparrow +4e^- \tag{1.9}$$

or

$$4OH^- \rightarrow O_2 \uparrow +2H_2O + 4e^- \tag{1.10}$$

Moreover, it is proposed that the electrolyte anions incorporate in the oxide and release electrons in the oxide conduction band. These electrons are accelerated by the field and promote the generation of more electrons as in an avalanche mechanism. These two processes, the oxygen evolution and the electrolyte anion incorporation, produce an electronic current j_e that doesn't contribute to the formation of Al_2O_3 but is contributing to the recorded current in the external circuit. Thus, the total anodic current j_T is:

$$j_T = j_{ion} + j_e \tag{1.11}$$

The oxide grows due to the j_{ion}, which is attributed to the O^{2-} and OH^- reaction with

Al^{3+}.

As it can be concluded, the generated electrons must be recorded at the external circuit, else we have to assume that a sink for electrons exists inside the oxide.

In order to quantify the electronic current recorded at the external circuit, we will compare the total recorded charge during the 1^{st} anodization with the total amount of Al produced. In practice we measured by Inductively Coupled Plasma Optical Emission (ICP-OES) and flame spectroscopy the quantity of Al^{3+} , (using a wavelength of 394.4 nm and a calibration curve has been established prior to any measurements) in:

1. the electrolyte solution after anodization
2. the solution in which the produced alumina was dissolved (either using 5% wt. H_3PO_4 or phosphochromic solutions, see below)

For these experiments, we used fresh electrolyte solutions 0.3 M of oxalic, sulfuric or selenic acid in hydrogenated or deuterated solvent. Note that prior to any anodization these electrolytes have been titrated as a reference.

By the number of moles of Al^{3+} coming from the dissolution of alumina and present in the electrolyte solution, the total quantity of Al^{3+} produced by the oxidation of aluminum is extracted, from which we can calculate the electrical charge ($Q_{titration}$) using the Faraday's law:

$$Q_{titration} = neF = 3n_{Al^{3+}}F \tag{1.12}$$

Then, $Q_{titration}$ is compared to the total electrical charge (Q_{tot}) used in the anodization by integrating the current passed in the circuit versus time. Finally we can also calculate the reaction efficiency (η) by the ratio of the number of moles of titrated Al^{3+} from the dissolution of alumina to the total number of moles of produced Al^{3+}, giving values in agreement with the literature (between 60% to 78%). Table 1.4 shows the different titration results from ICP-OES when using 5% wt H_3PO_4 to dissolve the produced alumina.

By comparing the values, the ΔQ differ from one electrolyte to another from 28.4% to 7.8%, suggesting some small deviations. Note that, if oxygen evolution occurs, Q_{tot} would have been larger than $Q_{titration}$. In all cases, $Q_{titration} > Q_{tot}$, indicating that an excess of Al^{3+} is measured. This excess may originate from the existence of native alumina prior to anodization and/or to the fact that we used phosphoric acid solution to dissolve alumina. Indeed, the dissolution time was fixed to 2h (except for selenic electrolyte, which was 2h15) and during this time the alumina can be fully dissolved and subsequent Al self-corrosion can occur releasing extra Al^{3+} in the solution. The largest ΔQ is observed for samples having

Electrolytes	Selenic/H_2O	Sulfuric/H_2O	Sulfuric/D_2O	Oxalic/H_2O	Oxalic/D_2O
Applied Voltage (V)	45	20	20	40	40
T (℃)	0.7	10	10	18	18
t_{ano} (h)	2	2	2	2	2
Current density j (mA.cm^{-2})	0.59	2.45	3.93	5.28	3.48
$Q_{titration}$ (C)	19.7	61	67.81	107.35	63.42
Q_{tot} (C)	15.33	54.13	62.9	97.77	57.49
ΔQ (%)	28.4	12.7	7.8	9.8	10.4
Efficiency η	0.784	0.687	0.749	0.663	0.732

Table 1.4: Experimental parameters used for the synthesis of nPAAMs (applied voltage, temperature and time). Total electrical charge calculated from current (Q_{tot}), electrical charge calculated from titration ($Q_{titration}$), percentage difference between the charges (ΔQ), real reaction efficiency (η).

the smallest amount of produced alumina, i.e. the largest possible self-corrosion. To validate this hypothesis we conducted similar titration experiments and dissolved the produced alumina with phosphochromic acid solution classically used in the two-step anodization process. Figure 1.14 shows the SEM images of the samples after dissolution of the produced alumina in (a) phosphoric acid during 2h and (b) in phosphochromic acid during 3h. The imprints of the formed pores are still visible after dissolution in phosphochromic while there are no imprints after dissolution in phosphoric acid.

Table 1.5 shows the titration results from flame spectroscopy. Note that the Q values are larger than the ones in Table 1.4 because larger samples were produced to improve the Al^{3+} detection by flame.

ΔQ is decreased in both cases from 28.4 to 8.4% for selenic and from 9.8 to 5.5% for oxalic and now Q_{tot} is larger than $Q_{titration}$. It suggests that some current does not contribute to the formation of alumina; it corresponds to a charge of 19.3 C and 32 C for selenic and oxalic, respectively, i.e. to a current density of 0.11 and 0.27 mA.cm^{-2}. This value is quite small and it could be attributed to the experimental error for the calculation of the current density.

However, this current density contribution might also come from oxygen evolution releasing electron in the external circuit according to equation 1.9,1.10.

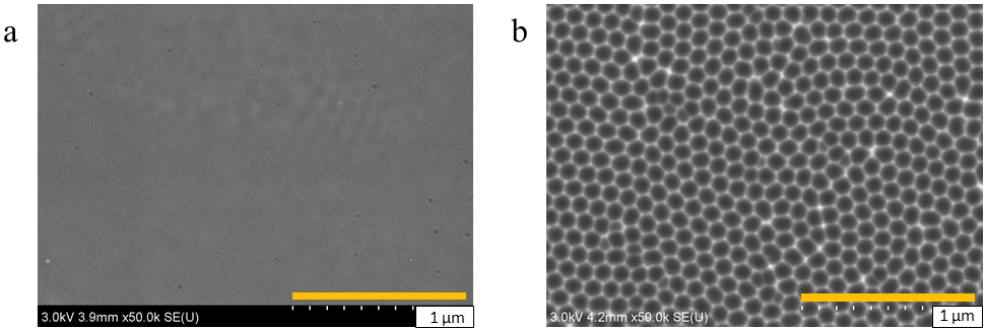

Figure 1.14: SEM images of aluminum after dissolution of the produced alumina in (a) phosphoric acid during 2h and (b) in phosphochromic acid during 3h. The first anodization was done in oxalic/H_2O electrolytes at 18 ℃ during 2h.

Electrolytes	Selenic/H_2O	Oxalic/H_2O
Applied voltage (V)	45	40
T (℃)	0.7	18
t_{ano} (h)	2	2
Current density j (mA.cm^{-2})	1.37	5
$Q_{titration}$ (C)	210	552.7
Q_{tot} (C)	229.3	584.7
ΔQ (%)	8.4	5.5
Efficiency η	0.714	0.593

Table 1.5: Experimental parameters used for the synthesis of nPAAMs (applied voltage, temperature and time). Total electrical charge calculated from current (Q_{tot}), electrical charge calculated from titration ($Q_{titration}$), percentage difference between the charges (ΔQ), real reaction efficiency (η).

Zhu, X.-F. et al [70] proposed that the current density due to this contribution (named here j_{O2}) should be equal to j_{O2} = (1- η)j, j being the total current density (see Table 2). This calculation gives 0.39 and 2.03 mA.cm^{-2}, clearly larger than the measured one (0.11 and 0.27 mA.cm^{-2}). It can be concluded that the residual charge is very low and probably in the experimental error of the measurement. Thus, the side reactions that involve charge transfer on the electrode, such as the ones proposed by the oxygen evolution model cannot hold true.

Our results are also in line with other works titrating the amount of Al [71] where the electronic current was considered as negligible. Then they show that the Al dissolution rate in electrolyte is linear with the current density, indicating that direct Al^{3+} ejection occurs instead of field assisted dissolution. Here, Figure 1.15 shows that the dissolution rate of Al in electrolyte with current density also scales linearly with current density. Interestingly this graph gathers data from different electrolytes (selenic, sulfuric and oxalic in H_2O) suggesting

that this behaviour is independent of electrolyte nature and only depends on the current density.

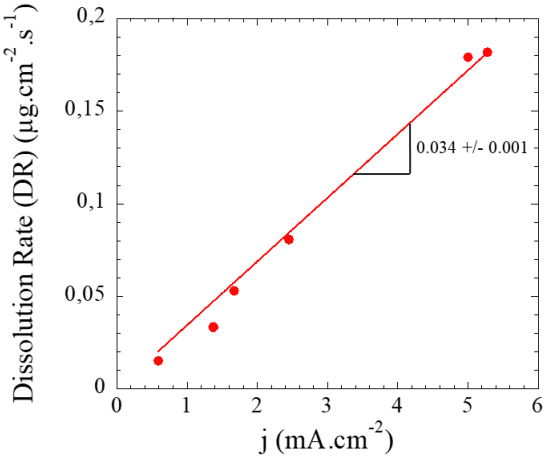

Figure 1.15: Al dissolution rate in electrolyte as a function of current density j. This plot gathers data from different electrolytes (selenic, sulfuric and oxalic in H_2O). The slope is in line with previous works [71] .

1.2.5 Influence of deuterium on pore organisation and growth rate

Apart from the classical electrolytes (oxalic, sulfuric, phosphoric), new experimental windows are explored in the aim of verifying theoretical models [72] for the porous alumina formation mechanism. The need of tuning the pore morphology and growth rate G_r led to the exploration of the effect of additives in the electrolytes such as ethylene glycol. For example, it has been reported that with the addition of ethylene glycol during citric acid anodization, burning effects can be supressed [30]. In another study, a certain ratio of ethylene glycol in oxalic acid electrolyte changed the growth of the nPAAM from nanopores to nanotubes [73]. A lower G_r accompanied with a smaller pore diameter (D_p) is observed when adding a certain amount of polyethylene glycol [74]. This additive increases the viscosity and decreases the acidity of the electrolyte mixtures. Other authors showed that, in glycerol solution of oxalic acid, the nPAAMs thicknesses are linearly dependent on the inverse of electrolyte viscosity [75]. Ethanol and ionic liquids have also been used to increase the G_r. Qin et al. found that 10% of ethanol can increase the G_r by a factor of 5 with a D_p of 15 nm while keeping the voltage low (25 V) [76]. Note that the addition of more ethanol has the reverse effect, i.e. decrease the G_r. Similarly Salerno et al. showed that the use of ionic liquids (1-Butyl-3-methyli- midazolium 2-(2-methoxyethoxy) ethyl sulfate and 1-Butyl-3-methy- limidazolium tetrafluoborate) in oxalic acid under galvanostatic conditions also increases the G_r[77].

In this context we chose to use deuterated solvent (heavy water, D_2O) and deuterated electrolytes (D_2SO_4) to:

1. investigate the structural pore organization (see below)

2. gain understanding on the chemical composition of nPAAMs by Small Angle Neutron Scattering (SANS, see Chapter 2).

So far, few works involved deuterated species for nPAAMs synthesis. Dorsey used deuterated electrolytes to elucidate the hydration of the anodic films by infrared absorption spectroscopy [78]. Lu and coworkers studied the diffusion of hydrogen/deuterium through the barrier layer in thin films synthesized on Si wafers by Secondary Ion Mass Spectroscopy [79].

In this section we will investigate the effect of deuterium substitution on the structural pore organization, morphology and growth rate. We will also compare the current densities of deuterated nPAAMs with the hydrogenated ones to gain understanding on the G_r evolution. Table 1.6 summarizes the different physical and chemical parameters of the different electrolytes used in this section. Note that for sulfuric electrolyte the applied voltage was fixed to 20 V since the breakdown voltage was 21 V in D_2O at 4 ℃. Electrolytes concentration is kept fixed at 0.3 M and pH and conductivity were also measured for all solutions. The viscosity of the electrolyte was taken equal to the viscosity of the solvent used (H_2O or D_2O).

Electrolyte	H_2SO_4/ H_2O	$H_2SO_4^a$/ D_2O	D_2SO_4/ D_2O	Oxalic/ H_2O	Oxalic/ D_2O
Applied voltage (V)	20	20	20	40	40
Concentration (M)	0.3	0.3	0.3	0.3	0.3
pH / pD^b	0.51	0.3 / 0.71	0.50 / 0.91	0.73	0.81 /1.22
Conductivity σ mS.cm^{-1} at 22 ℃	133.5	84.2	73.7	46.9	25.6
solvent viscosity cP at 20 ℃	1	1.25	1.25	1	1.25

Table 1.6: Physical and chemical parameters of the different electrolytes used in this study. [a] contains 0.16% v/v of H_2O. [b] The pD of heavy water is generally measured using pH electrodes giving an apparent pH value and the true acidic pD can be estimated directly from the measured pH as pD= pH + 0.41 [80].

1.2.5.1 Pore morphology and organization

Sulfuric acid electrolyte Figures 1.16a, 1.16b and 1.16c show the SEM images of nPAAMs synthesized in, respectively, deuterated sulfuric acid in D_2O (D_2SO_4/D_2O), hydrogenated sulfuric acid in D_2O (H_2SO_4/D_2O) and hydrogenated sulfuric acid in H_2O (H_2SO_4/H_2O) at T=10 ℃ under 20 V during 8 h. Image analysis give similar pore densities but different pore diameters D_p of 19.6±3.0 nm, 15.8±3.4 nm and 15.6±3.0 nm for H_2SO_4/H_2O, H_2SO_4/D_2O and D_2SO_4/D_2O, respectively, corresponding to D_p decrease of around 20% when using deuterated water (see Table 1.7). When anodizing during a shorter time (2 h) the pore diameters are smaller (around 12.5 nm, see Figure 1.16e) and remain similar whatever the electrolyte used, indicating that the pore etching is time dependent and enhanced in H_2O after a long time. This can be explained by a stronger acidity of the hydrogenated electrolyte (see pH values in Table 1.6).

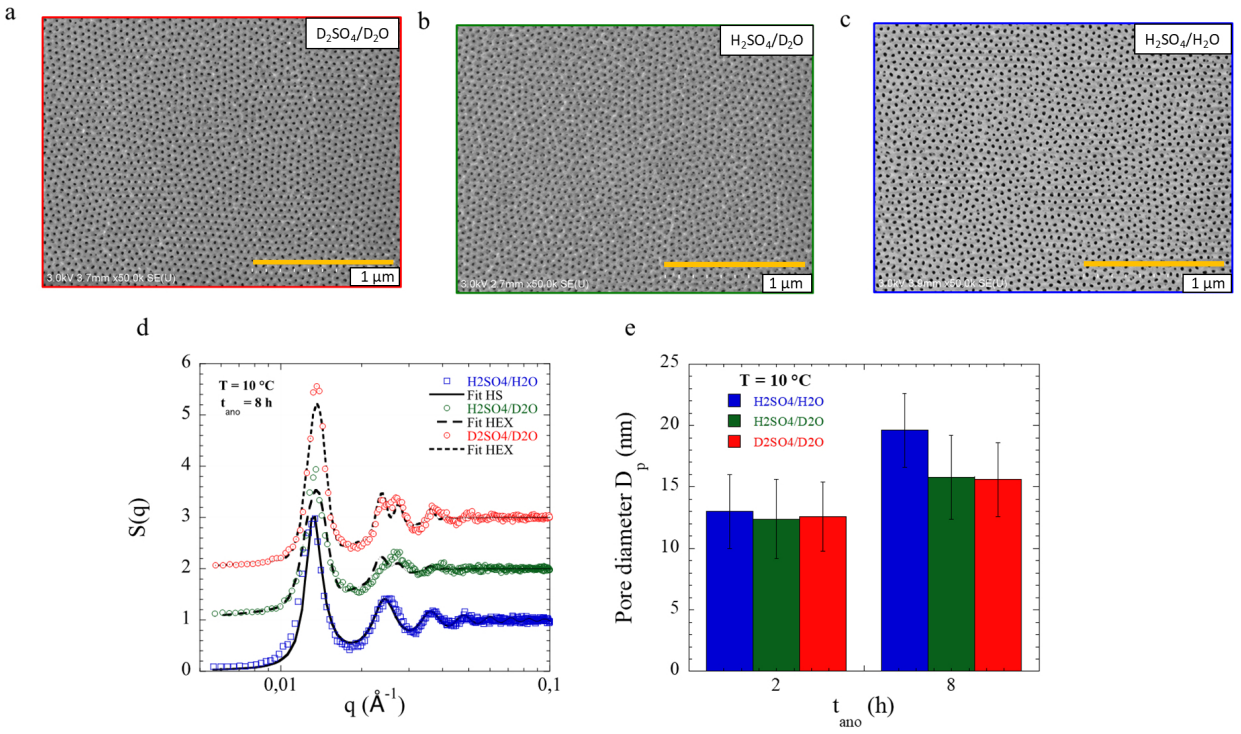

Figure 1.16: SEM images of top surface of (a) D_2SO_4/D_2O, (b) H_2SO_4/D_2O and (c)H_2SO_4/H_2O nPAAMs. (d) Structure factor S(q) derived from the SEM images analysis fitted with hard sphere model for H_2SO_4/H_2O and with a hexagonal model for H_2SO_4/D_2O and D_2SO_4/D_2O. The curves have been shifted vertically for clarity. (e) Pore diameter for the three systems after 2 h and 8 h anodization.

The structure factor S(q) derived from the SEM images are shown in Figure 1.16d. They are fitted with a hard sphere model for H_2SO_4/H_2O and a hexagonal model for H_2SO_4/D_2O

and D_2SO_4/D_2O (the parameters are also listed in Table 1.7). Compared to the hydrogenated sample the the S(q) of the deuterated one, shows clear peaks at intermediate q coming from a better hexagonal pore organization, as observed on the SEM images and confirmed by a larger hexagonal grain size. Note that the deuterated nPAAMs S(q) cannot be fitted with a hard sphere model. Interpore distances D_{int} remain unchanged while the grain size of ordered domains is larger for the deuterated samples. Thus the pore organization is more hexagonally ordered when the nPAAMs are synthesized in deuterated electrolytes and the pore diameters are smaller.

Electrolytes	H_2SO_4/H_2O	H_2SO_4/D_2O	D_2SO_4/D_2O	Oxalic/H_2O	Oxalic/D_2O
t_{ano} (h)	8	8	8	11h30	11h30
D_p (nm)	19.6+/-3	15.8+/-3.4	15.6+/-3	56+/-7	44+/-8
n ($*10^{10}$ cm^{-2})	4.4	4.5	4.2	1.2	1.1
Porosity (%)	16	12	9	28	17
D_{int} (nm)	52.6	52.8	52.7	101	101
σ_{int} / η^*	0.49	0.098	0.084	0.065	0.063
Grain size (nm)	-	314	370	785	898
P_{ord}	0.154	0.124	0.089	0.529	0.251

Table 1.7: Structural parameters obtained from SEM analysis of the nPAAMs synthesized in the different electrolytes at T=10 ℃: pore diameter D_p, pore density n, porosity, interpore distance D_{int}, D_{int} standard deviation σ_{int}, grain size and ordering parameter P calculated from Pashchanka [81]. * For H_2SO_4/H_2O the S(q) is fitted with a hard sphere model giving an ordering parameter η. Also the grain size cannot be determined with this model.

Temperature (℃)	4	7	10	15	20
D_p (nm)	13.6 ± 2.8	13.8 ± 2.6	14.0 ± 3.0	15.4 ± 2.8	22.2 ± 2.0
D_{int}	52.4	52.4	53.4	52.6	53.4
σ_{int}	0.085	0.091	0.104	0.087	0.074
δ ($Å^{-1}$)	0.0019	0.0020	0.0018	0.0020	0.0016
Grain size (nm)	331	0 314	349	314	393

Table 1.8: Structural parameters obtained from SEM analysis of the nPAAMs synthesized in D_2SO_4/D_2O at different temperature for an anodization time of 6 h.

We now turn to find out what experimental parameters optimize the ordering of nPAAMs synthesized in D_2SO_4/D_2O and how D_p is affected. Figure 1.17 shows the influence of temperature on the nPAAMs ordering. The SEM images (Figure 1.17a) analysis showed a

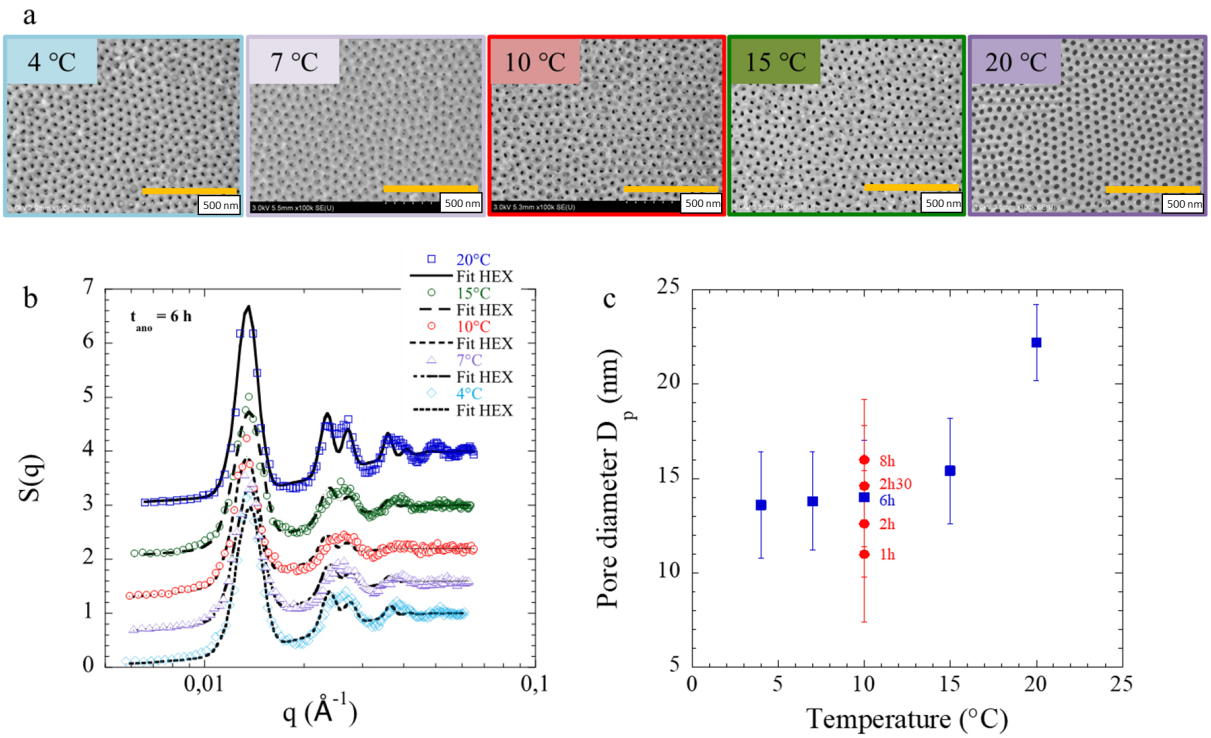

Figure 1.17: (a) SEM images of nPAAMs synthesized in D_2SO_4/D_2O during 6 h at different temperatures. (b) Structure factor S(q) derived from the SEM images analysis of nPAAMs prepared in D_2SO_4/D_2O at different temperatures with the corresponding hexagonal fits. (c) Evolution with temperature of pore diameters at a given anodization time (6h, blue squares) and with time at a given temperature (10℃, red circles).

slight increase of pore diameter up to 15 ℃ and a clear increase at 20 ℃ (Figure 1.17c, blue squares and Table 1.8. Similarly the S(q) analysis show quite similar ordering between 4 ℃ and 15 ℃ and a slightly better ordering at 20 ℃ (smaller σ_{int} and a larger grain size, see Table 1.8). The increase of anodization time doesn't change the ordering (see Figure 1.18a and Table 1.9, slightly better after 6 h of anodization) but an increase of pore diameter is observed as expected due to the etching in acidic solution.

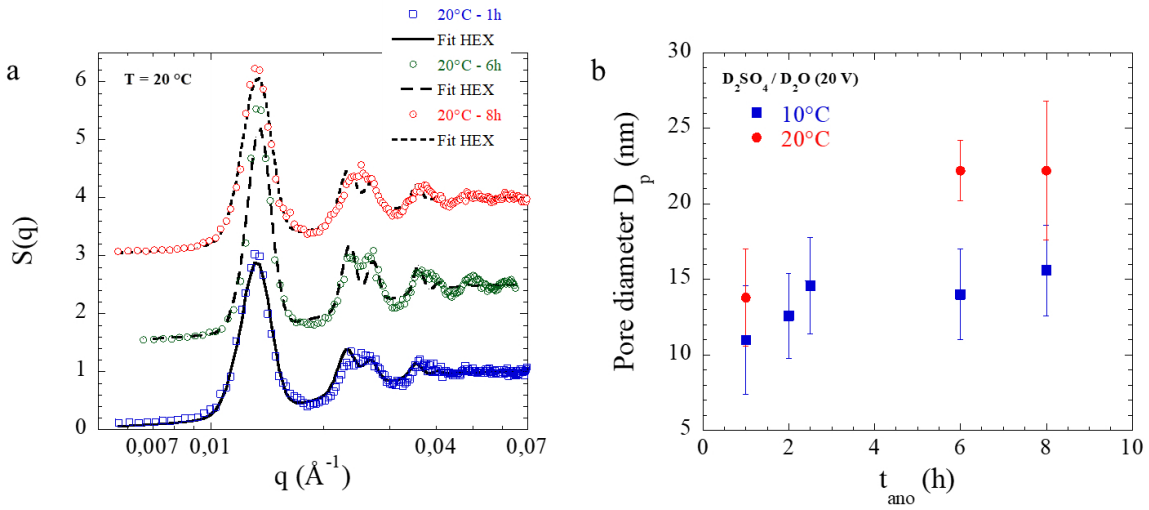

Figure 1.18: (a) Structure factor S(q) derived from the SEM images analysis of nPAAMs prepared in D_2SO_4/D_2O at 20 ℃ during different times (1 h, 6 h and 8 h). (b) Evolution with anodization time of pore diameters of nPAAMs prepared in D_2SO_4/D_2O at 10 ℃ (blue squares) and 20 ℃ (red circles).

Time (h)	1	6	8
D_p (nm)	13.8 ± 3.2	22.2 ± 2.0	22.2 ± 4.6
D_{int}	54	53.4	53.7
σ_{int}	0.083	0.074	0.077
δ (Å^{-1})	0.00196	0.0016	0.0019
Grain size (nm)	320.6	392.7	330.7

Table 1.9: Structural parameters obtained from SEM analysis of the nPAAMs synthesized in D_2SO_4/D_2O at 20 ℃ at different anodization times.

Oxalic acid electrolyte Similar analyses have been performed with oxalic electrolyte. Note that here the oxalic acid remains hydrogenated. Figure 1.19 shows the SEM images of nPAAMs prepared in Oxalic/H_2O and Oxalic/D_2O and Figure 1.19 show the corresponding S(q) derived from the images analysis fitted with an hexagonal model. Similar trends are observed in oxalic: a decrease of pore diameter in deuterated solvent and a slightly better hexagonal organization: the grain size increases from 785 nm to 898 nm (14 % increase, see Table 1.10).

The apparent increase of ordering when using deuterated solvent can be reconcile with the recent work of Pashchanka and Schneider [81]. They proposed an empirical parameter P_{ord} derived from the concept of self-organized electrohydrodynamic convection to quantify the degree of ordering and predict the ordering of nPAAMs based on the different physical and chemical experimental parameters:

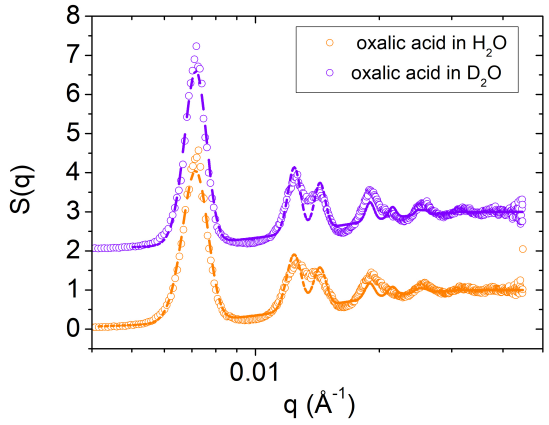

Figure 1.19: (a) Structure factor S(q) derived from the SEM images analysis of nPAAMs prepared at 18 ℃ during 8 in a) oxalic/H_2O (purple cicles)) (b) oxalic/D_2O (orange circles).

Electrolytes	Oxalic/D_2O	Oxalic/H_2O
Anodization time (h)	11h30	11h30
D_p (nm)	44±8	56±7
n $*10^{10}$ (cm^{-2})	1.1	1.2
Porosity (%)	17	26
D_{int} (nm)	101	101
σ_{int}	0.063	0.065
Grain	898	785

Table 1.10: Structural parameters obtained from SEM analysis of the nPAAMs synthesized in oxalic acid (using H_2O or D_2O): pore diameter D_p, pore density n, porosity, interpore distance D_{int}, D_{int} standard deviation σ_{int}, grain size.

$$P_{ord} = \frac{q_{av}\Delta V}{\eta\sigma} = \frac{10^{-pH}\Delta V}{C\eta\sigma} = \frac{10^{-pH}\Delta V}{C\eta\sigma} \tag{1.13}$$

where,

1. q_{av}=$10^{-pH}/C$ the average charge
2. ΔV the applied voltage
3. C the electrolyte concentration
4. η the electrolyte's viscosity
5. σ the electrolyte's conductivity

The optimal value is found to be 0.057 ± 0.024 (i.e. $0.033 < P_{ord} < 0.081$) [81]. In particular the P_{ord} values of optimal ordering is 0.033 and 0.055 for sulfuric and oxalic

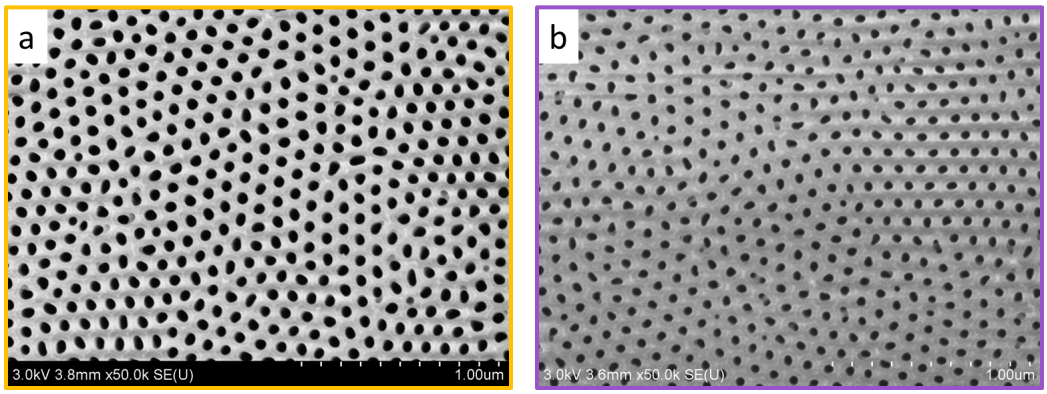

Figure 1.20: a) SEM image of top surface of nPAAMs prepared in 40 V oxalic acid for 11h and 30m at 18 ℃ a) H_2O b) D_2O .

nPAAMs synthesized at 0 ℃, respectively. Since, here the best ordering is observed at 20 ℃ for sulfuric and 18 ℃ for oxalic we cannot directly compare our P_{ord} values to the ones in the literature, only qualitative evolution can be made between electrolytes. Table 1.7 shows the calculated P_{ord}. The value varies in the order: D_2SO_4/D_2O <H_2SO_4/D_2O <H_2SO_4/H_2O and oxalic/D_2O <oxalic/H_2O. It decreases in deuterated solvent and tends to the proposed P_{ord} interval.

1.2.5.2 Relation between growth rate and current density

The effect of D_2O on the growth rate can be explored through the current density j_{av}. The growth rate was calculated from the thickness of the oxide obtained by cross section SEM images. In Figure 1.21 the growth rate G_r vs current density j_{av} is plotted for samples prepared in hydrogenated and deuterated electrolytes. Each set of experiments at different electrolytes can be fitted with a line. However the slope is different between H_2SO_4/H_2O and D_2SO_4/D_2O: 1.20 and 1.51 µm.$cm^2.h^{-1}.mA^{-1}$. For a given j the G_r is larger in deuterated solvent. On the contrary this effect is less pronounced for oxalic electrolytes (slope of 1.54 of H_2O compared to 1.61 for D_2O). This trend can also be correlated to the reaction efficiency determined by Al titration (see below), which is higher in D_2O (see Figure 1.22).

As shown previously by titration, the total amount of aluminum Al^{3+} agrees with the amount titrated in electrolyte and the one obtained by titration of the dissolved porous oxide. Thus, the activation energy for the oxidation of aluminum can be calculated from the measured current. Figure 1.23 shows the linear evolution of lnj_{av} (lnj_{av} is the average current density) with 1/T (T is the temperature). From the slope one can extract the activation energy of alumina synthesis. At the first anodization there is no difference between the hydrogenated or deuterated electrolytes (Table 1.11). During the second anodization the

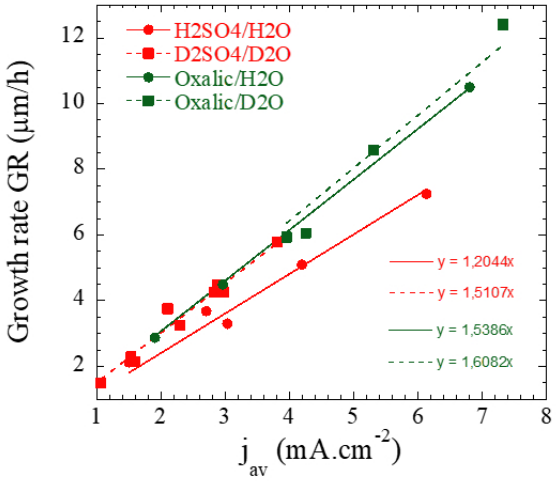

Figure 1.21: a) Growth rate (G_R) as a function of average current density (j_{av}) for H_2SO_4/H_2O (red circles), D_2SO_4/D_2O (red squares), oxalic/H_2O (green circles) and oxalic/D_2O (green squares) .

activation energy slightly decreases for D_2SO_4/D_2O compared to H_2SO_4/H_2O (from 57.8 to 52.6 $kJ.mol^{-1}$). This decrease is not drastic to really conclude on a clear effect of deuterium on the activation energy.

	E_a 1^{rst} ($kJ.mol^{-1}$)	% difference with H_2SO_4/H_2O	E_a 2^{rst} ($kJ.mol^{-1}$))	% difference with H_2SO_4/H_2O
H_2SO_4/H_2O	52.9	-	57.8	-
H_2SO_4/D_2O	51.4	2.8	55.5	4
D_2SO_4/D_2O	52.3	1.1	52.6	9
Oxalic/H_2O	48.6	-	48.5	-

Table 1.11: Activation energies E_a extracted from the Arrhenius plot of Figure 1.23 .

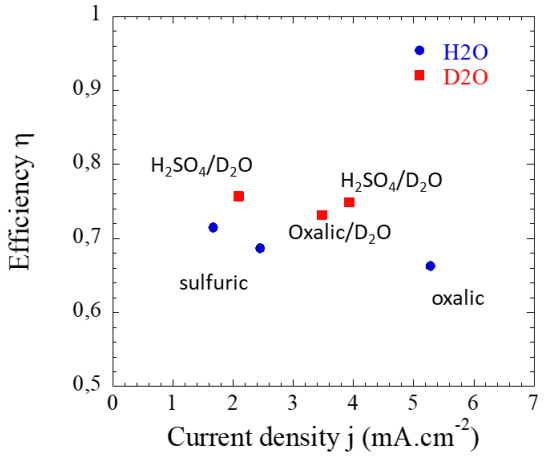

Figure 1.22: a) Reaction efficiency determined by titration of Al^{3+} (see above) as a function of current density.

1.2.5.3 Conclusions

The deuterated electrolytes can be used to decrease the pore diameter and increase the pore ordering. It was also found that, for a given j, the G_r is increased in deuterated sulfuric electrolytes compared to the hydrogenated one.

1.2.6 Post treatments of as prepared nPAAMs

In this section we will present the different possible post treatments of nPAAMs: pore widening, aluminum dissolution, detachment to obtain free standing nPAAMs and annealing.

1.2.6.1 Pore widening of as prepared nPAAMs

As experimentally observed, the porous alumina cell is separated in two layers with different composition [82]. The first layer is closer to the pore channel and consists of alumina which is contaminated with electrolyte roots such as oxalates, sulfates or phosphates depending on the acid used for the synthesis [82] and the amount and extent of roots incorporation increases with the concentration of the electrolyte and is proportional to the applied voltage [83] . The second layer consists of a more pure alumina and extents until the skeleton of the porous structure. For the technique of SANS (Small Angle Neutron Scattering), where the nPAAM will be measured with the polyelectrolyte, the existence of inhomogeneities can complicate the analysis of the results. In this context, the purification of the material is achieved through the chemical etching of the contaminated layer . This is done by immersing the synthesized

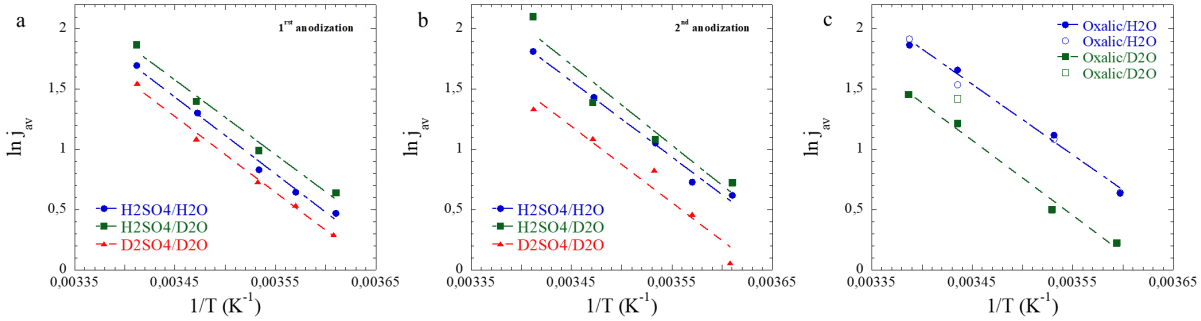

Figure 1.23: a) Growth rate (G_R) as a function of average current density (j_{av}) for H_2SO_4/H_2O (red circles), D_2SO_4/D_2O (red squares), oxalic/H_2O (green circles) and oxalic/D_2O (green squares) .

nPAAMs in phosphoric acid solution (H_3PO_4 5 wt.% at 30 ℃) for a given amount of time. In previous studies the pore diameter was followed as a function of etching time [84]. Its evolution can reveal changes in the etching dissolution rate which are related with the anion incorporation gradient along the pore wall. It is known that the anion contaminated oxide, close to the pore has higher solubility than the rest inner layer. Figure 1.24 shows the SEM images of nPAAMs prepared in oxalic acid at different etching time.

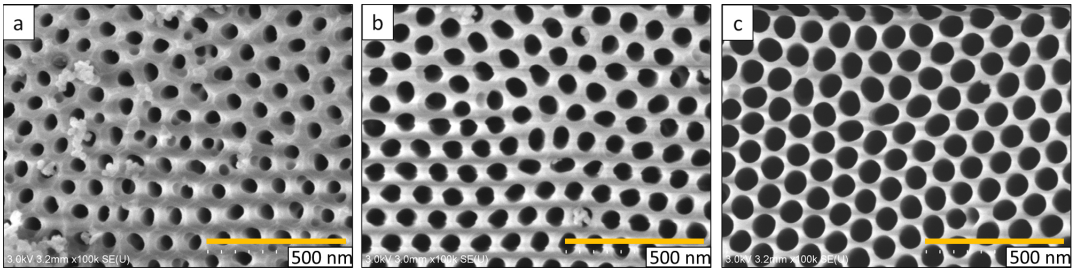

Figure 1.24: SEM top view of nPAAMs prepared in oxalic acid (0.3 M, 40 V, T=18 ℃) , immersed for different times in phosphoric acid solution 5 wt.% at 30 ℃ . a) as prepared b) after 20min c) after 30min

Figure 1.25, presents the evolution of the calculated pore diameter as a function of the etching time. The slope of this plot gives the dissolution rate of the porous alumina. A change in the etching rate occurs after 30 min, indicating the crossover between the contaminated layer and the more pure alumina. We can estimate the extent of the anion incorporated layer by the difference of D_p between the initial and the one at the change of the slope. This gives a thickness of about 15 nm for the incorporated layer. This is confirmed by further Electron

Dispersive X-ray spectroscopy (EDX) (Figure 1.26), showing a decrease of the C/Al ratio as the pore wall gets thinner.

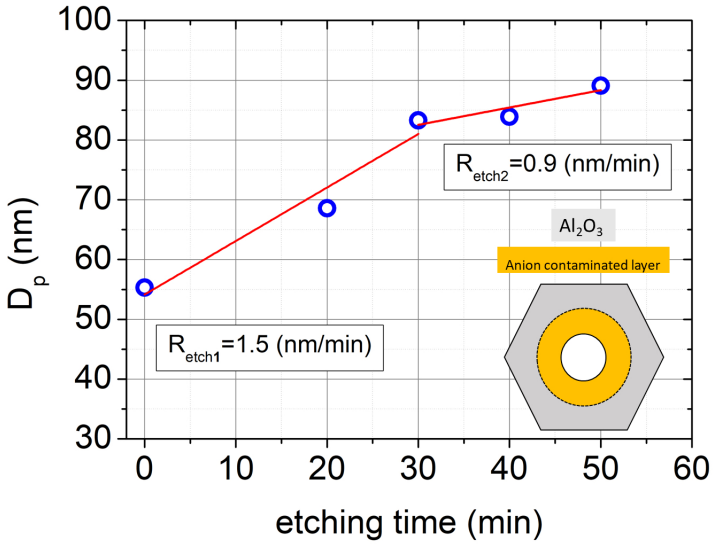

Figure 1.25: Evolution of nPAAMs pore diameter as a function of the etching time in phosphoric acid 5 wt% at 30 ℃. The nPAAMs was synthesized using oxalic acid (0.3 M, 40 V, T=18 *celsius*).

1.2.6.2 Self-standing nPAAMs

For various applications as well as for their characterization the nPAAMs need to be deprived from their aluminum substrate. Several protocols have been developed for this process, either by chemically dissolving the aluminum substrate or by separating the membrane from the substrate by means of electrochemistry. The first chemical method to be introduced involves the immersion of the sample inside a solution of copper chloride and hydrochloric acid (3.4 g of $CuCl_2\,2\,H_2O$ in 50 mL of 38 wt.% HCl and 100 mL of water). The etching is based on the reduction of copper cations on the aluminum substrate. As a consequence aluminum cations are dissolved inside the electrolyte. The process is described by equation 1.14 .

$$3Cu^{2+}_{(aq)} + 2Al_{(s)} \rightarrow 3Cu_{(s)} + 2Al^{3+}_{(aq)} \tag{1.14}$$

In order to avoid contact of the acid with the top surface of the membrane and the undesirable enlargement effects due to the acidity of the solution, the nPAAM is floated with the aluminum substrate on the solution surface.

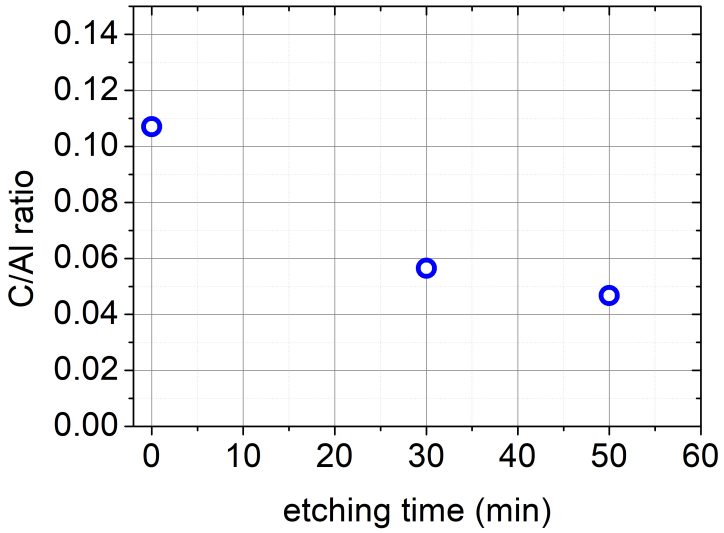

Figure 1.26: Plot of the C/Al ratio, measured by EDX of samples prepared in oxalic acid as a function of the etching time in different times in phosphoric acid 5 wt% at 30 ℃.

1.2.6.3 Annealed nPAAMs

In order to study and modify the composition of the nPAAMs to a more pure alumina, thermal annealing was employed on detached membranes. It is known that nanoporous alumina membranes pass from an amorphous to polycrystalline alumina during thermal annealing while contaminants such as incorporated anions and hydroxides are evaporated. In this section we are interested in studying the effect of annealing on the pore structure as it has been reported that this is conserved up to temperatures of 900 ℃ [85].

Initially, membranes prepared with oxalic acid and without the aluminum substrate were annealed in air at constant temperatures in the range of 500-900 ℃ and heating rates between 1-5 ℃. After the annealing, curling of the membranes was observed that was more severe for the higher temperatures and higher heating rates. Moreover membranes became more fragile and easier to crack.

The macroscopic curling is reported in the literature and is explained by the difference in the thermal expansion coefficient between the relative more pure alumina of the inner wall and the anion contaminated layer. To overcome this effect, one approach is to perform etching cycles combined with annealing [86]. Additionally, it has been reported that for membranes with barrier layer, they curl up towards the barrier layer. For this reason samples that were heated at high temperatures were prior chemically etched in phosphoric acid solution 5 wt % at 30 ℃ for approximately 30 min. In certain cases, the use of ceramic alumina plates as

	R_p (nm)	σ_p	P (%)	D_{int} (nm)	wall (nm)
as prepared	26.5	1.2	31.9	104	25.5
annealed ℃	33.6	1.8	37.5		18.4

Table 1.12: SEM structural characteristics before and after thermal annealing at 900 ℃ for 2h. The membrane was prepared in 0.3 M oxalic acid under 40 V and T=18 ℃ for 8h of anodization.

a load on the samples reduced the buckling as already reported [87].

In Figure 1.27 the SEM image of the top surface of an annealed membrane prepared in oxalic acid is presented.

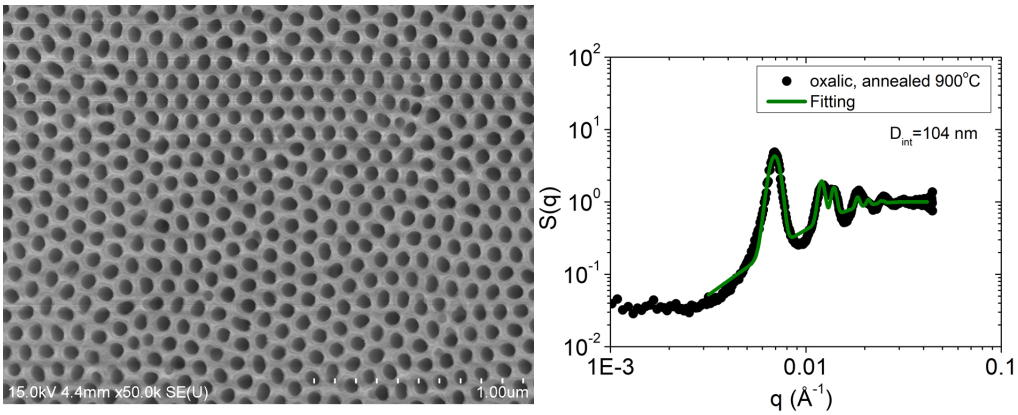

Figure 1.27: SEM image and structure factor *S(q)* of membrane prepared in oxalic acid 0.3 M, under 40 V and T=18 ℃, after thermal annealing in air at 900 ℃ for 2 hours, heating rate 1 ℃/min.

The pore structure remains intact and the structure factor gives close results as the as prepared membranes . In Table 1.12 the structural characteristics derived from SEM are presented for a sample prepared with conditions 0.3 M oxalic acid , 40 V, T=18 ℃ before and after thermal annealing.

The skeleton shrinks by 28% after thermal annealing and an increase of 7 nm in the pore radius is recorded. This effect is expected to happen as the sample crystallizes to phases with higher densities as seen in Table 1.13.

Based on literature, the density of the as prepared membrane is 2.945 g/cm^3 and we can calculate the density of the annealed membrane at 900 ℃ [45] using:

$$d_{annealed} = \frac{(1-P_1)}{(1-P_2)} d_{Al_2O_3} = 3.21 g/cm^3 \tag{1.15}$$

Al_2O_3 polymorphs	density g/cm^3
γ-Al_2O_3	3.65-3.67
δ,θ-Al_2O_3	3.6-3.65
α-Al_2O_3	3.99

Table 1.13: Densities of alumina polymorphs (data taken from [88].

where

P_1 and P_2 is the Porosity before and after the thermal annealing.

This value for the density will be used in the discussion for the composition of the membrane in chapter 2.

1.2.6.4 Direct detachment protocols for obtaining free standing membranes

Two different protocols can be used to obtain free standing nPAAMs: voltage pulse detachment or the use of a 3^{rd} anodization step. For free standing nPAAMs , i.e membranes without the barrier layer, a technique using pulsed voltage can be applied with a mixture of perchloric and ethanol solution [89]. The voltage reduction multiplies the pore density at the bottom side of the membrane while reducing their diameter and their barrier layer thickness. In this way a layer of a porous network is produced with a very thin barrier layer which can be dissolved by increasing the electrolyte's temperature. This method produces asymmetric nPAAMs with different pore diameters at each side. The membranes can be further etched in acidic solution in order to increase the pore diameters at the bottom part. The specific protocol worked only for very thick porous alumina sample, (of 168 μm) and the detachment was partial. Because of this drawback we preferentially use a protocol involving a 3^{rd} anodization.

This new protocol was introduced in order to synthesise highly ordered opened nPAAMs at both sides and is based on a third anodization step in a highly concentrated electrolyte [90] . This step produces a thin porous layer adjacent to the aluminum substrate, with higher solubility than the first oxide due to the higher contamination from the electrolyte species. As a consequence, dissolution in an acidic bath proceeds at a high rate for this thin layer that finally is dissolved while the less soluble previously formed membrane is separated from the aluminum substrate. This process is presented in Figure 1.28.

A crucial parameter for the successful detachment is the thickness of the third anodized layer. If it is too thin the separation in the dissolution step is not efficient while if it is too thick, prolonged dissolution times are needed which can result in nPAAM damaging. The membranes that were successfully detached were membranes prepared in oxalic acid at 40 V. The 3^{rd} anodization step is conducted in 12 M sulfuric acid. The applied voltage is the same

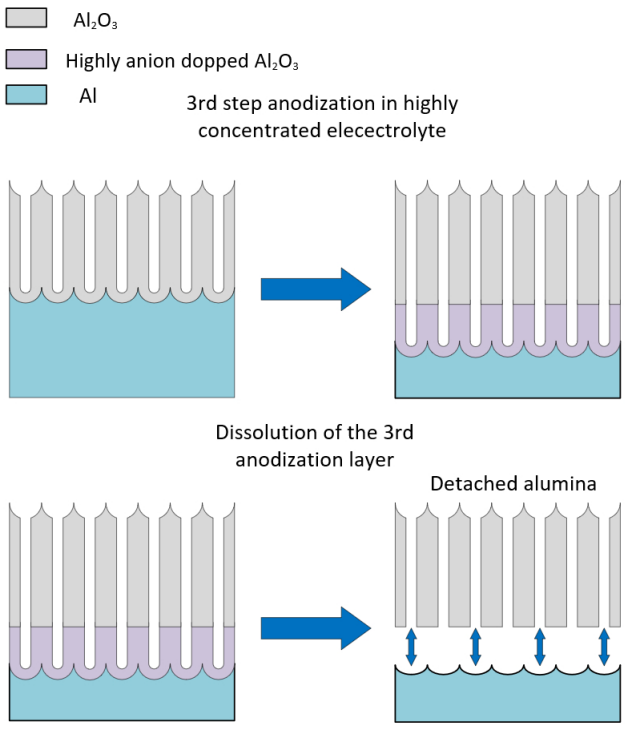

Figure 1.28: Detachment of a porous anodic alumina membrane based on a third anodization step.

as the previous anodization step, in our case 40 V and the temperature is set at 0 ℃. The third step is performed for 7 min. During this time, a large amount of heat is dissipating inducing temperature increase of the solution up to 10 ℃.

After the third anodization step the sample is immersed in the aqueous solution of 6 wt.% H_3PO_4 + 1.8 wt.% CrO_3 at 30 ℃. After 30 min the sample is taken out of the solution and its edges are peeled off with a scalpel to facilitate the detachment, while a plastic transparent film of about 60µm is placed under the oxide membrane. For some samples the immersion time inside the dissolution solution had to be prolonged for a few minutes as the detachment was not possible.

The repeatability of the process needs intensive fast cooling and precise knowledge of the layer of the porous oxide formed at the 3^{rd} anodization step. As seen in Figure 1.30 and in Table 1.14 the pores at the bottom surface have a larger diameter than at the top surface. Figure 1.29 shows the current density evolution with time during the 3^{rd} anodization for three samples prepared in the same conditions. At first the current density is small but increases quickly to reach a sharp maximum after around 45-50s and finally a plateau. This evolution is similar for the three samples, indicating a good repeatability of the 3^{rd} anodization process. The full understanding of this curve will need further experimental

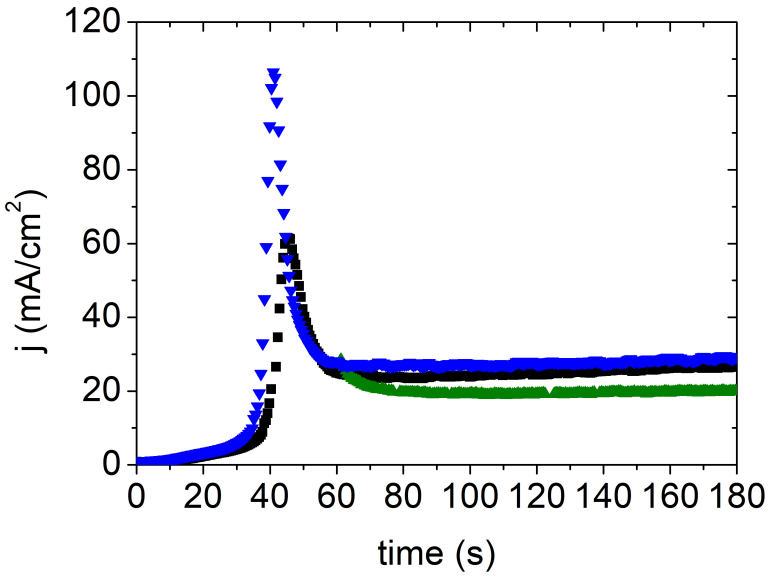

Figure 1.29: Third step anodization in sulfuric acid 12 M under 40 V and temperature set to T=0 ℃ for membranes prepared with oxalic acid under the same anodization conditions. The green incomplete graph for the first seconds of the 3rd step is due to blocking of the PC interface.

D_p top (nm)	D_p bottom (nm)	etching time (s)
41	64	27
39	65	33
32	55	38
32	61	38
44	64	41

Table 1.14: Table pore diameter for the top and bottom surface of detached membranes.

investigations. The detachment protocol by a third step anodization produces efficiently membranes with asymmetric pore diameters and allows for the preparation of large nPAAMs surface very convenient for experimental techniques used in the following chapters (e.g flow and ζ-potential measurements).

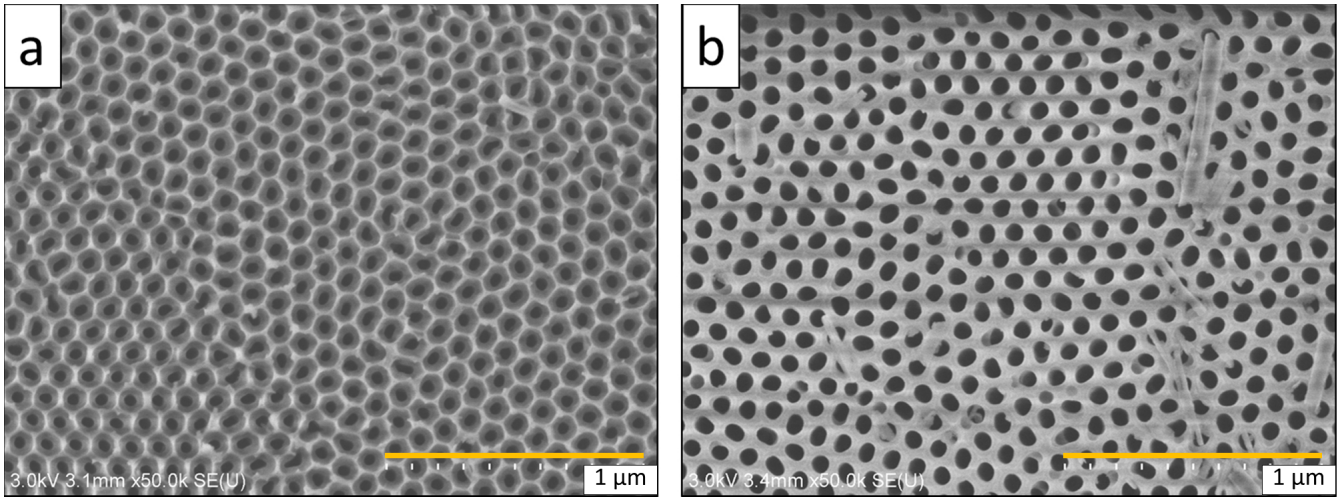

Figure 1.30: SEM image of detached membrane a) Top view, D_p=44 nm b) bottom view D_p=66 nm

1.3 Nanoporous alumina membranes on silicon wafers for neutron reflectivity measurements

The synthesis of nanoporous alumina on silicon wafers was realized in order to study the penetration of polyelectrolyte with neutron reflectivity (NR). As a first step, the characterisation of the bare nPAAM on silicon wafers will be presented. NR gives access to the thickness and the chemical composition of different layers at the surface of a substrate [91]. The composition is obtained through an important parameter named the scattering length density (SLD) that depends on the interaction between the neutron and the nature of the studied materials (see also Chapter 2).

In practice, a neutron beam is sent in grazing incidence (i.e. with a low incident angle) on the surface of the sample, then is reflected and/or refracted and finally detected as a function of the scattering vector q. The ratio between the detected intensity and incident intensity is called reflectivity, R. The reflectivity corresponds to the specular reflections due to the changes in refractive index in the sample along the perpendicular direction to the surface. These changes are characterized by a SLD profile that can be extracted from the fitting of the NR and the thickness of the layer is probed by the presence of fringes in the NR curve.

To measure with reflectivity, the low roughness and strong adhesion of the nPAAM on the Si wafer is desired. Anodization of aluminum on silicon wafers exhibits different structural characteristics than the anodized aluminum foils and greatly depends on the sputtered aluminum film morphology which is tuned by the sputtering conditions [92, 93] . The low

deposition rate of aluminum, is a key parameter in producing films with small crystallites that contribute to acquisition of smoother porous oxides. On the other hand, low deposition rates prohibit the growth of thick films and limit the thickness of the anodization layer of the 1^{st} step. As a consequence, the appropriate thickness to be reached decreases and the pore ordering drops off. Nevertheless, ordering is not affecting the signal in the neutron reflectivity spectrum. Another structural characteristic that has been observed during anodization of aluminum on silicon substrate at the Si/PAAM interface is an inversion of the barrier layer taking place when anodization proceeds in transforming the whole aluminum film into alumina [94]. In this section, the synthesis of nPAAMs on Si wafers will be presented, as well as a structural characterisation by SEM and the obtained reflectivity spectra.

1.3.1 Synthesis of nPAAM on silicon wafer

From this perspective, n-type silicon wafers with an aluminum layer of $1\mu m$ sputtered on the top surface and the edges were purchased. The silicon wafers were left coated with their native oxide. Prior to anodization the silicon back surface should be masked with insulating material, for example nail-polish because under high field it can be oxidized. Electrical contact was achieved by gluing with silver-paste an aluminum foil. The electric contact was also insulated up to a certain height. The first sample noted as "No.1" was anodized inside the same electrochemical cell which was used for the anodization of the Al foil. After anodization, the sample presented a colour gradient, possibly due to thickness differences along the sample. This was interpreted as electric field effects which might be due to the short distance between the electrodes. The neutron reflectivity data can be interpreted under the condition that the sample's thickness of the different layers stays constant along the sample surface (with some error due to roughness or diffusion of the interfaces). To avoid such effects, the anodization setup had to be modified as seen in Figure 1.32. The cell was replaced by a long plastic container in order to increase the electrode distance (9 cm). Moreover, the container was placed inside the cryostat bath for keeping the temperature constant.

Depending on the chosen thickness of the nPAAM, different interfaces can be probed when a neutron beam is totally reflected at the interface. As seen in the scheme of Figure 1.31, when the thickness of the nPAAM is short, neutrons can probe the interface of nPAAM with the solution, thus providing information for the entrance of the pores. This is very important when studying polymers as different phenomena can occur at this interface (plugging, adsorption). On the other hand when the thickness of the nPAAM is too long, neutrons probe only a length of about 200 nm of the pores.

For this reason, two types of samples were synthesized, short and long ones. For the

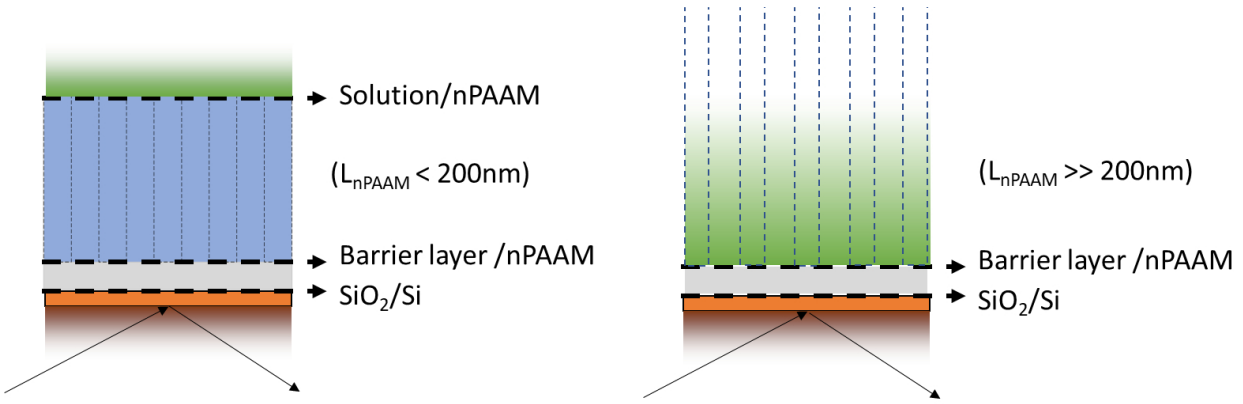

Figure 1.31: Scheme of the probed interfaces by NR depending on the thickness a nPAAM on a Silicon wafer, measured in mixture of H_2O/D_2O.

long samples, the anodization was made in a single step. In the case of short nPAAMs, we proceed in a two step anodization. A summarizing table of the samples and the synthesis details is given in Table 1.15.

For the samples anodized in two steps, after the 1^{st} step, the nail-polish was removed and the dissolution process followed. Two approaches were tested. The first one involved puring a few millilitres of phosphochromic acid at room temperature on the anodized surface. The surface was wetted and left for almost 3 hours. The second approach was to fully immerse the wafer inside a beaker with phosphoric acid solution 5 wt.% at 30 ℃ . The samples were characterized by SEM and measured by neutron reflectivity. The characterization with SEM gives the basic geometrical structure needed for the fitting of the neutron reflectivity data.

The pre-anodized sample is shown in Figure 1.33. The samples showed a milky diffusive reflectance prior to anodization due to the large aluminum grains created during the sputtering process. It was noticed that after anodization the samples presented an interference pattern in the form of a colour gradient near the edges of the film. The sample exhibits transparency and colored stripes, more prominent at the edges. The transparency is a result of the transformation of all the aluminum film while the colors implicate different thickness of the formed oxide. The different thickness can be caused either by non-homogeneous electric field during the anodization or due to the sputtering process.

1.3.1.1 Film after one step anodization

The film morphology after the 1^{st} anodization step is observed in the SEM images of Figure 1.34a for the sample No.1. The surface consists of large grains which are covered on all of

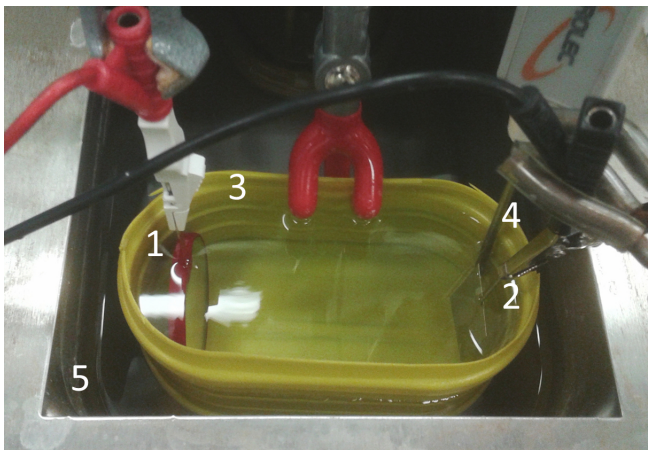

Figure 1.32: Anodization cell for synthesis of thin nPAAMs. 1: Sample, 2: Pt foil, 3: plastic container, 4: Thermocouple, 5: Cryostat's bath.

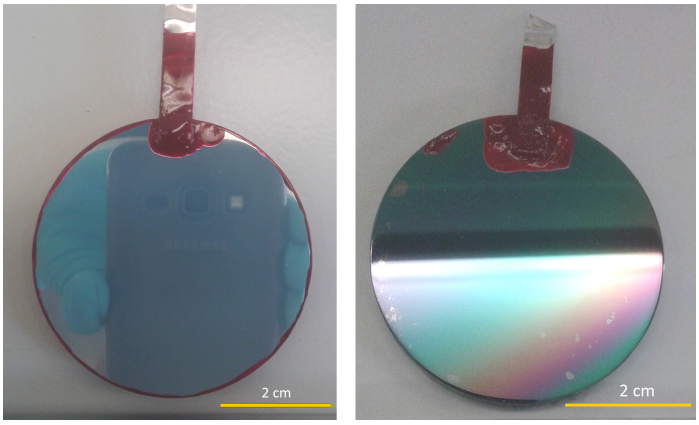

Figure 1.33: Left:Picture of sample before anodization Right: Picture of sample after complete anodization of aluminum

Sample No.	1	2	3	4
Anodization 1^{st} step	0.3 M oxalic 40 V, T=18 ℃	0.3 M oxalic 40 V, T=18 ℃	0.3 M oxalic 40 V, T=1 ℃	0.3 M sulfuric 20 V, T=10 ℃
Etching	5 wt.% H_3PO_4 30 ℃ (20min)	6 wt.% H_3PO_4 and 1.8 wt.% CrO_3 20 ℃ (2h 46min)	5 wt.% H_3PO_4 30 ℃ (20min)	5 wt.% H_3PO_4 30 ℃, (10min)
Anodization 2nd step	no	yes	yes	no

Table 1.15: Table of sample names of nPAAMs and the synthesis details.

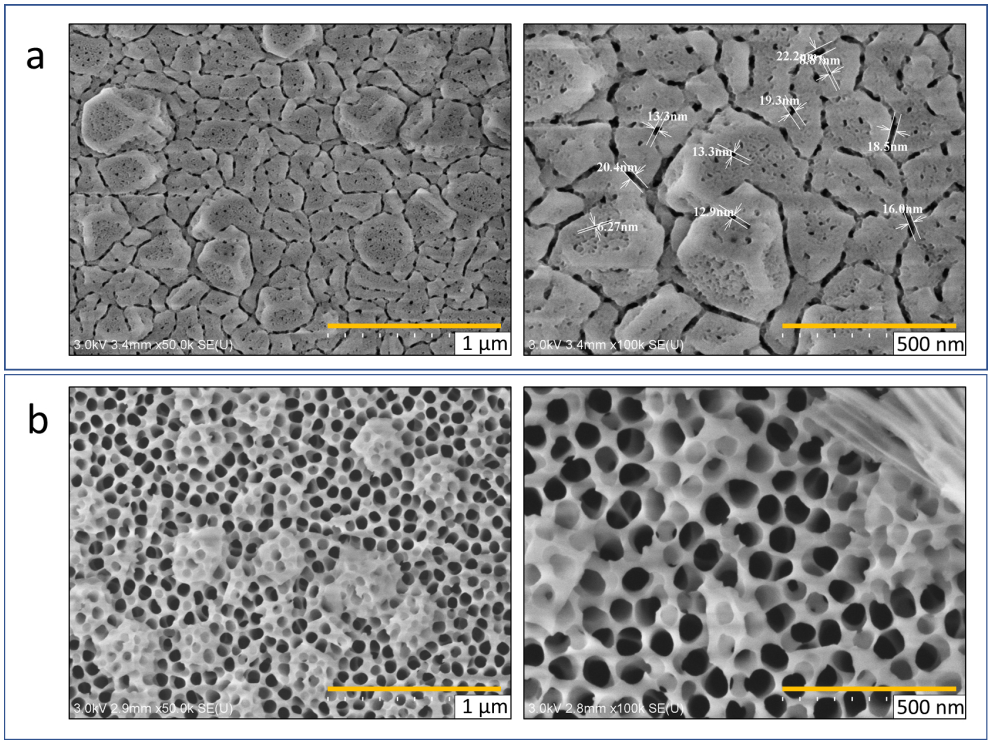

Figure 1.34: SEM image of sample prepared with one step anodization in oxalic acid 0.3 M 40 V, T=18 ℃ . a) after 1 step anodization b) after chemical etching in H_3PO_4 5wt.% at 30 ℃ for 20 min.

their faces with pores. The boundaries of the grains seem perforated and the pores consist of two populations, one above 10 nm and one below. To improve the flatness and pore ordering on the top layer ,the sample was subject to etching in H_3PO_4 5wt.% at 30 ℃ for 20 min. Figure 1.34b shows that the first layer with the grains is removed partially and a porous network of larger pores is revealed. For all samples prepared with one anodization step the etching process will be followed. Regarding the SEM analysis, due to the remaining grain parts, the SEM image after the etching process, is cropped and analysed only from areas with no grains.

It is concluded that etching after the 1^{st} anodization step is necessary to reduce the surface roughness and reveal the porous network underneath.

1.3.1.2 Thin nPAAMs prepared in oxalic acid

Surface morphology :

The samples No.1 and No.2 have the same morphology as seen in the SEM images of Figure 1.35. The pores are disordered and grains expand on the whole sample surface. The pores on these grains appear on all of their surfaces. The sample No.3 presents a very thin

Sample No.	D_p (nm)	σ_p (nm)	D_{int} (nm)	packing	P (%)	$n * 10^{10}/cm^2$
1	66	5	82	0.22	37	1.2
2	64	5	88	0.27	29	1.2
3	82	15	99	0.47	56	1.2

Table 1.16: Structural parameters calculated from SEM images for samples prepared in oxalic acid 0.3M under 40V.

oxide without any barrier layer or grains covering the surface. The silicon surface is exposed, some pores have merged into one and what remains from the porous oxide is the skeleton. By analysing the SEM images the structural parameters such as the the pore diameter D_p, porosity and pore density can be derived. Furthermore, the structure factor *S(q)* is derived for all samples (Figure 1.35), as previously described from the whole SEM image but the fitting is done by using a hard sphere model [95] . This is justified because of the large deviation from the hexagonal lattice. The fitting parameters are the "effective radius", r_{eff} which gives the interpore distance as in equation 1.16 . The second parameter is related to the packing of the object, thus its ordering and is the "volume fraction" which we will name as "packing". The obtained values are presented in Table 1.16.

$$r_{eff} = \frac{D_{int}}{2} \tag{1.16}$$

In comparison to anodization of thick aluminum foil the pore diameter is larger and with higher polydispersity while the pore density is kept the same. The interpore distance for the samples No.1 and No.2 is lower than this obtained in thick aluminum foil anodization (100 nm). The scaling constant k in the relation D_{int}=kV corresponds to 2.02 nm/V and 2.2 nm/V for sample No.1 and No2. On the other hand for sample No.3, D_{int} is 99 nm and it gives a scaling constant of 2.5 nm/V which is closer to the one obtained for anodization of foils.

Current density and growth of nPAAMs on silicon The growth of the nPAAM thin film on the Si wafer is directly connected to the evolution of the current density. In Figure 1.36a the current density evolution is shown for sample No.1. The current density in the first seconds is constant and then slowly increases. After 520 seconds a small decrease is observed and then the current density increases quickly until it reaches 22 mA/cm^2. At this point bubbles were observed on the whole surface of the sample. After reaching 700s the current density decreases exponentially until the experiment is stopped at around 1000 seconds. This last part of the curve is attributed to perforation of the barrier layer and oxidation of silicon substrate [96]. The cross section SEM images in 1.36b,c show a thin nPAAM of almost the same thickness along the Si wafer (around 1.2 µm). The pores are not ordered and a closer

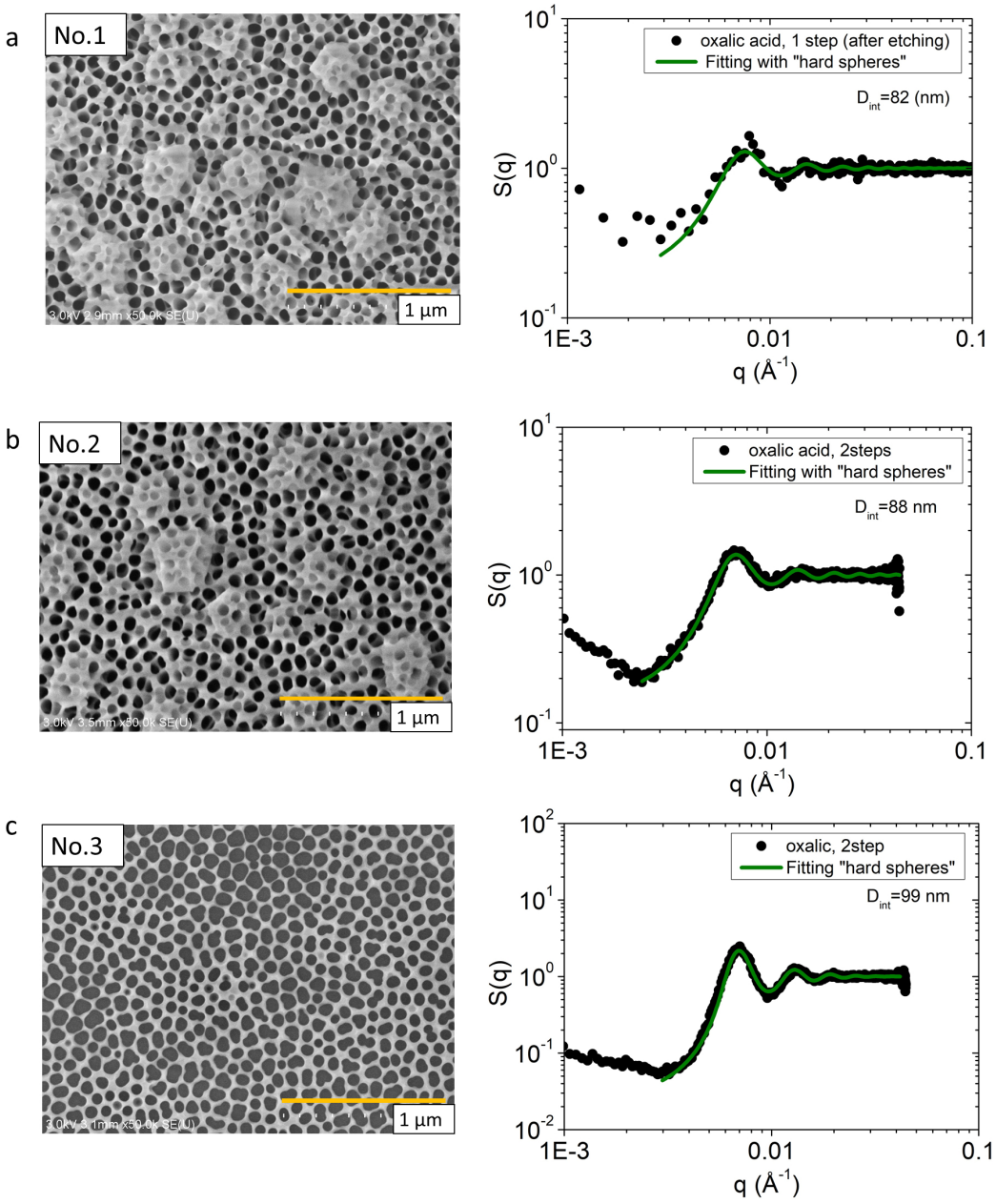

Figure 1.35: Structure factor S(q) of samples prepared in oxalic acid 0.3 M and 40 V a) sample No.1 b) sample No.2 c) sample No.3.

look at the interface of the nPAAM with the silicon in 1.36d reveals the absence of a barrier layer. Moreover, a thin layer of about 20 nm with characteristic protrusions can be seen on the silicon wafer, at a part where the nPAAM has been detached. These protrusions might be silicon oxide that has been formed inside each pore due to perforation of the barrier layer during synthesis.

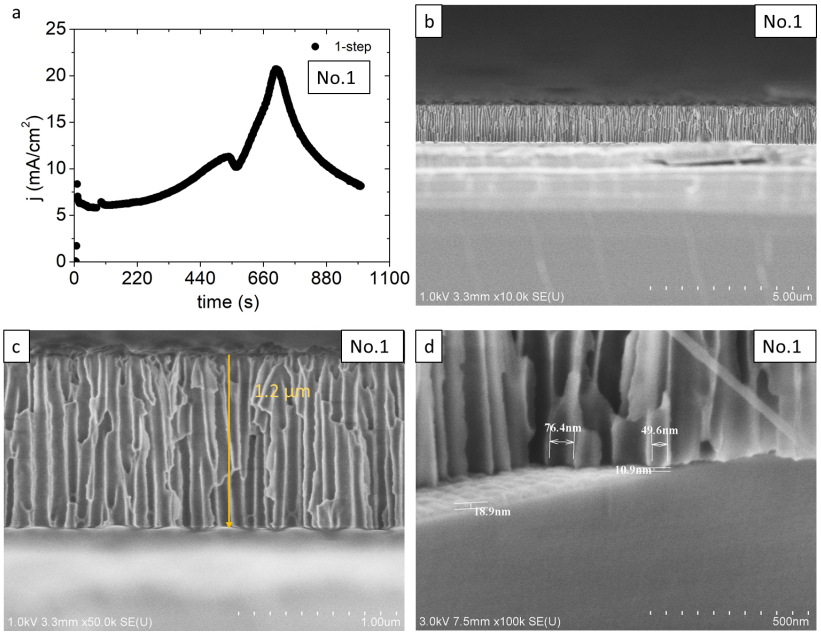

Figure 1.36: a) Current density evolution of sample No1. (0.3 M oxalic acid, 40 V, (T=18 ℃ , 1-step and etching). b,c) SEM cross section image of sample No.1 d) tilted SEM image at the interface of the nPAAM and silicon .

The current density of sample No.2 is shown in Figure 1.37a and it can be seen that it follows the typical stages of decrease, rising and attaining a constant value. The only difference is that during the 2nd step as the aluminum is consumed the current starts to decrease until it reaches practically zero. The cross section SEM image of the sample (Figure 1.37b) shows a layer of constant thickness along the wafer. In Figure 1.37c certain structural characteristics are present. The layer consists of one thick highly porous layer of 857 nm and a short one of 353 nm. This can be explained due to insufficient etching of the layer of the first anodization step. The layer was only radially etched at the pore walls and remained on top of the aluminum substrate. At the second step, the rest of the aluminum substrate was anodized and produced the shorter layer. At the end of each pore, the barrier layer has inverted, producing hemispherical voids 20-30 nm in size, on top of the silicon wafer (1.37d). Finally, at the top interface of the nPAAM with air, the grains can be seen that reach a size of 80-90nm. This sample can be seen as a bilayer or ”duplex” nPAAM.

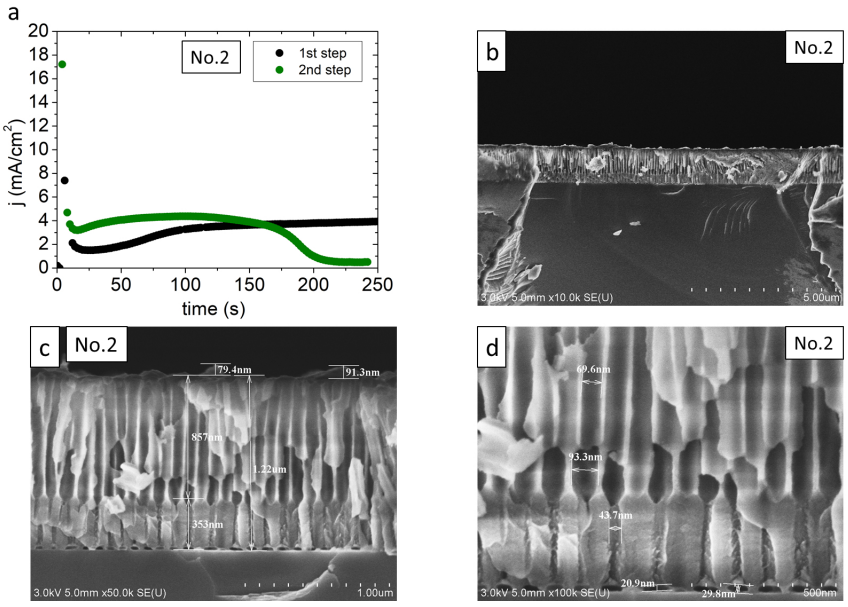

Figure 1.37: a) Current density evolution of sample No.2. (0.3 M oxalic acid, 40 V, (T=18 ℃ , 2-steps). b,c,d) SEM cross section image of sample No.2.

The current density for the thinnest sample No.3 follows the typical shape in the first anodization step but a different behaviour is observed at the second step where the current density presents only the phase of the first stage (Figure 1.38a,b). The current density acquires a high value at the first seconds of the anodization and then decreases, which corresponds to the stage of the barrier layer formation. Then no further rise in the current is observed, but rather a continuous decrease as the aluminum substrate has been consumed. In cross section images of Figure 1.38c,d the layer seems rough with a thickness ranging between 70 and 160 nm and without any barrier layer.

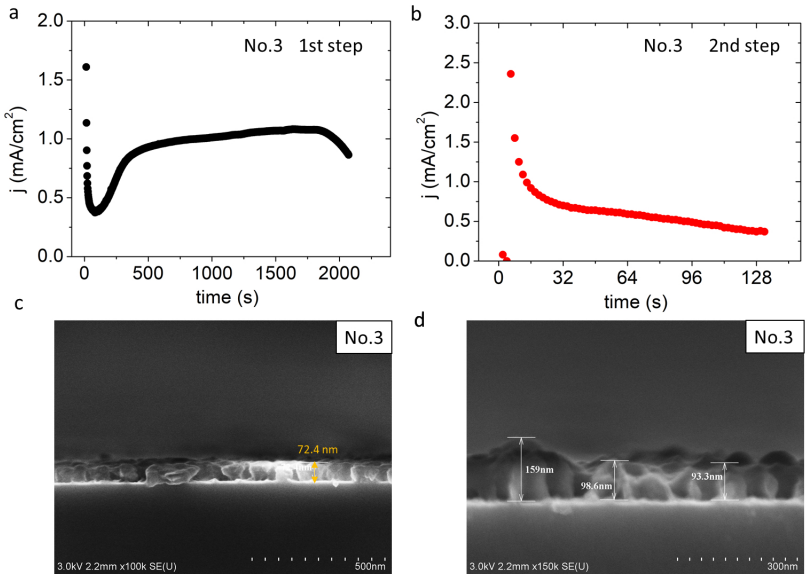

Figure 1.38: a) Current density evolution of sample No.3 during the first anodization step. b) Current density evolution during the second anodization step (0.3 M oxalic acid, 40 V, (T=18 ℃ + etching) ,c,d) SEM cross section image of sample No.3.

1.3.1.3 Thin nPAAM on silicon wafer prepared in sulfuric acid

Surface morphology The sample No.4 was prepared in 0.3M sulfuric acid under applied voltage of 20 V and temperature of 10 ℃.

The sample was subjected to chemical etching after the first anodization step. The top surface still contains some grains as seen in the SEM image of Figure 1.39. In Table 1.17 the structural parameters are presented. The sample has a pore diameter very close to the value for aluminum foil anodization ($\simeq 20nm$), the pores are polydispersed and the interpore distance remains the same.

Sample No.	D_p (nm)	σ_p (nm)	D_{int} (nm)	packing	P (%)	$n * 10^{10}/cm^2$
4	25	6	49	0.12	14	3

Table 1.17: Structural parameters of sample prepared in sulfuric acid 0.3 M under 20 V and T=10 ℃.

Current density and growth of nPAAMs on silicon The current density shows the typical behaviour as seen in Figure 1.40a. From the SEM images in Figure 1.40b,c,d it can be seen that the nPAAM consists of one porous layer of about 1.25 µm with several grains of a size of 100 nm on the top of the nPAAM. The channels are disordered (as seen with the

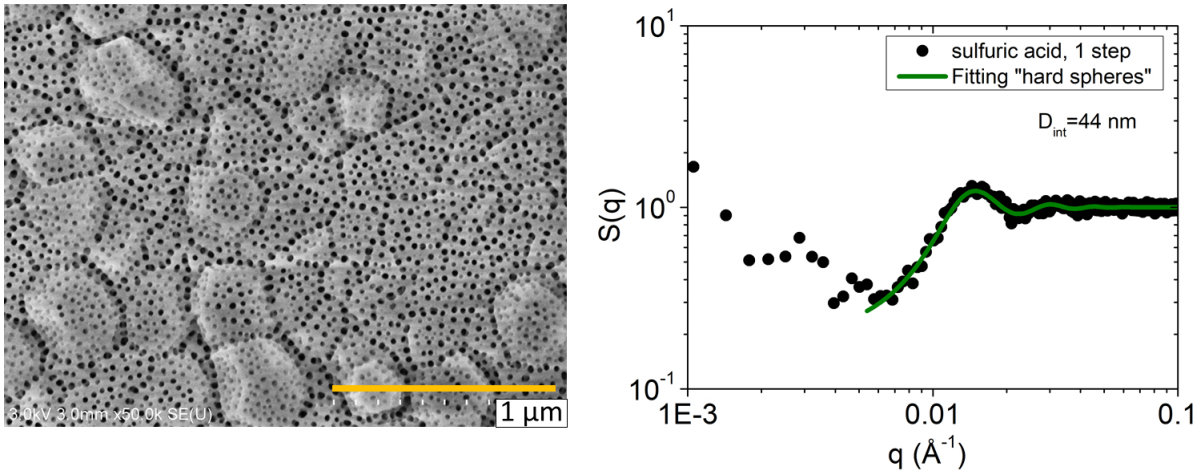

Figure 1.39: Left: SEM top view of sample prepared in sulfuric acid 0.3 M under 20 V, T=10 after chemical etching ℃ Right: Derived S(q) fitted with a hard sphere model.

S(q) fitted with a hard sphere model) and at their end no barrier layer exists but rather a thin gap of about 30 nm.

1.3.1.4 Conclusions on synthesis of thin nPAAM on Si wafers

The structural characteristics of thin nPAAM synthesized on Si wafers present different morphology than those obtained with aluminum foil anodization, signifying the effect of the type of Al substrate during. Clearly, an etching step is necessary after the first anodization step in order to reveal the porous network that is hidden by morphology of the top surface (large grains, pore distribution). The inverted barrier layer, which is characteristic on anodized aluminum on silicon substrates can be chemically dissolved. Apart from the inversion of the barrier layer, anodization of the whole aluminum substrate risks of oxidizing the silicon wafer.

1.3.2 nPAAMs characterization by Neutron Reflectivity (NR)

The nPAAMs synthesized on Si wafers were then characterized by Neutron Reflectivity (NR), as described in the introduction of this section. The NR experiments were performed on the HERMES time of flight reflectomer at Laboratoire Léon Brillouin (LLB, CEA Saclay). Two angles were used (0.69 °and 2°) to access the widest q range with a neutron white beam (having a large wavelength range) from 2 to 22 Å. Two geometries can be used: i) measurement in air: the neutron beam is sent on the top of the nPAAM or ii) measurement

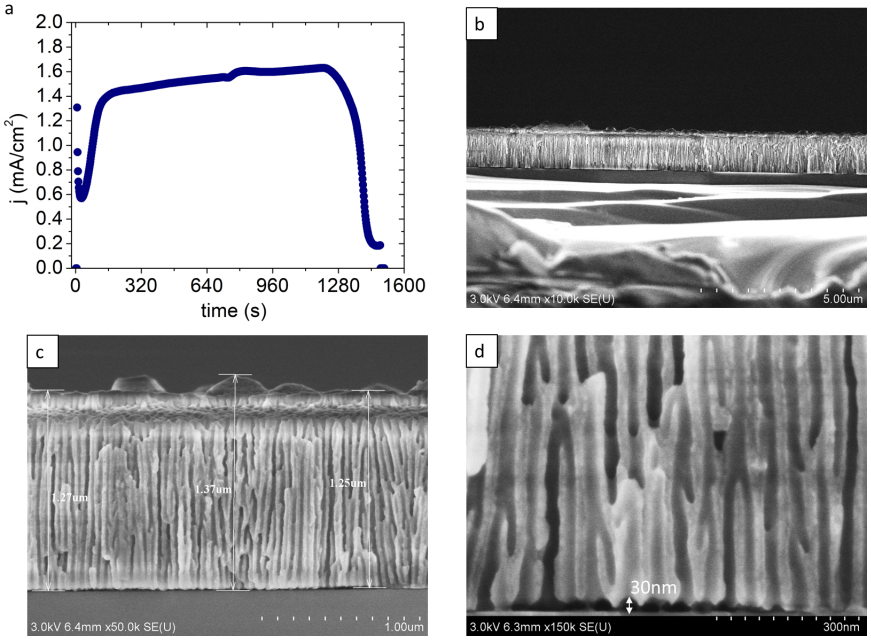

Figure 1.40: a) Current density evolution of sample No.4. (0.3M sulfuric acid, 20V, (T=10 ℃, 1 step + etching). b,c,d) SEM cross section images of sample No.4.

in a solvent: the neutron beam passes through the silicon wafer which is transparent to neutrons,(see Figure 1.41). Here the analysis of the data was done using the Motofit software [97].

A typical NR curve in log-log is shown in the insert of Figure 1.42. The NR is characterized by a plateau at low q (corresponding to the total reflection, R=1) followed by a decrease at a specific q value named the critical q, q_c. Below q_c the beam is totally reflected. Above it the beam is partially refracted inside the porous layer. q_c provides information about the SLD (scattering length density) of the layer through the following equation:

$$SLD_{layer} = SLD_{air} + \pi(\frac{q_c}{4\pi})^2 \tag{1.17}$$

Note that if the SLD of the layer is larger than the one of the Si substrate then the q_c is related to the layer. Usually the NR is presented in a Rq^4 representation that highlight any features from the layer and the good agreement between the experimental data and the fit.

Figure 1.42 show the NR of sample No.4 (nPAAM synthesized with sulfuric acid) measured in air. The NR fitting is always a delicate process if no structural information is known from another technique, specifically for nPAAMs. Here we'll use the SEM section images to fix certain NR fitting parameters. The instrumental resolution is also taken into account in the fitting. Note that due to the low absorption cross section of alumina interfaces can be

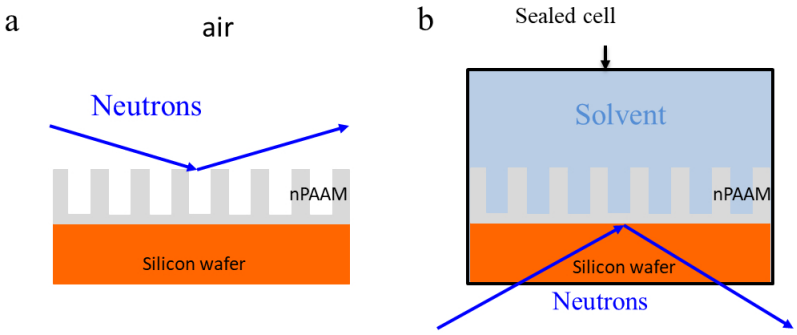

Figure 1.41: Possible geometries for NR measurements: (a) in air and (b) in a solvent passing by the silicon wafer.

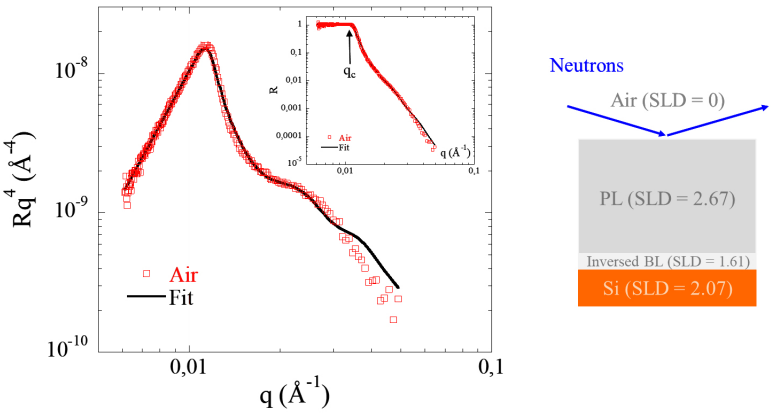

Figure 1.42: NR curve of sample No.4 (synthesized in sulfuric acid) in Rq^4 representation. In inset is shown the R=f(q) curve. Right: scheme of the model used to fit the data. The nPAAM is composed of a porous layer (PL) and an inverted barrier layer (BL).

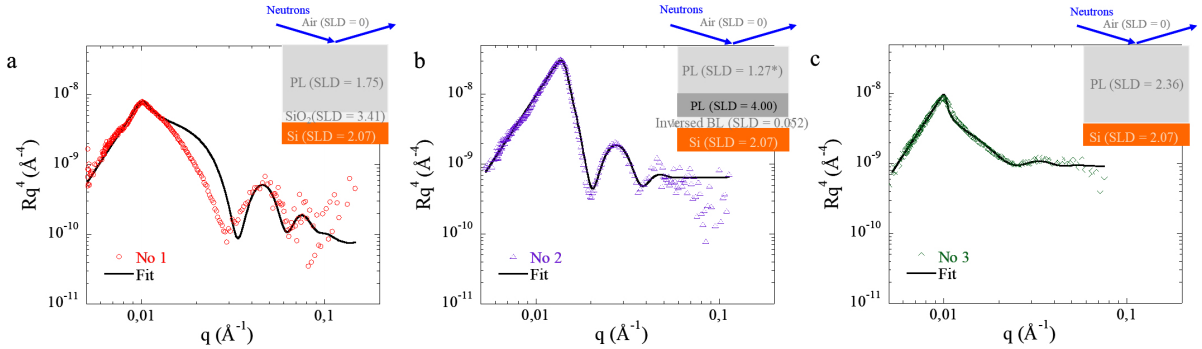

Figure 1.43: NR curves of sample No. 1, 2 and 3 (synthesized in oxalic acid) in Rq^4 representation with the corresponding fits. The schemes in insert represent the model used to fit the data. The * in (b) indicates that this value has some uncertainties.

probed deep into the porous layer down to the Si substrate.

Two layers are necessary to fit the data: one thick porous layer and one thin inverted barrier layer. The best fit gives a SLD of the porous layer and inverted barrier layer of $2.67 * 10^{-6}$ Å^{-2} and $1.61 * *10^{-6}$ Å^{-2}, respectively. The thickness of the PL is too thick to be probed by NR, only the inverted BL thickness is available: 43.4 nm, in good agreement with SEM images. The SLD of alumina can be then calculated if one knows the porosity ϕ (determined by analysis of the SEM section):

$$SLD_{alu} = \frac{SLD_{PL}}{1-\phi} \tag{1.18}$$

With $\phi = 40\%$ (note that it is higher than the surface porosity, due to pore branching) one finds a SLD of $4.46 * 10^{-6}$ Å^{-2} , consistent with alumina having a density of 3.1 g.cm^{-3}. Then, with this value and the SLD obtained by the fit and assuming that the composition of the alumina is the same in the whole sample, the porosity of the inverted layer can be determined and a value of 64% is found. Finally, with this example, we showed that NR can provide quantitative information about the composition and structure of the nPAAMs.

Now we will present the NR data of the different nPAAMs prepared in oxalic acid and measured in air. Figure 1.43 shows the Rq^4 representation with the best fits and a scheme describing the different layers. Here again SEM images helped for the NR fitting. In the fits the thickness of the porous layer is fixed for thick sample (above 500 nm) since NR cannot probe it.

For sample No.1 we previously saw that the Si were oxidized, so we assume the presence of silicon oxide layer (SiO_2) with a fixed SLD of $3.41 * 10^{-6}$ Å^{-2} at the interface of the Si with a thickness as a fitting parameter. The thickness of the porous layer is fixed with SEM

value and its SLD is a fitting parameter. The fit gives a SiO2 thickness of 20.7 nm and a SLD of the PL of 1.75*10^{-6} $Å^{-2}$. The fit is not perfect, indicating that some others layers might have to be added. Then assuming a porosity of 62% of the PL one finds a SLD of alumina of 4.61*10^{-6} $Å^{-2}$.

For sample No.2, the nPAAM is decomposed in three layers: one porous layer with high porosity (PL1), one porous layer with low porosity (PL2) and an inverted barrier layer (IBL). The thickness of the two PLs are fixed with the SEM values and the one of IBL is a fitting parameter. The best fit give a SLD of PL1,PL2 and IBL at 3.02 and 4.06*10^{-6} $Å^{-6}$ and 0.06*10^{-6} $Å^{-2}$, respectively, indicating that i) the SLD of alumina is 4.5*10^{-6} $Å^{-2}$ (assuming a porosity of 33% for PL1 and 10% for PL2) and ii) the IBL is highly porous (SLD_{air} = 0). The thickness of the IBL is 32.5 nm with a roughness of 6 nm, in good agreement with SEM.

For sample No.3 the data is fitted with one layer having a thickness of 28.4 nm and a SLD of 2.36*10^{-6} $Å^{-2}$. Assuming a porosity of 56% it gives a SLD for alumina of 5.37*10^{-6} $Å^{-2}$, larger than the previous one. One might explain this discrepancy by the fact that porosity in the section is difficult to estimate. Inversely a SLD of alumina of 4.6*10^{-6} $Å^{-2}$ gives a porosity of around 49%. Due to the high roughness the obtained values are not reliable for such thin samples.

Conclusions on NR It is shown that by NR the different structural characteristics of the nPAAMs synthesized on silicon wafer can be probed but complementary techniques such as SEM are necessary to understand the reflectivity curve. In addition, an average SLD of the nPAAM wall was derived and is close to 4.6*10^{-6} $Å^{-2}$.

1.4 General conclusions of Chapter 1

In this chapter tuning of the structure of nPAAMs was presented by synthesis in different electrolytes. The pore diameter can be varied in the range of 10-90 nm. The current density is proportional to the reaction rate and is a global parameter through which samples prepared under different anodization conditions can be compared. By modifying the solvent of the electrolyte new experimental windows can be explored. The substitution of hydrogen to deuterium in the electrolyte (D_2O vs of H_2O, and D_2SO_4 vs H_2SO_4 brings a shift towards a higher ordering of the pores for nPAAMs prepared in sulfuric acid under 20 V and T=10 ℃. Another effect of the deuterium is that the growth rate increases while the dissolution of the pore wall due to the acidity of the solution is less pronounced. Titration of the Al in alumina and in the electrolyte shows that the anodization efficiency is close to 100%, thus

no other reactions that involve charge transfer on the electrode take place, such as the ones described by the oxygen evolution mechanism for nPAAM formation. Post treatments such as chemical etching and annealing can be used to decrease the amount of anion incorporation. The experimental approaches in studying PE in nPAAMs demand the synthesis of different types of nPAAMs such as with or without the Al substrate, open through, or on silicon wafers.

The protocol for the direct detachment by using a 3^{rd} anodization step provides efficiently self-standing membranes with enlarged pore diameters at the bottom side where detachment took place. The current evolution during the 3^{rd} anodization step presents a characteristic behaviour different from the typical anodization and needs further study to rationalise the nPAAM detachement. Anodization of sputtered aluminum on silicon substrate produces less ordered samples and more polydispersed. Nevertheless, it allows for NR measurements that can provide the SLD of the nPAAM wall and used in future studies with the NaPSS.

Chapter 2

Structure and composition of nanoporous alumina membranes

In this Chapter the chemical composition of nPAAMs prepared under three different electrolytes (oxalic, sulfuric, selenic acid) will be investigated by Small-Angle Neutron Scattering, combined with supplementary techniques such as Thermogravimetric Analysis (TGA), Fourier Transform Infrared Spectroscopy (FTIR) and X-ray Diffraction (XRD). In order to understand better the nPAAMs, post treatments were employed such as chemical etching and thermal annealing, as well as synthesis in deuterated electrolyte. Finally, the filling properties and reactivity of the nPAAMs were tested in water and DMSO.

2.1 Introduction

2.1.1 Chemical composition of nPAAMs

It has long been known that the membrane is an amorphous oxide that contains protons, species coming from the electrolyte used during the anodization and physically adsorbed water. The amount and the local arrangement of the above species in the alumina matrix depends greatly on the anodizing conditions (electrolyte nature and concentration, anodizing voltage, temperature) [82] ,[98]. Numerous studies dealt with the quantification and identification of the contamination species using TGA [99], FTIR [100], Secondary Ion Mass Spectroscopy (SIMS) [78], Rutherford backscattering [83], [101] and Electron Dispersive X-ray Spectroscopy (EDX) [102, 103].

Other works focused on the local structure of the oxide as it is known that the incorporated electrolyte species form a distinct region adjacent to the pore channel while the inner material consists of a more pure alumina. The extent of the contaminated region has

been studied by different techniques. For example, the study of the nPAAMs dissolution rate during chemical etching revealed the relative ratios of the two layers [104]. A common technique is the direct observation of the pore wall with TEM and EDX [105]. The inner and outer layer present different contrast (due to their difference in composition) thus their boundaries can be identified [106]. The existence of the duplex structure was explained by the difference in the ionic mobilities of the anionic species [107]. The ionic mobility is defined as the maximum velocity acquired inside a medium of viscosity η , under the force of an electric field E as given by equation 2.1.1,

$$\mu_{ion} = \frac{u}{E} = \frac{zE}{6\pi\eta r_{ion}} \tag{2.1}$$

where r_{ion} the ionic radius and z the ion valence

Due to their smaller size the anions O^{2-} and OH^{-} migrate at a higher velocity than the oxalate $C_2O_4^{2-}$, if oxalic acid is used as electrolyte. It is evident that depending on the electrolyte and anodization voltage the relative ratio of the inner to anion contaminated layer changes. In the case of anodization in 0.3M oxalic acid under 40V, the layer reaches 25 nm and is gradually decreasing in the amount of the contaminants from the pore channel towards the inner wall material [108]. High resolution TEM provided a refined view on the pore wall with three layers starting from an amorphous anion and water contaminated close to the pore channel, an intermediate anion contaminated semicrystalline and a deeper pure crystalline alumina [109] .

In one of the first studies of the cell material with an electron beam by G.E Thomson et al. [82], it was observed that the oxide comprised of crystallites of the order of 2 nm. Moreover, during prolonged exposure to the beam the crystallites increased in size, coagulated until the double layer structure couldn't be probed by the beam. Due to the destructive nature of the technique, uncertainty was raised on the initial existence and size of this nanoscale substructure. The existence of crystallites was proposed by J.P O'Sullivan by studying the mechanism of hydrothermal sealing of nPAAMs and it was proposed that the nPAAMs bulk material consisted of anhydrous alumina microcrystallites whose surface was covered by hydroxyls and acid ions. Furthermore, the intercrystallite regions was found to be totally permeable to water molecules [100]. Mardilovich et al. during water treatment of nPAAMs found that the alumina matrix could hold up to 7 %wt. of H_2O molecules [110]. On the contrary flow studies with hydrogen gas and organic solvents showed no permeation for nPAAMs having the barrier layer [111]. To solve this contradiction, Mardilovich et al. proposed that only the amorphous anion contaminated region is permeable to molecules while the crystalline pure alumina of the inner layer of the pore wall and barier layer remains

impermeable [110]. The lower scale porosity has not been studied in detail and seems to be forgotten since its first implications of its existence. A better understanding of this characteristic can provide information on the mechanism of formation of the nPAAMs and plays important role when the membrane is used for example for molecular transport studies.

It is widely known that the composition of alumina is also affected when in contact with water . Alumina reacts with water giving various types of aluminum hydroxide. The transformation of the alumina is based on the dissolution of Al^{3+} in the water solution, the formation of charged aluminum hydroxide complexes and their possible precipitation on the solid surface. The above processes depend on the pH of the solution and equilibrium between the solid surface and the solution might last after several months [112]. In the case of anodized aluminum, this reactivity of alumina with water is exploited in the process of hydrothermal sealing. The process takes place inside hot water and involves the filling of the pores due to the precipitation of aluminum hydroxide complexes that are formed in abundance due to the elevated temperature. Although the efficiency of sealing process has been studied for various types of porous alumina membranes [113], [114], little information exists on the transformation and evolution in low temperature and short time scales. It is evident that any measurement that involves the alumina membrane water system is affected by this transformation. For example, the reaction of nPAAMs with water has huge effect on its permeability performance during flow measurements [115].

2.1.2 Probing the composition by Small Angle Scattering techniques

The nPAAMs present complexity in their composition and certain aspects such as bulk hydrogen content, substructure and stability in water cannot be fully probed by the so far used experimental techniques due to limitations in their resolution, destructive nature and sensitivity. Small Angle Scattering (SAS) techniques can overcome this issue because they are non destructive, sensitive to very small changes in composition, can be used to study binary systems and also to give acess to average structural information over a large volume. A lot of Small Angle X-ray scattering (SAXS) [116, 117, 116, 118, 119, 120] and SANS [121, 122, 123] studies are concerned with the pore ordering of the nPAAMs but a few focused on the composition.

Small-Angle Neutron Scattering (SANS) appears to be a powerful tool to characterize both the pore organization (D_p and D_{int}) and the chemical composition by determining the different scattering length density (SLD) of the material using the contrast variation method[123, 124, 122, 125]. This method consists in cancelling the confining medium scat-

tering using an appropriate mixture of deuterated/hydrogenated solvent whose SLD matches the one of the confining medium, the so-called "matching point". Such approach allows the determination of the composition of the materials. Previous works done on AAO membranes showed that i) multiple scattering effects might arise due to high pore density[126, 122, 121] and that ii) AAO cannot be perfectly matched[123, 124]. Contrast variation shows a minimum but the scattering intensities remains still high. Imperfect matching comes from inhomogeneities in composition in the AAO due to the presence of contaminants (anions from the electrolyte or water molecules) that organize as a shell around the pores[99, 102, 127]. Complementary neutron diffraction data showed the existence of bayerite clusters in the alumina bulk [124]. Perfect matching is challenging and as a consequence the scattering signal becomes more difficult to analyze. To overcome this issue and decrease the scattering from the AAO some authors proposed a tilting (25^o - 30^o) relative to the incident beam[128, 129]. However, due to such complexity, few studies attempted at reproducing the experimental SANS data. Marchal et al.[123] fitted the SANS high q-range of commercial Anodisc membranes by a Porod law to extract its specific surface. Lefort et al.[4] used a combination of a cylinder form factor with a hexagonal structure factor to fit homemade AAO under one contrast condition, considering that the AAO are homogeneous in composition. But no works, so far, fully reproduced the SANS scattering curves under several contrast conditions and solvents.

Finally, the full fitting of the experimental scattering data of nPAAMs with a cylinder model was presented only in a SANS and a SAXS study [125, 130] and a core-shell cylinder model was used in a SAXS study of [120]. In the following SANS will be used to investigate the chemical and structural aspects of nPAAMs as prepared under different conditions. This technique will be combined with TGA, XRD and FTIR of nPAAMs prepared under different conditions.

2.2 Experimental aspects

2.2.1 Sample preparation

As detailed in Chapter 1, the samples were prepared by anodization on both sides of aluminum foil 99.999% of 320 μm. For samples that were post treated with annealing, 1 side anodization was carried out and the aluminum substrate was chemically removed. It should be noted that the presence of the aluminum foil doesn't affect the measurement as it is transparent to the neutron beam.

Instrument	sample to detector total distance d (m)	neutron wavelength λ(Å)	q range (Å^{-1})
PAXY (LLB)	6.7	15	2×10^{-3} - 0.5
	3	6	
	1	6	
D11 (ILL)	39	6	2×10^{-3} - 0.4
	8	6	
	1.4	6	

Table 2.1: Measurement configuration for experiments performed on D11 (ILL) and PAXY (LLB) spectrometers.

2.2.2 SANS measurements and nPAAMs alignment

From SANS one can probe the pore organisation and the nPAAMs composition from the analysis of the scattering intensity. For centrosymetric objects the scattering intensity I(q)) is generally expressed by the relation (2.2):

$$I(q) = \Phi \Delta\rho^2 V P(q) S(q) \tag{2.2}$$

With Φ the volume fraction of scattered objects (here nanopores), $\Delta\rho^2 = (\rho_{Al_2O_3} - \rho_{solvent})^2$ the contrast term, V=π $(D_p/2)^2$ L_p the volume of the nanopore, P(q) the form factor and S(q) the structure factor.

In order to characterize the membranes prepared under different anodization conditions we performed sets of experiments at instruments PAXY (LLB) ad D11 (ILL). The configuration is shown in Table 2.1.

The nPAAMs were cut into squares of approximately 1×1 cm and placed inside circular cells, closed by quartz windows. Inside the cell, a mixture of deuterated and hydrogenated solvent was poured, while a Teflon o-ring of about 300 µm protected from leaks. Prior to loading in the cell, each membrane was immersed inside the corresponding solvent for some seconds to be wetted in order to avoid air bubbles being created inside the cell. The membranes were measured with their pore axis aligned with the neutron beam, as depicted in Figure 2.1.

The good pore alignment along the neutron beam is done for each sample by evaluating the isotropy of the 2D scattering interference pattern on the detector. Ideally, for a perfectly aligned sample the interference pattern consists of concentric rings as shown in Figure 2.2. In order to make the alignment we use two goniometers which can perform tilting and rotation of the sample by steps of 0.002°. The sample is tilted in one direction (X or Y) to create

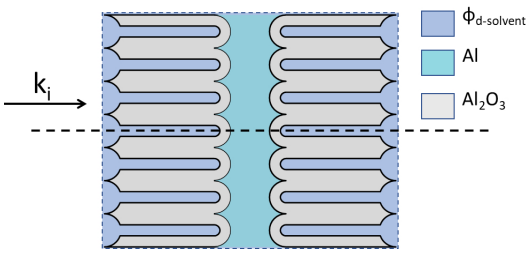

Figure 2.1: Positioning of sample towards the incident neutron beam (noted as k_i) for measurements with SANS .

Figure 2.2: Detector's interferance pattern for sample with pore axis aligned to the neutron beam .

strong anisotropy and the appearance of non-aligned spots on the other direction (Y or X) (See Figure 2.3).

2.2.3 Multiple Scattering and optimal SANS conditions

In the following paragraphs certain aspects concerning the scattering behaviour of nPAAms will be developed. As an example we will use measuremens of membranes prepared under 40V and T=18 ℃ for 11h and 30min (L=171µm). The SANS scattering spectra of the membranes, immersed in mixtures with different volume fractions of D_2O (Table 2.2) are presented in Figure 2.4.

ϕ_{D_2O}	0.000	0.500	0.618	0.677	0.707	0.732	0.8	1
$\rho_{solv} \times 10^{-6}$ Å^{-2}	-0.56	2.89	3.70	4.10	4.31	4.48	5	6.39

Table 2.2: Scattering length densities of the different H_2O/D_2O mixtures.

By a first look we can identify the presence of peaks in the low q range. The lowest intensity was achieved for the ϕ_{D_2O}=73.2%. Even at this lowest intensity (10^2) in the low q region, peaks still exists. In the middle and high q, the intensity scales as q^{-3} power law, as expected for scattering from aligned cylinders.

As we move away from this point of low intensity, for 100% and for the sample measured in air (0%), the intensity increases up to 10^5 cm^{-1}, the peaks diminish and in the middle q range the slope of the curve changes gradually to q^{-6}. Given that a very precise alignment procedure is followed, we attribute this effect to multiple scattering. Another supporting element for such behaviour can be extracted by looking the transmission for each contrast.

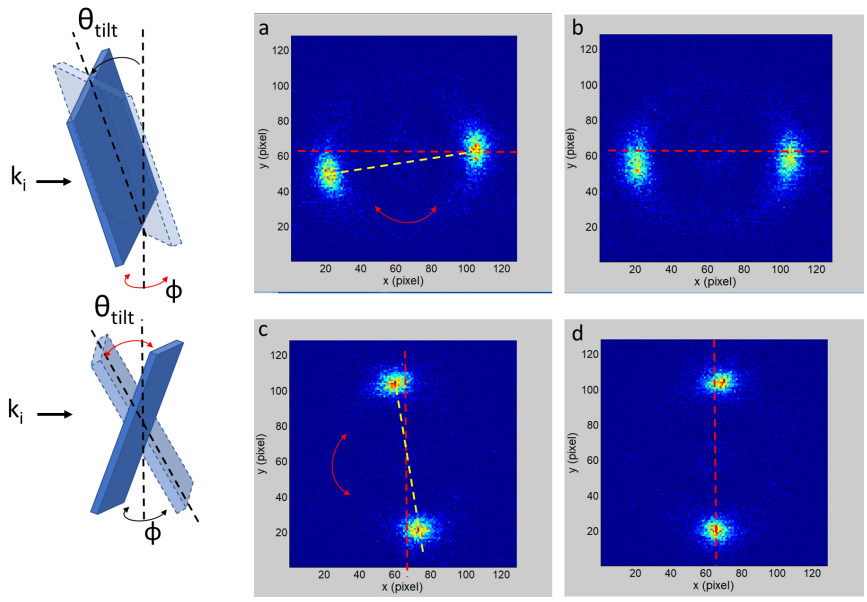

Figure 2.3: Detector's interferance pattern for sample with pore axis aligned to the neutron beam .

The transmission is defined as the ratio between the number of transmitted neutrons through the AAO over the total number of neutrons of the incident beam.

The transmission of the samples measured in the low q configuration, as a function of the D_2O volume is shown in Figure 2.5).

Remarkably, the transmission is 90% for a very small range of contrasts near 70% of ϕ_{D_2O}. For all contrasts the transmission is very low. Such a behaviour can be attributed to multiple scattering as the theoretical scattering cross section of absorbance of alumina is very low. Although multiple scattering is always present in a measurement its extent is qualitatively figured out by the low transmission values $T < 0.5$ and high scattering intensity in the low q range ($I > 10^4$ cm^{-1}) [131]. Multiple scattering is undesirable in SANS because it distorts the scattering signal with a contribution that cannot be treated in the context of single-scattering approximation analysis. For this reason the study of nPAAMs with SANS will be focused on samples measured around the lowest intensity point.

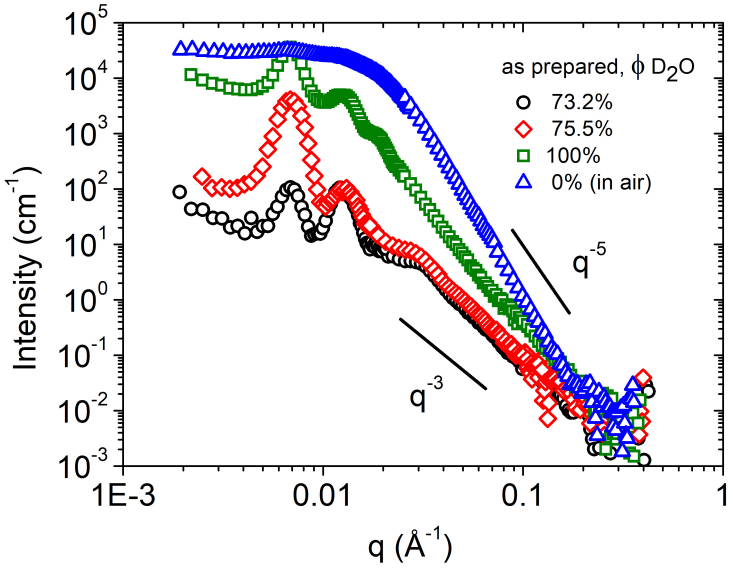

Figure 2.4: Spectra of nPAAMs synthesized in 0.3M oxalic acid under 40V for 11h and 50m (171µm, obtained for different volume fractions of D_2O .

2.3 Results

2.3.1 nPAAMs prepared in oxalic acid

In this section nPAAMs prepared in oxalic acid 0.3 M under 40 V and T=18 ℃ will be presented. The membranes were measured with no post treatments ("as prepared") and after chemical etching. In order to access the structure and the composition of the membranes contrast variation was employed in different volume fractions of D_2O.

2.3.1.1 Contrast variation of "as prepared" nPAAMs : evidence of heterogeneities in composition

Figure 2.6 shows the scattering intensity of "as prepared" nPAAMs in H_2O/D_2O mixtures (between 67.7%, 75.5% D_2O).

The first peak q_1 corresponds to the interpore according to the following relation,

$$q_1 = \frac{2\pi}{D_{int}} \tag{2.3}$$

This can be seen also from the extraction of the structure and form factor from the SEM image as analysed in Chapter 1 and shown in Figure 2.7. The structure and form factor

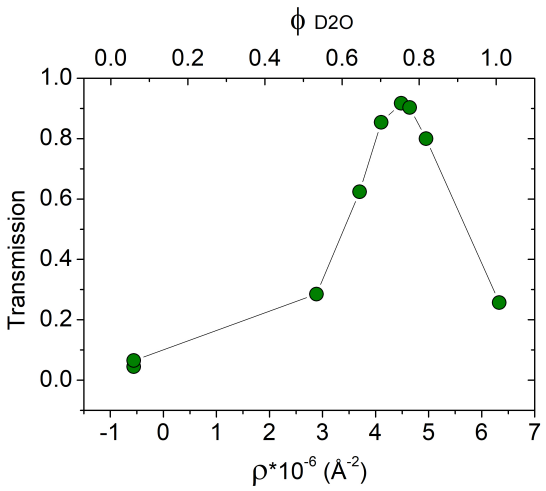

Figure 2.5: Transmission of sample for different volume fraction of D_2O at small angles (6m, 15 Å, PAXY (LLB)).

start to convolve after q_1. The peak is found near $q_1 \simeq 0.006$ Å^{-1} which gives a value for the interpore distance $D_{int} \simeq 100$ nm, in good agreement with the values derived from the SEM analysis. Moreover, for the plotted contrasts of Figure 2.6 the intensity at high q scales to q^{-3} which ensures for non strong multiple scattering effects.

Even if some first elements on the existence of multiple components in the material have been given by the scattering spectra, a global view can be acquired by studying the scattering intensity at a certain q value as a function of the scattering length density of the solvent (ρ). Such contrast variation plots can provide the appropriate volume fraction of D_2O where the scattering intensity of the nPAAMs is the lowest. Such the fraction is called the "matching point".

In Figure 2.8 a typical contrast variation plot for the determination of the matching point of the nPAAms is shown. The plot is obtained by taking the square root of the intensity at a certain q and plot it as a function of the volume fraction of the solvent or equivalently of the scattering length density ρ_{solv}. According to relation 2.2 the scattering intensity should be parabolic with a clear minimum, i.e $\sqrt{I}$ should be linear with $\Delta\rho$ (or ϕ_{D_2O}). In this kind of representation, certain values after the point of lowest intensity are put in negative sign in order to present the data on the same line. Then the linear fitting function of the graph gives the abscissa for zero scattering intensity which is the matching point. The chosen wavevectors q here correspond to the first two peaks in the low q region (q_1 and (q_2)) and to the oscillations in the intermediate q region (q_3) as seen in Figure 2.7. The points affected with multiple scattering are not included in the plot.

A matching condition tends to be accomplished for q_1 with an output value of $\rho_{Al_2O_3}$=4.44∗

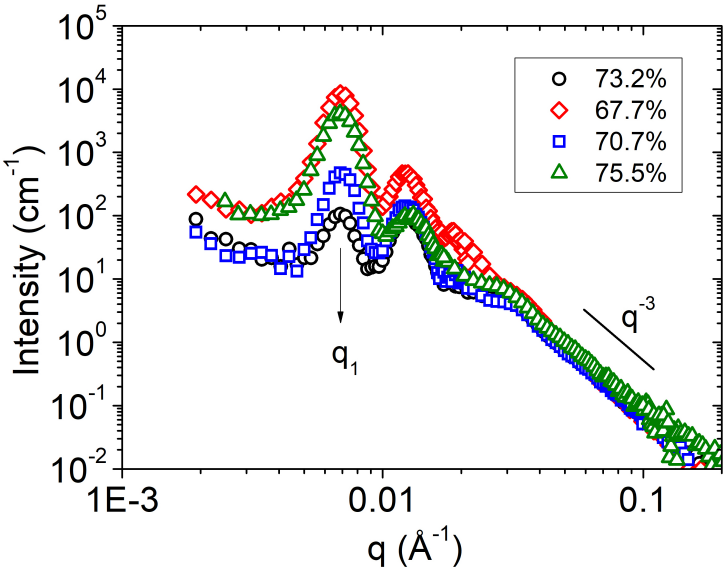

Figure 2.6: SANS scattering spectra of nPAAMs synthesized in 0.3 M oxalic acid under 40 V for 11h30 (L=171 µm),for different volume fractions of D_2O .

10^{-6} Å^{-2} and a corresponding volume fraction D_2O of 72.3%. From a theoretical point, the above value is close to $\rho_{Al_2O_3}$=$4.45 * 10^{-6}$ Å^{-2} for alumina of density 3.1 g cm^{-3}.

On the contrary, the linear fits for q_2 and q_3 have a very low regression coefficients, indicating that the matching doesn't converge to a unique point. The fact that the scattering intensity doesn't converge and shows dissimilar trend for the different q values underlines the existence of more than one composition in the "as prepared" nPAAMs.

The contamination of the pore wall with anion electrolyte roots is a possible reason for this heterogeneity and the mismatch of the nPAAMs when measured in SANS. Nevertheless, the existence of hydroxides in the bulk of the skeleton due to reaction of OH^- groups migrating through the barrier layer and reacting with Al^{3+} have to be studied as well.

A qualitative view on the different chemical species present in the nPAAMs can be acquired by the IR spectroscopy. In Figure 2.9 the transmission spectra of a nPAAM prepared in 0.3M oxalic acid under 40V is presented. The broad peak in the region of 3400 cm^{-1} belongs to vibration of -OH bond of water molecules. At 2342 cm^{-1} we observe A smalL peak that belongs to CO_2 present in the air. In the region of 1500 cm^{-1}, the band is saturated from symmetric and antisymmetric stretching of carboxylate anions (1547, 1465 cm^{-1}) [132].

When the nPAAMs is heated at 300 ℃ the peaks in the IR spectra change. In Figure 2.10 it is observed that -OH from water starts to decrease while CO_2 decreases. The water is

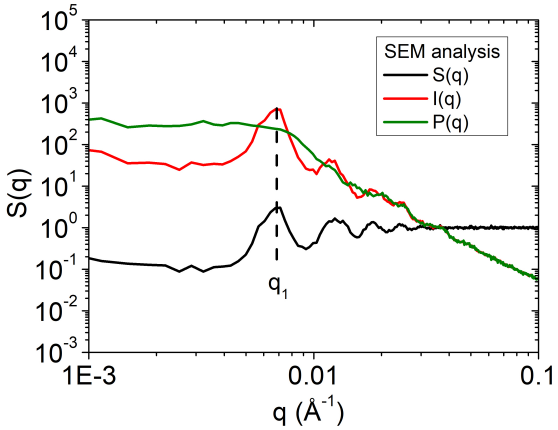

Figure 2.7: Structure and form factor derived from SEM image analysis for sample prepared in oxalic acid 0.3 M under 40V and T=18 ℃.

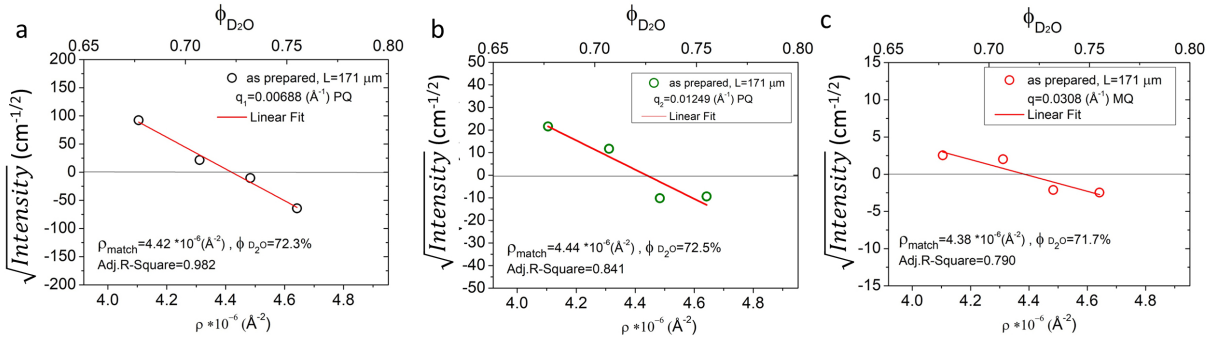

Figure 2.8: Contrast variation graph for nPAAM prepared in 0.3M oxalic acid under 40 V and T=18 ℃ measured in different volume fractions of D_2O at a) q_1 (1^{st} peak position) b) q_2 (2^{nd} peak position) c) q_3 position

condensed inside the pores and with heating above 100 ℃ it evaporates. The CO_2 decrease in transmission is enhanced as the carboxylates that are embedded inside the alumina start to decompose with an increase in temperature. It is known that most of the CO_2 stays trapped inside the alumina lattice until the temperature reaches 900 ℃ where alumina starts to crystallize.

More quantitative information on the contaminants can be also derived through TGA(Thermogravimetric Analysis). nPAAMs prepared with oxalic acid, detached from the substrate were measured with TGA from room temperature until 987 ℃ with a heating rate of 2℃/min under nitrogen atmosphere. In Figure 2.11 the weight loss as a function of temperature is presented. The first weight loss until 230 ℃ is attributed to water evaporation adsorbed inside the pores and equals to 0.7 %. Other oxalic impurities $H_2C_2O_4$ can be

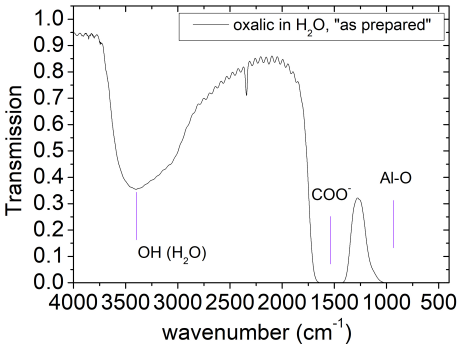

Figure 2.9: IR spectum of nPAAM prepared under 40V 0.3M oxalic acid T=18 ℃ for 8 hours (L=60 µm). Note that the Al substrate has to be removed to perform IR measurement.

neglected. This limit was chosen according to Thermal Differential Analysis (DTA) from literature [133]. Then, from 230 ℃ until 600 ℃, the weight loss is due to dehydroxilation and decomposition of aluminum oxalate $Al_2(C_2O_4)_3$ mainly into CO as presented in [127]. Moreover in this paper, mass spectroscopy coupled to the TGA analysis was used to distinguish between the amount of OH, CO_2 and CO. The ratio of OH to the total amount of CO_2 and CO is about 1/3 (i.e 0.13%). The largest loss happens at 900 ℃ and can reach 5.3 % and is attributed to decomposition of the same species that is CO_2 trapped in the alumina lattice. A smaller amount of CO_2 is also reported to evaporate after 1000 ℃ in the region of the transition to $\alpha - Al_2O_3$ but here this temperature was not reached due to the instrument limits.

To conclude, as prepared membranes in oxalic acid have shown multiple scattering effects in SANS. Signs of this effect is the very high intensity, the peak broadening and the change in the slope. These effects are minimized when measuring close to the matching point. The scattering intensity normalized by the sample thickness is the same for all the samples prepared under different times which means that there exists reproducibility. Most of the contamination of the membrane is due to the anion incorporated species, in this case it is oxalates, which can be removed by annealing above 900 ℃.

To conclude, due to multiple scattering and to minimize its effects (very high intensity, peaks broadening and change in slope at high q, nPAAMs have to be measured in a small range of solvent SLD. By doing so, we observe that full nPAAMs matching cannot be achieved due to its heterogeneities in composition. From TGA and IR measurements we showed that the contamination of nPAAMs is due to anion incorporated species, in this case oxalate, which can be removed by annealing above 900 ℃.

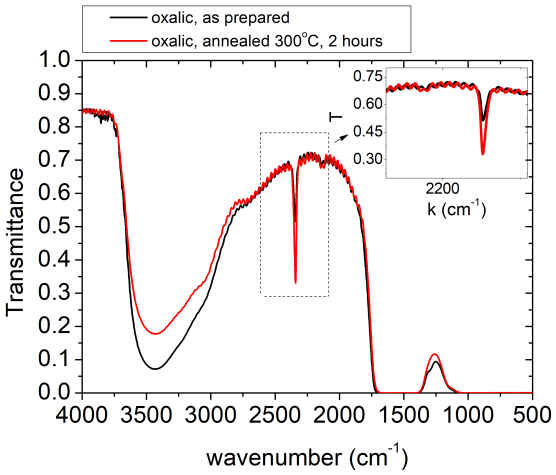

Figure 2.10: Spectra of as prepared membrane in oxalic acid 0.3 M under 40 V before and after thermal annealing at 300 ℃ for 2 hours.

2.3.1.2 Full SANS interpretation: fitting strategy

In this section we will detail the model used to fit the SANS data. In order to proceed to the fitting of the experimental SANS data we will have to constrain certain parameters, thus the structure factor derived from the SEM analysis (as described in Chapter 1) will be used.

The form factor we use is a core-shell cylinder model as depicted in Figure 2.12 and expressed as:

$$P(q,\alpha) = \frac{\phi_s}{V_s} F^2(q) + bckg \tag{2.4}$$

$$\begin{aligned} F(q) = (\rho_{core} - \rho_{shell}) V_c \frac{sin(\frac{qLcos\alpha}{2})}{\frac{qLcos\alpha}{2}} \frac{2J_1(qR_p sin\alpha)}{qR_p sin\alpha} \\ + (\rho_{shell} - \rho_{Al_2O_3}) V_{shell} \frac{sin(\frac{qLcos\alpha}{2})}{\frac{qLcos\alpha}{2}} \frac{2J_1(q(R_p+t) sin\alpha)}{q(R_p+t) sin\alpha} \end{aligned} \tag{2.5}$$

where

- ϕ_s: surface porosity
- ρ_{core}: scattering length density of the core
- ρ_{shell}: scattering length density of the shell
- $\rho_{Al_2O_3}$: scattering length density of alumina
- L: Length of the cylindrical object

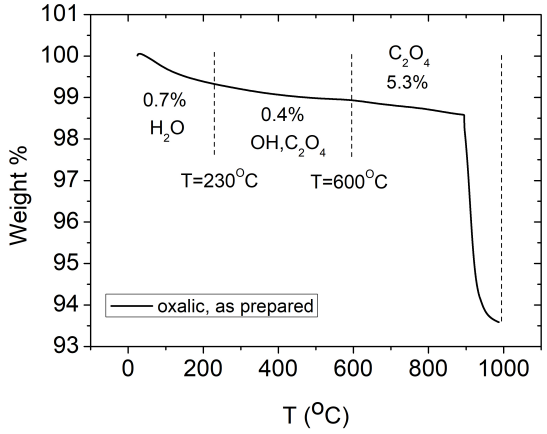

Figure 2.11: Weight loss (%) as a function of temperature for membrane prepared in 0.3 M oxalic acid under 40 V and T=18 ℃ .

- V_c: volume of the core, V_c=πR_p^2L
- V_s: volume of the core-shell, V_s=$\pi(R_p + t)^2$L
- J_1: Bessel function of the first kind
- α the angle between the pore axis and the normal to the incident beam
- t: the thickness of the shell

Here the surface porosity ϕ refers to the surface fraction of the scattering object which in our case is the core plus the shell and is given by relation 2.6:

$$S = n\pi(R_p + t)^2 \tag{2.6}$$

where,

n: pore density (pores cm^{-2})

This value is correlated to the pore radius which is adjusted during the fit. The interpore distance D_{int}, σ_{int} and D_p are taken initially from the SEM characterisation and adjusted during the fit if necessary.

For cylinders aligned with their pore axis parallel to the neutron beam, α=90° and *F(q)* becomes:

$$F(Q) = 2V_c(\rho_{core} - \rho_{shell})\frac{J_1(QR)}{Qr}J_1(QR_p) + 2V_s(\rho_{shell} - \rho_{Al_2O_3})\frac{J_1(Q(R_p+t))}{Q(R_p+t)} \quad (2.7)$$

In the model it is possible to account for polydispersity in the radius and the shell. The type of the distribution is a gaussian given by equation 2.8.

$$f(x) = \frac{1}{\sqrt{2\pi}\sigma}exp(-\frac{(x-x_{mean})^2}{2\sigma^2}) \quad (2.8)$$

where

1. x_{mean}: the mean value
2. σ : the standard deviation

The fitting parameter is the polydispersity ratio defined as the mean value over the standard deviation σ of the distribution, as in equation 2.9.

$$PD = \frac{\sigma}{\chi_{mean}} \quad (2.9)$$

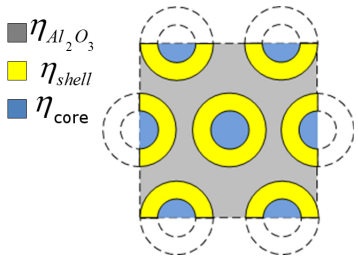

Figure 2.12: Fitting model scheme of an hexagonally arranged core-shell cylinders.

In Table 2.3 the fitting parameters are presented. The parameter c_L is a scaling parameter to correct for the Porod invariant [134].

The parameter δ is the inverse of the grain size of the ordered domains. In this case we have to consider the coherence length of the neutrons in the transversal direction relative to the beam path. The neutron coherence length gives the maximum probing length of our sample because it gives the maximum extent in which the neutrons can interfere. The transversal coherent length of the neutron beam is given by

$$L_T = \frac{\lambda}{\Delta\Theta} \quad (2.10)$$

where

Fitting paramaters
Porosity ϕ_s
D_{int} (nm)
σ_{int} (nm)
δ
cL
$\rho_{core} * 10^{-6}$ (Å^{-2})
$\rho_{shell} * 10^{-6}$ (Å^{-2})
$\rho_{Al_2O_3} * 10^{-6}$ (Å^{-2})
R_p (nm), s_p
t (nm), σ_t

Table 2.3: Model parameters

1. λ : the neutron wavelength

2. $\Delta\Theta$ the divergence of the direct beam

For the samples measured at LLB at 15 Å we have a $\Delta\Theta$=0.002 and L_T=750 nm . Equivalently, this gives δ=0.00084 Å^{-1}. For ILL measurements $\Delta\Theta$=5.4×10^{-4} giving a L_T of 1112 nm i.e δ=0.00056 Å^{-1}

Here, we have to consider two cases:

1) If the grain size G of the ordered domains as measured by SEM is smaller than the L_T, then the parameter δ is a fitting parameter.

2) If the grain size G is larger than L_T, then the δ is set to the L_T.

In order to avoid any overlapping of the scattering objects, the length of the shell must be smaller than,

$$t < \frac{D_{int} - 2R_p}{2} \tag{2.11}$$

Finally, the experimental resolution is taken into account by the fitting software, through the use of the experimental error on q.

2.3.1.3 Application of the model to the "as prepared" nPAAMs

The fitting of the as prepared nPAAMs (named OA2) is presented for a samples measured at D11-ILL spectrometer. The structural parameters obtained by the SEM analysis are presented in Table 2.4.

The fits of the as prepared sample "OA2" are presented in Figure 2.13 for three different volume fractions of D_2O. The fit is constrained to q values $0.3 * 10^{-3}$ Å^{-1} as the increase in the scattering intensity below this range is attributed to microscopic fractures, due to

sample	Spectrometer	R_p (nm)	σ_r (nm)	D_{int} (nm)	σ_{int}	$\delta(\text{Å}^{-1})$	grain size (nm)	n$\times 10^{10}$ (cm^{-2})	L (μm)
OA2	D11 (ILL)	21	4	106	0.06	0.0006	1047	1.1	58.4

Table 2.4: Sructural parameters of nPAAM OA2 obtained by SEM analysis.

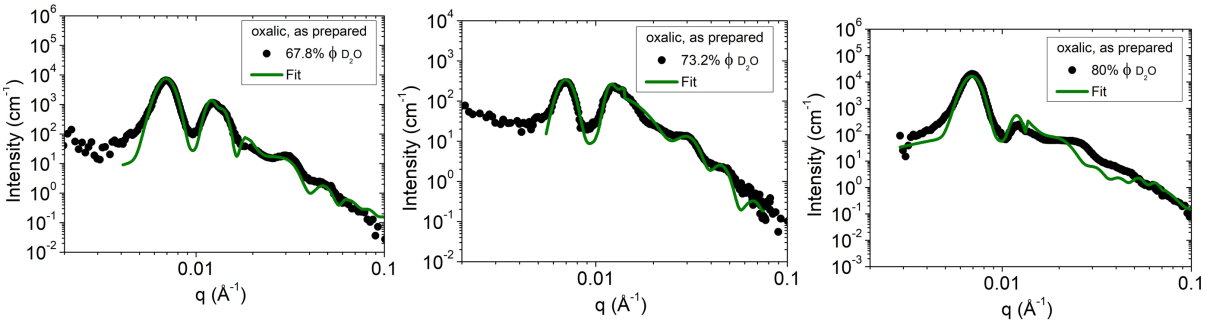

Figure 2.13: Experimental SANS data with fit of sample "OA2" for different volume fractions of D_2O (measurements performed at D11): 67.8%? 73.2% and 80%.

cutting of the sample. All the parameters derived from the fit of sample "OA2" are presented in Table 2.5. It is observed that the geometrical characteristics such as the D_p and D_{int} are close to the values obtained from the SEM characterisation.

The D_p from SANS is slightly smaller than the SEM since SANS probe the whole sample and SEM only the surface. The corresponding grain size equals to 785.4 nm and is less than the one observed by SEM (1047 nm). It can be concluded that in terms of structure the SANS measurements confirms the SEM analysis.

In terms of composition, the data cannot be fitted with a simple cylinder model and the use of a shell is necessary with an extent of 10 nm. Moreover, it is observed that the scattering length densities $\rho_{\text{Al}_2\text{O}_3}$ and ρ_{shell} related to the nPAAM outer and inner material depend on the solvent by which the pores are filled. Their relative differences are shown in Table 2.6. Note that for the 67% the $\rho_{\text{AL}_2\text{O}_3}$ and ρ_{shell} are equal, so the data can be fitted without any shell.

The causes of such an effect can be the following:

1. transformation of the alumina due to reaction with water [112]

2. diffusion of the solvent in a porous layer

The absolute values of the scattering length densities provided by the fit lay within the experimental error.

$T_r(8m,6)$	0.9127	0.9187	0.9456
ϕ_{D_2O}	0.678	0.732	0.8
Fitting paramaters			
ϕ_s	0.29	0.29	0.29
D_{int} (nm)	104	104	104
σ_{int}	0.06	0.06	0.06
δ	0.0006	0.0006	0.0006
cL	30	8	15
$\rho_{core} * 10^{-6}$ ($\mathring{A}^{-2}$)	4.11	4.47	4.95
$\rho_{shell} * 10^{-6}$ ($\mathring{A}^{-2}$)	4.14	4.5	4.96
$\rho_{Al_2O_3} * 10^{-6}$ ($\mathring{A}^{-2}$)	4.14	4.49	4.99
R_p (nm)	18	18	18
σ_p (nm)	9	18	18
t (nm)	10	10	10
σ_t (nm)	2	2	2

Table 2.5: Fitting results for sample "OA2" for as prepared sample in 0.3 M oxalic acid under 40 V, T=18 ℃, thickness 58.4 µm.

ϕ_{D_2O}	0.678	0.732	0.80
(ρ_{core}-ρ_{shell})	0.03	0.03	0.01
(ρ_{core}-$\rho_{Al_2O_3}$)	0.03	0.02	0.03
(ρ_{shell}-$\rho_{Al_2O_3}$)	0	0.01	0.03

Table 2.6: Scattering length density differences for as prepared sample OA2 in 0.3 M oxalic acid 40 V.

2.3.1.4 Effect of chemical etching

In order to obtain nPAAMs less contaminated (i.e without a shell), chemical etching was employed. The samples were prepared under the same anodization conditions as the samples "OA1" and "OA2". The etching was done in phosphoric acid 5 wt. % at 30 ℃ for 50 min. In Figure 2.14a the SANS spectra of the etched nPAAMs "OA1 etched" are shown for the same D_2O volume fractions of the as prepared samples. The scattering intensity differs in the low q region compared to the as prepared sample while for the middle q the slope still scales to q^{-3}. The different shape of the peak between the as prepared "OA1" and the etched sample "OA1 etched", as seen in Figure 2.14a implicates a modification in the pore form factor *P(q)*.

In Figure 2.15 the contrast variation plot are shown for the "OA1 etched" sample at the same three q wavevectors used for the as prepared sample. The contrast variation curve shows the same behaviour as the as prepared membranes for all contrasts. Contrast matching is not possible and a small deviation exists in the 1^{st} q position which can be explained by a shift of the form factor *P(q)* to lower wavevector and its convolution with the structure

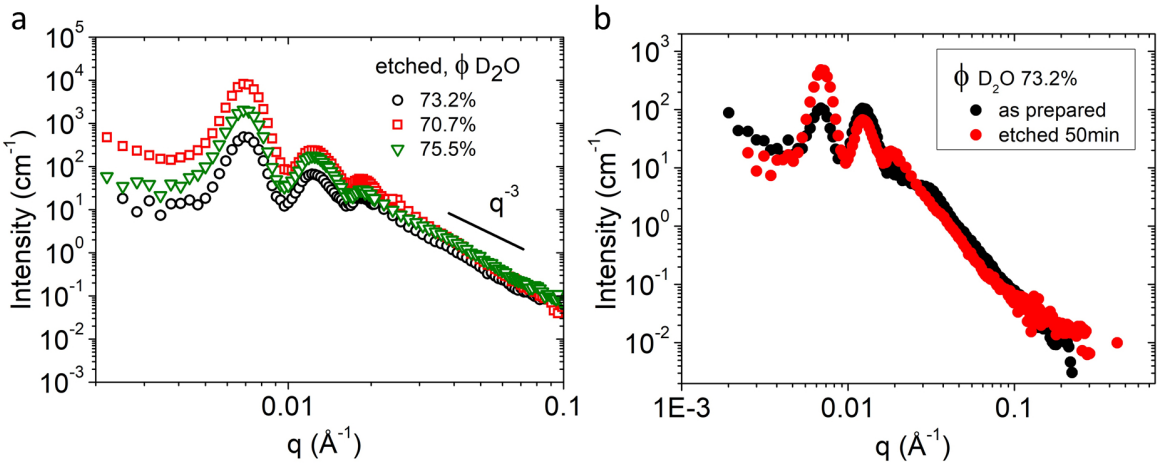

Figure 2.14: a) SANS spectra of nPAAMs OA1 etched for 50min in phosphoric acid for different volume fractions of D_2O . b) Spectra of the as prepared and the etched nPAAMs at a similar volume fraction $\phi_{D_2O} = 73.2$ %

.

factor *S(q)*.

Figure 2.16 shows the fit of OA2 etched SANS data. In order to constrain the fit, the pore radius value R_p value is taken from the SEM analysis shown in Table2.7.

sample name	Spectrometer	R_p (nm)	σ_r (nm)	D_{int} (nm)	σ_{int}	δ (Å^{-1}	grain size (nm)	n*10^{10} (cm^{-2})	L (µm)
OA2 etched	ILL	29	5	107	0.07	0.0006	1047	1.1	58.4

Table 2.7: Structural parameters of nPAAM OA2 obtained by SEM analysis.

It is found that the pore radius has increased from 18 nm for the as prepared sample "OA2", to 29 nm for the "OA2 etched" sample. This means that the anion incorporated layer of 10 nm in thickness as derived from the fit of the as prepared sample has been etched away. For this reason the fitting model will not include a shell.

As seen in Figure 2.16 this strategy works well for the volume fractions of 70.7 % and 73.2% but this is not the case for the 75.5 % where a shell had to be taken into account. Moreover, the volume fraction of D_2O that gives the lowest intensity on all peaks, is shifted relatively to the previous as prepared sample "OA1", "OA2" and the etched sample "OA1 etched". The corresponding value is achieved for D_2O=75.5% instead of 73.2%. These two elements indicate a chemical modification on this specific sample that might have been caused from prolonged immersion in the cell with water and transformation to a hydrated alumina (see section below).

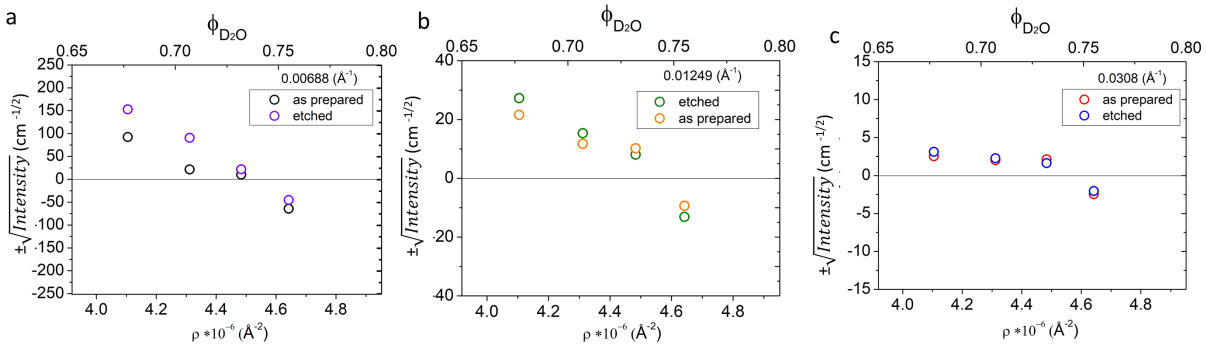

Figure 2.15: Contrast variation plot for nPAAMs prepared in 0.3 M oxalic acid under 40 V and T=18 ℃ and etched for 50min in 5% wt. H_3PO_4. a) q_1 peak position b) q_2 peak position c) q_3 peak position q position

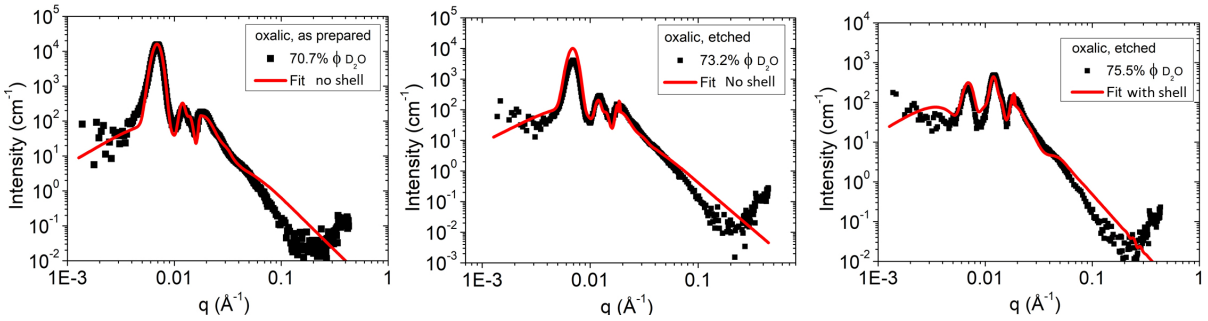

Figure 2.16: Experimental SANS data with fits of sample "OA2 etched" for different volume fractions of D_2O (measurements performed at D11): 70.7%? 73.2% and 75.5%.

The values extracted from the fit are shown in Table 2.8. The pore diameter measured in SEM fits well with the SANS data but with a smaller standard deviation. As in the as prepared sample, the scattering length density of alumina is adjusted to the solvent. The scattering length differences are shown in Table 2.9.

ϕ_{D_2O}	0.707	0.732	0.755
Fitting paramaters			
ϕ_s	0.31	0.31	0.82
D_{int} (nm)	104	104	104
σ_{int}	0.03	0.03	0.03
$\rho_{core} * 10^{-6}$ (Å^{-2})	4.31	4.48	4.64
$\rho_{shell} * 10^{-6}$ (Å^{-2})	-	-	4.66
$\rho_{Al_2O_3} * 10^{-6}$ (Å^{-2})	4.36	4.44	4.63
R_p (nm)	29	29	29
t (nm)	-	-	13
σ_p (nm)	2.9	2.9	2.9
σ_t (nm)	-	-	3.6

Table 2.8: Fitting results for sample "OA2 etched" prepared in 0.3M oxalic acid under 40V, T=18 ℃, thickness 58.4 µm and etched for 50min in phosphoric acid.

ϕ_{D_2O}	0.707	0.732	0.755
(ρ_{core}-ρ_{shell})	-	-	0.02
(ρ_{core}-$\rho_{Al_2O_3}$)	0.05	0.04	0.01
(ρ_{shell}-$\rho_{Al_2O_3}$)	-	-	0.03

Table 2.9: Scattering length densities contrast differences for sample "OA2 etched"

2.3.1.5 Deuterated membranes prepared in oxalic acid

Previously we concluded that most of the contaminants are due to oxalate species embedded in the alumina lattice and the amount of OH is negligible, as derived from the TGA analysis. However, it is not known how this small amount can affect the SANS spectrum because neutron scattering might be greatly affected. If this small amount of hydrogen dominates the scattering then an isotopic substitution of hydrogen with deuterium is expected to modify the spectra due to the large difference in the scattering length between H (ρ_D=$0.667 * 10^{-6}$ Å^{-2}) and D ($\rho_H = -0.374 * 10^{-6}$ Å^{-2}).

sample	Spectrometer	R_p (nm)	σ_r (nm)	D_{int} (nm)	σ_{int}	δ(Å^{-1})	grain size (nm)	n*10^{10} (cm^{-2})	L (µm)
OA D_2O	PAXY (LLB)	22.1	8	101	0.06	0.0007	898	1.1	122
OA H_2O	PAXY (LLB)	28	5	105	0.07	0.0007	898	1.1	164.8

Table 2.10: Sructural parameters of nPAAM OA2 obtained by SEM analysis.

In the following paragraphs the contribution of H in the scattering spectra will be evaluated by means of isotopic substitution of the solvent during the synthesis. Instead of preparing solutions of electrolytes in H_2O, we used D_2O during the synthesis (as described in Chapter 1). By comparing the scattering spectra of nPAAMs prepared in the same an-

odization conditions but with different solvent, the scattering contribution due to H can be evaluated.

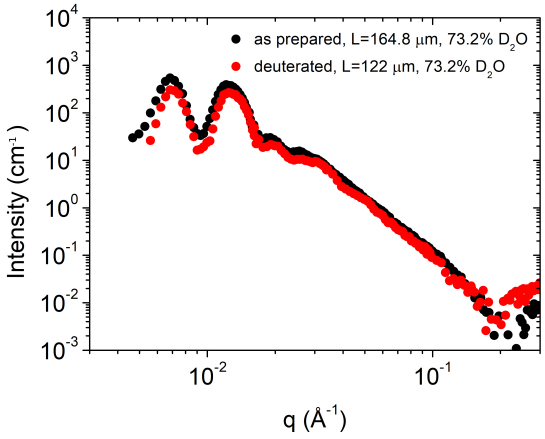

Figure 2.17: Scattering spectra for samples prepared under 40V 0.3M oxalic acid T=18 ℃ in H_2O and D_2O.

Two samples prepared in oxalic acid 0.3 M under the same anodization conditions but one prepared in H_2O solvent and the other in D_2O were measured by SANS. The SEM characterization of both samples is given in Table 2.10. The major structural difference between the two samples is the pore diameter and the interpore distance (see Figure 2.18. The small difference in the interpore distance is expected to shift slightly the position of the peaks in the *S(q)*. The fit will provide more information on the pore diameter as probed from the bulk of the membrane.

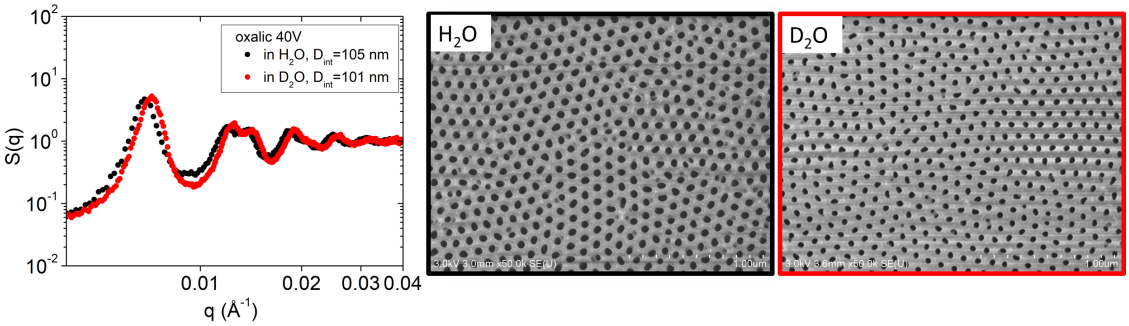

Figure 2.18: Structure factor S(q) and corresponding SEM nPAAMs of samples prepared under 40V 0.3M oxalic acid T=18 ℃ in H_2O(black) and D_2O (red).

In Figure 2.17 the SANS spectrum of a nPAAM prepared in D_2O is compared to the

nPAAM preparedin H_2O under the same anodization conditions. The two samples were measured at the same volume fraction ϕ_{D_2O}=73.2 %. It is observed that the two spectra have the same shape except for a small shift of the peaks to higher wavenumbers which is more evident for the 1^{st} peak and can be explained by the shift in the $S(q)$ as seen in Figure 2.18.

40V in 0.3M oxalic acid with solvent:	OA H_2O	OA D_2O
ϕ_{D_2O}	0.732	0.732
Fitting paramaters		
Porosity	0.29	0.29
D_{int} (nm)	105	103
σ_{int} (nm)	0.07	0.07
$\rho_{core} * 10^{-6}$ ($\mathring{A}^{-2}$)	4.48	4.48
$\rho_{shell} * 10^{-6}$ ($\mathring{A}^{-2}$)	4.493	4.493
$\rho_{Al_2O_3} * 10^{-6}$ ($\mathring{A}^{-2}$)	4.486	4.486
R_p (nm)	21.4	21.4
t (nm)	7.2	7.2
σ_p ($\mathring{A}$)	2.1	2.1
σ_t ($\mathring{A}$)	1.4	1.4

Table 2.11: SANS scattering spectra for nPAAMs with fit for samples prepared under 40 V 0.3 M oxalic acid T=18 in H_2O and D_2O.

Figure 2.19 shows the fits of the SANS curves and Table 2.11 presents the results. Note that the average pore diameter are the same, suggesting that the enlargement due to the acidity of the solvent proceeds only at the top surface of the membrane and is larger in H_2O than in D_2O, revealing different reaction kinetics. (see also next section).

As the shape of the SANS spectrum doesn't change, it can be concluded that the contribution from deuterium is not detected by SANS. Nevertheless, TGA results of the nPAAM prepared in D_2O shows a larger weight loss relative to nPAAMs prepared in H_2O (Figure 2.20).

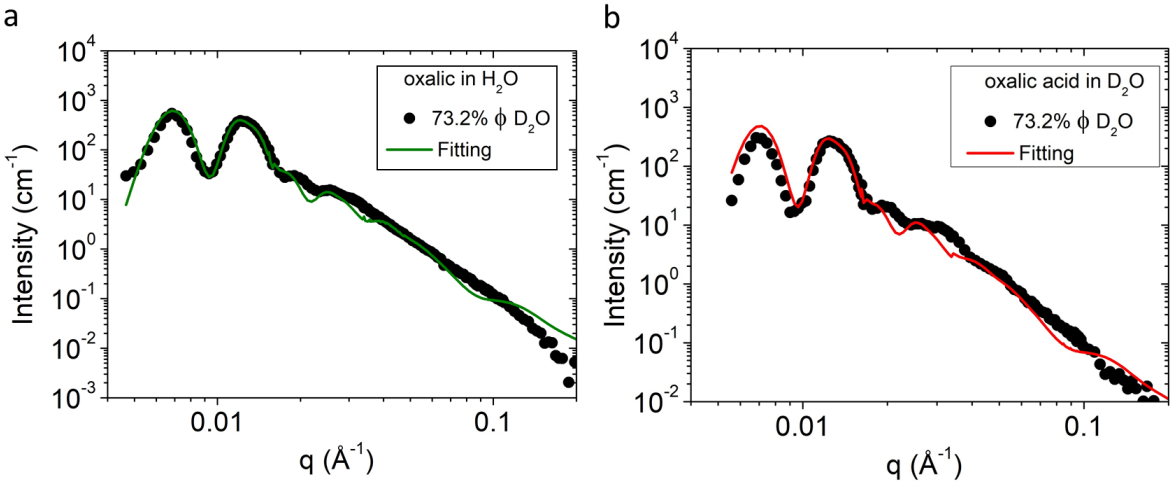

Figure 2.19: Fitting results for nPAAMs prepared under 40 V in 0.3 M oxalic acid in H_2O and oxalic acid in D_2O T=18 ℃.

2.3.1.6 Effect of water solvent

In the previous section oN studying nPAAms prepared in D_2O, it was shown that any contamination of the membrane wall with hydrogen during the synthesis is negligible and cannot be the reason of the formed shell that the neutrons probe. A possible origin that was had to be verified is the contamination due to the water mixture that was used for the SANS measurements. It is known that alumina is not stable in water solutions and forms hydrated alumina [112]. Moreover a common process that is used in the industry in order to reduce the porosity of the aluminum oxide and improve its corrosion resistance is hydrothermal sealing. This process involves the immersion of porous alumina films in boiling water and transforms the porous oxide into $\gamma - AlO(OH)$ known as boehmite. Therefore, when measuring the sample in SANS, inside a water mixture, a transformation process might take place but with longer kinetics due to lower working temperatures.

The stability of the nPAAMs was studied with SANS and SEM for different immersion times in water. The evolution of the SANS spectrum is presented for the sample "OA H_2O" immersed inside a H_2O/D_2O mixture with 73.2% D_2O for different numbers of days. It can be seen in the SANS spectra (Figure 2.23a) that the first peak shape starts to change slightly after 4 days of immersion. In the following 8 and 18 days, the intensity increases while at high q the incoherent scattering increases as a function of the immersion time (Figure 2.23b)). It is mentioned that for the background subtraction, the value of the freshly measured sample was used (i.e 0 days).

The above changes denote a change in the composition of the membrane. The sample

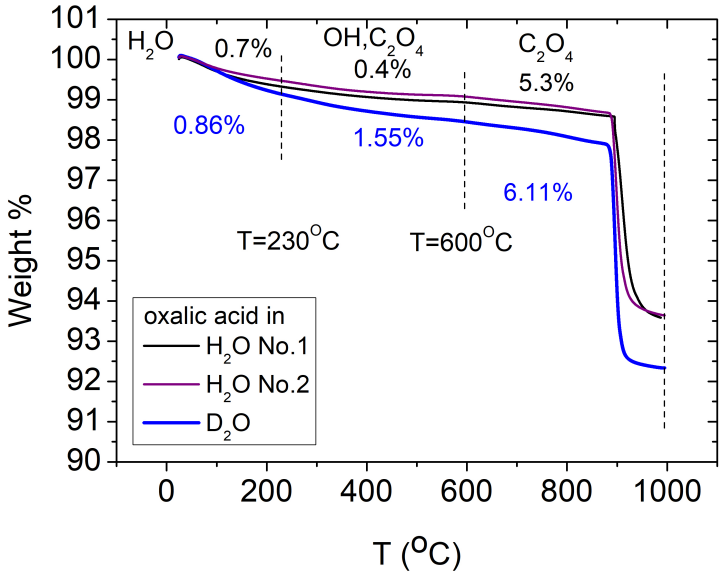

Figure 2.20: TGA diagrams of nPAAM prepared in 0.3M oxalic acid 40 under 40 V and T=18 ℃ for t=8h, in H_2O (black and purple) and in D_2O (blue).

had not loose its pore structure even after 18 days (Figure 2.24) but a fibrous thin mesh covers the top surface. Fitting of the spectra was tried but it was not probable to reproduce the data, due to possible multiple scattering effect.

For the previous samples all the SANS measurements were performedin solvent with 73.2% D_2O, the solvent consists mostly of D_2O. The isotopic effect was tested for two pieces of a nPAAM prepared in oxalic acid 0.3M under 40 V and one immersed one in H_2O and the other in D_2O. After 1 month they were measured by SANS in 73.2 % volume fraction of D_2O.

In Figure 2.21 the SANS spectra are presented and compared to the initial spectrum (black cirles). The scattering intensities for both samples had increased indicating that the samples had been modified. Between the two samples the difference in the scattering spectrum is more pronounced for the one immersed in H_2O. In the high q region the incoherent scattering of the sample immersed in H_2O is larger than the one in D_2O, indicating the larger amount of H incorporated.

Indeed, from the SEM image in Figure 2.22a it is observed that the pore structure has been transformed to a non porous layer that covers the surface of the nPAAM. According to the section of the SEM image (Figure 2.22b this non porous layer proceeds up to a certain thickness in the membrane equals to 1.95 μm). On the contrary, for the sample left in D_2O, the pore structure is still visible as seen in Figure 2.22c,d with a minor effect of

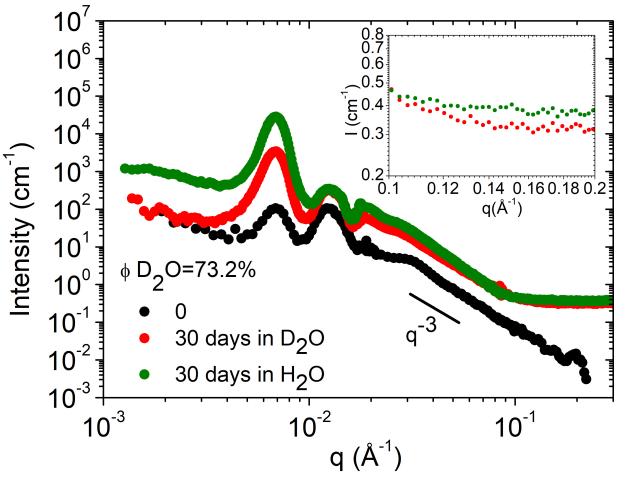

Figure 2.21: a) Scattering spectra for samples prepared under 40V 0.3M oxalic acid T=18 *celsius* and left for 30 days inside H_2O (green) and D_2O (red). Inset graph: Incoherent scattering at q=0.14 Å^{-1}.

transformation with the appearance of a few and small crystallites on the top surface. This difference between the immersion in D_2O and H_2O can be explained by the slower reaction kinetics in D_2O.

Kinetics of the transformation can be followed by observing the evolution of the scattering intensity at high q. At high q, neutrons are scattered incoherently and the scattering intensity attains a constant value. The plateau value depends on the incoherent scatterers, in our case the amount of hydrogen (σ_{inc_H}=80.27 barn vs σ_{inc_D}=2.05 barn). As it is observed in Figure 2.25, the background of a membrane measured in air is very low due to the small amount of hydrogen that the sample contains.

As a consequence, when the membrane is measured in mixture of H_2O and D_2O the intensity at high wavevectors is proportional to the fraction of H_2O. It can be claimed that the scattering incoherent background of the samples depends only on the solvent. The prolonged immersion of the sample in water hydrates alumina and as a result the incoherent scattering of the sample increases with time as shown in Figure 2.26.

sample	Spectrometer	R_p (nm)	σ_r (nm)	D_{int} (nm)	σ_{int}	δ(Å^{-1})	grain size (nm)	n*10^{10} (cm^{-2})	L (μm)
OA4-H_2O	PAXY (LLB)	28	4	101	0.07	0.0008	785	1.1	164.8

Table 2.12: SEM structural parameters of membrane prepared in 0.3 M oxalic acid under 40 V, T=18 ℃, anodized for 11 hours and 30min.

In order to avoid the reaction of alumina with water, piece of the same membrane prepared

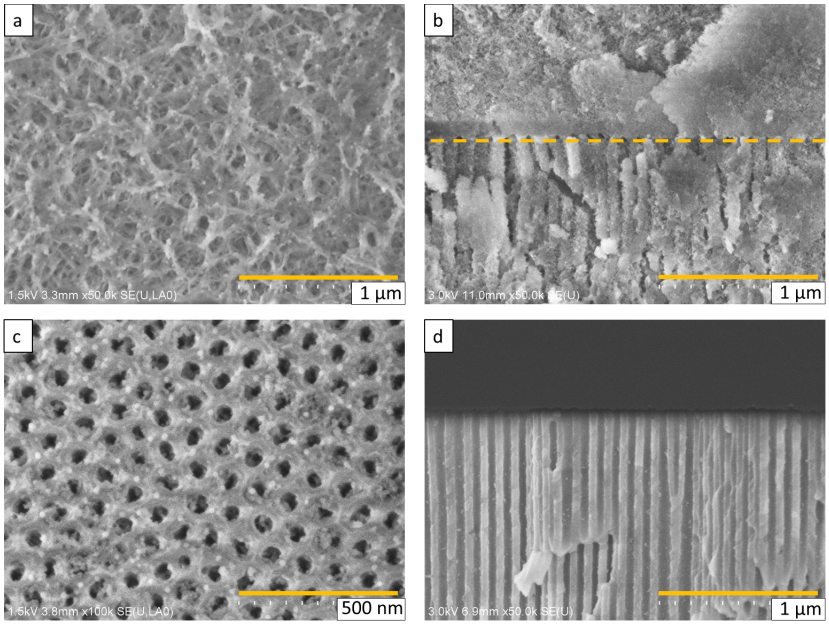

Figure 2.22: SEM image of sample prepared under 40V in 0.3M oxalic acid, T=18 , immersed for 30 days inside H_2O a) top view , b) section (yellow dashed line marks the interface between the transformed part and the nPAAM) , inside D_2O: c) top view, d) section.

in oxalic acid 40 V was also measured using Dimethyl Sulfoxide (DMSO) as a solvent. The choice of DMSO was made as it is also a polar solvent and enables for proper wetting of the hydrophilic alumina surface. The sample was prepared under the same conditions as the sample "OA H_2O" and the SEM characterization and measured in different volume fractions of d-DMSO/DMSO. The structural parameters of this nPAAM (named OA4-H2O) determined by SEM are listed in Table 2.12

Caution was taken in the preparation of the mixtures of DMSO/d-DMSO in order to avoid contact with water, as DMSO is highly hygroscopic, the solutions were prepared under nitrogen atmosphere.

Contrast variation was performed on the sample and in Figure 2.27 the SANS spectra are presented for two different volume fractions of d-DMSO. Both of the curves exhibit the same characteristics as observed in the samples measured in D_2O solvents, such as the peaks at the expected positions and the slope of -3. The first spectrum corresponds to an equivalent volume fraction of ϕ_{D_2O}=73.8 % and it can be seen that the peaks intensity is totally different than the one obtained in D_2O. This cannot be explained by a different pore structure as seen from the values given by the SEM characterisation (Table 2.12).

Unlike the sample measured in D_2O the lowest intensity was obtained for an equivalent volume fraction of ϕ_{D_2O}=76.1%. From the contrast variation plots in Figure 2.28 it is ob-

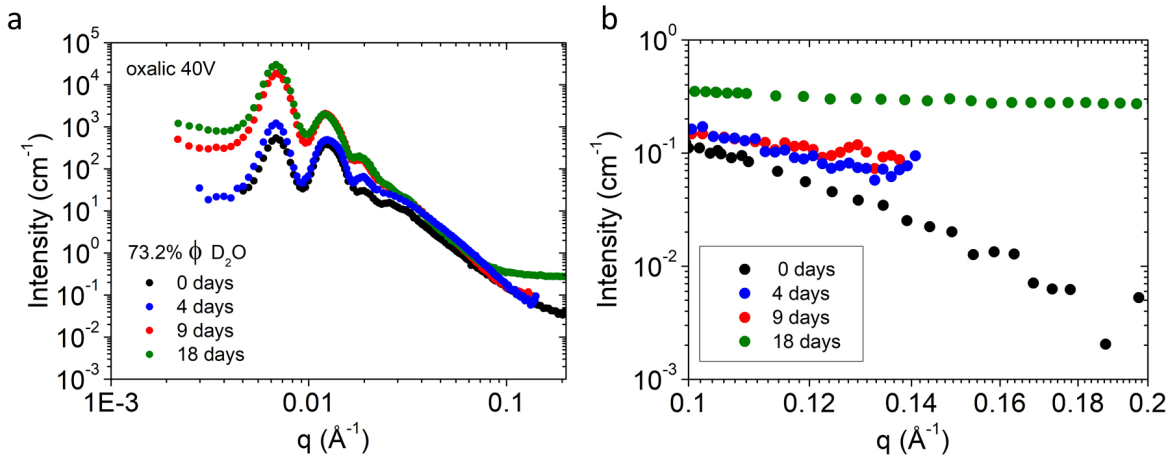

Figure 2.23: a) Evolution of scattering spectrum of a sample prepared in 0.3M oxalic acid under 40 V and T=18 ℃ , immersed for different periods of time in 73.2% D_2O and measured at the same solvent. (b) Detail of the scattering of the spectra in the high q region

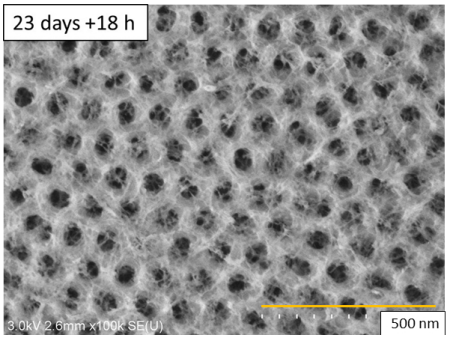

Figure 2.24: SEM image of a membrane prepared in oxalic acid 0.3 M under 40V, immersed inside 73.2% ϕ_{D_2O} for 23 days and 18h.

served that the point of lowest intensity is shifted to higher scattering length densities for all the wavevectors compared to the sample measured in D_2O.

In Figure 2.29 the fit of the experimental data of the nPAAM measured in DMSO is presented. Contrary to nPAAM measured in water, the fitting model didn't include any shell. Although the shape of the peaks can be well reproduced, the intensity of the 1st peak is not well reproduced for the sample measured at equivalent ϕ_{d-DMSO} 76.1% and 79%.

The fitting parameters are presented in Table 2.13. It can be seen that even in DMSO, the scattering length density of the membrane $\rho_{Al_2O_3}$ has to be adjusted to the measuring d-DMSO mixture and the relative differences are presented in Table 2.14. This provides evidence that another scale of porosity exists in the membranes bulk material that allows for

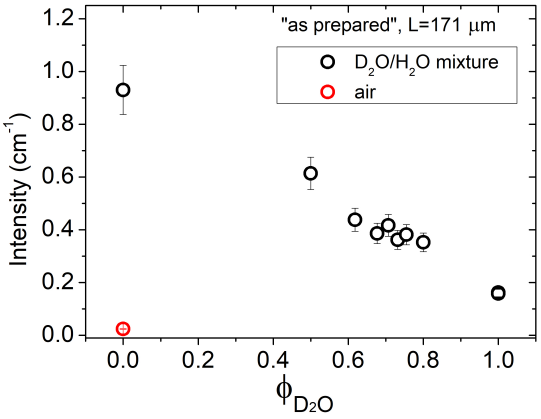

Figure 2.25: Incoherent scattering intensity at high q ($q \approx 0.1$ Å^{-1})) before subtraction as a function of the measuring solvent fraction of D_2O for membrane prepared in 0.3M oxalic acid under 40V, T=18 ℃ for 11 hours and 50 min (171 µm) .

ϕ_{d-DMSO}	85.9%	88.9%	92.6 %	95.5%
equiv ϕ_{D_2O}	73.8	76.1	79	81.3
Fitting paramaters				
Porosity	0.3	0.3	0.3	0.3
D_{int} (nm)	101	101	101	101
σ_{int}	0.04	0.04	0.04	0.04
$\rho_{core} * 10^{-6}$ (Å)$^{-2}$)	4.52	4.68	4.89	5.04
$\rho_{Al_2O_3} * 10^{-6}$ (Å)	4.542	4.66	4.866	5.07
R_p (nm)	28	28	28	28
σ_p (nm)	4.2	4.2	4.2	4.2

Table 2.13: Fitting parameters of sample "OA4-H2O", prepared in 0.3 M oxalic acid, under 40 V and T=18 ℃, measured in DMSO.

solvents to infiltrate. The fact that in DMSO no shell is needed to fit the data marks that there is no transformation of alumina.

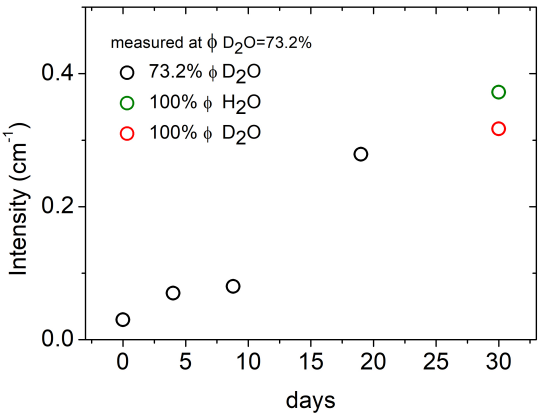

Figure 2.26: Scattering intensity at high q (q≈0.2 $Å^{-1}$) of sample prepared in oxalic 0.3 M under 40 V as a function of the immersion time in volume fraction ϕ_{D_2O}=73.2 % (black), and D_2O=100% (green), 100% H_2O (red) at q =0.14 $Å^{-1}$.

ϕ_{d-DMSO}	85.9%	88.9%	92.6 %	95.5%
equivalent ϕ_{D_2O}	73.8%	76.6%	79 %	81.3%
(ρ_{core}-$\rho_{Al_2O_3}$)	0.022	0.02	0.024	0.03

Table 2.14: Scattering length density differences for the sample "OA4-H2O" measured in DMSO solutions.

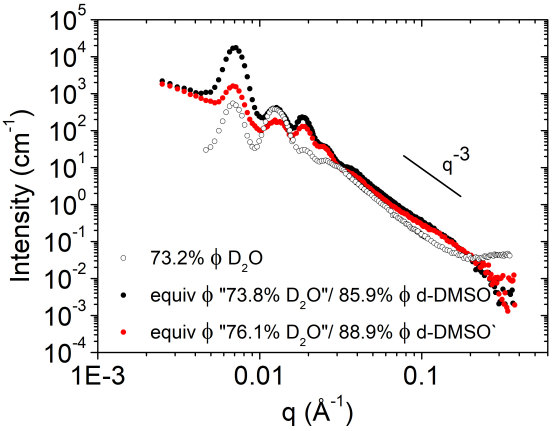

Figure 2.27: a)SANS spectra of sample "OA4-H2O" measured at 85.9 % (equivalent 73.8% ϕ_{D_2O} (black) and 88.9 %(red) volume fraction of d-DMSO (equivalent 76.1% ϕ_{D_2O}). The nPAAM OA measured at 73.2% ϕ_{D2O} is given for comparison.

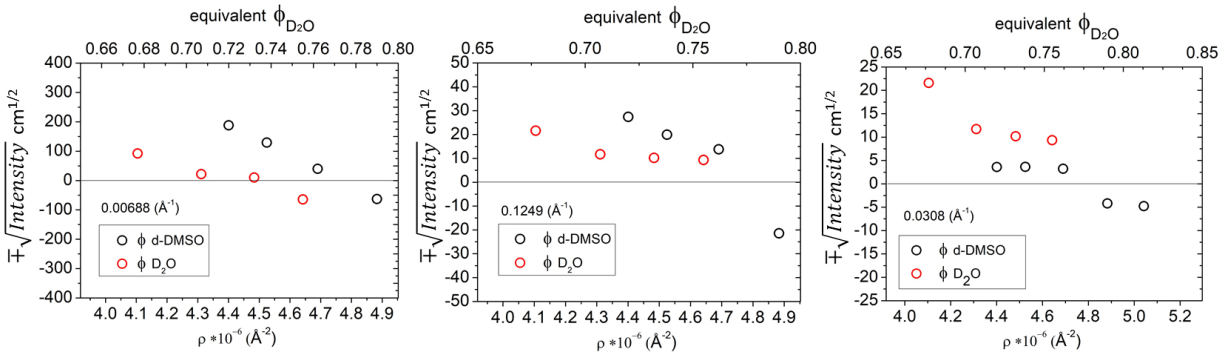

Figure 2.28: Contrast variation of sample "OA4-H2O" measured in different volume fractions of d-DMSO compared to contrast variation of sample "OA1" measured in D_2O.

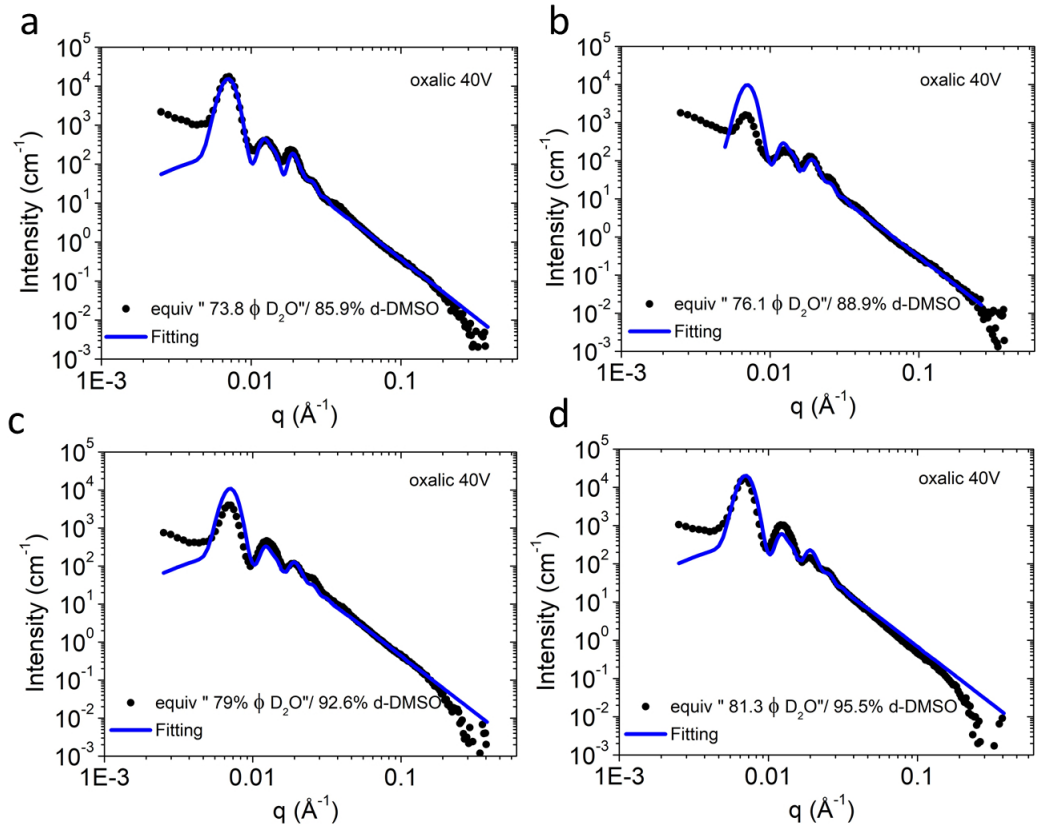

Figure 2.29: Fitting of SANS spectra of sample "OA4-H2O", prepared in 0.3 M oxalic acid, under 40 V and T= 8 ℃ (L=168.4 µm) a) ϕ_{d-DMSO}= % (equivalent volume fraction of ϕ_{D_2O}=73.8%). b)ϕ_{d-DMSO}=88.9% (equivalent ϕ_{D_2O}=76.1%). c) ϕ_{d-DMSO}=92.6% (equivalent ϕ_{D_2O}=79%) d) ϕ_{d-DMSO}=95.5% (equivalent ϕ_{D_2O}=81.3%).

2.3.1.7 Annealed nPAAMs

One approach for removing the contaminants of the nPAAms is thermal annealing them. It is known that during thermal treatment at high temperatures (above T>600 ℃) the membrane's skeleton transforms from an amorphous oxide to a polycrystalline one in the order amorphous $\rightarrow \gamma \rightarrow \delta \rightarrow \theta \rightarrow \alpha - Al_2O_3$ as depicted in the diagramm of Figure 2.30(taken from [110]). In the same study it was found that due to the high temperature the incorporated species are decomposed but they are not released immediately as they are trapped inside the oxide lattice. Their evaporation is enabled during the phase transition of the oxide after 800 ℃.

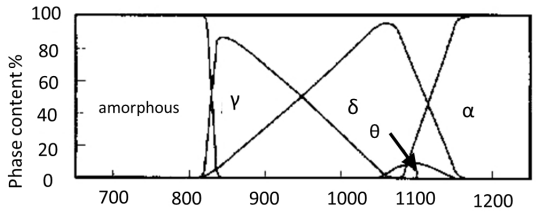

Figure 2.30: Phase transition diagramm of alumina prepared in oxalic acid during thermal annealing. Reprinted from [110].

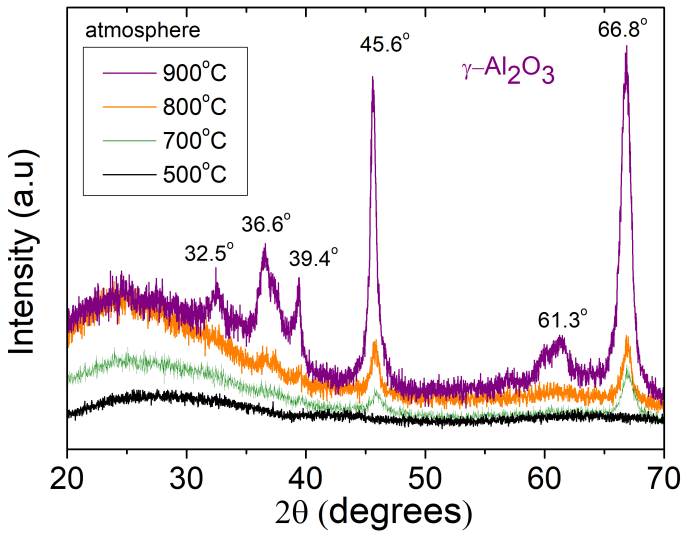

Figure 2.31: XRD spectrum of nPAAMs prepared in oxalic acid 40V after annealing at different temperatures (between 500-900 ℃) under air atmosphere. (The spectra have been shifted for clarity).

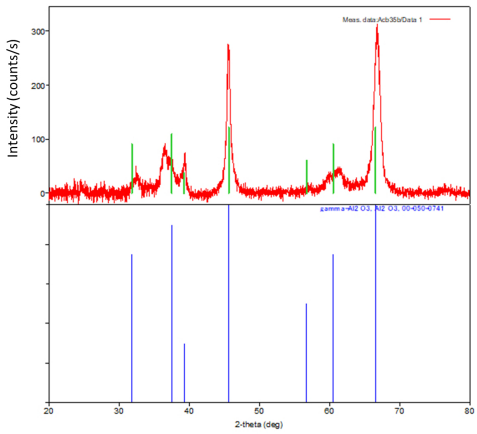

Figure 2.32: XRD peaks identification of the nPAAM annealed at 900 ℃.

sample name	Spectrometer	R_p (nm)	σ_r (nm)	D_{int} (nm)	σ_{int}	$\delta(\text{Å}^{-1})$	grain size (nm)	n*10^{10} (cm^{-2})	L (µm)
AN1	PAXY (LLB)	30	2	103	0.05	0.001	628	1	55.8
AN2	PAXY (LLB)	28.9	2	106	0.05	0.001	628	1	30

Table 2.15: SEM characterization of nPAAMs synthesized in 0.3 M oxalic acid under 40 V and T=18 ℃. AN1: etched in H_3PO_4 5wt% for 20min at 30 ℃and annealed at 900 ℃. AN2: etched in H_3PO_4 5wt% for 50min at 30 ℃ annealed at 500 ℃.

Moreover the amount of carbon reached 2.5 % and was attributed to incorporation of oxalate anions during the anodization in the oxalic acid electrolyte. The carbon was lost during the thermal annealing in two stages. The first one took place in a very narrow range of temperature between 830-840 ℃ and half of the carbon was lost. This temperature coincided with the transition temperature in the final stage of transformation from amorphous to $\gamma - Al_2O_3$. The remaining carbon was measured by FTIR and found to be in the form of CO_2 embedded in the alumina matrix. This remaining carbon was released during the second loss stage which occurred at higher temperatures (1075-1150 ℃) at the onset of the crystallization to $\alpha - Al_2O_3$. It was concluded that the anion decomposition and release process is bound to the oxygen sub lattice transformation. Other experimental studies confirmed the thermal decomposition of oxalates by means of PL (Photoluminescence) and the connection of the anion incorporation loss with the phase transitions by IR spectroscopy [132, 135].

Samples preparation: Membranes prepared in 0.3M oxalic acid under 40V and T=18 ℃ were deprived of their aluminum substrate via chemical etching in $CuCl_2$+HCl solution. Then, they were annealed between 500 ℃ and 900 ℃ for 8 hours inside a furnace under air at a rate of 2 ℃/min.

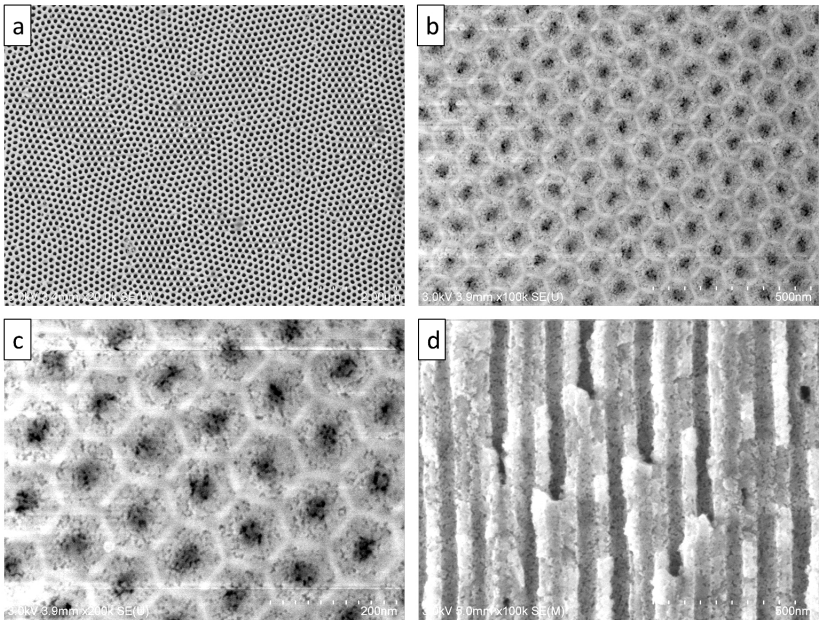

Figure 2.33: a) SEM images of sample AN1 (etched and annealed at 900 ℃). a) top surface view. b) bottom view of the barrier layer (. c) bottom view of the barrier layer. d) cross section.

In Figure 2.31 the XRD diffractogram of oxalic nPAAMs annealed at different temperatures is presented. It can be seen that the appearance of peaks starts at 700 ℃ with the first peaks formed at angle θ=45.6 ˚and 66.8 ˚that correspond to $\gamma_{Al_2O_3}$. As the temperature rises up to 900 ℃ more peaks emerge. The identification of the XRD peaks corresponding to 900 ℃ is given in Figure 2.32 and as it can be seen the peaks correspond to $\gamma - Al_2O_3$. A small shift of the peaks to higher angles is attributed to misalignment in the height level of the sample during measurement.

Although annealing brings changes in composition, the pore structure is kept almost intact and only an increase in the pore diameter was observed due to the crystallization and shrinkage of the pore wall (as observed with SEM Chapter 1). For this reason the samples are appropriate to measure in SANS to probe the change in composition and investigate matching possibilities as the material tends to be purified. Samples prepared in 0.3 M oxalic acid under 40 V were deprived from their aluminum substrate and were chemically etched in H_3PO_4 5wt.% at 30 ℃ for 20 minutes by floating the membranes on top of the solution, in order to remove the barrier layer and to prevent curling during the thermal annealing over 500 ℃. Such defects are due to differences in the thermal expansion coefficients of the two layers (pure alumina-anion contaminated) of the cell wall. Moreover, geometrical constrains such as the existence of the barrier layer at the bottom of the membrane also contribute to this effect. The samples were annealed at 500 ℃ at a rate of 5 ℃/min for 2h and at 900 ℃

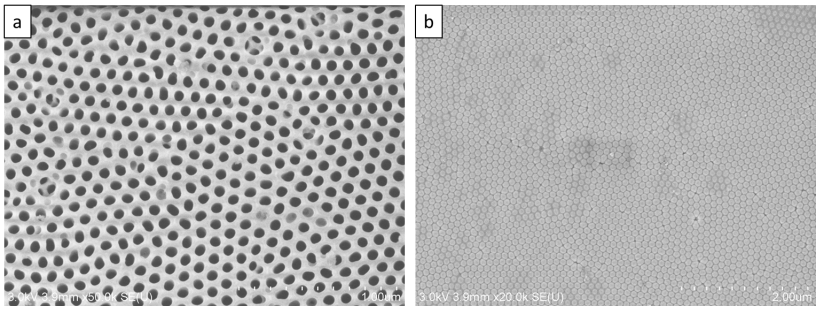

Figure 2.34: a) SEM images of sample AN2 (etched and annealed at 500 ℃). a) top surface view b) bottom view of barrier layer.

at a rate of 1 ℃/min durig 8h under air inside a furnace. The SEM characterization of the two samples is given in Table 2.15.

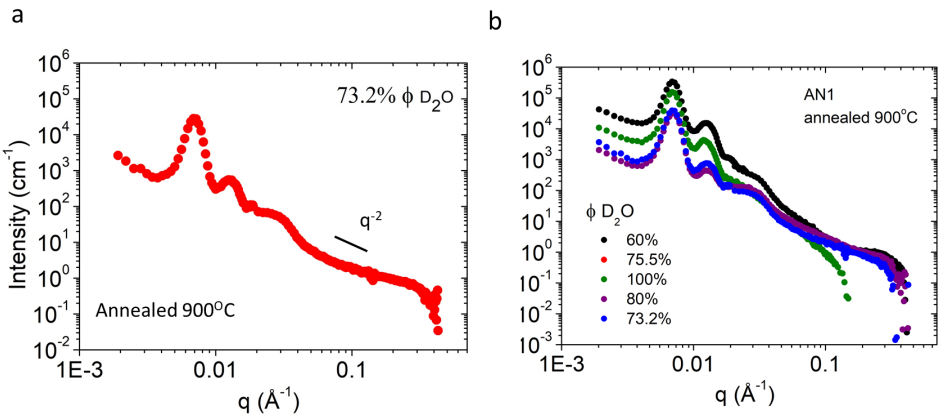

Figure 2.35: a) SANS spectrum of sample AN1 measured at 73.2% D_2O b) SANS spectra of sample AN1 measured at different mixtures of H_2O/D_2O.

From the SEM cross section of the sample AN1 (Figure 2.33d) it can be seen that the nPAAM presents holes in its wall, with a size approximately 5nm. These defects are also evident on the side of the barrier layer (Figure 2.33)b,c but not on the top side (Figure 2.33a). Moreover, the outer part of the nPAAM wall which consists of more pure alumina is not affected. Thus, the defects might arise during the removal of the electrolyte contaminants in the anion incorporated layer. This is something expected at this temperature of 900 ℃ crystallization takes place. On the contrary, nPAAM AN2 doesn't present these defects as the annealing temperature is lower than the crystallization one (Figure 2.34).

In Figure 2.35a the SANS spectrum is presented for sample AN1 annealed at 900 ℃ measured at 73.2% ϕ_{D_2O}. It can be seen, that the shape of the curve is really different

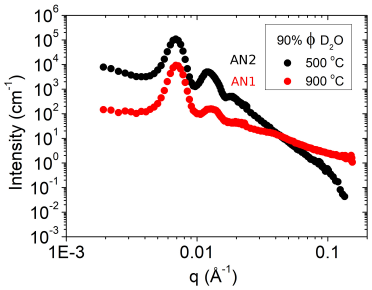

Figure 2.36: a) SANS spectrum of sample AN1 and AN2 measured at 90% D_2O .

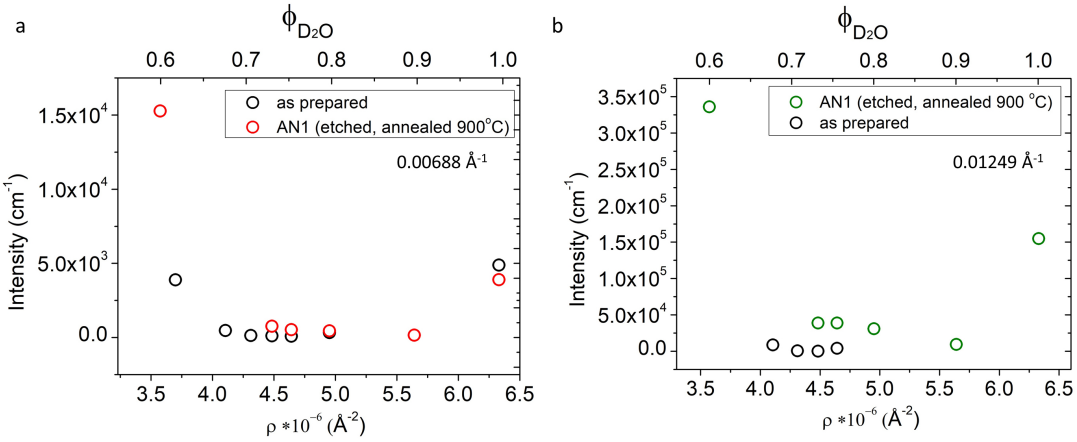

Figure 2.37: a) Contrast variation of sample AN1.

than the one measured as prepared, indicating a change in the composition of the nPAAM. Moreover, in the middle q region, the intensity scales to q^{-2} which also marks a change at the interface, probably arising from the holes along on the wall and present in all of the SANS spectra measured at different mixtures of D_2O(Figure 2.35).

In Figure 2.36, the SANS spectra of the two annealed samples AN1 and AN2 measured at the same mixture 90% D_2O are presented. It is observed that the sample AN2 presents the q^{-3} behaviour in the middle q region. In addition, the different shape of the plots marks that the two samples differ in composition, something expected as crystallization appears after 700 ℃.

Indeed, contrast variation plot of sample AN1 in Figure 2.37a is shifted relative to the as prepared one, towards higher scattering length densities, indicating a change in composition. Due to crystallization an increase in the density of the material takes place, during the transformation from amorphous (2.945→ g cm^{-3}) to $\gamma_{Al_2O_3}$(≈ 3.7 g cm^{-3}) that corresponds to a scattering length density $\rho_{\gamma_{Al_2O_3}}$=5.31 ∗ 10^{-6} $Å^{-2}$.

2.3.2 nPAAMs prepared in sulfuric acid

In the following paragraphs SANS measurements of nPAAM prepeared in 0.3 M sulfuric acid under 20 V and T=10 ℃ will be presented. The effect of etching and synthesis in D_2O will also be examined.

2.3.2.1 As prepared versus etched nPAAMs

sample name	Spectrometer	R_p (nm)	σ_r (nm)	D_{int} (nm)	σ_{int}	$\delta(\text{Å}^{-1})$	grain size (nm)	n*10^{10} (cm^{-2})	L (μm)
SA1	D11 (ILL)	10	4	55.3	0.1	0.002	314	4.2	44.6
SA1-E	D11 (ILL)	16	2	55.5	0.1	0.002	314	4.2	44.6

Table 2.16: SEM characterization of nPAAMs synthesized in 0.3M sulfuric acid, under 20V and T=10 ℃, as prepared (SA1) and etched (SA2). The etching was performed in 5 wt.% of H_3PO_4 for 22 min at T=30 ℃.

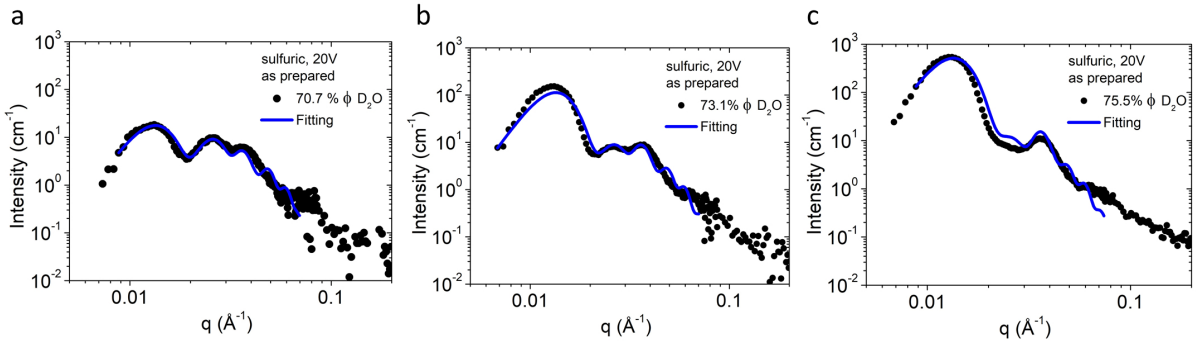

Figure 2.38: SANS spectra for as prepared nPAAMs in 0.3 M sulfuric acid under 20 V and T=10 ℃ at three different D_2O volume fraction: 70.7%(a), 73.1%(b) and 75.5 (c). The blue lines correspond to the best fits.

In Table 2.16 the SEM characterization is presented for two samples coming from the same synthesis conditions (0.3M sulfuric acid, 20V, T=10 ℃ t=8h). One piece was kept as prepared and the second was etched for 22 min in 5 wt.% of H_3PO_4 at T=30 ℃. The derivation of the interpore distance D_{int} was done by fitting an hexagonal structure factor to the SEM data and not the hard sphere model.

In Figure 2.38 the SANS spectra with the best fitting are shown for the as prepared sample "SA1" and it can be seen that the lowest intensity is achieved for ϕ_{D_2O} of 70.7 %. In Table 2.17 it is observed once again as in the oxalic acid nPAAMs that the shell and the alumina scattering length densities ρ_{shell}, $\rho_{AL_2O_3}$ have to be adjusted to the scattering length density ρ_{core} of the filling solvent.

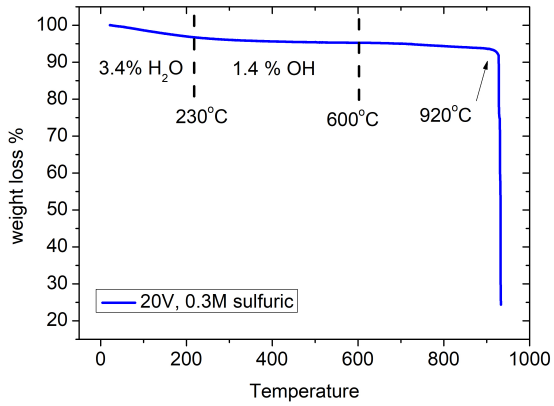

Figure 2.39: TGA diagram of a nPAAM prepared in sulfuric acid under 20 V and T=10 ℃.

ϕ_{D_2O} (%)	70.7	73.1	75.5
Fitting paramaters			
Porosity (%)	34		
D_{int} (nm)	53.4		
σ_{int} (nm)	0.1		
$\delta(\mathring{A}^{-1})$	0.001		
$\rho_{core} * 10^{-6}$ $(\mathring{A}^{-2})$	4.31	4.48	4.64
$\rho_{shell} * 10^{-6}$ $(\mathring{A}^{-2})$	4.323	4.49	4.64
$\rho_{Al_2O_3} * 10^{-6}$ $(\mathring{A}^{-2})$	4.31	4.47	4.61
R_p (nm)	10		
σ_p (nm)	1.5		
t (nm)	5.6		

Table 2.17: Fitting results of nPAAM "SA1" synthesized in 0.3 M sulfuric acid under 20 V, T=10 ℃ .

By using the values given by the fit in Table 2.17 the ratio of the shell radius t to the alumina cell wall w (i.e 2w=$D_{int} - D_p$) can be calculated and is found to be 0.33 which is larger than 0.23 for the membrane prepared in oxalic acid. In the literature the anion incorporated layer of nPAAms prepared in sulfuric acid contains the sulfate anion SO_4^{-2} and it is thought that it migrates under field inside the alumina wall. Due to its smaller ionic radius, the incorporation depth is larger than in the case of oxalate, thus creating a wider shell [20]. Moreover, the nPAAMs in sulfuric acid contain larger amounts of water. In Figure 2.39 the TGA curve is presented for a sample prepared in 0.3M sulfuric acid under 20V and T=10 ℃ . Indeed, the amount of water and the weight loss in the region between 230 ℃ and 600 ℃ is larger. In the middle range of temperature 230-600 ℃ the exact ratio of OH and possibly S that is lost is unknown. The weight loss attributed to the evaporation of SO_2

is recorded near 920 ℃. The abrupt and huge drop of the loss at 920 ℃ is attributed to membrane pieces that fell off the balance during the evaporation.

$\phi_{D_2O}(\%)$	70.7	73.1	75.5
$(\rho_{\phi_{D_2O}}\text{-}\rho_{shell})$	0.013	0.01	0
$(\rho_{D_2O}\text{-}\rho_{Al_2O_3})$	0	0.02	0.03
$(\rho_{shell}\text{-}\rho_{Al_2O_3})$	0.013	0.02	0.03

Table 2.18: Scattering length density differences for as prepared sample in 0.3M sulfuric acid under 20V, T=10 ℃.

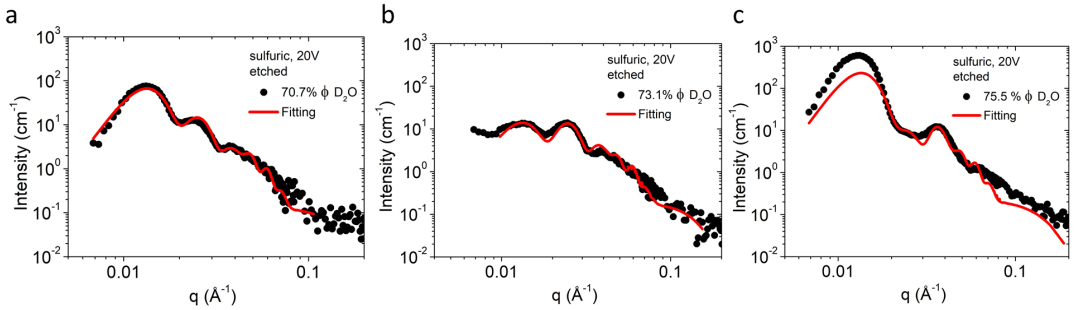

Figure 2.40: SANS spectra (ILL-"D11") for etched nPAAMs at three different D_2O volume fractions: 70.7%, 73.1% and 75.5%. The red continuous lines correspond to the best fit.

In Figure 2.40 the SANS spectra of the etched sample "SA1-E" are presented. It can be seen that the lowest intensity is shifted to ϕ_{D_2O} of 73.1% indicating that the composition of the nPAAMs has changed after the etching process. Etching the as prepared sample and enlarging the pore diameter from 10 to 16 is expected to remove the shell layer. Nevertheless, the etched sample still has to be fitted with a shell of a smaller extent (3nm) and the scattering length densities are also adjusted to the filling solvent.

$\phi_{D_2O}(\%)$	70.7	73.1	75.5
Fitting paramaters			
Porosity (%)	51		
D_{int} (nm)	53.4		
σ_{int}	0.1		
δ	0.001		
$\rho_{core} * 10^{-6}$ (Å^{-2})	4.31	4.48	4.64
$\rho_{shell} * 10^{-6}$ (Å^{-2})	4.32	4.496	4.60
$\rho_{solv} * 10^{-6}$ (Å^{-2})	4.3	4.476	4.61
R_p (nm)	16		
σ_p (nm)	1.6		
t (nm)	3		

Table 2.19: Fitting results of sample "SA1-E" synthesized in 0.3 M sulfuric acid under 20 V, T=10 ℃, etched for 22min in 5 wt.% H_3PO_4 at 30 ℃.

$\phi_{D_2O}(\%)$	70.7	73.1	75.5
(ρ_{core}-ρ_{shell})	0.01	0.016	0.03
(ρ_{core}-$\rho_{Al_2O_3}$)	0.01	0.02	0.02
(ρ_{shell}-$\rho_{Al_2O_3}$)	0.02	0.02	0.01

Table 2.20: Scattering length density differences for etched sample "SA1"-E in 0.3 M sulfuric acid under 20 V, T=10 ℃.

2.3.2.2 Membranes prepared in D_2SO_4-D_2O

The effect of synthesis in D_2O on the composition was studied with SANS by comparing samples that were prepared under 20 V at 10 ℃ in a) 0.3 M H_2SO_4 in H_2O and b) 0.3M D_2SO_4 in D_2O. The SEM characterization is given in Table 2.21.

sample	Spectrometer	R_p (nm)	σ_r (nm)	D_{int} (nm)	σ_{int}	δ(Å^{-1})	grain size (nm)	n*10^{10} (cm^{-2})	L (µm)	t (h)
SA1	D11 (ILL)	10	4	55.3	0.1	0.002	314	4.2	44.6	8
d-SA1	D11 (ILL)	16	2	53.4	0.08	0.0022	285.6	4.1	18.8	2h30m
SA2	PAXY (LLB)	11	2	54.4	0.1	0.002	314	4.2	52	8
d-SA2	PAXY (LLB)	8	2	52.6	0.08	0.0014	448	4.4	72.2	8

Table 2.21: SEM characterization of nPAAMs synthesized in 0.3 M sulfuric acid, under 20 V and T=10 ℃.

It should be noted that the first step anodization of the sample "d-SA1" took place in H_2SO_4 for 2 hours, thus it can explain the smaller grain size measured with SEM compared to the second deuterated sample "d-SA2". The SANS spectra of the samples are presented in Figure 2.41 measured at two different volume fractions ϕ_{D_2O} 73.1% and 75.5%.

In both cases the spectrum of the samples prepared in D_2SO_4/D_2O is different than

sample	Porosity (%)	Dint (nm)	sigma int	G (nm)	hk	cL	L (micron)	R (nm)	sigma (nm)	t (nm)
SA1	34	53.4	0.1	628	3	7	44.6	10	1.5	5.6
SA2	32	53.4	0.05	314	3	7	52	10	2	5.6
d-SA1	32	53.1	0.1	628	3	7	18.8	6.5	1	8.6
d-SA2	32	52.7	0.05	628	3	7	72.2	9.8	1.5	6.3

Table 2.22: Structural parameters of nPAAMs prepared in 0.3 M sulfuric in H_2O and d-sulfuric acid in D_2O under 20 V and T=10 ℃ .

sample	ρ_{D_2O}	ρ_{shell}	$\rho_{Al_2O_3}$
SA1	4.48	4.49	4.47
d-SA1		4.48	4.53
SA2	4.64	4.64	4.615
d-SA2		4.63	4.59

Table 2.23: Scattering length density values for npAAMs prepared in 0.3 M sulfuric in H_2O and d-sulfuric acid in D_2O under 20 V and T=10 ℃ measured at 73.1% and 75.5 % ϕ_{D2O}.

from the one prepared in 0.3 M H_2SO_4/H_2O. The experimental data were fitted with the core-shell cylinder model and the fitted parameters are presented in two tables, one that contains structural information (2.22) and one that has the composition related parameters (2.23). From these values the average shell to alumina ratio can be calculated and found to be equal to 0.5 for the sample prepared in H_2SO_4/H_2O and 0.40 for the samples prepared in D_2SO_4/D_2O. In Table 2.23 the scattering length density differences are being presented between the solvent, the shell and the alumina wall compared for the deuterated and hydrogenated samples. It can be seen that the two samples differ in their $\Delta\rho$ with the deuterated sample having larger values which is consistent with the higher scattering length density ρ_{D2O} of deuterium. As we saw in the TGA graph, the samples prepared in sulfuric acid are more hydrophilic and contain much more hydroxyls. Thus, when the nPAAM is synthesized in deuterated medium the amount is large enough to create a difference in the shape of the SANS spectra.

sample	ρ_{D_2O}-ρ_{shell}	ρ_{shell}-$\rho_{Al_2O_3}$	ρ_{D_2O}-$\rho_{Al_2O_3}$
SA1	0.01	0.02	0.01
d-SA1	0.00	0.05	0.05
SA2	0	0.025	0.025
d-SA2	0.01	0.04	0.05

Table 2.24: Absolute scattering length density differences for npAAMs prepared in 0.3 M sulfuric in H_2O and d-sulfuric acid in D_2O under 20 V and T=10 ℃ measured at 73.1% and 75.5 % ϕ_{D2O}.

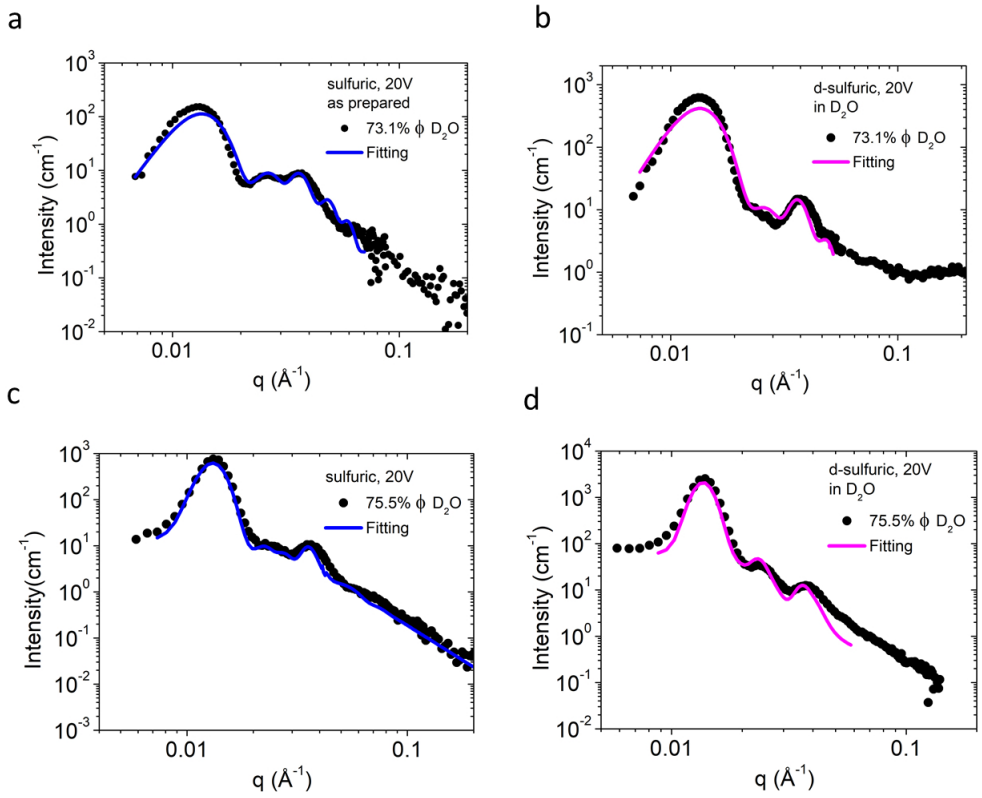

Figure 2.41: Fitted SANS spectra for nPAAMs prepared under 20 V and T=10 ℃ in a) 0.3 M sulfuric acid in D_2O (sample "SA1", measured at "D11"), b) 0.3 M d-sulfuric in D_2O ("SA1-d", "D11") c) "SA1", "PAXY" d) 0.3M d-sulfuric in D_2O ("d-SA2", PAXY) .

2.3.3 nPAAM prepared in selenic acid

nPAAMs prepared in selenic acid will be presented in the following section. The membranes were prepared in 0.3 M selenic acid under 45 V and T=0 ℃ and as seen from the SEM characterisation in Table 2.25 they have the same pore diameter as the nPAAMs prepared in sulfuric acid but their interpore distance is larger. Moreover, the nPAAMs have just recently being synthesized and recently some information has been obtained about their cell composition.

sample name	Spectrometer	R_p (nm)	σ_r (nm)	D_{int}	σ_{int}	$\delta(\text{Å}^{-1})$	grain size (nm)	n*10^{10} (cm^{-2})	L (μm)
SC1	"PAXY" (LLB)	9.7	3	106.9	0.1	0.0012	524	1.3	60

Table 2.25: SEM characterization of nPAAMs synthesized in 0.3 M selenic acid, under 45 V and T=0 ℃ .

In Figure 2.42 the SANS spectra for three different volume fractions of D_2O is presented.

The lowest intensity was observed for $\phi_{D_2O} = 73.2\%$, as in oxalic and sulfuric but also in this sample matching was not possible. By a first look in the curve at low q, apart from the 1st peak that corresponds to the structure factor S(q), a second peak is observed which means that a shell with a large extent must be present. If the shell was smaller, in the scale of the pore diameter, then this peak would have appeared in the middle q region.

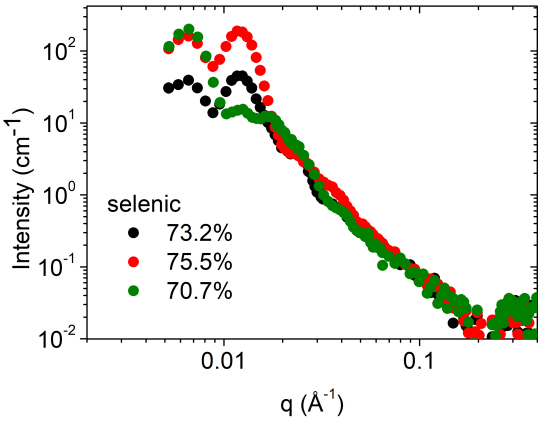

Figure 2.42: SANS spectra for as prepared sample in 0.3 M selenic acid under 45V and T=0 ℃ measured in different volume fractions of D_2O.

In order to have a better view on the contamination of the sample, TGA and IR measurements were performed. In Figure 2.43b the IR spectrum is shown for a sample prepared in 0.3M selenic acid under 45V and T=0 ℃, anodized for 23 hours (L=38 μm). The broad band between 2500-3500 belongs to physically adsorbed water and the absorption peak at 1640 cm^{-1} belongs to H_2O bending mode. A big drop in the transmission is observed near 1000 cm^{-1}, propably due to the characteristic vibrations of SeO_4 [136].

The TGA plot shown in 2.43a of the nPAAM prepared in selenic acid shows similiar behaviour as the oxalic. The first part until 230 ℃ is due to H_2O, then from 230 ℃ - 600 ℃ a small amount of OH is present and finally a huge drop of 11.1% is observed at 800 ℃. The water and OH loss is almost the same as in oxalic acid but the loss at 800 ℃ is higher for the nPAAM prepared in selenic acid.

In Figure 2.44 the scattering spectra for the nPAAMs measured in DMSO at the contrast as in D_2O shows a very different behaviour. The second peak in the low q region seems suppressed. The scattering intensity is higher than the one measured in water. Also, the minimal intensity is observed for 92.6% d-DMSO which is an equivalent contrast as 79.1 % D_2O.

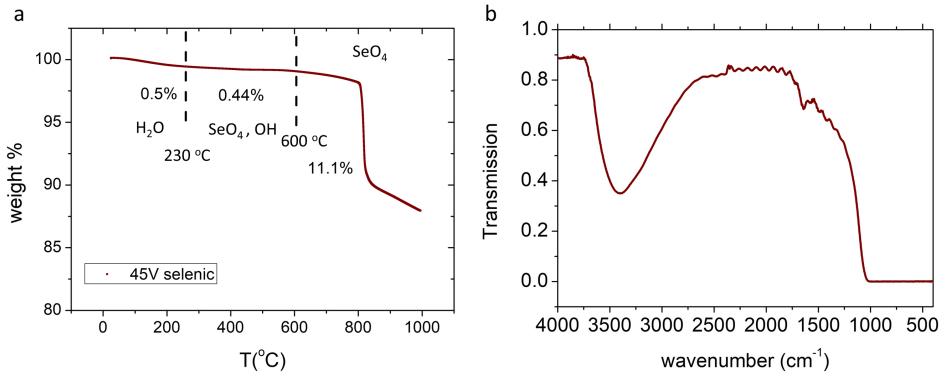

Figure 2.43: a)TGA curve of sample prepared in 0.3M selenic acid under 45 V and T=0 ℃ for 23 hours b)IR spectrum of sample prepared in 0.3M selenic acid under 45V and T=0 ℃ for 23 hours .

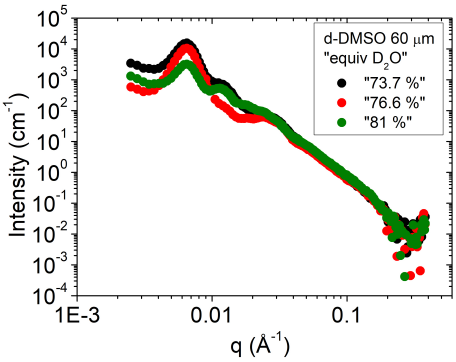

Figure 2.44: SANS spectra for as prepared sample in 0.3 M sulfuric acid under 45V and T=0 ℃ measured in different volume fractions of d-DMSO.

2.4 Discussion on data fitting

We pointed out in the fitting section of the nPAAM prepared in oxalic acid that the scattering length densities of the contaminated shell and the alumina matrix issued from the fit of contrast variation experiment lays within experimental error on the scattering length density of the solvent. This should suggest that we can neglect the contribution of the shell and take into account only a cylinder model. However, neglecting this shell does not allow to reproduce the ”M” shape of the scattering curve close the so called matching point. Moreover, a single phase model (without shell) should result in the existence of total matching condition, which we do not observe. The model of aligned core-shell cylinder used to fit the scattering curve

is given by :

$$I(Q) = \frac{\phi_s}{V_s} F^2(Q) S(Q)$$

where ϕ_s is the volume fraction (i.e equivalent to the surface fraction) of cylinders, $S(Q)$ is the structure factor, $V_s = \pi(R_p + t)^2 L$ the volume of the core-shell cylinder and $F(Q)$ the amplitude of the scattered wave :

$$F(Q) = 2V_c(\rho_{core} - \rho_{shell})\frac{J_1(QR_p)}{QR_p} J_1(QR_p) + 2V_s(\rho_{shell} - \rho_{Al_2O_3})\frac{J_1(Q(R_p + t))}{Q(R_p + t)}$$

Both functions $\frac{J_1(Q(R_p))}{Q(R_p)}$ and $\frac{J_1(Q(R_p+t))}{Q(R_p+t)}$ oscillate with a frequency depending only on the radius of the pores R_p and the shell thickness t. The resulting shape of the form factor depends then on these two functions and their relative weight determined by $V_c(\rho_{core} - \rho_{shell})$ for the contribution of the core and $V_s(\rho_{shell} - \rho_{Al_2O_3})$ for the contribution of the shell. But the amplitude of the overall form factor will depend on L and the contrasts differences at fixed pore radius and shell thickness.

We can illustrate this by fitting the scattering curve of an 'as prepared' oxalic acid membrane immersed in a 73.2% D_2O solvent assuming different length of the cylinder from 7 nm to 1.4 μm and setting both scattering length densities of the matrix and the shell as fitting parameters . As shown in Figure 2.45, the fits are identical. And the scattering length densities reported in Table 2.26 all satisfies a constant relative weight w defined as :

$$w = \frac{V_c(\rho_{core} - \rho_{shell})}{V_s(\rho_{shell} - \rho_{Al_2O_3})} \tag{2.12}$$

As the chosen cylinder length decreases, the core/shell and shell/matrix contrasts increase in order to compensate the loss of intensity. Since the previously fitted tiny contrast do not seem to be physical, this may suggest that the cylinder length we need to take into account to model the data has to be much smaller than the one measured by SEM. Additionally, in the above model, we neglect the longitudinal projection of the wave vector denoted $Q_z = -\frac{Q^2\lambda}{4\pi}$. For $L \approx 100$ μm, the condition $Q_z L << 1$ is not fulfilled which should lead to a deviation from the $I \approx Q^{-3}$ power law observed experimentally.

Another experimental evidence that the length is a critical parameter is that the scattering intensities of nPAAMs with different thickness superimpose at high q as seen in Figure 2.46. They should be shifted if the real length of the nPAAM is taken into account.

Grigoriev et. al[122] suggested that the cylinder length probed is related to the coherent longitudinal length L_z of the lattice. They measured it by measuring the variation in the scattered intensity of the Q component parallel to the cylinder axis Q_z as a function of the tilting angle of the pore axis with respect to the incident beam.

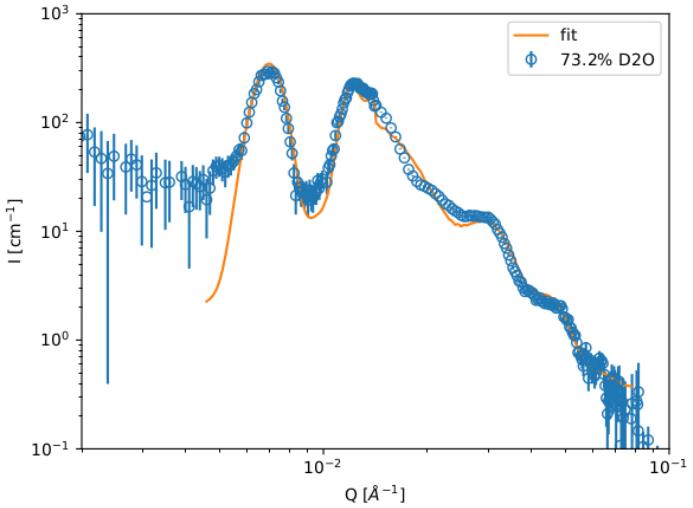

Figure 2.45: Experimental data with fit of sample "OA2" for $\phi_{D2O} = 0.731$ (measurements performed at D11). The solid line corresponds to 5 identical fits by varying ρ_{shell} and $\rho_{Al_2O_3}$ for L =70, 700, 7000 and 14000 Å.

Table 2.26: Fitting parameters for data plotted in Figure 2.45 and corresponding relative ratio of the core/shell contribution.

L (Å)	R_p (Å)	t (Å)	ρ_{core} (Å^{-2})	ρ_{shell} (Å^{-2})	$\rho_{Al_2O_3}$ (Å^{-2})	relative ratio w
70	180	100	$4.47\,10^{-6}$	$6.39\,10^{-6}$	$5.79\,10^{-6}$	-1.32
700	180	100	$4.47\,10^{-6}$	$5.07\,10^{-6}$	$4.89\,10^{-6}$	-1.38
7000	180	100	$4.47\,10^{-6}$	$4.66\,10^{-6}$	$4.60\,10^{-6}$	-1.31
14000	180	100	$4.47\,10^{-6}$	$4.61\,10^{-6}$	$4.56\,10^{-6}$	-1.16

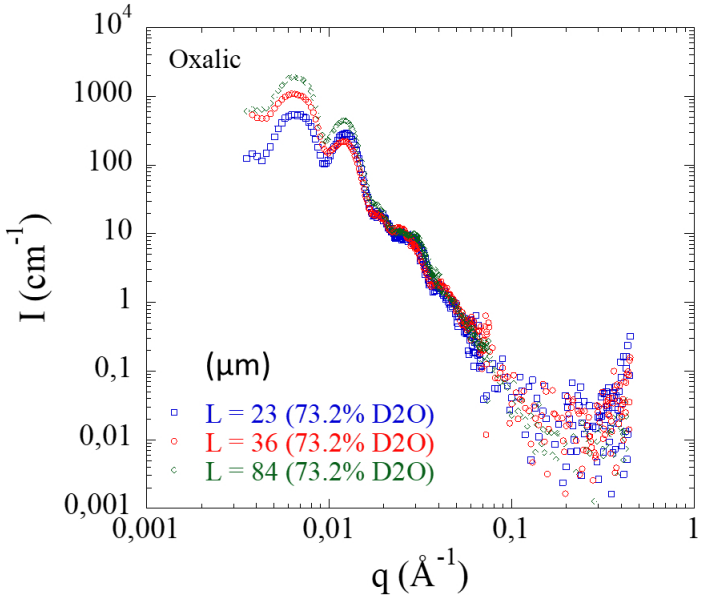

Figure 2.46: SANS spectra of nPAAMs prepared in 0.3 M oxalic acid under 40 V with different thicknesses, measured at 73.2% D_2O .

The longitudinal coherent length is then given by :

$$L_z = \frac{2\pi}{\Delta Q_z} = \frac{2\pi}{Q_{10}\sin(\delta)}$$

where Q_{10} is the 10 correlation peak position, for oxalic q=0.0068 $Å^{-1}$ and δ the width of the rocking curve. One must emphasize that such procedure is no longer valid when multiple scattering occurs. We used the same procedure to determine longitudinal coherence length of our oxalic acid membranes and found an average value of $L_z = 1.4$ μm. Figure 2.47a shows the rocking curve of a nPAAMs in 73.2% D_2O (L=23μm), fitted with a lorenzian distribution. The same analysis was done for different thicknesses and the calculated L_z are plotted in Figure 2.47b. The longitudinal coherence length L_z is independent of L and an average value of 1.4 μm is determined.

The scattering curves issued from contrast variation experiments were then fitted using this value as a fixed parameter. As expected, we observed a good agreement between the model and the experimental data (Figure 2.48) and the corresponding scattering length densities (Table 2.27) of both the shell and the matrix present higher differences out of the experimental error except for the 67.8% D_2O/H_2O mixture. We observe that the change in contrast of the shell is more sensitive to the change in the scattering length density of the

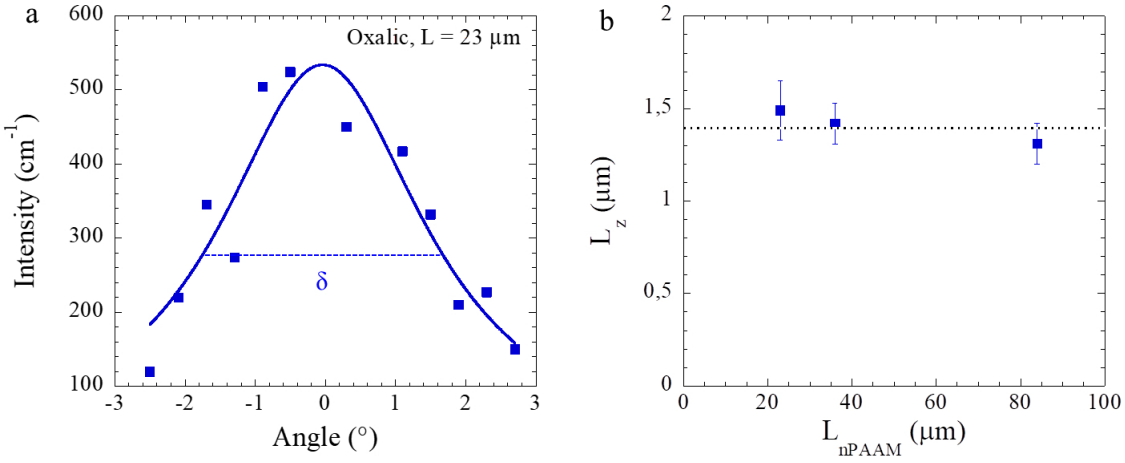

Figure 2.47: a) Rocking curve of a nPAAMs prepared in 0.3 M oxalic acid under 40 V, L=23 μm in thickness, measured at 73.2% D_2O b) Average longitudinal coherent length derived from measured rocking curves of nPAAMs prepared in oxalic acid, under 40V with different thicknesses.

D_2O/H_2O mixture than the alumina matrix indicating a possible higher degree of hydration.

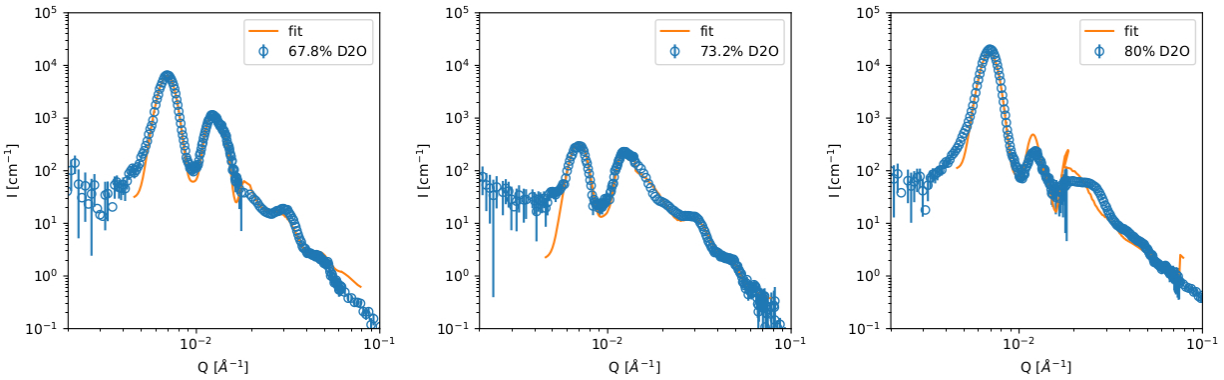

Figure 2.48: Experimental data with fit of sample "OA2" for different volume fraction of D2O (measurements performed at D11). The solid lines corresponds fit by fixing L to 1.4 μm.

To conclude this discussion dealing with SANS data fitting of nPAAM, we have showed that determining the geometrical parameters describing this system is feasible by using a core-shell cylinder form factor for which both the shell and the matrix are hydrated by the solvent. The main difficulty lies in the determination of the actual scattering length densities because of longitudinal coherence effects. We used a previously proposed method in order to determine the effective cylinder length that is probed during SANS measurements which leads to satisfactory differences in contrasts. However, due to both hydration of the contaminated shell and the matrix one cannot determine this length precisely by fitting the

Table 2.27: Fitting results for data "OA2" for as prepared nPAAM in 0.3 M oxalic acid under 40 V, T=18 %, thickness= 58.4 μm. $L_z = 1.4$ μm

ϕ_{D2O}	0.678	0.732	0.8
Fitting parameters			
Porosity	0.29	0.29	0.29
D_{int} (nm)	104	104	104
σ_{int}	0.03	0.03	0.03
δ	0.0006	0.0006	0.0006
cL	11.85	5.41	12.66
$\rho_{core} \times 10^{-6}$ ($\mathring{A}^{-2}$)	4.11	4.47	4.95
$\rho_{shell} \times 10^{-6}$ ($\mathring{A}^{-2}$)	4.28	4.61	4.93
$\rho_{Al_2O_3 \times 10^{-6}}$ ($\mathring{A}^{-2}$)	4.29	4.56	4.77
R_p (nm)	18	18	18
t (nm)	10	10	10

contrast variation scattering curves. Replicating the membrane structure with a material of well known scattering length density which is not subjected to hydration may deliver a final answer to this question.

2.5 General conclusions of Chapter 2

In this chapter, a better understanding of the nPAAMs prepared in different electrolytes was presented by using as a basic technique SANS. Depending on the measurement conditions, the nPAAMs show strong multiple scattering that can be identified by the low transmission, high scattering intensity and distortion of the peak shape. A strategy was proposed to suppress this effect by measuring near the average matching point. However, the membranes cannot be contrast matched and this holds for as prepared, etched and annealed membranes. For the first time, the fitting of the experimental data using a core/shell cylinder model is presented. Membranes measured in D_2O have to be fitted with a shell whereas in DMSO there is no need for a shell. Therefore, the duplex layer anion contaminated structure cannot be the origin of the inhomogeneity as it should have been present in the DMSO measurement as well. Moreover, in the case of oxalic samples the hydrogen content embedded in the alumina during synthesis cannot give rise to the mismatch as the oxalic acid nPAAM prepared in D_2O shows exactly the same scattering spectrum. On the contrary, in sulfuric acid the amount of incorporated hydrogen is significant if one compares the deuterium labeled nPAAM.

In the case of measuring the nPAAMs in water there is an evolution of the spectrum with time and an increase in the incoherent scattering at high q. It can be concluded that

the alumina transforms with time to some aluminum hydroxide form and drastic changes take place in the scattering spectra after 4 days of immersion. Moreover, the kinetics of transformation is lower in D_2O than in H_2O.

An important part in the matching limitation is related to the phenomenon of the adjustment of the scattering length density of the shell and the alumina to the measuring solvent, which seems to be independent of the type of solvent. This behaviour can be explained by considering the substructure of the nPAAMs as has been previously proposed, consisting of nano crystallites of alumina, stacked together to form a network. The inter crystallite area forms a porous network fully permeable to the measuring solvent. The porosity of this region must have a gradient with lower porosity found in the deeper alumina wall. The difference in the scattering spectra between water and DMSO probably is related to the wetting ability of the substructure.

Finally, in order to determine the scattering length densities of the nPAAMs, the length parameter in the fitting model should be elucidated.

Chapter 3

Surface charge of nanoporous alumina membrane

This chapter will focus on the surface charge of bare nPAAMs prepared in oxalic acid. The charge appears as a result of the amphoteric character of alumina according to which, when immersed in a solution, depending on the pH it can be negatively or positively charged. Before studying charged species like polyelectrolytes inside the nPAAMs, it is essential to characterize first the charge behaviour of the bare membrane. Because of the cylindrical geometry of the membranes, the use of specifically designed experimental technique for the charge characterization is necessary: the so-called streaming potential. Here, the sign of the charge is explored inside aqueous solutions of different pH. that have been prepared with or without the use of buffers. The effect of the buffer solution on the sign of the charge and the potential use of tuning the charge by the buffer solution is discussed. All measurements where conducted with an experimental device developed by Didier Lairez, at Laboratoire des Solides Irradiés at École Polytechnique.

3.1 Origin of the surface charge in metal oxides and its measurement by streaming potential

The surface of a metal oxide presents a number of lattice defects such as oxygen or metal vacancies, uncoordinated surface planes, interstitial atoms. When the oxide is immersed inside water or an electrolyte, stabilization of the surface is energetically favoured and occurs by a number of processes like hydroxylation, adsorption of solute molecules, charge transfer reactions [137]. In water solutions, uncoordinated aluminum cations react with adsorbed water to form metal-hydroxyl groups *MOH*. Surface charge is induced by the protonation

and deprotonation of these groups as described by the following reactions,

$$MOH + H^+ = MOH_2^+ \tag{3.1}$$

$$MOH = MO^- + H^+ \tag{3.2}$$

Another contribution to the charge comes from the adsorption of hydroxide metal complexes $M^{z+}[(OH)_n^-]^{(n-z)-}$. These species form in the solution due to the solubility of the metal cations [138]. The described processes are pH dependent and their relative populations give rise to a net surface charge.

With the appearance of surface charge, a layer of ions, counter ions and water molecules is build-up adjacent to the solid surface to counterbalance the surface charge. Their spatial arrangement gives rise to a charge distribution which is described by the electric double layer (EDL) models.

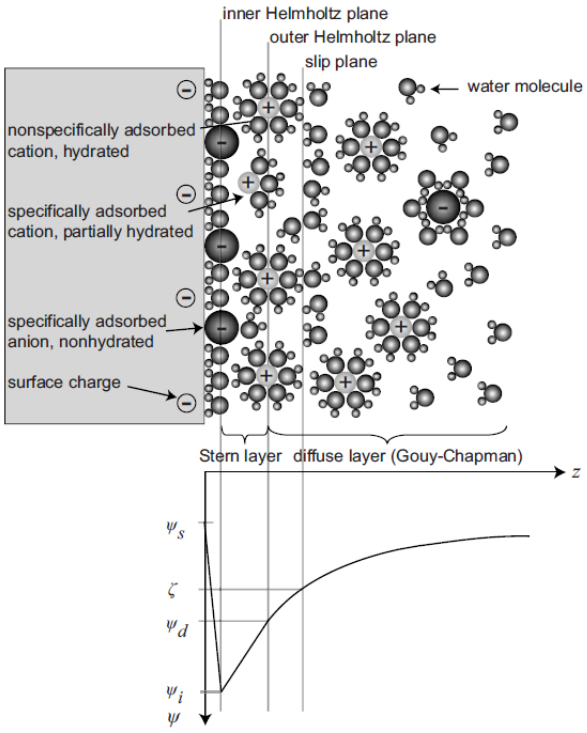

Figure 3.1: The electric double layer model of Gouy-Chapman-Stern and the potential distribution ψ as a function of the distance z away from the solid surface Image taken from [139] .

According to the Gouy-Chapman-Stern model represented in the scheme of Figure 3.1, the layer can be divided in one immobile and one mobile layer. The immobile layer lies between

two planes named as the inner and outer Helmholtz plane. The inner Helmholtz plane is defined from the centers of strongly adsorbed co-ions and counter ions on the solid that have lost their water solvation shell. Further away the outer Helmholtz plane is constituted by hydrated counter-ions. Adjacent to the outer Helmholtz plane a layer of co-ions, counter-ions and water molecules exists which are mobile. This layer defines a slipping plane, that is a diffuse layer which is mobile and the potential at this plane is called the ζ- potential. The potential distribution depends on the surface charge density and the screening ability of the electrolyte. Thus, the ζ- potential is affected by the pH, as it is directly related to the surface charge density and the ionic strength of the solution. There exists a pH where the net charge equals zero and is called the isoelectric point (IEP). The experimental determination of the IEP is made by measuring the pH at which the ζ - potential equals zero.

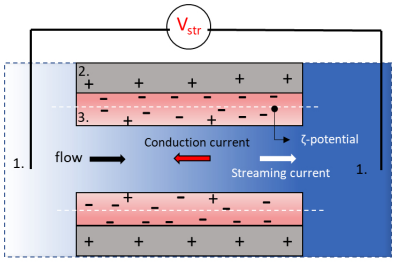

Figure 3.2: Schematic depiction of the streaming potential measurement: 1.electrodes 2. pore wall 3. Electric double layer.

The ζ - potential is experimentally accessible and is a very important parameter to describe the stability of dispersions of charged particles. Through ζ-potential measurement the IEP can be found, the pH that defines a change in the interactions (from attractive to repulsive and vice versa) between charged particles that are dispersed in a polar solvent.

The experimental determination of the ζ-potential depends on the geometry of the sample. For dispersed objects in a solution the usual techniques are electrophoretic light scattering [140]. In the case of porous membranes one of the techniques that is used to determine the ζ - potential is the streaming potential.

The technique is schematically depicted in Figure 3.2 for a positively charged membrane. A porous membrane separates two tanks filled with an electrolyte solution in which two electrodes are immersed. The membrane consists of single straight pore channels (see Chapter 1 for the synthesis). The pore wall in this case is positively charged and adjacent to the surface wall, an EDL builds up with a thickness κ^{-1} (called the Debye length) in order for the solution to respect global electric neutrality. If pressure difference is applied across the membrane, the electrolyte flows through the pore channel and drifts the excess charge of the diffusive layer along the channel. The drifted charge has a net opposite sign relative to the

one of the pore walls and thus creates a current named the streaming current I_{str}. Under laminar flow conditions and under the framework of the Gouy-Chapman-Stern theory for the electric double layer, the streaming current is given by:

$$I_{\text{str}} = -\zeta\epsilon\frac{\pi r^2 \Delta P}{\eta l} \tag{3.3}$$

where,

- ζ the electric potential at a distance from the pore-wall at which the fluid velocity becomes zero
- ϵ the electric permittivity
- r the hydrodynamic radius of the pore
- l the length of the pores
- η the viscosity of the solution
- ΔP the difference of hydrostatic pressure between the two origins of the pore channel

The streaming current creates an accumulation of charges and thus an electric potential which in turn cancels the streaming current. This electric potential at the steady state where the current is zero, is called the streaming potential $U_{\text{str}} = I_{\text{str}}/G$, where $G = \sigma\pi r^2/l$ is the pore conductance and σ the conductivity of the solution. Thus, with the use of equation 3.3 one gets,

$$U_{\text{str}} = -\zeta \times \frac{\epsilon\Delta P}{\sigma\eta}, \tag{3.4}$$

In order to measure the streaming potential, once pressure difference is applied, a voltage difference must be applied across the membrane in order to maintain the current to zero. This continuous adjustment of the applied voltage is achieved by the use of a PID controller and gives access to the streaming potential $U = -U_{\text{str}}$.

The advantage of measuring the streaming potential in order to access ζ-potential is that it is independent of the membrane's geometrical characteristics.

3.2 Surface charge of nanoporous alumina membranes

In the literature regarding electrokinetic phenomena in nPAAMs most of the studies deal with electrosmosis. In the study of [141] the surface charge of the membrane is acessed by

measuring the electroosmotic flow rate in different buffer solutions. It was found that the IEP depended on the buffer used for the pH adjustement, thus leading to the hypothesis of adsorption of certain buffer species such as phosphate. Adsorption of Sr^{2+} has also been reported in studies of diffusion of radioactive ^{85}Sr and through the adsorption behaviour the IEP was estimated close to pH=9 for commercial Anodisc (Whatman) membranes [142]. A more quantitative view on the charge of Anodisc membranes is given in [143]. In the case of membranes prepared in oxalic acid the technique of tangential streaming potential has been used [144], [143]. The technique differs from the transversal streaming potential because the electrolyte flow takes place between two parallel sheets of the membrane under study and not through the pore channel. This, the measured charge is the one of the membrane's surface which might differ from the one of the pore surface. The surface charge was associated to the deprotonation and protonation reactions given by 3.5, 3.6 and the IEP was found to vary from pH=6 to 8 depending on the pore diameter.

$$[AlOH_2^+] \rightarrow [AlOH] + [H^+] \tag{3.5}$$

$$[AlOH] \rightarrow [AlO^-] + [H^+] \tag{3.6}$$

3.2.1 Experimental setup

The cell consists of two parts made of PMMA with an aperture at one of their sides as seen in the scheme in Figure 3.3. The membrane is placed in between the two tanks and sealing is achieved with the use of two O-rings. For measuring smaller membrane pieces, teflon rings with diameter of 5 mm and O-rings, were added at each side of the membrane. The two tanks with the membrane in between can slide inside a metal guide. By using a screw, pressure can be gently applied on the sides of the two tanks and the cell is sealed. Each half cell carries a feedthrough with a Ag/AgCl electrode wire of 2 mm thickness. The feedback voltage is automatically applied and thus measured by using an Axopatch-200B amplifier working in "I=0" mode. The whole cell is placed inside a copper box to reduce electrical noise. The cells have an inlet used for filling with the solution and applying air pressure via a syringe pump in the range of 0.2-0.5 bar. The pressure is measured by a differential pressure transducer. The experiment is controlled by a computer interface and can perform measurements continuously.

The Debye length can be calculated through equation 3.7 for our system that comprises of an electrolyte of 50 mM KCl, T=20 ℃.

$$\kappa^{-1} = \sqrt{\frac{\varepsilon\varepsilon_0 k_B T}{e^2 N_A 2C}} \tag{3.7}$$

where,

- ε_0 :vacuum permittivity
- ε : dielectric constant of solvent
- k_b: Boltzmann constant
- T : Temperature (Kelvin)
- e: elementary charge
- N_A: Avogadro's number
- C: electrolyte concentration in solution

The calculated value is κ^{-1}=1.35 nm and taking into account that R_p=20 nm of the nPAAM we calculate the parameter,

$$\kappa R_p = 14.8 \tag{3.8}$$

which is quite low, thus the Smoluchowski equation can be used for the calculation of the ζ-potential.

Laminar flow exists when the Reynolds number given by 4.6, is Re<2000 [145]. This holds true for the order of magnitude of volumetric flow rates that have been used and the viscosity of the solution.

$$Re = \frac{\rho \upsilon D_H}{\eta u} \tag{3.9}$$

where

- ρ: fluid density (g cm^{-3})
- υ : mean velocity
- D_H: the hydrodynamic pore diameter
- η: dynamic viscosity

The surface conduction σ_s of the pore channel can be ignored as we work in high conductivity medium. In this case the conductivity equals just the specific conductivity σ_b according to equation 3.10,

$$\sigma = (\sigma_b + \frac{4\sigma_s}{D_H}) = \sigma_b \tag{3.10}$$

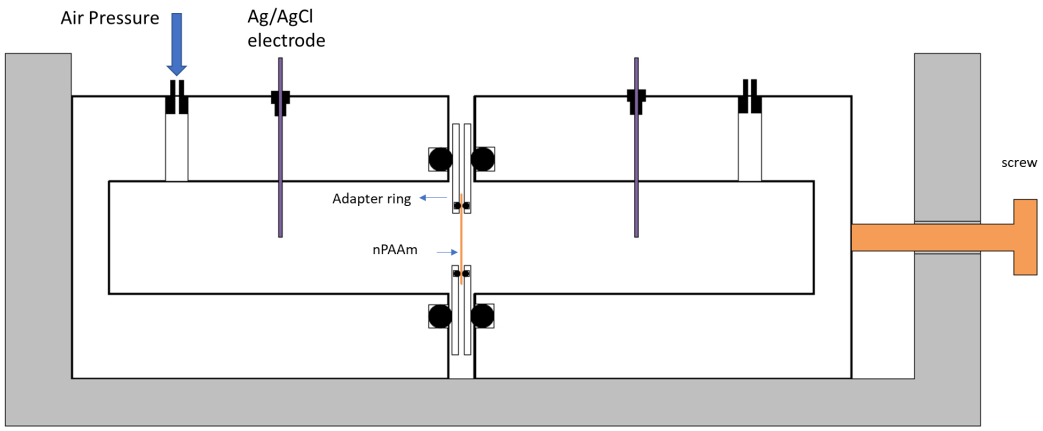

Figure 3.3: Schematic depiction of the experimental setup.

The conditions described above let for using the relation 3.4

3.2.2 Sample preparation

The nPAAMs were synthesized in 0.3 M oxalic acid under 40 V and T=18 ℃ with a second step of anodization time of 8 hours. In order to measure them with streaming potential, alumina had to be detached from the substrate and remove their barrier layer by using the 3^{rd} anodization step protocole described in Chapter 1. In Figure 3.4 the top and bottom surface of a detached membrane is shown. As mentioned in Chapter 1, the pore diameter differs between the top and bottom surface. The detached membranes presented similar pore diameters between 30 and 40 nm for the top side and 60 nm for the bottom. As will be discussed in Chapter 4, flow measurements show that the hydrodynamic pore diameter is closer to the pore diameter of the top surface. Their thickness was about 60 µm. The membranes were first wetted by immersion in the measuring solution and caution was taken during loading in the cell in order not to create any bubbles.

In Figure 3.5 the current (I) versus voltage (V) curve is plotted for a membrane measured in a buffer solution of 2 mM Acetic acid/Acetate and 50 mM of KCl having a pH of 4, assuming that σ_{pore}=σ_{bulk}. The slope of this curve directly provides the conductance of the

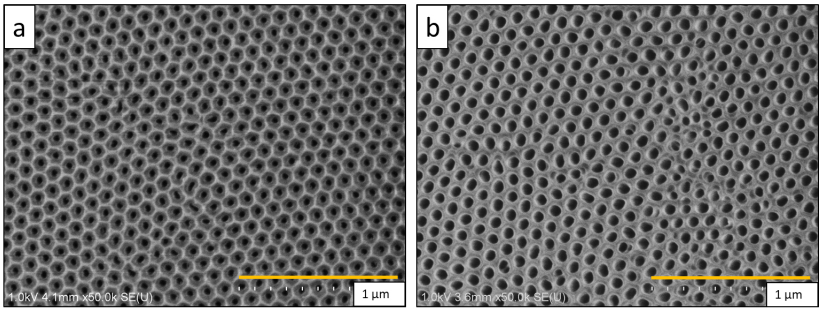

Figure 3.4: SEM image of a detached nPAAM prepared in 0.3 M oxalic acid under 40 V a) top surface D_p=35 nm b) bottom surface D_p=55 nm .

nPAAMs. Two measurements have been performed in similar conditions to evaluate the variability of G. We found 0.1509×10^{-3} (shown in Figure 3.5) and 0.7×10^{-3} S (not shown). In water the measured value was 0.57×10^{-3} S (not shown). The expected conductance for one pore channel is calculated through equation 3.11.

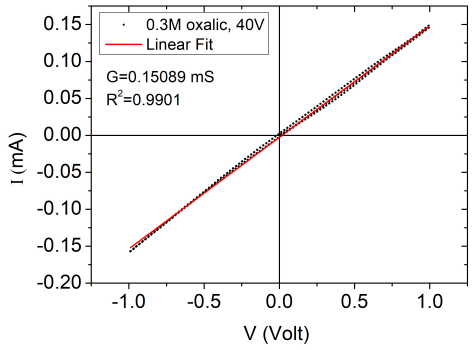

Figure 3.5: a) Intensity versus Voltage curve for a membrane prepared in 0.3 M oxalic acid under 40 V, T=18 ℃ measured at pH=3.5 in Acetic acid/Acetate buffer solution.

$$G_p = \sigma_{bulk}(\frac{4L}{\pi D_p^2})^{-1} \tag{3.11}$$

where,

- D_p the diameter of the circular surface exposed to the solution
- σ_{bulk} the bulk conductivity of the electrolyte :
- L the thickness of the membrane

Table 3.1: Table of parameters used for the calculation of conductivity

pore density $\times 10^{10}$ (cm^{-2})	membrane surface (cm^2)	thickness L µm	σ (S/m)	G_p (theory) (1 pore) $\times 10^{-11}$ (S)	G (theory) $\times 10^{-3}(S)$	G experimental $\times 10^{-3}$(S)
1.1	0.238	60	0.631	1.32	35	0.1509 and 0.7

The case of N pores is calculated by considering the array of pores as parallel resistances of R_p and the total conductance G given by:

$$G = \frac{1}{R_{tot}} = \frac{N}{R_p} = NG_p \tag{3.12}$$

In the above description the resistance at the two entrances of the pore channel is neglected because of the high aspect ratio of the membrane L$\gg D_p$.

In Table 3.1, the parameters used for the calculation of the conductance is shown. The pore diameter is calculated from the top surface. The enlarged bottom pore diameter is an effect of the detachment process and is expected to be limited in the vicinity of the surface. Moreover, from permeability measurements of such asymmetric membranes (see next Chapter), the hydrodynamic radius corresponds to the one at the top surface. It is observed that the experimental conductance is much lower than the theoretical one. Similar trend is observed for nPAAMs in water (pH=6) with an experimental value of G=0.6*10^{-3} S. The decreased conductance was observed in more than one samples so it cannot be attributed to reproducibility issues. A lower G than expected has already been observed for single nanopores, indicating that the ion transport can be modified at the nanometer scale with $\sigma_{bulk} \succeq \sigma_{pore}$ [146]. However, in our case R_p is large (20 nm) and $R_p \gg \kappa^{-1}$. A lower value of G (an order of magnitude) has already been observed by impedence spectroscopy for nPAAMs [147] but the reason is not clearly understood. Another explanation would be that the residual difference is due to entrance effects as the measured area contains a large number of pores and their mutual interaction results in a sublinear scaling of the global conductance with the number of pore channels (G$\sim \sqrt{N}$) [148]. Further measurements in different conditions (such as concentration of added salt) and with different pore diameters are needed in order to understand.

Finally, to tune the pH, buffer solutions were prepared by mixing different acids and bases at appropriate concentrations given in [149]. The buffer species provide a more stable pH as they counterbalance dilution effects of the measuring solution. Their concentration was kept at 2 mM in order to have the conductivity fixed by the 50 mM KCl in all of the

pH region	Buffer nature	
Acidic	Acetic acid/Acetate	
Neutral	HCl/KOH, H_2O	NaH_2PO_4/NaOH
Basic	KOH	NH_3/NH_4^+, Borax , NaH_2PO_4/NaOH

Table 3.2: Buffer solutions used for tuning the pH

solutions. The pH of the buffer solutions was measured before and after the measurement and not any large deviations were observed. The conductivity of each solution was measured and used for the calculation of the ζ-potential . For some solutions the pH was adjusted by HCl/KOH in order to check if there is an effect of the buffer species on the ζ-potential. The different species in use and the pH region covered is given in Table 3.2.

3.2.3 Effect of buffer solutions on the ζ -potential

In Figure 3.6, the ζ- potential is presented as a function of the pH for a membrane, measured using different types of buffer solutions. In acidic pH the membrane is positively charged and a value of 13 mV ± is reached at pH=4. It is observed that in the basic and neutral pH region (6-11), the ζ -potential depends on the type of buffer in use. When the buffer solution is made with KOH the ζ -potential is positive while when phosphate buffers and borax are used it is negative. It is expected that for alumina, measured in non adsorbing electrolytes, the IEP equals 8 for ionic strength of 10^{-3} mol L^{-1} and 8.5 for 10^{-2} mol L^{-1} [150]. Thus, below this value it is expected to be positive.

Here, the IEP is around pH=9.6.

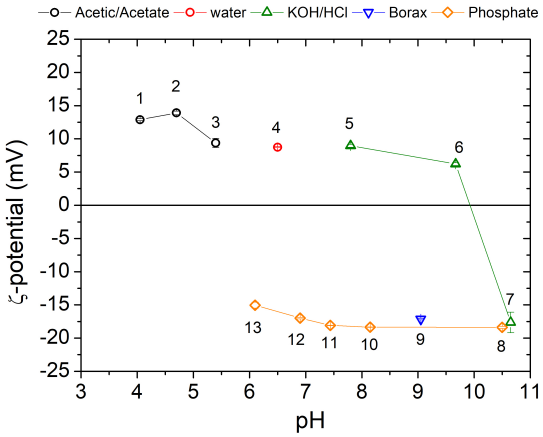

Figure 3.6: The ζ-potential as a function of pH dependency for a nPAAM prepared in 0.3 M oxaic acid under 40 V, measured in different buffer solutions using streaming potential experiment.

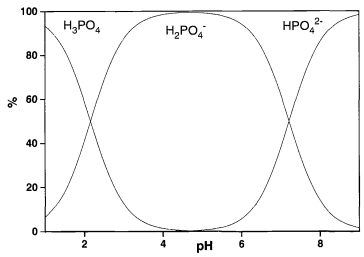

Figure 3.7: Speciation of phosphoric acid in a low ionic strength solution.

Here, the adsorption of the negatively charged phosphate species can explain the negative charge for pH from 6 to 11. For the phosphate buffer the ζ-potential tends to decrease with

the decrease of the pH. Figure 3.7 shows the domains of predominance of the different species of H_3PO_4 as a function of the pH. At high pH, HPO_4^{2-} is dominant and can adsorb at the nPAAM surface and reverse the net charge of the membrane. At intermediate pH the concentration of the divalent species HPO_4^{2-} gives its place to monovalent $H_3PO_4^-$ as the pH decreases.

The adsorption of the phosphate species can be then exploited to tune negatively the charge of the nPAAM in the neutral region(pH≈6) and avoiding

1. working at basic conditions where the dissolution of alumina is expected to take place
2. the grafting of small molecules whose charges depend on the pH

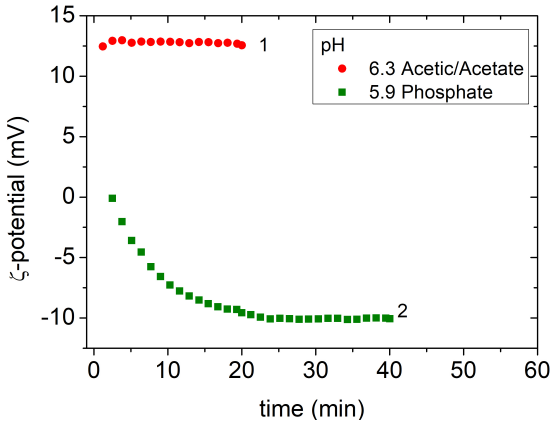

Figure 3.8: Kinetics of adsorption of phosphate species on nPAAM
For comparison the ζ evolution with time is also shown in Acetic/Acetate buffer.

In Figure 3.8 the ζ -potential of a nPAAM is plotted as a function of time, measured in Acetic acid/Acetate and in phosphate buffer solution. It can be seen that in the Acetic acid/Acetate the ζ -potential is constant while in phosphate the adsorption kinetics is probed and equilibrium is reached at about 25 min. Thus, before plotting the ζ-potential, the kinetic effects should be checked and the values should be taken at equilibrium. The values plotted in the experimental curve of Figure 3.6 have been obtained by averaging the results of the ζ -potential measurement after reaching equilibrium. The desorption of the phosphate species is reversible only at acidic conditions. In Figure 3.9 the ζ -potential as a function of time is presented for a nPAAM measured in a series of buffers (Acetic acid/Acetate and phosphate). First the phosphate buffer is introduced in the cell and the ζ -potential acquires a negative value due to adsorption. Then passing of the acidic buffer of pH=5.4 doesn't change the charge. The value slightly increases to -5mV. Then the sign returns to positive constant

value after passing Acetic acid/Acetate buffer at a lower pH (pH=4.7) and reach a constant value after 8 minutes.

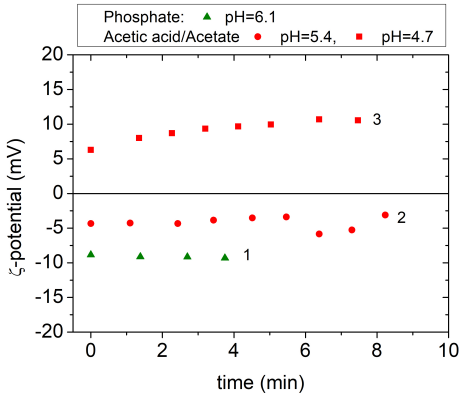

Figure 3.9: ζ- potential evolution of a nPAAM measured in the buffer sequence: 1 Phosphate pH=6.1, 2 Acetic acid/Acetate pH=5.4, 3 Acetic acid/Acetate pH=4.7.

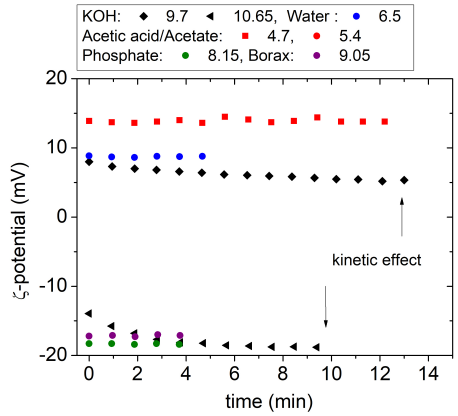

Figure 3.10: The ζ-potential as a function of time of a nPAAM prepared in 0.3 M oxalic acid under 40 V, measured in different buffer solutions .

In Figure 3.10 the ζ -potential is plotted as a function of time for different buffers. For two buffers, the ζ -potential decreases slightly with time. The KOH buffer at pH=9.7 and pH=10.65 presents a monotonic decrease of 2 mV during the 14 minutes of measuring time. As this pH is near the IEP and the reversal is steep, equilibrium cannot be reached and the ζ -potential value tends slowly to the sign reversal. The same effect can be seen when the pH is adjusted by NH_3/NH_4^+. In the ζ -potential curve of a similar sample (Figure 3.11a it is observed that charge reversal takes place around pH=8. The kinetic effect is observed in Figure 3.11b) at pH=7.9 and pH=8.7 and takes about 45 minutes for equilibrium to be

reached. In Figure 3.11a) the ζ-potential values vs pH are plotted after reaching equilibrium. Note that the pH value of water indicates carbonation. It can be concluded that the IEP lies close to pH=8. This pH is slightly lower than pH=9.6 found in Figure 3.6.

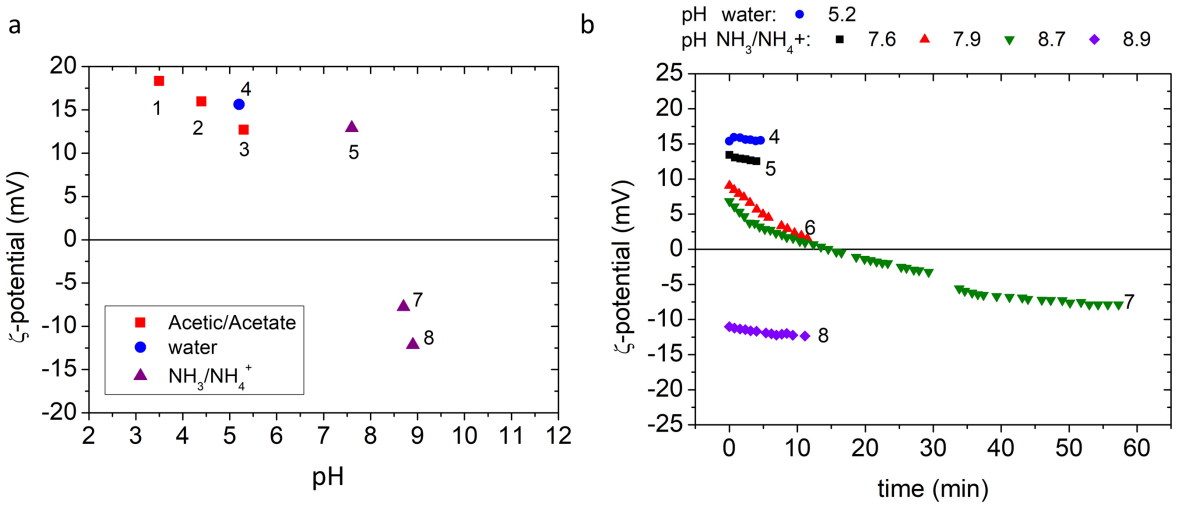

Figure 3.11: a) ζ -potential as a function of the pH for a nPAAM (the sequence of measurment is noted by numbers). b) Time evolution of the ζ-potential for measurements performed in NH_3/NH_4^+ .

3.2.3.1 Reproducibility of measurement for nPAAMs prepared in oxalic acid

We will discuss the measurement reproducibility for nPAAMs prepared in oxalic acid. The nPAAMs present some variation in the ζ-potential values, measured at the same buffer species and pH. In Figure 3.12 the ζ-potential vs pH is plotted for different samples prepared under the same anodization conditions and measured with the same buffer solutions. The variation is lower at the low acidic and high basic conditions, while it increases in the middle pH range (5-7). At low pH (pH≈4) and high pH (≈9-10), the variations are small, the ζ-potential measurement is reproducible. However, in intermediate pH (4.5-6.5), the variations are more pronounched. Due to these variabilities we won't focus on the absolute value of the ζ but only on its sign.

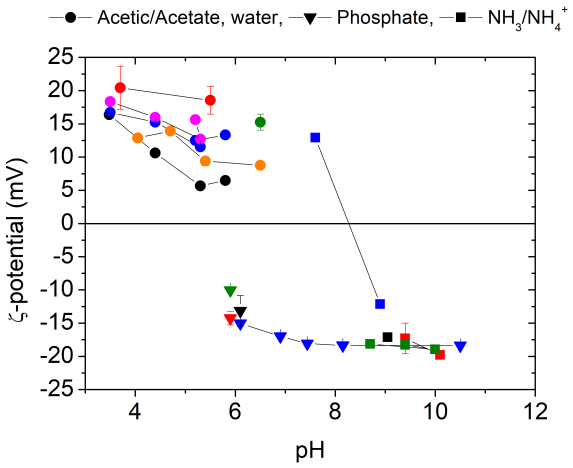

Figure 3.12: a) ζ -potential as a function of the pH for different nPAAMs prepared in the same anodization conditions (0.3 M oxalic acid, 40 V, T=18 ℃.

3.2.4 Transformation of nPAAMs and effect on the ζ -potential

In Chapter 3 it was shown that nPAAMs react with water thus their composition changes. More specifically the degradation mechanism involves the dissolution of aluminum, the formation of hydroxide complex of the form $(Al_{13}O_4(OH_{24})H_2O_{12})^{7+}$ and their deposition back to the surface as $Al(OH)_4^-$ in neutral pH conditions [115].

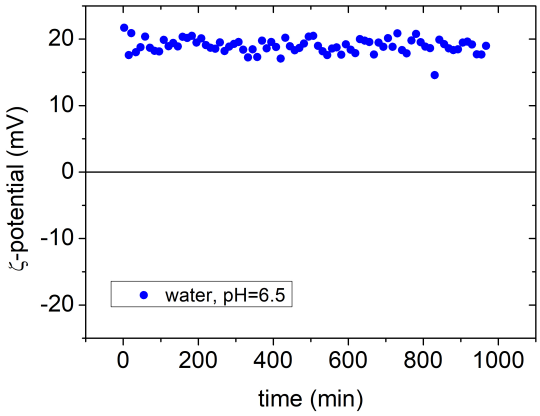

Figure 3.13: ζ- potential evolution of a nPAAM measured in water pH=6.5 (with 50mM KCl) during 16 hours .

This process might bring changes in the charge and for this reason the evolution of the ζ-potential was followed with time. In Figure 3.13 the ζ- potential is presented as a function

of the measuring time for a nPAAM measured in water (pH=6.5). During the 16 hours of measurement (one point every 15 min) the ζ- potential stays constant at 18.8 $\pm$ 1.2 mV. It can be concluded that there is not effect on the ζ- potential due to prolonged immersion in the water solution (at least in the studied time-scale).

3.2.5 ζ- potential of commercial Anodisc membranes

The ζ- potential was also measured for commercial membranes Anodisc (Whatman), with nominal pore diameter 200 nm. In Figure 3.14 an SEM image of the top and bottom surface of an Anodisc-Whatman nPAAM with nominal pore diameter 200 nm is presented. It is known that Whatman-Anodisc membranes consists of two assymetric sides. One thick one which is called the "support" layer and a thinner one which is referred to as the "active" layer. In Figure (3.14a), the SEM top view image of the "active layer" is shown. The thickness of the "active layer" doesn't exceed L=1 µm as has been previously reported [151]. This surface consists of a web-like structure. The "support" layer (3.14b) consists of pores with a pore diameter about D_p=200 nm of about 60µm in thickness.

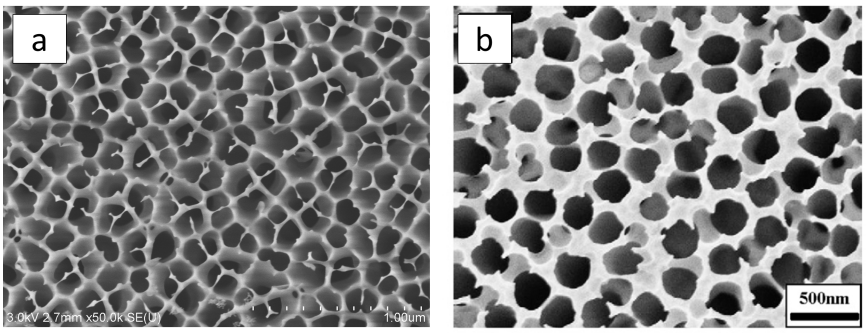

Figure 3.14: a) Top view by SEM of one of the sides of an Anodisc-Whatman nPAAM with nominal pore diameter D_p=200 nm. The side is characterised by a mesh-like structure b) SEM image of the other side of the Anodisc-Whatman with nominal D_p=200 nm (taken from [152].)

In Figure 3.15 the result of the ζ-potential is shown for two membranes of Anodisc (Whatman). The membranes show an IEP around pH=8 and the ζ-potential in water is 10 mV, similar to the home-made nPAAMs. The measured value is in agreement with previous work on Anodisc membranes [143].

Kinetic effects were also observed in the commercial Anodisc membranes. In Figure 3.16 the ζ- potential vs time is plotted for the Anodisc nPAAM measured in NH_3/NH_4^+ buffer solution near the IEP (pH=7.6 and 8.7). A constant ζ- potential is reached after 20 min.

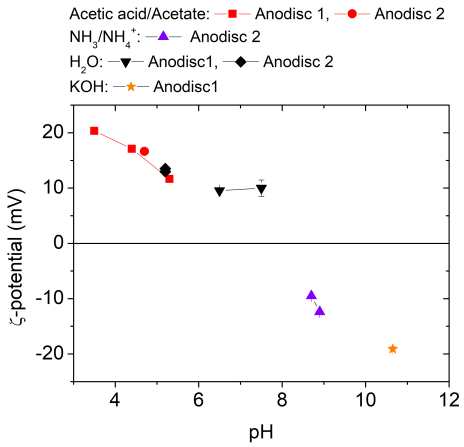

Figure 3.15: ζ- potential as a function of pH for two Anodisc (Whatman) nPAAMs .

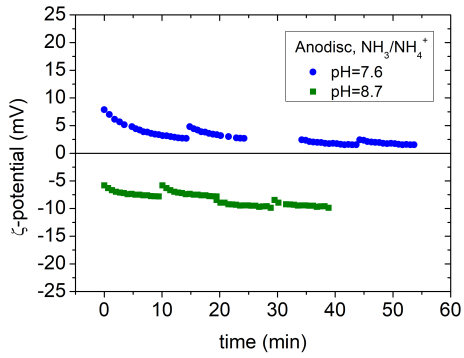

Figure 3.16: ζ- potential evolution of an Anodisc-Whatman nPAAM measured in NH_3/NH_4^+ buffers .

3.2.5.1 ζ- potential of nPAAM prepared in H_2O vs D_2O

The effect on the ζ-potential of a nPAAM prepared in D_2O solvent during the synthesis of the nPAAM in 0.3M oxalic acid was tested. In Figure 3.17 a comparison plot is given for the ζ- potential as a function of pH for one membrane prepared hydrogenated (black circles) and one deuterated (blue squares). The buffer in which the membranes were measured were Acetic/Acetate, water and KOH. It is observed that for both the nPAAMs the ζ-potential follow the same trend, indicating that the synthesis in D_2O doesn't modify the charge behavior of the nPAAMs.

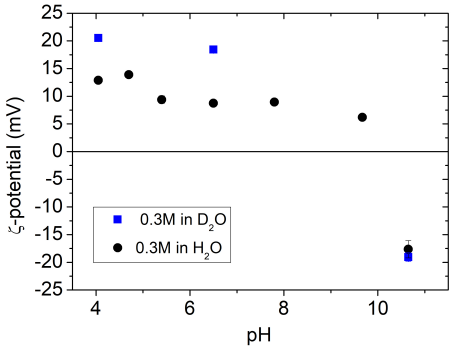

Figure 3.17: ζ- potential as a function of pH for nPAAM prepared in 0.3M oxalic acid/H_2O (black circles) and 0.3M oxalic acid/D_2O (blue circles) measured in non adsorbing buffer species.

3.3 General Conclusions of Chapter 3

To summarize, in this chapter the ζ- potential was measured as a function of pH by streaming potential technique. The samples were nPAAMs prepared in oxalic acid and commercial Anodisc-Whatman membranes. It is found that the IEP depends on the buffer species in use for the pH tuning. When the pH is tuned with KOH or NH_3/NH_4^+, the IEP lies around pH=8 and when phosphate is used the IEP shifts to lower pH due to adsorption of phosphate. The adsorption of phosphate presents long kinetics and is reversible in acidic conditions, thus it provides an interesting and convenient way to tune the pH without permanent modifications of the membrane with methods such as silanization. Long kinetics of charge reversal was also observed near the IEP for the non adsorbing buffers tuned by NH_3/NH_4^+. The ζ-potential in water is stable with time for long measurement times. Moreover, membranes prepared in oxalic acid in H_2O and D_2O were compared and similar ζ-potential dependency on pH is observed.

Chapter 4

Experimental approaches in studying polyelectrolyte confinement

4.1 Introduction

In this Chapter, we will present some experimental approaches to study the behaviour of polyelectrolyte (PE) inside nPAAMs. As mentioned in the introduction, developing experimental strategy to investigate the confinement of PE is critical. Here we will study sodium polystyrene sulfonate (NaPSS) and combine different techniques (FTIR, TGA, streaming potential, flow and SANS) to describe penetration and conformation inside nPAAMs.

4.2 Characterisation of the polyelectrolyte

4.2.1 Indroduction

Polyelectrolytes are polymers that carry an electric charge when dissolved in a polar solvent. The emergence of the charge takes place with the dissociation of ionic groups found on the backbone or on the side groups of the polymer chain. The sign of the polyelectrolyte's charge can be negative or positive. In the case when the polyelectrolyte consists of both positive and negative charges the term polyampholyte is used. The charge is the reason for their hydrophilic character which is an advantage for water based applications. Polyelectrolytes exist in nature such like are the proteins and the DNA, and also in synthetic form like, sodium polystyrene sulfonate(NaPSS), polycarboxylic acids, polyphoshates.

The properties of polyelectrolytes differ from the neutral polymers due to their electrostatic interactions which come into effect at longer length scales than other shorter range interactions such as van der Waals, or hydrophobic [153]. For example, the repulsive inter-

actions between the charged groups of the polyelectrolyte chain result in a more stretched conformation relatively to neutral polymers [154]. The stability of a polyelectrolyte solution is also affected from the charge. In dilute conditions, repulsive electrostatic forces can prevent flocculation of the polyelectrolyte.

The electrostatic interactions can be tuned in a number of ways. This is accomplished either by modifying the polyelectrolyte chain or by changing the solvent.

For example, during synthesis of the polyelectrolyte, the frequency of the ionizable chemical groups be changed. As a result the charge fraction *f*, given by 4.1, varies between 0 and 1 [155].

$$f = \frac{b}{l} \tag{4.1}$$

where

- b : the monomer length
- l: the distance between the charges

Following the classification of acids, polyelectrolytes can be strong or weak. For weak polyelectrolytes the number of ionized groups and thus the charge fraction, depends on the pH of the solution. Another way to affect the interactions is to change the ionic strength of the solution by adding salt. The counter ions will electro statically screen the ionized groups by diffusing close to the chain and decrease the intra chain interactions.

The condensation of counter ions is a subject of special scientific interest with the most known developed theory being the one of Manning-Oosawa [156], [157].

Polyelectrolytes can adsorb on oppositely charged surfaces [158]. In the case of strong polyelectrolytes, the charge fraction of the chain is high and their conformation resembles a rod. A high number of ionized groups are available to adsorb and this leads to the formation of a monolayer with loops and tails [159].

The polyelectrolyte sodium-polystyrene sulfonate (NaPSS) consists of repeated units of the styrene monomer with a sodium sulfate group replacing one hydrogen on the benzene ring (Figure 4.1). In a polar solvent such as water, the sodium sulfate group dissociates and the chains are charged negatively while the sodium counter-ions are released in the solution. The polyelectrolyte can be synthesized by sulfonation of polystyrene. Sulfonation doesn't affect the initial number of monomers present on the polymer chain but the frequency of the sulfonate group on the polyelectrolyte chain can be tuned by the synthesis. Thus the fraction of charged monomers f can be tuned between 0 and 1.

We choose to study this polyelectrolyte fully charged (i.e f=1) because it is a widely studied polyelectrolyte and a lot of bibliography exists on its characterisation in solution

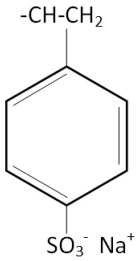

Figure 4.1: The monomer unit of sodium polystyrene sulfonate (PSS)

and is related to a number of applications. Moreover, it is a strong polyelectrolyte, thus the charge fraction is fixed and similar for all the pH range.

4.2.2 Experimental part: NaPSS characterisation

For the experiments commercial NaPSS (powder, Sigma Aldrich) of two different molecular weights (M_w) were used for the preparation of all solutions. The large amounts of polyelectrolyte needed for the experiments justify the choice of using commercial NaPSS. The nominal values of their molecular weight were 70.000 and 500.000 g mol^{-1} (named 70 kDa and 500 kDa in the following). Due to their hydrophilic character, polyelectrolytes adsorb water molecules when let in air. In order to calculate the amount of water contained in the polyelectrolyte mass, measurement was performed after the drying of the polyelectrolyte. A known mass of the polyelectrolyte was placed inside an aluminum pan and left in an oven at 150 ℃ for a certain amount of time. Then it was taken out of the oven and was directly weighted. The process continued until a plateau on the weight vs time was reached. In Figure 4.2a the kinetics of water mass loss is presented for NaPSS 500kDa with the measured water content being 11 % wt. By applying the same process for NaPSS 70 kDa, the weight loss found was 14% wt. A water content of 9% wt was found by performing TGA on NaPSS 70 kDa (Figure 4.2b). All the concentrations that have been presented will be corrected for the water content of 9%wt. Note that TGA shows that NaPSS present different stages in the weight loss due to its degradation process [160].

The polydispersity and the average molecular weight M_w was characterized by size exclusive chromatography (SEC), performed at Institute Charles Sadron, Strasbourg. The samples measured were NaPSS 70 kDa and 500 kDa. Moreoever, for a sample of NaPSS 70 kDa, dialysis was performed to study for the effect of purification. The initial concentration of the polyeletrolyte solution was 16 g/L. The sample was placed inside a cellulose bag with a molecular cut off of 6 kDa and let for 1 day in the bath. Then it was dried out with the use of lyophilisator. The SEC results are shown in Table 4.1.

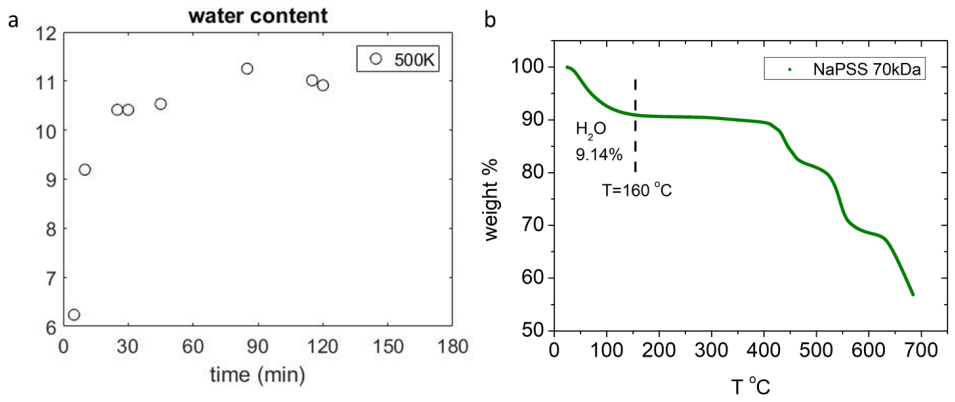

Figure 4.2: Water mass loss % as a funtion of drying time for NaPSS M_w=500kDa. b) TGA curve of NaPSS 70kDa with indicated the weight loss of 9.14% until T=160 ℃

nominal M_w g mol^{-1}	M_w g mol^{-1}	Mn g mol^{-1}	polydispersity
70.000	79.000	43.300	1.83
70.000 dial-1 day	81.600	42.900	1.90
500.000	1.304.000	632.300	2.06

Table 4.1: Characterisation of commercial NaPSS with nominal M_w 70.000 and 500.000 g mol^{-1} by size exclusion chromatography.

It can be seen from the results of Table 4.1 that the NaPSS is polysdispersed and a huge discrepency in the M_w exists for the 500 kDa. For this reason, in the experiments the 70kDa NaPSS will be used.

In order to access qualitatively the conformation of the polyelectrolyte, the viscosity of the polyelectrolyte in water and in the presence of salt was measured [154]. In general, the viscosity reflects the chain conformation in the solution. The three regimes of polyelectrolytes with no added salt are:

- dilute
- unentangled semidilute
- entangled semidilute regime

In the dilute region the chains are separated from each other but still experience electrostatic interactions. The cross-over from the dilute to the unentangled semidilute regime is done at the concentration c^*. Experimentally, c^* is defined as the concentration where the

	c*(g/L)
no salt	12
no salt after dialysis	12
1mM	
50mM	26

Table 4.2: c* of different NaPSS solutions

viscosity of the solution is twice the viscosity of the solvent (i.e η_{sp}=1) Over this concentration the chains are close to each other but they do not overlap. In this regime the viscosity scales as $c^{1/2}$. As the concentration increases, we pass to the entangled semidilute regime where the vicosity depends on $c^{3/2}$. This happens at concentration c_e and the chains are entangled.

In Figure 4.3 the specific viscosity is plotted as a function of concentration for NaPSS polyelectrolyte with nominal M_w of 70 kDa. The specific viscosity is defined as following:

$$\eta_{sp} = \frac{\eta - \eta_s}{\eta_s} \tag{4.2}$$

where

- η solution's viscosity
- η_s solvent's viscosity

In order to see the effect of residual salt on the initial polyelectrolyte powder, dialysis was performed for 1 day in order to purify the polyelectrolyte from the excess salt. Moroever, high and low salt concentration was tested (1mM and 50mM). In Figure 4.3 the results of the viscosimetry are plotted with the scaling laws (straight lines) that correspond to each regime, described in Boris et. al.[161]. The unentangled semidilute regime starts around 0.2 (g/L) that corresponds to a $c^{1/2}$, for the no salt added and dialysed polyelectrolyte and the entangled regime at 100 g/L. When salt is added the electrostatic interactions are screened, the chain conformation is less extended and the chains overlap at higher concentrations. The curve with the 1 mM KCl seems to deviate from the no added salt curves but more points are needed after the concentration of 10 g/L to elucidate if the c_e is shifted to higher concentrations. The effect of the added salt at 50 mM clearly shows that in this condition the polyelectrolyte's viscosity follows the law of $\eta \propto$ c, typical for neutral polymers. The added salt at this concentration is enough to vanish the electrostatic interactions between the chains. For monodisperse PE, the entering into the $c^{1/2}$ regime coincides with η_{sp}=1 [28]. Table 4.2 presents the obtained values.

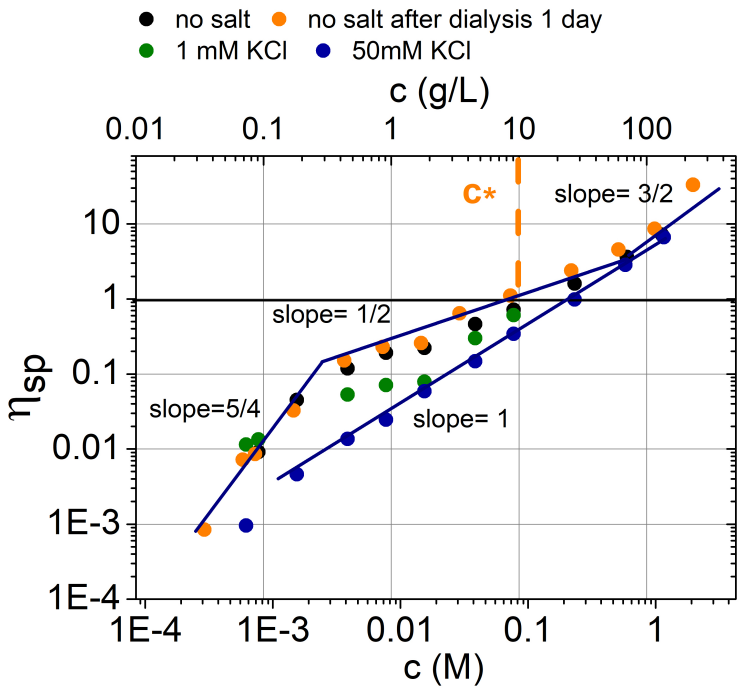

Figure 4.3: Specific viscosity of NaPSS 70kDa as a function of PE concentration for different salt concentration.

One of the powerful techniques to study conformation of polyelectrolytes is SANS. The advantages include the ability to probe hydrogen and the difference in the scattering length density between H and D which allows to use contrast variation and measure the organisation of the chains in the solution, as well as the average chain conformation. Still, in dilute solutions the SANS signal is disrupted by the incoherent scattering of the solvent and long measurement times are needed. This is why in SANS, measurements with polyelectrolyte where made in the entangled semidilute regime (see below).

4.3 NaPSS inside nanoporous anodic alumina

4.3.1 Loading NaPSS on nPAAMs

One of the most difficult questions that has to be answered when studying polymers inside porous materials is to verify if the polymer is inside the pores. Notably, one has to elucidate between signal coming from the surface and from the bulk of the porous matrix.

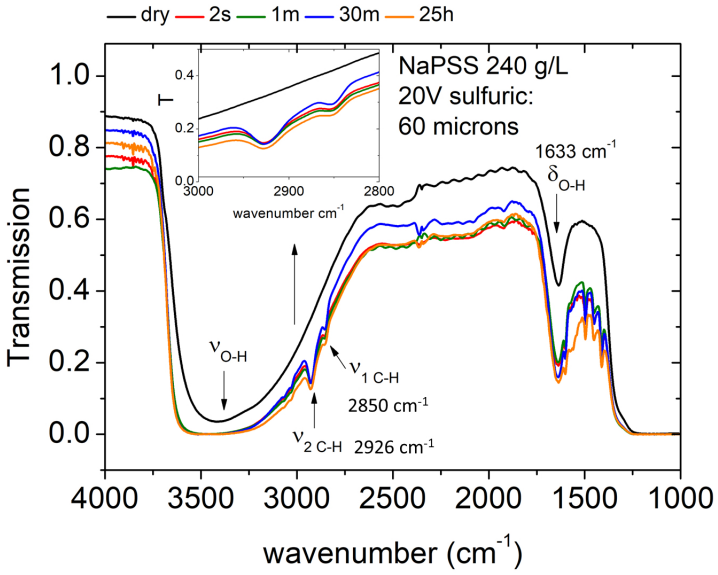

Figure 4.4: FTIR spectra of nPAAM prepared in sulfuric acid, loaded with NaPSS, for different immersion times.

As a first approach, FTIR spectroscopy was used in a kinetic study of NaPSS loading in nPAAMs. For this study, two nPAAms were prepared , one in 0.3 M oxalic under 40V(D_p≈40 nm) and another in 0.3M sulfuric acid under 20 V (D_p≈20 nm). The anodization time was adjusted in order to have a membrane of about 60 microns in thickness. For oxalic acid 8 hours of anodization at 18 ℃ was used and for sulfuric 16 hours at 10 ℃. Their aluminum substrate was removed in by wet chemical etching described in Chapter 1. The membranes were cut in equal pieces of about 1 cm^2 and immersed inside a NaPSS solution at 240 g/L for different times. Then they were removed from the solution and the residual polymer solution present on the top of the nPAAM, was expelled by the use of a plastic thick film.

In Figure 4.4 the IR spectra of a nPAAM prepared in sulfuric acid and immersed in NaPSS solution for different times is presented. The samples were measured after drying in air for several hours. The dry membrane (black line) shows a broad adsorption band around 3400 cm^{-1} that is ascribed to water stretching vibration. The absorption peak at 1633 cm^{-1}

is also caused by water deformation [162]. These two peaks are related with the hydration of the nPAAM. The saturated band close to 1000 cm^{-1} is due to aluminum sulfate bonds [132]. For the nPAAMs immersed in NaPSS the spectra look similar. At 2926 cm^{-1} is the assymetric and at 2850 cm^{-1} is the symmetric vibration of C-H. Due to the convolution with the OH vibration, quantification of the amount of NaPSS is not possible but its presence is evident. Nevertheless in terms of time scales, the membrane immersed for h shows slightly lower transmission at the characteristic polyelectrolyte vibrations.

Similarly, the same kinetic effect was observed for the oxalic membranes, (Figure

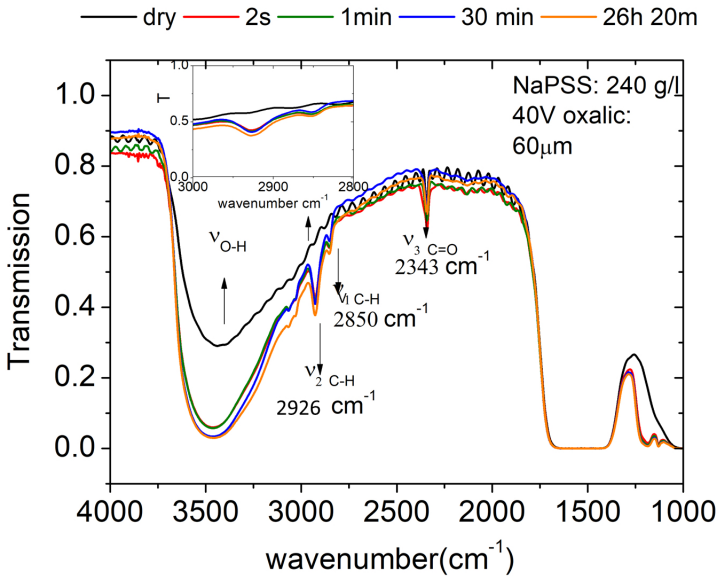

Figure 4.5: FTIR spectra of nPAAM prepared in oxalic acid, immersed in NaPSS solution before and after rinsing with water. The bare nPAAM is shown for comparison.

In order to check for adsorption, FTIR measurements were performed on

- bare nPAAMs
- on not rinsed nPAAM after immersion in NaPSS solution during 17h
- on the bare nPAAM after rinsing with water

a membrane that was immersed in the NaPSS for 17h, was measured after drying for several minutes and after rinsing with water. As it can be seen in Figure 4.6 there is still some trace of the vibration of C-H at 2926 cm^{-1} in the rinsed spectrum, indicating adsorption of the polyelectrolyte on the membrane.

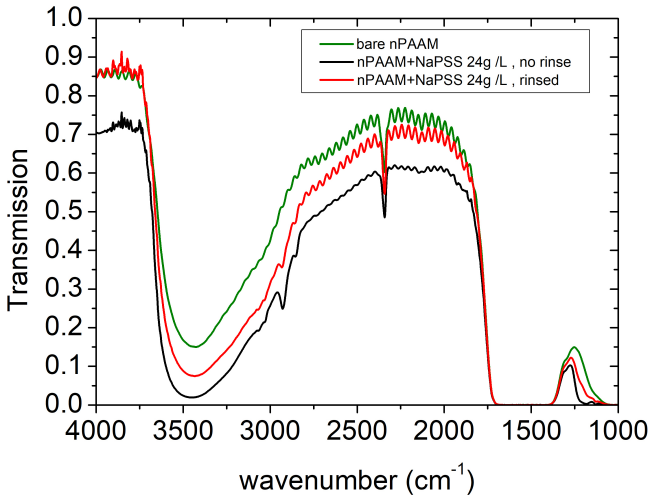

Figure 4.6: FTIR spectra of nPAAM prepared in oxalic acid, loaded with NaPSS, for different immersion times.

4.3.2 Kinetics of adsorption of NaPSS probed by streaming potential measurements

The charge properties of the nPAAMs appear to be advantageous in studying the adsorption of the polyelectrolyte inside the pore walls of a nPAAM. This study can be realized by streaming-potential. The ζ potential can be measured at a pH region where the membrane's charge is positive (the case of nPAAms in water). If adsorption of the negative NaPSS occurs, then the ζ potential will inverse to negative values. The technique is sensitive only on the charges fixed at the internal surface of the pores of the membrane, thus the contribution from the top and bottom surface can be neglected. Moreover, the adsorption can be monitored in-situ, thus giving information on the kinetics of the adsorption.

The nPAAMs used for adsorption studies were presented in Chapter 3. They were studied by streaming potential measurements and their charge dependency on the pH was extracted. Solutions of NaPSS were prepared at 50mM KCl of added salt and with concentration of the polyelectrolyte ranging from 0.014 g/L to 1.4 g/L. Before each measurement, the streaming potential of the bare membrane was measured inside the solvent to verify for the expected charge (positive in water and negative in phosphate buffer).

In Figure 4.7, the ζ-potential is monitored with time for a membrane in a water solution of NaPSS of 0.14 g/L in 50mM KCl. At this pH the membranes ζ-potential is positive and for the measured membrane the value was 15 $\pm$ 1.5mV. As it can be seen, the membrane's ζ-potential gradually reverses from positive to negative, until it is stabilized to -20mV. This

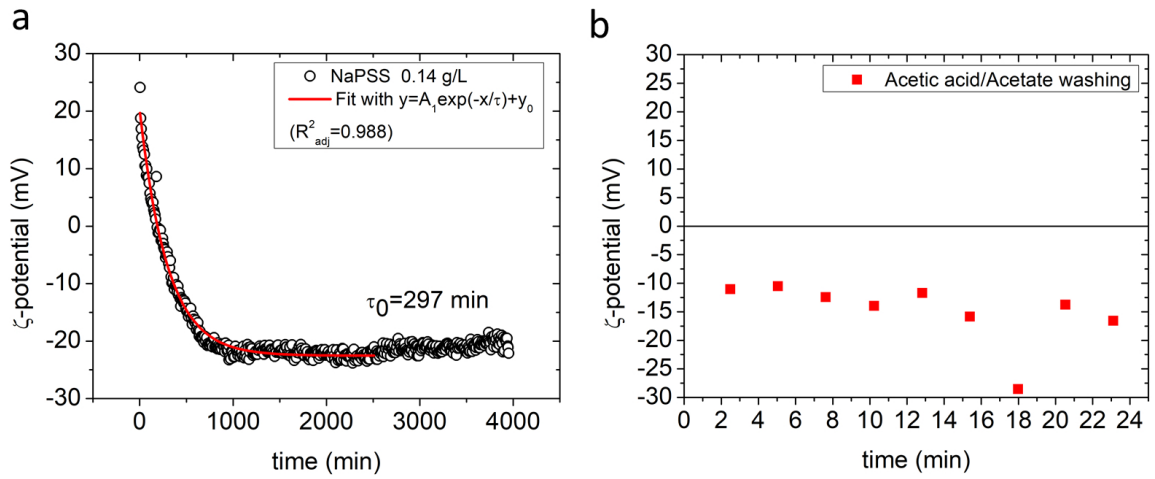

Figure 4.7: a) ζ-potential as a function of time of a nPAAM in NaPSS at 0.14 g/L in water solution with 50mM added KCl. b) ζ-potential of the same membrane after washing with Acetic acid/Acetate buffer at pH=4.

indicates the adsorption of the negatively charged NaPSS chain. The fitting of the data with an exponential decay equation (4.3), gives a characteristic adsorption time of 297 min.

$$\zeta = A_1 exp - \frac{t}{\tau_0} + \zeta_{plateau} \tag{4.3}$$

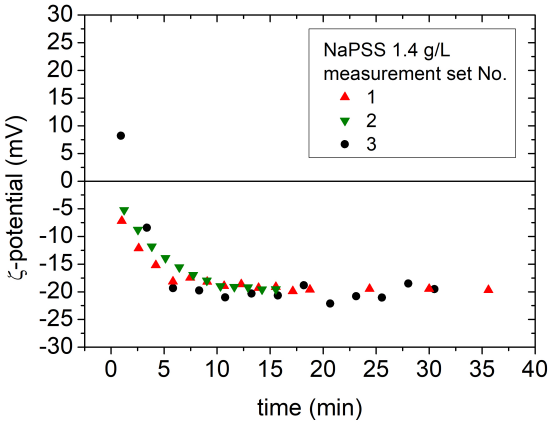

Figure 4.8: ζ-potential adsorption kinetics of NaPSS in water 50mM KCl at 1.4 g/L for three different nPAAMs.

The adsorption is reproducible as seen in Figure 4.8 .The adsorption of 1.4 g/L NaPSS with 50mM added salt in nPAAM follows the same kinetics for three different nPAAMs prepared with the same anodization conditions.

Right after the adsorption experiment of NaPSS, the cell was filled with Acetic acid/Acetate buffer of pH=4 and the ζ-potential was measured again for a period of 24 min. The measured value was -10 mV, indicating that the polyelectrolyte is irreversibly adsorbed on the pore surface. The ζ-value increases from -20 mV to -10mV, suggesting either some desorption of loosely adsorbed chains or modification of the conformation of the adsorbed layer.

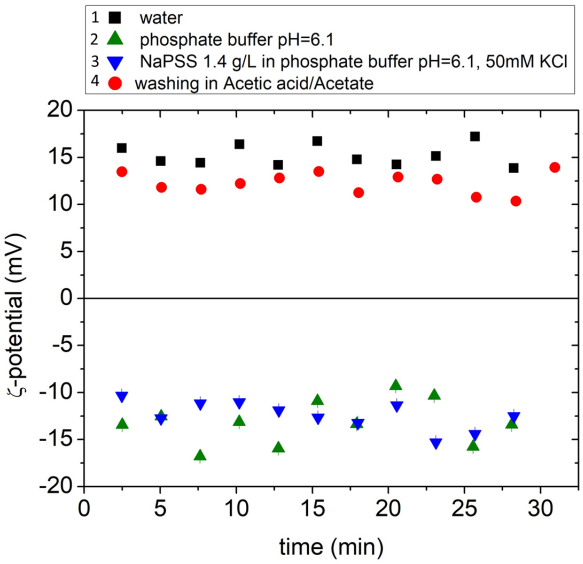

Figure 4.9: ζ-potential as function of time for nPAAM measured in the following solutions in sequence: water+50mM KCl(black squares), phosphate buffer+50mM KCl (pH=6.1) (green,verse triangles), NaPSS 1.4 g/L in phosphate buffer (pH=6.1)+50mM KCl(blue inverse triangles), Acetic acid/Acetate buffer (pH=4) (red circles).

In Chapter 3, it was shown that the nPAAM is negatively charged when the phosphate buffer is used. The ζ-potential was monitored for a nPAAM in a solution of NaPSS 1.4 g/L in phosphate buffer at pH=6.1 with 50mM KCl and is shown in Figure 4.9 (blue,inverse triangles). The ζ-potential remained negative as in the case of bare membrane in phosphate buffer (green, triangles). When the membrane was then measured in the acetic acid/acetate pH=4 buffer solution, the ζ-potential inverted to positive values, indicating that no NaPSS adsorption took place.

All the adsorption kinetics are done under pressure which means that the chains are subjected to shear stress when they are adsorbed on the surface. To see the effect of the shear stress, a nPAAm was left inside the measurement cell with a solution of 0.36 g/L of NaPSS. After some minutes a measurement was performed and the system was left again at rest. The experiment continued in the same way by measuring at different time intervals that reached several minutes. The two graphs of ζ-potential as a function of time are shown

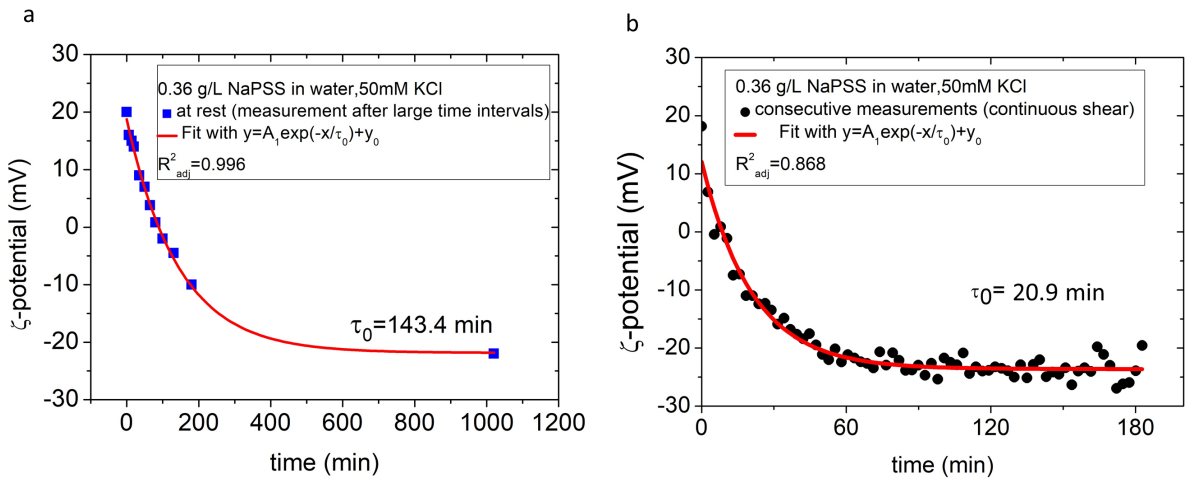

Figure 4.10: ζ-potential as a function of time of a nPAAM in NaPSS solution of0.36 g/L with 50mM added KCl a) at rest. b) under continuous pressure.

in Figure 4.10. It can be seen the sample left at rest shows 4 times slower kinetics. The applied pressure reaches 0.3 bar and can affect the penetration of the chains at the pore entrance.

From all the measurements performed at different concentrations of NaPSS in water with 50mM KCl, the characteristic time τ_0 was derived by fitting with an exponential decay function given by equation 4.3. In Figure 4.11, the ζ-potential vs time is plotted for all the given concentrations of NaPSS. For all the concentrations the charge inverses except for the lowest concentration at 0.014 g/L which doesn't tend to negative values. The fitting of this sample results in an amplitude of A_1=5.1mV but the coefficient of determination R^2_{adj} is low, thus longer experiments are needed to conclude (Table 4.3). The characteristic time as a function of concentration is shown in Figure 4.12 and it can be concluded that there is a dramatic increase on the characteristic adsorption time as concentration of NaPSS decreases, specially for the concentrations below 0.64 g/L. It can be observed that the plateau value of the ζ-potential is constant within the error of the measurement (Figure 4.13).

In order to gain a better insight on the result and the dependency of the adsorption on the concentration, information of the size of the chain should be examined in both the bulk and in the adsorbed layer. From Dynamic Light Scattering (DLS) measurements the hydrodynamic diameter D_H was determined for different concentrations of NaPSS 70kDa with 50mM KCl added salt (Table 4.4). The determined diameter is about 22 nm and is constant for the three measured concentrations, consistent with the fact that we are below c^*. The pore diameter is 40 nm, thus on average, no geometrical constraint is imposed on

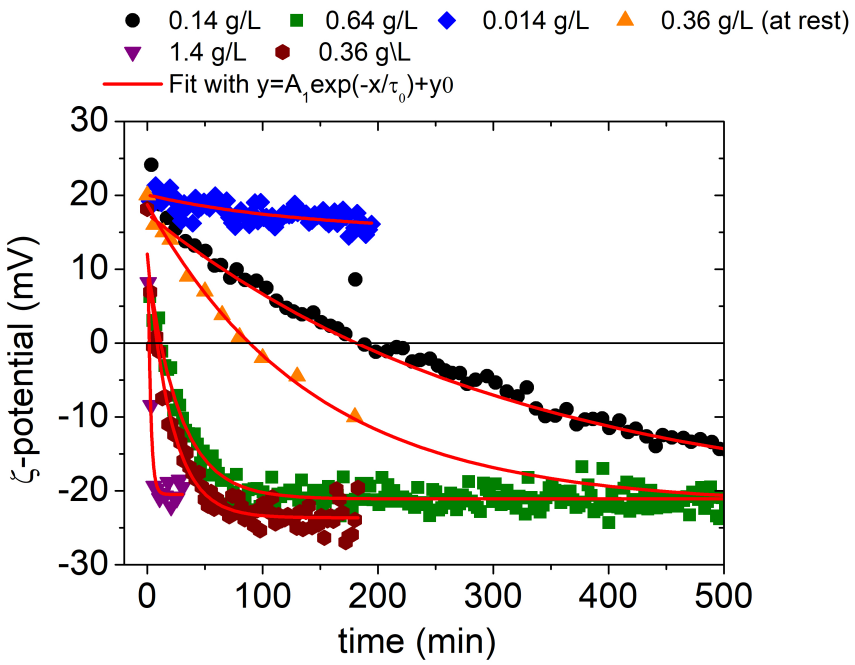

Figure 4.11: ζ-potential as a function of time of a nPAAM measured in NaPSS solution with 50mM added salt for different concentrations. Sample noted as "0.4 g/L (at rest)" (orange triangles) was measured with large time intervals.

the chain from the pore entrance. The physical process that determines the adsorption rate and its dependency on the concentration takes place inside the channel.

c (g/L)	A_1 (mV)	τ_0 (min)	R^2_{adj}	$\zeta_{plateau}$ (mV)
0.015	5.1	138.8	0.609	14.9
0.14	42.7	297	0.988	-22.5
0.36	35.7	20.9	0.868	-23.6
0.36 (at rest)	40.6	143.4	0.996	-21.8
0.64	31.9	27.8	0.89	-21.1
1.4	43	2.3	0.963	-20.5

Table 4.3: Derived fitting parameters of ζ-potential as a function of NaPSS concentration. The good agreement of the fits with the experimental data is given by the R^2_{adj} square.

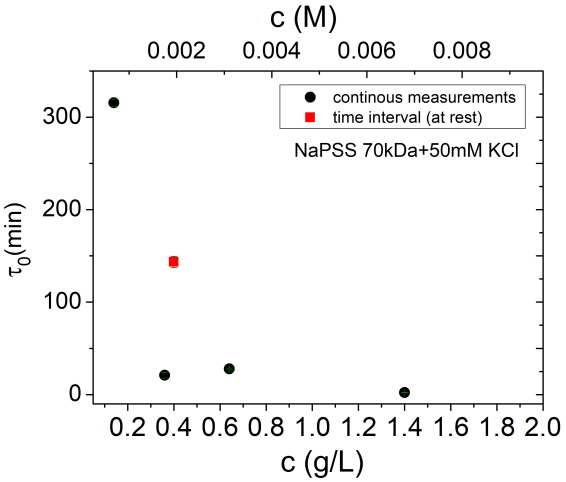

Figure 4.12: Characteristic time τ_0 as a function of concentration of NaPSS solution in water with 50mM KCl determined by streaming potential.

c $\times 10^{-3}$(M)	c (g/L)	D_H (nm)	polydispersity
6.8	1.4	22.3	0.37
2.2	0.46	22.3	0.41
0.41	0.091	22.6	0.39

Table 4.4: Hydrodynamic diameter D_H for NaPSS 70kDa with 50mM added KCl, at different concentrations.

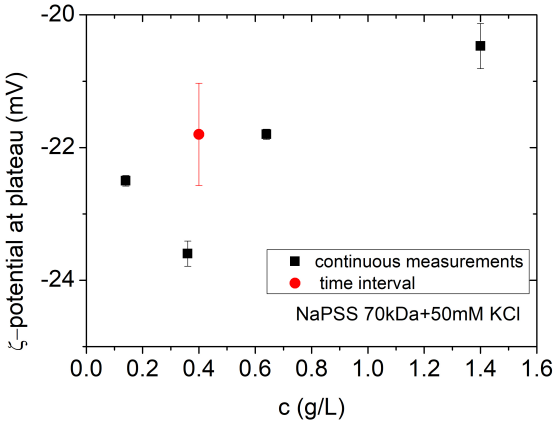

Figure 4.13: ζ-potential value at the plateau of a nPAAM, as a function of concentration of NaPSS 70 kDa solution with 50mM added salt. Measurement with time interval of several minutes (red triangle).

4.4 Description of the flow measurements

4.4.1 Implementation of flow measurements on nPAAMs for examining the adsorption of nPAAMs

One experimental technique that can provide information on the adsorption of NaPSS inside the nPAAMs and under certain assumptions can give the thickness of the adsorbed layer is the measurement of the flow rate of a solvent passing through the membrane. The method has been used in order to measure the diameter of the pore in nPAAMs [163]. Furthermore, for polymer brushes formed inside nanopores the method has been extended to derive the thickness of an adsorbed layer in different solvent conditions by [164]. The last method provides also with a very helpful graphical representation of the experimental results. The method will be applied for bare membranes in order to derive the pore radius and then for membranes that have been used in adsorption experiments of NaPSS, including the ones used in the ζ-potential.

The experimental device is schematically depicted in Figure 4.14 with numbers indicating each element. The teflon cell is pushed at the end of a glass tube, 200 cm in height and graduated every 2 cm. The cell comes with plastic cap inside which the membrane is mounted, sandwiched between two teflon rings. All contact points between the different pieces is achieved by o-rings. The cap is screwed gently on the cell and sealing is established.

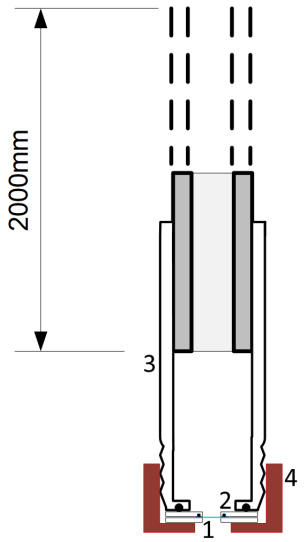

Figure 4.14: Schematic representation of the set-up used for flow measurements (1: membrane, 2: teflon rings, 3: teflon cell, 4: cap.)

The tube is filled up to 158 cm with a solvent that flows through the membrane due to

gravity. The macroscopic flow rate can be calculated by measuring the time needed for the level of the fluid to drop a height of 2 cm on the tube. The macroscopic flow rate Q_{macro} is described by:

$$Q_{macro} = \frac{dV_{macro}}{dt} = \pi r_{tube}^2 \frac{dh}{dt} \tag{4.4}$$

where,

- Q_{macro}: the volumetric flow rate
- r_{tube} : the radius of the tube
- dh/dt : velocity of the drop in the level of the fluid

The flow Q through a cylindrical channel is described by the Hagen-Poiseuille equation 4.5.

$$Q = \frac{\pi R^4}{8\eta L}\Delta P = \frac{\pi R^4}{8\eta L}\rho g h \tag{4.5}$$

where,

- R: tube radius
- η: viscosity of the solution passing through the channel
- L: length of the channel
- ρ: density of the solution
- g: gravitational acceleration
- ΔP difference in pressure between the two ends of the tube

The equation holds for laminar flow inside the pore, which is justified by the low Reynolds number R given in the following relation,

$$R = \frac{QD}{\nu A} \tag{4.6}$$

where,

- Q: volumetric flow rate
- D: hydrodynamic diameter

- ν: the kinematic viscosity
- A: the cross sectional area of the tube

The Hagen-Poiseuille equation can be applied in the case of nPAAMs. Due to the monodispersity in the pore radius distribution of the nPAAMs each pore can be seen as a channel with radius R_p and length L which is the membrane's thickness. The total volumetric flow rate of the membrane will be given by multiplying equation 4.5 by the number of pores N that are exposed to the flow of the solution. Thus, knowing the effective area S of the membrane and substituting the transmembrane pressure with the hydrostatic pressure, the relation transforms to equation 4.7.

$$Q_{pore} = N\frac{\pi R_p^4}{8\eta L}\Delta P = nS\frac{\pi R_p^4}{8\eta L}\rho g h \tag{4.7}$$

with

- h: the height of the level of the fluid.
- n: pore density (cm^{-2})
- S: the effective area of flow through the membrane

The observed macroscopic flow rate (equation 4.4) should equal the flow rate described by the Hagen-Poiseuille relation for flow through the pore channels (equation 4.7). This yields the following expression,

$$\pi r_{tube}^2 \frac{dh}{dt} = \frac{nS\pi Rp^4}{8\eta L}\rho g h \tag{4.8}$$

According to [164], seperation of variables and integration, the following is obtained,

$$-ln(h/h_0) = \frac{nSR_p^4\rho g}{r_{tube}^2 8\eta L}t \tag{4.9}$$

with t the time needed for the level of the fluid to drop to a height equal h. The effective area S is given by the size of the o-ring of the teflon rings. This effective diameter D_{eff} is determined by,

$$D_{eff} = I.D + w \tag{4.10}$$

where

- I.D: nominal internal diameter of the o-ring

- w: the thickness of the o-ring

The effective area S was determined experimentally by measuring the surface of an imprint left on the membrane after passing a dilute dye solution. Note that depending on the sample size, S can be changed by changing the size of the O-ring.

The equation 4.9 is of the form of a linear equation of the type y=Ax from which the pore radius R_p can be derived from the slope.

4.4.1.1 Flow measurements on bare nPAAMs

In this section an example of the flow measurement will be presented for bare nPAAMs detached from the Al substrate. In Figure 4.15 the SEM image of a nPAAM prepared in oxalic acid and detached is shown. As shown in Chapter 1 , the detached membranes present an asymmetry between the top and the bottom surface which seems to be only a surface effect. The pore diameter of the two sides (top, bottom) is shown along with the other geometrical characteristics of the nPAAM in Table 4.5.

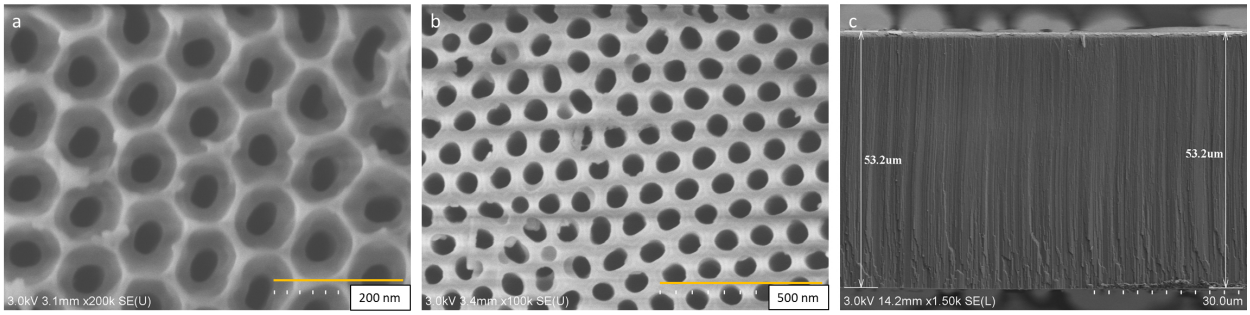

Figure 4.15: Membrane prepared in oxalic acid, detached for flow measurements a) top surface b) bottom surface c) section.

sample	R_p top nm	σ nm	R_p bottom nm	σ nm	n*10^{10} pores/cm^2	L µm
OF1	22.1	3	33	3.7	1	53

Table 4.5: Geometrical characteristics of the sample "OF1" derived from SEM images

The membrane is mounted inside the cell and tubed is filled up with pure water. A chronometer is used to record the time at each graduation. The first graduation corresponds to time t=0 s. At the end the experimental data consist of two columns *time(s)* and *height(cm)*. Throughout the experiment the temperature is recorded with a thermometer.

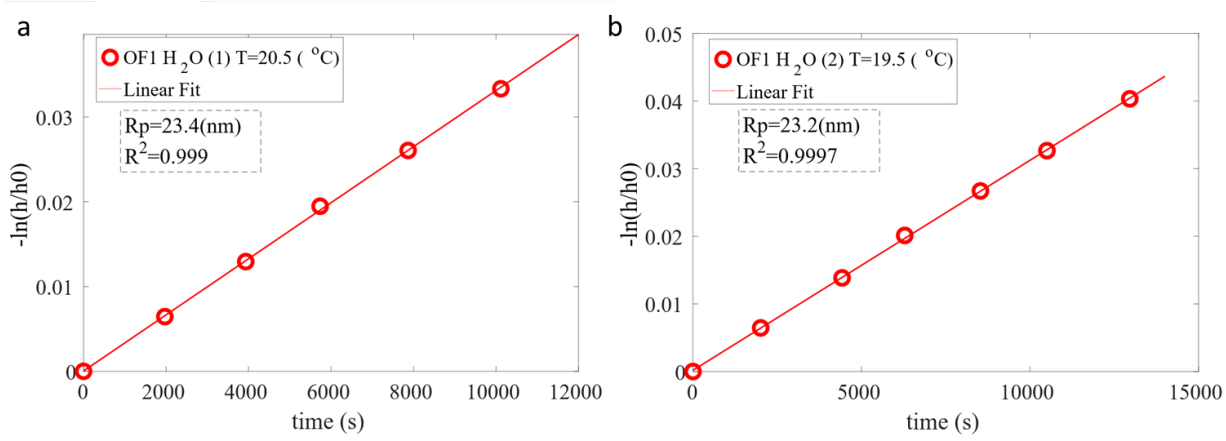

Figure 4.16: Experimental curve for flow of water through nPAAM sample "OF1" a)Experiment No1 b) Experiment No2.

The height used for the calculations is increased by 5.6 cm which is the additional height from the column's end until the membrane. The tube's diameter and effective diameter of the exposed membrane's surface to the flow for this sample is given in Table 4.6.

tube's diameter cm	D_{eff} cm	extra height cm
0.8	0.94	5.6

Table 4.6: Parameters used for the calculation of the pore radius.

The solvent parameters are presented in Table 4.7. The values for viscosity and density were taken from [165].

solvent	viscosity mPa.s	density g/cm^3	Temperature ℃
water	1.0016	0.9982	20.5

Table 4.7: Water solvent parameters used for the calculation of the pore radius of sample OF1.

In Figure 4.16 the experimental data of flow of water is presented for the sample "OF1" for two measurements . The slope of the fitted data provides a pore radius of R_p=23.4 nm and R_p=23.2 nm with a good correlation R^2. It should be noted that before the second measurement, the membrane was put out of the cell and loaded again. This was done in order to know the repeatability of the measurement due to the loading process. The pore radius is found to be closer to the pore radius of the top surface, as determined from the SEM images (Table 4.5). This confirms that the pore channel is straight and the effect of

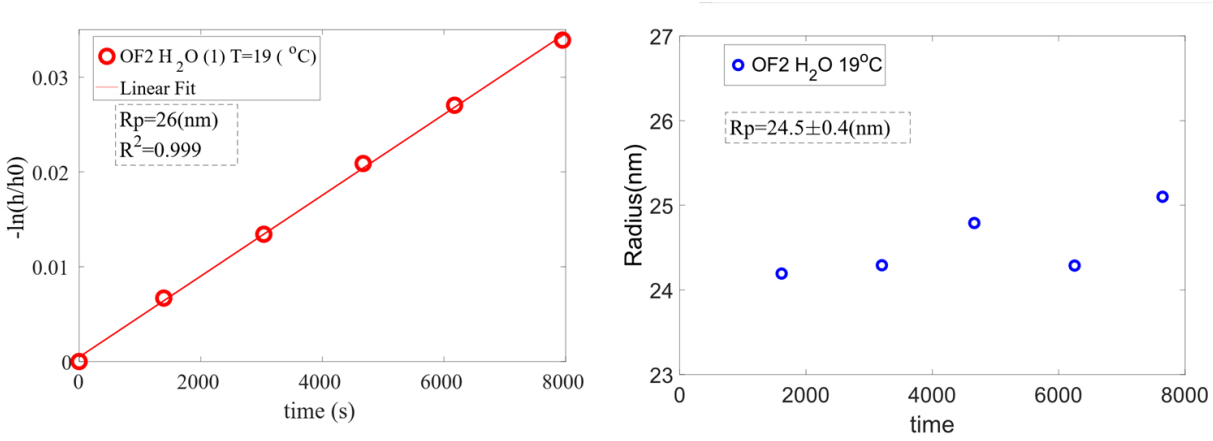

Figure 4.17: Flow of water through nPAAm sample "OF2" a)Experimental curve obtained by continuously decreasing hydrostatic pressure b) Pore radius obtained by measurements at the same hydrostatic pressure drop (constant ΔP) .

enlargement of the pore at the bottom side due to the detachment protocol doesn't proceed deep in the channel.

Measurements can also be performed by keeping the same pressure drop. This is done by measuring the time needed for the solution to drop 1 cm in height, replenishing with new solution the column and start the measurement again. These measurements will be referred to as constant "ΔP". An example is presented in Figure 4.17. The difference between the two techniques is about 6% on the pore radius.

The hydrodynamic radius measured by flow was found to depend on the passing solvent. In Figure 4.18 the pore radius evolution with time derived from flow measurements at constant ΔP is plotted for different solvents. Each experiment was made by a piece coming from the same nPAAm prepared in oxalic acid. In all the solvents, the initial pore radius decreases with time until a constant pore radius is measured. The decrease takes place in the first 40 minutes for water and toluene and reaches about 1.5 nm. For DMSO, the decrease take place in longer times (about 2 hours) and reaches 3 nm with large fluctuations. This result needs more experiments to elucidate whether it is due to swelling or changes in the surface chemistry of the pore wall. Another observation is that depending on the pore radius, the radius measured by SEM is lower than the one measured with flow of solvents (Figure 4.20b).

Since flow measurements provide a hydrodynamic pore radius, the pore size derived from SEM might differ. The Hagen-Poiseuille equation is based at the boundary condition of zero fluid velocity at the pore/solution interface. However, the surface chemistry of the pore and its interactions with the flowing medium might change this condition. The flow that is

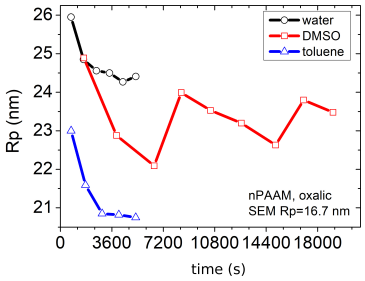

Figure 4.18: Evolution of the pore radius measured by flow in different solvent on three pieces coming from the same nPAAM prepared in oxalic acid. (constant ΔP) .

governed by the non zero velocity at the pore walls while the velocity profile remains laminar is known as slip flow and is presented in the scheme of Figure 4.19.

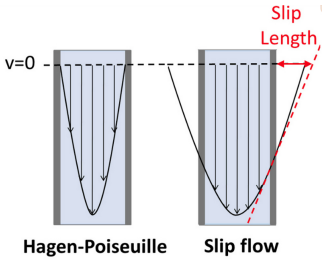

Figure 4.19: Scheme taken from [166]. Left: Parabolic velocity profile corresponding to Hagen-Poiseuille flow of a fluid inside a pore (boundary condition v=0 m/s at the pore/solution interface). Right: Slip flow, with boundary condition $v \neq 0$.

Slip flow is usually studied by flow of different solvents on as prepared or modified pore channels.

If the pore radius obtained by SEM R_{SEM} can be corresponded to a Hagen-Poiseuille flow, then the experimental results show an enhanced flow. The factor of enhanchement is given by the ratio of the two flow rates which yields to:

$$\epsilon_{flow} = (\frac{R_{flow}}{R_{SEM}})^4 \tag{4.11}$$

where R_{flow} is the radius taken from flow measurements.

In Figure 4.20b the pore radius from SEM and flow are compared. It can be observed that there is a tendency to deviate from the 1:1 ratio. The enhancement factor for experiments performed in water, toluene and DMSO is plotted as a function of the SEM pore radius is shown in Figure 4.20a . As one can see, for the water there is an increase in the enhancement factor with a decrease in the pore radius as already observed [167].When the solution becomes

apolar, ϵ decreases, indicating that flow enhancement greatly depends on the interaction between the solvent and the nPAAMs. More data is necessary to confirm this effect.

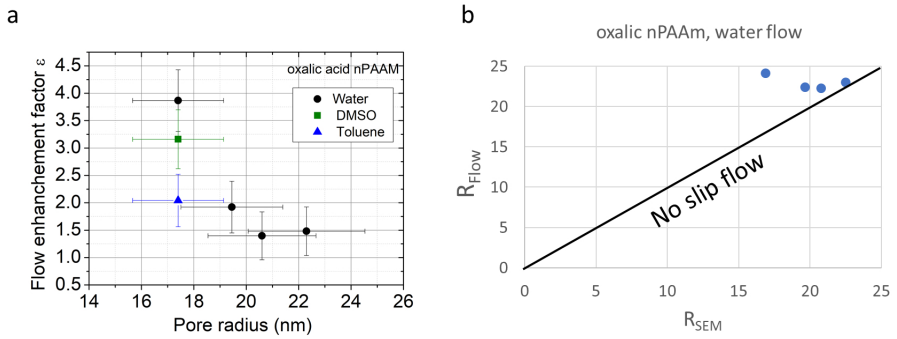

Figure 4.20: a)Flow enhanchement as a function of pore radius b) Radius measured with flow (R_{flow}) as a function of the radius measured by SEM R_{SEM} using the constant ΔP method.

4.4.1.2 Membranes with polyelectrolyte

Similar flow measurements were performed on commercial nPAAMs of Whatman-Anodisc of nominal pore diameter $D_p = 0.2$ µm and thickness 60 µm. Moreover, the adsorption of NaPSS of different concentrations was tested. First, flow measurements of different bare membranes were performed in water in order to check for the reproducibility in the derived pore radius. Then, a membrane was incubated inside NaPSS solution and let for 30 min.

The membrane was taken out of the solution, washed with water and placed in the flow tube for measurements with water. The flow measurement started directly and no time was left for the membrane to dry except for one membrane. For every drop of 1 cm in the level, its duration was recorded, a pore radius was derived and plotted versus the experiment's time. The plot in Figure 4.21 shows the evolution of the pore radius with the time while water flows through the channels. It can be seen that the pore radius for all the membranes is lower than for the bare and it evolves until it reaches a plateau. Certain differences exist between the samples. For the sample noted as "135 g/L (dry)" the initial radius is higher than the final at the plateau. The initial radius is close to the one for the bare membrane (128 nm) and it gradually reaches a radius of 118.5 nm. Unlike the rest of the samples, the membrane was left to dry before the flow experiment so the initial state of the polyelectrolyte chains is dried and collapsed on the alumina pore surface. As water flows, with time the chain is swollen back to a certain thickness while all the non adsorbed chains are removed. For the sample that was not let to dry, for the same NaPSS concentration 135 g/L, the

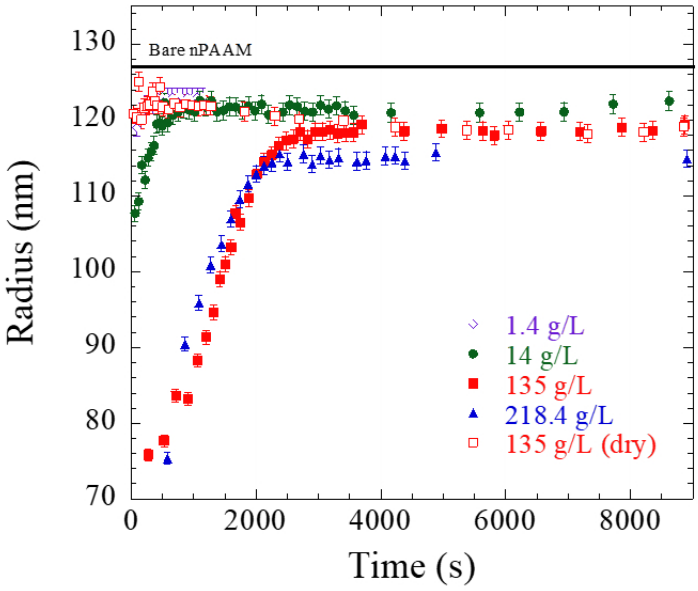

Figure 4.21: Evolution of the pore radius measured by flow of water, of Whatman-Anodisc membranes (nominal D_p = 0.2 µm) after their incubation in NaPSS solution of different concentrations. (constant ΔP) .

initial radius is quite small and quickly rises up to the same plateau value of 118.5 nm . All the membranes measured in wet state follow the same trend, thus it can be understood that chains that are not adsorbed are washed away by the water and only the adsorbed layer remains when the plateau in the radius is reached.

In Table 4.8 the NaPSS chain adsorbed hydrodynamic thickness of the adsorbed layer, is given for the four different concentrations , assuming an homogenous coverage of the pore surface.

NaPSS 70kDa c (g/L)	Pore radius nm	thickness h (nm)
1.4	123	3.7 ± 2.5
14	121.4	5.3 ± 2.5
135	118.5	8.3 ± 2.4
218	115	11.8 ± 2.4

Table 4.8: Hydrodynamic adsorbed layer thickness of NaPSS inside Whatman-Anodisc (average experimental pore radius R_p=126.7 nm)for three different concentrations.

A different type of experiment was tried, one in which the flowing solution contains the

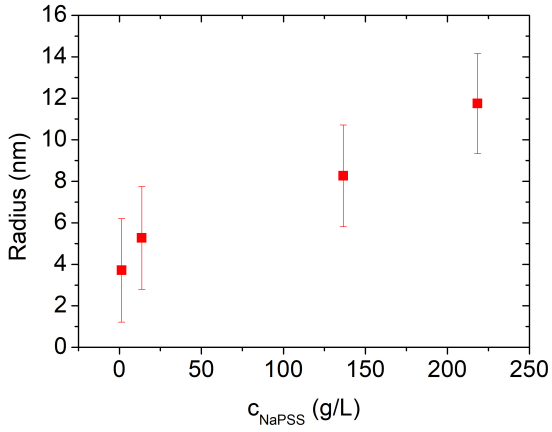

Figure 4.22: Hydrodynamic thickness of layer derived from experiment presented in Figure 4.21.

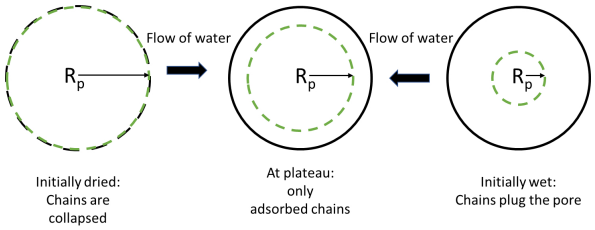

Figure 4.23: Schematic representation of the pore seen from the top with NaPSS chains in dried or wet condition after washing .

polyelectrolyte. This can be considered as an in-situ adsorption experiment. Two polyelectrolyte solutions where prepared at 1.35 g/L with two different solvents, one with pure water and one in phosphate buffer, both at the same pH (pH=6.2). In Figure 4.24a, the pore radius derived from flow measurement is plotted as a function of the measuring time. For the nPAAM measure in water solvent, the pore radius for each measurement is derived by measuring the time needed for the level to drop from 150 to 148 cm (constant ΔP measurement). It is observed that as the time increases, a decrease in the pore radius is observed. After about 3750 seconds, the column is emptied from the NaPSS solution and is filled with water to perform again the same measurement. It can be seen that the pore radius is increased again until reaching a plateau at 3.3 nm below the initial pore radius of 126.7 nm. The first part of the experimental curve can be explained by the following processes:

- Diffusion of the negative polyelectrolyte at the pore wall and adsorption on the positive wall top and internal surface. After adsorption the surface gets negatively charged thus

preventing from further adsorption of chains.

- Accumulation of the incoming negative on the top of the membrane due to hydrostatic pressure and electrostatic repulsion by the adsorbed polyelectrolyte layer. The non adsorbed chains cannot diffuse into the solution due to the continuous incoming of more chains.

After removal of the NaPSS solution and filling with solvent, the non adsorbed chains can diffuse in the pure water solvent and transported through the pores, until the pore remains only with the adsorbed layer. This stage corresponds to the second part of the curve where the pore radius increases up to a certain value (red squares in Figure 4.24).

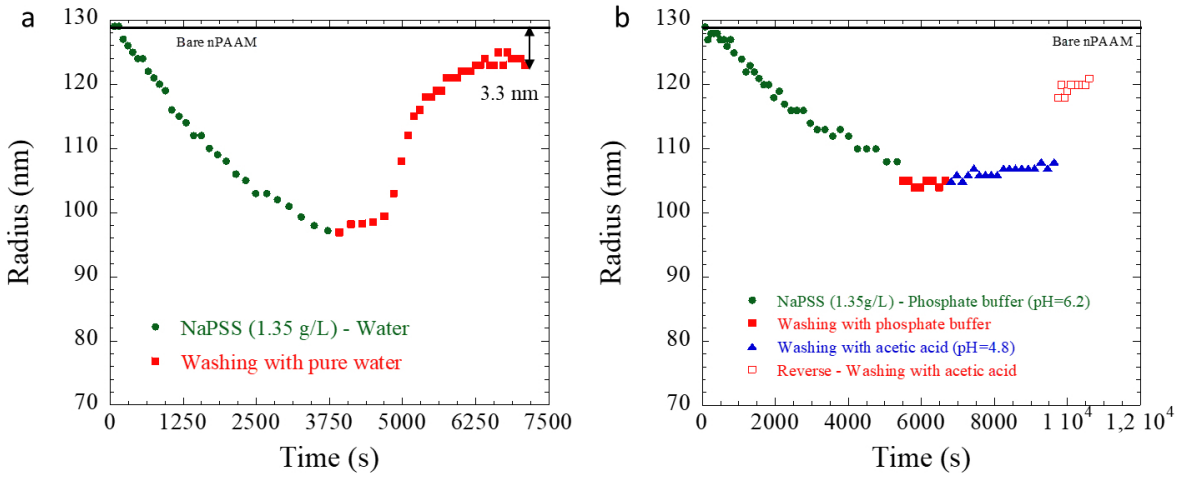

Figure 4.24: In situ adsorption of NaPSS 70kDa solution at 1.35 g/L and subsequent washing with solvents a) in water (green circles), washed in water (red squares) b) in phosphate buffer (green circles), washed with phosphate buffer, washed with acetic acid, reversed the membrane-washed with acetic acid (empty red squares).

For the NaPSS solution in phosphate buffer, the solution was let to flow and at each graduation the time was recorded. From each experimental point the pore radius was calculated and the situation is similar. The pore walls are negatively charged and the chains start to accumulate due to repulsion from the negative surface and transportation of chains due to the flow (Figure 4.24b) . The tube is emptied and the membrane is washed with phosphate buffer solution for some minutes where the pore radius remains constant for the same amount of time as in the case of the water solvent. Then buffer of acetic acid is passed through the membrane and the chains start to diffuse in the solution and through the pore resulting in the increase of the pore radius but much slower than in the case of the water solvent. This

adsorption during	c (g/L)	Pore radius bare nPAAM (nm)	pore radius after adsorption (nm)	Difference (nm)
streaming potential measurement	0.14	22.3/22.4	22.5	0.15
	0.36 (at rest)	22.6	23	0.4
	0.64	223.3/22.4	23.1	0.75
incubation in solution for 50 min	0.64	22.3/22.4	22.4	0

Table 4.9: Table with derived pore radius from flow measurements in bare nPAAMs and after adsorption of NaPSS of different concentrations.

might be the effect of adsorption of polyelectrolyte because there was not enough time to be washed by the previous phosphate buffer and now in acetic acid, the walls are positive, thus facilitating the adsorption inside the channel while washing. Finally, reversal of the membrane brings about the abrupt increase in the pore radius which confirms the plugging effect of the pore on the top surface due to the accumulation of chains. A simple model for this process is provided in Figure 4.25.

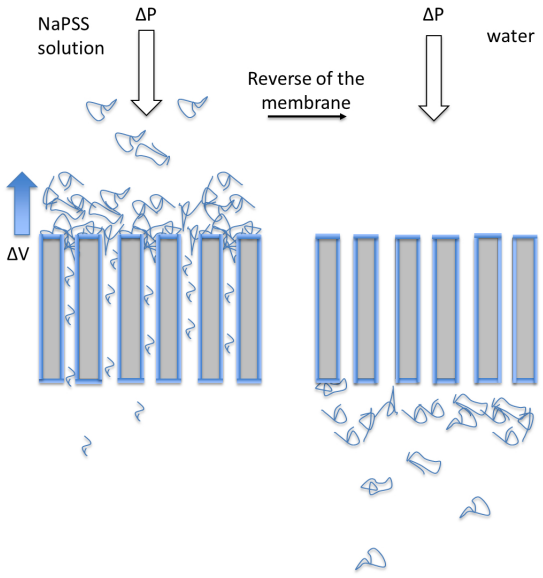

Figure 4.25: Scheme model of the plugging of polyelectrolyte chains due to accumulation at the top surface of the membrane.

The samples that were used for adsorption kinetics by streaming potential were also measured with flow in pure water and compared to pieces of the same membrane without polyelectrolyte.

Moreoever, another membrane was immersed in NaPSS solution of 0.64 g/L with 50 mM

added salt for 50 min and measured after with flow. The results are shown in Table 4.9. It can be seen that no significant difference in the pore radius is detected. As the results from streaming potential measurements indicate adsorption, the results from flow measurements could be explained by low surface coverage of the polyelectrolyte chains whose adsorbed layer is not enough to create a hydrodynamic measurable thickness or NaPSS chains adopt a flatten conformation of the nPAAM surface.

4.4.2 SANS measurements on nPAAMs with NaPSS

Through flow measurements and streaming potential the adsorption of polyelectrolyte chains was studied. No polyelectrolyte adsorption took place when the membrane was charged negatively inside a phosphate buffer solution while irreversible adsorption was observed for the membrane immersed in water solution (positive walls). Still, the two techniques alone cannot provide information on the density profile of the polyelectrolyte inside the pore under positive or negative conditions. To answer this question, SANS was performed on nPAAMs with different pore diameter, with positively or negatively charged walls.

One major issue in the SANS experiment is that the scattering intensity of the system nPAAM with polyelectrolyte is that there is residual scattering of the nPAAM even at the best matching conditions. In Figure 4.26 the SANS spectrum of the NaPSS solution at c=135 g/L is shown in water and in phosphate buffer solution (pH=6.1) in 73.2% D_2O. The peak at q=0.135 $Å^{-1}$ is related to the characteristic size ξ (here $\xi = 4.6nm$). The size and the peak position is consistent with previous experimental data for NaPSS [168]. As seen in the inlet scheme model of Figure 4.26, the distance ξ is related to the mesh size of the polyelectrolyte entangled conformation in the semi-dilute regime. The increase of the intensity at low q values is due to possible aggregates. Even at this high concentration, the scattering intensity of the polyelectrolyte is below 0.1 cm^{-1}. Due to the low signal, the background subtraction of the samples containing polyelectrolyte is not trivial. The polyelectrolyte is hygroscopic and the amount of water molecules on the chain might change with humidity. Then there is possible exchange between hydrogen on the chain and deuterium of the solvent. Following the approach of [26], the value of the incoherent scattering for the NaPSS solution samples was determined by imposing the scaling relation $I \sim q^{-1}$ at the high q, on the experimental data. This scaling behaviour belonging to rigid rods is expected for polyelectrolytes.

In the following, the spectra of the nPAAMs with and without polyelectrolyte will be compared in an aligned configuration. Then another measuring approach will be used: the tilting of the membrane. Tilting has been already employed in systems with polymers inside membranes. The effect of tilting is to reduce the scattering intensity of the membrane as it breaks the correlations coming from the structure factor *S(q)* [128], [129].

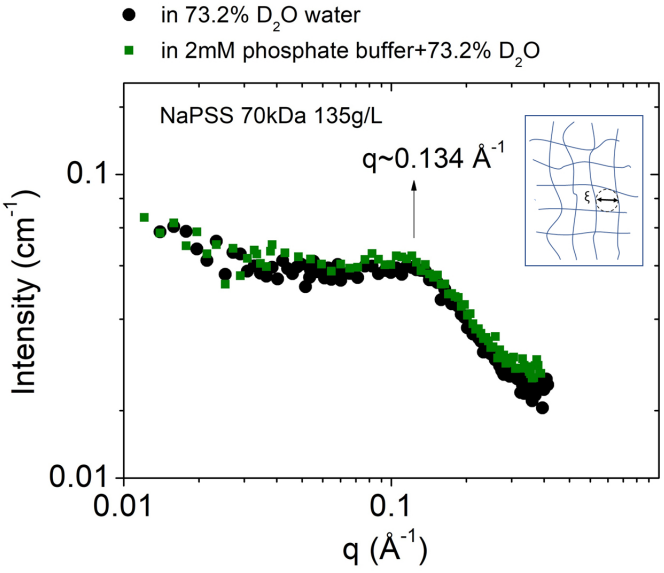

Figure 4.26: SANS spectra of NaPSS solution at 135 g/L in water (black circles) and in phosphate buffer 2 mM (pH=6.1) (green squares). Inlet: scheme model of the characteristic mesh of the polyelectrolyte conformation in the semi-dilute regime.

4.4.2.1 NaPSS in nPAAMs prepared in oxalic acid

In this section SANS spectra will be presented for membranes prepared in oxalic acid and measured with NaPSS 70kDa for positive and negative pore walls. The pore diameter is much larger than the polyelectrolyte's mesh size ξ. All membranes were immersed inside the NaPSS solutions for approximately 30 min prior to any SANS measurements.

In Figure 4.27a a bare membrane immersed in 73.2% D_2O is compared to one immersed inside NaPSS solution at 135 g/L in 73.2% D_2O (corresponding to a NaPSS volume fraction of 7% v}v. Filling of the pores with this solution, creates a contrast difference which results in a different spectrum for the membrane bearing NaPSS. The total scattering length density (SLD) of the polyelectrolyte prepared solution in 73.2% D_2O equals 4.3 $*10^{-6}$ $Å^{-1}$ while the solvent in which the bare membrane was measured was 4.48 $*10^{-6}$ $Å^{-1}$,73.2% D_2O). However, this is the contrast of the polymer bulk solution and the concentration of NaPSS might differ inside the pore. To resolve this the SANS curve with the NaPSS inside the membrane was compared to SANS measurements of the bare membrane measured at different volume fractions of D_2O. The aim was to find at which volume fraction of D_2O the two curves overlap.

As seen in 4.28 it overlaps with the bare nPAAM filled with 67.7% of D_2O corresponding to an SLD of 4.10 $*10^{-6}$ $Å^{-1}$. This SLD gives a a concentration of 310 g/L (1.84 M). It can

be concluded that the there is an increase in the concentration of the electrolyte inside the pore relatively to the bulk solution.

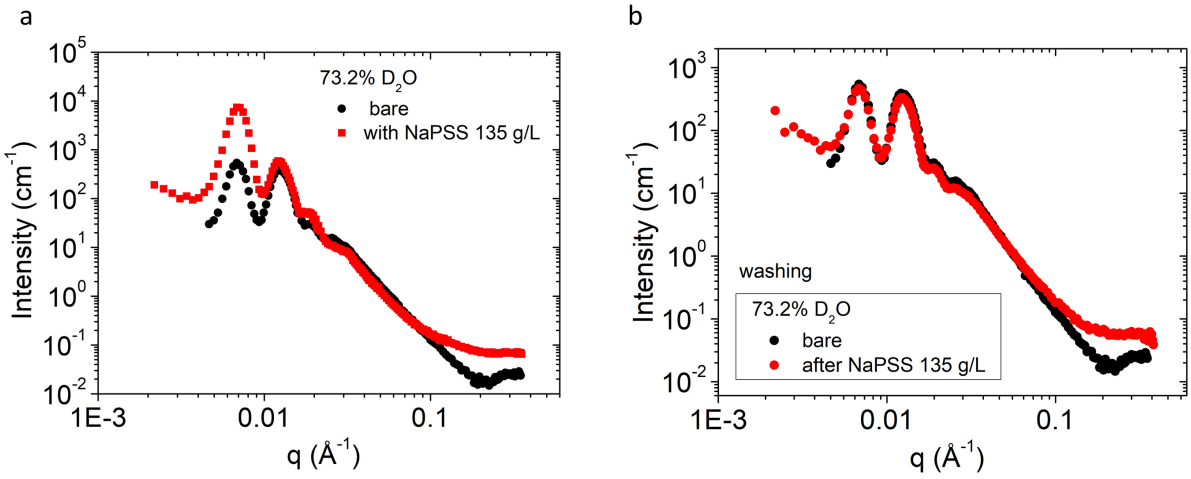

Figure 4.27: SANS curves of nPAAM charged positively in water, with (red squares) and without NaPSS (black circles). a)Bare vs. polyelectrolyte bearing nPAAM (NaPSS at 135 g/L) in 73.2% D_2O b) Comparison of bare membrane with one after the polyelectrolyte has been washed with water, measured in 73.2% D_2O.

The high q region of Figure 4.27 is more difficult to explain as incoherent scattering dominates (mostly due to hydrogen) in this region. The idea was to remove this contribution in order to reveal coherent scattering that can be translated into structure correlations, specially for nPAAMs that will be measured in a tilted configuration. The contributions to incoherent scattering are generally:

- hydrogen atoms in the membrane
- hydrogen atoms from the solvent
- hydrogen atoms from polyelectrolyte

An experimental approach to derive the incoherent scattering is rather complicated. Idealy one has to measure known sets of different thickness and concentration of the polyelectrolyte solutions.

In the following analysis we will try to reveal as much as possible from the polyelctrolyte coherent signal and certain approximations will be made. As seen in Chapter 2 the incoherent scattering of the bare membrane derived from measurements in air, is much lower than for the one obtained from measurements in a solvent. Thus, the incoherent scattering of a membrane measured inside a solvent comes mainly from the solvent. The value is picked

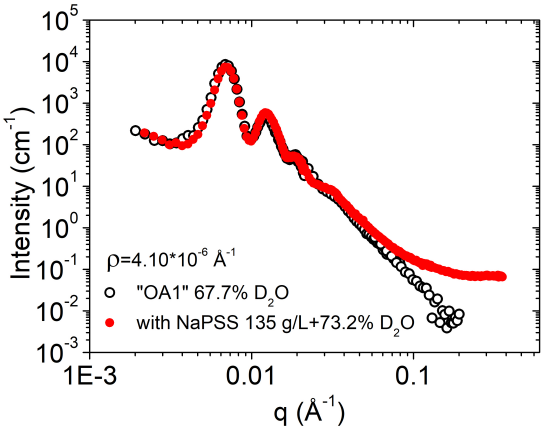

Figure 4.28: Comparison between a SANS spectrum measured in 67.7% D_2O ($\rho_{67.7\%-D_2O}$=4.10∗10^{-6} Å^{-1}) for a bare membrane and the spectrum obtained for a membrane filled with NaPSS at 135 g/L in 73.2% D_2O.

up from the constant part of the curve and subtracted from the data to get a q^{-3} scaling corresponding to the cylinder form factor. Now the contribution of the solvent inside the membrane that contains NaPSS would be modified to,

$$Inc_{NaPSS/nPAAM} = (1 - \phi_{NaPSS}) * Inc_{nPAAM} \tag{4.12}$$

where ϕ_{NaPSS} is the volume fraction of NaPSS inside the pore and Inc_{nPAAM} is the membrane's bare background. The result of the ϕ_{NaPSS} taken from Figure 4.28 can be used for the membranes measured with NaPSS in water. After removal of the above contribution, what remains to the background is the incoherent scattering coming from the polyelectrolyte which for the moment won't be treated.

Coming back to the SANS curve, it can be seen that the intensity is higher at high q for the membrane with the NaPSS, indicating again the presence of the polyelectrolyte inside. Then, the membrane is washed with water and is immersed again into 73.2% solvent for measurement (Figure 4.27b). After washing the low q regions superimposes with the non-filled nPAAM. At high q the scattering intensity of the membrane that has been washed from NaPSS passes over the intensity of the bare, thus, a certain amount of adsorbed chains are still present in the washed sample and responsible for the higher incoherent scattering. As we know from the streaming potential measurements that adsorption takes place, however, the fact that no changes are probed in the low q regions means that concentration of NaPSS in the adsorbed layer close to the wall must be very low or the layer is thin and not detectable by SANS.

It can be understood that the polyelectrolyte's signal is hindered by the nPAAM scattering. As discussed in Chapter 2, full matching is not possible for the bare nPAAMs. One way to reduce the scattering contribution from the membrane is to tilt it. The scattering spectra of an aligned bare membrane and of a tilted one at 13 °are shown in Figure 4.29a where a large decrease in the scattering intensity can be seen. For the tilted sample, note that the scattering data has been normalized using the effective length of the sample, given by equation 4.13,

$$L_{eff} = \frac{L}{cos(13^{\circ})} \tag{4.13}$$

where L the real thickness of the sample.

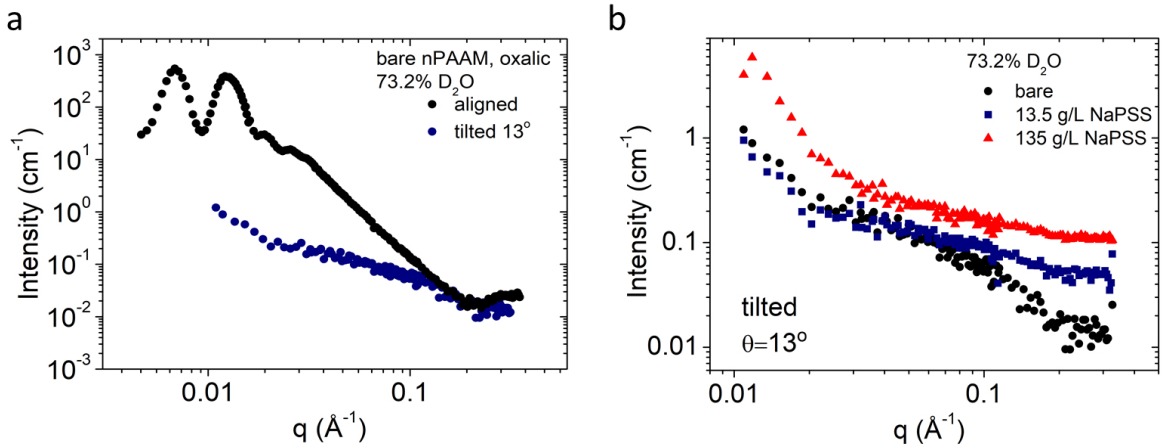

Figure 4.29: a)SANS spectra measured in 73.2% D_2O of an aligned membrane in comparison with a bare nPAAM tilted at 13 . b) Comparison of SANS spectra for bare tilted membranes (black squares) and for nPAAMs filled with NaPSS at different concentrations (13.5 g/L in blue squares, 135g/L in red triangles).

Nevertheless, the polyelectrolyte contribution is still hard to distinguish (Figure 4.29b) even for the highest concentration at 135 g/L. The background of the solvent of the bare membrane was used for subtraction. The washing of the membrane in water and measuring again at 73.2% D_2O results in the curve of Figure 4.30 (green triangles). Once more, the polyelectrolyte is inside the membrane but further than this we cannot conclude.

The situation seems similar in the case of nPAAMs with negative walls. In Figure 4.31 the membrane bearing NaPSS at 135 g/L is compared in 73.2% D_2O and in 2mM phosphate buffer+73.2 D_2O. Some small differences occur mainly in the middle q region, (as seen in the inset), and in the high q region. For the middle q the difference might be due to an adsorbed layer for the membrane having positive walls. At high q the difference is 0.015 cm^{-1} and

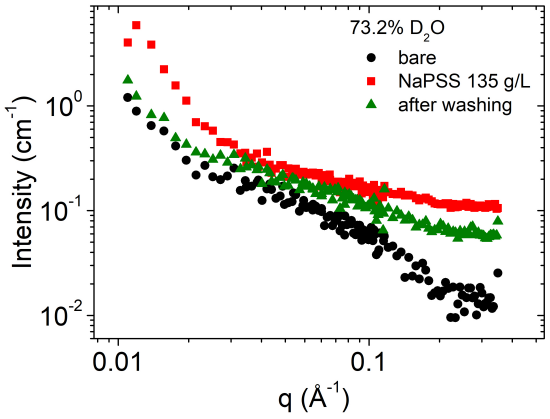

Figure 4.30: Comparison of the SANS spectra of a bare membrane (black circles) to a membrane that has been measured in NaPSS 135 g/L +73.2% D_2O (red squares) and after washing the NaPSS with water (green triangles).

might be due to the presence of residual polyelectrolyte layer on top of the membrane while loading the cells. On average we can say that the concentration of NaPSS is the same inside the pore for both positive and negative walls.

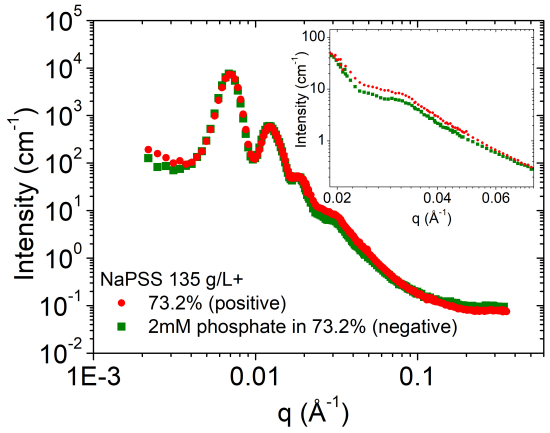

Figure 4.31: Comparison of the SANS curve of the same nPAAM with NaPSS 135 g/L in 73.2% D_2O in positive (red circles) and negative walls (green squares) before washing.

The SANS curves for a membrane with negative walls with NaPSS at 135 g/L is shown in Figure 4.32a. In the graph the curve is compared to a bare membrane that comes from a different sample and was measured at the same solvent. At low q the behaviour is similar to the case of positive walls. The pores are filled with the polyelectrolyte and this creates

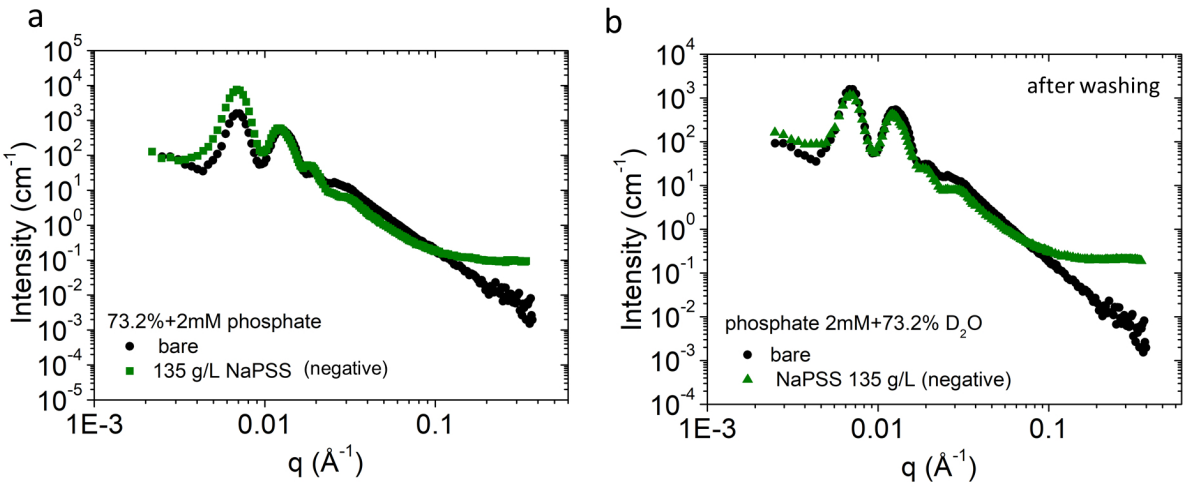

Figure 4.32: a) Comparison of the SANS spectra of a bare membrane and one with NaPSS at 135 g/L, measured at the same solvent of 2mM phosphate+73.2% D_2O. b) SANS spectra of the bare membrane and the one after washing the NaPSS with phosphate buffer, measured both at the same solvent.

a contrast difference that changes the shape of the curve. At high q, the polyelectrolyte's incoherent scattering dominates. Washing of the membrane with phosphate buffer brings the scattering curve back to the bare membrane's shape in the low q region (4.33. At high q there is still incoherent scattering and it can be concluded that some chains are still inside the pore. The SANS spectra of the bare membranes, filled with NaPSS and after washing with phosphate buffer in tilted condition are shown in Figure 4.33. Once more, no coherent signal can be revealed for the membranes with the NaPSS.

4.4.2.2 NaPSS inside nPAAMs prepared with sulfuric and selenic acid

nPAAMs with smaller pore diameters were measured aligned and in a tilted configuration. The nPAAMs were prepared in sulfuric acid and selenic acid as described in Chapter 1. The yielded pore diameter D_p=20 nm for both nPAAMs is similar to the polyelectrolyte size . In Figure 4.34 the SANS results are presented for a membrane prepared in sulfuric acid. It can be seen in the aligned measurement sets that there is a huge decrease in the intensity at low q and that the shape of the curve changes in all the q region. The spectra are similar in water and phosphate buffer: there is polyelectrolyte inside the pores irrespective of the wall charge. Moreoever, at the middle and low q the characteristic dependency I $\sim q^{-3}$ of bare nPAAM gives its place to a q^{-1}. The measurements at a tilted configuration are shown in Figure 4.34b but the data for the membrane with NaPSS in 73.2% D_2O shows lower scattering than for the bare which makes the specific measurement not reliable.

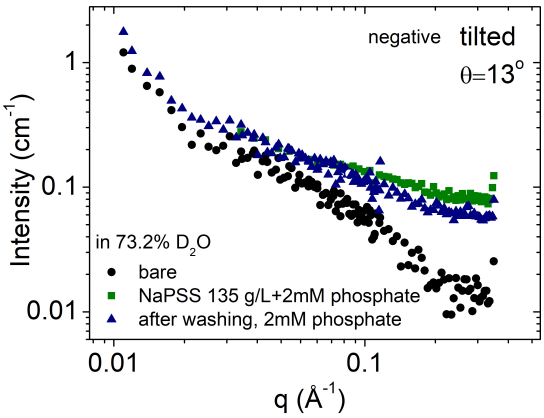

Figure 4.33: Comparison of the SANS curves in tilted condition of a bare nPAAM (black circles), filled with phosphate buffer with NaPSS 135 g/L in 73.2% D_2O(green squares) and after washing with the buffer (blue triangles).

In Figure 4.35 the SANS spectra with and without NaPSS solution are presented for a nPAAM membrane prepared in selenic acid. Two nPAAMs, one measured in NaPSS 135 g/L+73.2% D_2O and the other in the same NaPSS solution with 2mM of phosphate added (negative walls) are plotted together with a bare nPAAM at 70.7%. The solvent at 70.7% D_2O is closest to the total SLD of the NaPSS in 73.2% D_2O and that is why they are compared together. At low q, the shape of the curves for the NaPSS in both positive and negative wall conditions, roughly follows the shape of the SANS curve of a bare membrane measured inside D_2O at 70.7%. The last gives a scattering length density of 4.31 $*10^{-6}$ $Å^{-1}$ which matches the prepared NaPSS solution. Thus, the concentration inside the pore is closer to the bulk solution. Evidently, the huge intensity at high q states that some residual layer of NaPSS has stayed between the nPAAM surface and quartz window of the cell when loading the samples.

4.5 Conclusions on Chapter 4

In this chapter the system nPAAMs filled with NaPSS 70 kDa were studied by different techniques. Permeation of the polyelectrolyte inside the channel takes place in both positive and negative charge of the walls. The pore filling behaviour, as probed by SANS in the low and high q region confirms it. Contrast variation on the bare membranes coupled with measurements with the polyelectrolyte can provide information on the solution concentration inside the pore.

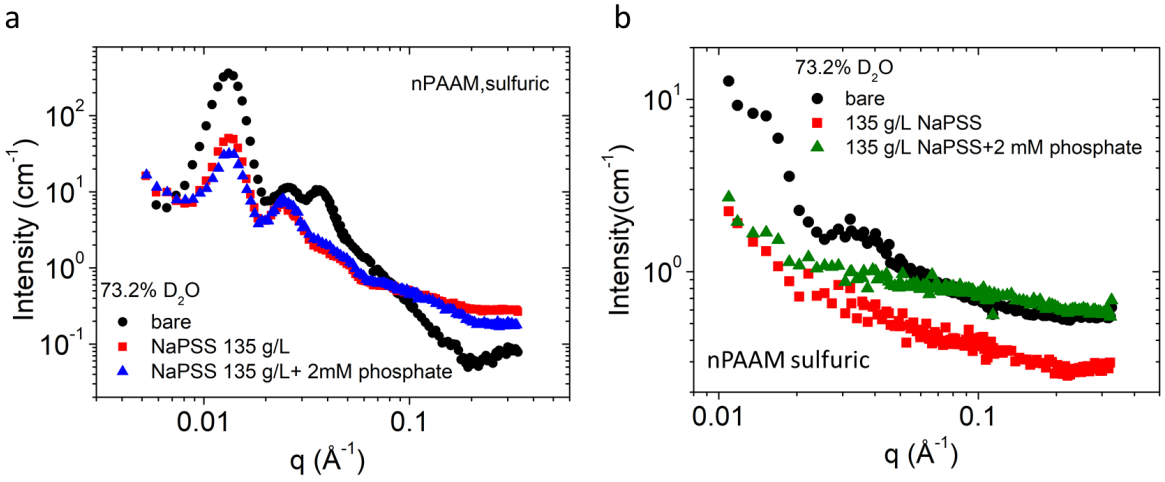

Figure 4.34: Comparison of SANS spectra for a nPAAM prepared in sulfuric acid.a) Aligned configuration: bare membrane (black circles) measured at 73.2% D_2O compared to NaPSS in 73.2% D_2O (red squares) and with NaPSS in 2 mm phosphate buffer (blue triangles). b) Same nPAAM in tilted configuration. Note:no subtraction of the solvent.

The charge of the pore walls determine whether adsorption will take place. Negative wall conditions at a neutral pH, in which the membrane is more stable chemically, can be achieved simply by immersing the membrane in a phosphate buffer solvent. Irreversible adsorption occurs in positive walls and the adsorbed layer can be probed in-situ by ζ-potential measurements. The obtained plots of ζ-potential were fitted with an exponential law and a characteristic time was derived which shows strong dependency on concentration of the NaPSS and the sampling rate. Moreover, the reach of a plateau of the ζ-potential reflects saturation of the available adsorption site except for the very low concentration (0.014 g/L) where more measurements are needed to really conclude.

The results from streaming potential were combined with flow measurements which can probe hydrodynamic size changes of the pore radius when the membrane is immersed in the polyelectrolyte. The flow measurements can be used only for nPAAMs with pore radius larger than 22 nm in the case of nPAAMs prepared in oxalic acid. The surface chemistry of the pore channel governs the type of flow in smaller pore radius. It can induce slip flow which might be different in the case of bare and polyelectrolyte bearing membranes. The adsorbed layer of polyelectrolyte inside pore channels of membranes prepared in oxalic acid (D_p=40 nm) show that the hydrodynamic thickness of the adsorbed layer is at the order of the experimental error of the measurement. For larger pores in commercial membranes (Anodisc-Whatman) and for higher polyelectrolyte concentrations the thickness of the adsorbed layer slightly increases with the concentration of the NaPSS solution and is in the

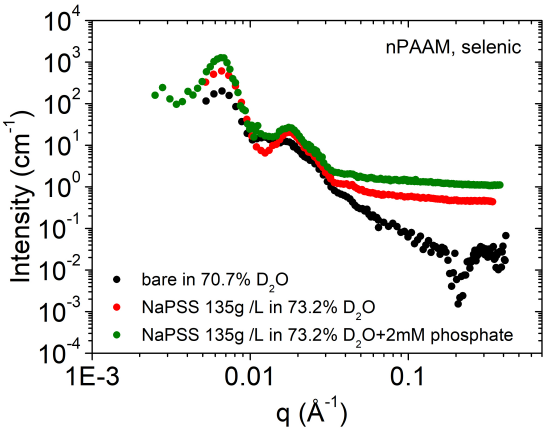

Figure 4.35: SANS spectra of nPAAM prepared in selenic acid (D_p=20 nm) and loaded with NaPSS solution in water 73.2% with (green) and without phosphate buffer (red).

range of 3-5 nm. Plugging effects can occur during in situ adsorption of polyelectrolyte with flow measurements, thus it is preferable to study adsorption of polyelectrolyte by ex-situ measurements.

Last, the density of the polyelectrolyte is very low in the adsorbed layer, something that is also concluded from the SANS measurements. No changes are observed in the spectra at the low q region after washing the NaPSS bearing membrane in water, even if a signal in the high q region exists.

CONCLUSIONS

General Conclusions

In this thesis we aimed at proposing experimental approaches to study the behaviour of polyelectrolytes (PEs) under confinement in a nanoporous medium. To that end, we chose as a confining medium nanoporous alumina membranes (nPAAMs). nPAAMs are obtained through the controlled anodization of aluminum and are composed of high-ratio parallel cylindrical channels with perfectly tunable pore diameters, interpore distances, lengths and porosity. We systematically used different experimental conditions to have access to a wide range of pore diameters and pore arrangement. Additionally we proposed and studied here an original synthesis in deuterated medium to reduce pore diameters down to 13 nm and improve the pore ordering. We also investigated the growth mechanism by the titration of Al^{3+} produced during the synthesis and discussed our results with the different proposed models. We concluded that no other reactions involving charge transfer on the anode (as oxygen evolution) occurred.

One important aspect of this work was the careful characterization of the nPAAMs. To study the behaviour of PE one has to perfectly understand the confining medium. We combined different techniques to characterize the structure and surface charges of the nPAAMs. First, SEM images were used to extract the pore arrangement and to quantify the pore ordering through the structure factor S(q) which can be fitted with an hexagonal model for the well ordered nPAAMs. Then this analysis allow us to use these results to fit the SANS data. During this thesis, SANS was used intensively to understand the structure and the composition of the nPAAMs. We proposed a detailed strategy to measure nPAAMs in optimal conditions. Multiple scattering, which is a side effect encountered for porous materials with high pore density, can be avoided either by decreasing the nPAAM thickness or by measuring it in a solvent mixture close to the "matching point". Using the contrast variation method we showed that the nPAAMs are heterogeneous in composition and can be modelled using a core/shell model. The composition of the nPAAMs was found to vary with the filling solvent, thus wetting of the wall must take place. Through the data fitting we identified the nPAAM length in the fitting model as a critical parameter. We showed that the real length lead to non-realistic results and thus cannot be used in the model. Thus, we propose to fit

using another correlation length. This point is critical since it governs the scattering length densities fitting parameters, i.e. the composition of the nPAAMs. We also probe by SANS the effect of chemical etching, annealing on the nPAAMs and their transformation in water.

Then the surface charge of the nPAAMs was accessed by streaming potential measurements giving the ζ-potential of the nPAAMs. The point of zero charge was determined at a pH of 9. We also pointed out the importance of the buffer solution on the surface charges. By using phosphate buffers we can inverse the sign of the nPAAMs passing from positive in pure water at pH=6 to negative in phosphate buffer at the same pH. This is a convenient way to tune the surface charge. It was found that the nPAAMs present a very low conductance even when the pore radius is larger than the Debye length. Further measurements with buffers of different salt concentration and of varying pH, are needed to understand the reason of such low values.

Finally we propose experimental approaches to study the behaviour of PE. The geometrical constrains and the presence of charges inside the nanoporous medium might modify the PE penetration and conformation. By combining different techniques (FTIR, TGA, streaming potential, flow measurements and SANS) we show that:

- NaPSS penetrates into the nanopores
- Adsorb irreversibly at the surface when the nPAAM is positively charged
- there is an effect of the concentration of NaPSS on the kinetics during adsorption inside the nPAAM
- The thickness of the adsorbed layer can be determined by flow measurements
- Plugging effects are present during adsorption of the PE under pressure

Perspectives Some complementary studies can be proposed to continue this work.

Concerning the synthesis of nPAAMs in deuterated solvent, an exploration of the anodization regimes in D_2SO_4/D_2O can be made in order to find the voltage at which the best ordering occurs. According to the experiments, the voltage should be shifted towards lower values than for the H_2SO_4/H_2O. The deuterated solvent can be used with selenic acid which yields nPAAMs with very small pore diameters. In applications where a high aspect ratio is needed, prolonged anodization will etch the pore. The lower acidity of the deuterated electrolyte can suppress this effect.

Detached nPAAMs prepared with other electrolytes such as selenic and sulfuric are needed for flow and streaming potential measurements with smaller pore diameters For now, some tests were made but their detachment is not yet feasible. Thus, their synthesis has to be

rationalised. The current during the detachement of the nPAAM presents a characteristic evolution with time that needs to be understood. More precisely the questions raised are:

What is the origin of the slow rise in the current during the first seconds of anodization?

When does the 3rd layer, highly contaminated oxide starts to form?

Titration of the Al^{3+} at the different stages determined by the behaviour of the current with time can help in understanding the growth mechanism during the 3^{rd} anodization step. The thickness of the higher contaminated oxide produced at the 3^{rd} anodization step is a crucial parameter. The growth rate can be examined by SEM. Moreover, the use of backscattering electron microscopy might reveal with a higher contrast the difference between the lower and the higher contaminated layers.

The nPAAM can be used for the preparation of a single solid state nanopores that can be used in studies like protein translocation [169]. M. Lillo et D.Losic [170], proposed the use of Focused Ion Beam to remove the barrier layer from one single nanopore.

In collaboration with Didier Lairez and Pierre-Eugéne Coulon at the Laboratoire de Solides Irradiés, (École Polytechnique), the first experiments to produce solid state single nanopore from a nPAAM have been made. An example is given in Figure 4.36, showing the barrier layer side of a nPAAM, where certain pores have been milled with an ion beam. Further study of the conditions of the ion milling as well as modifying the synthesis (for example by changing the concentration of the electrolyte) at the end of the anodization can contribute in the efficiency of the milling and the reproducibility of the results.

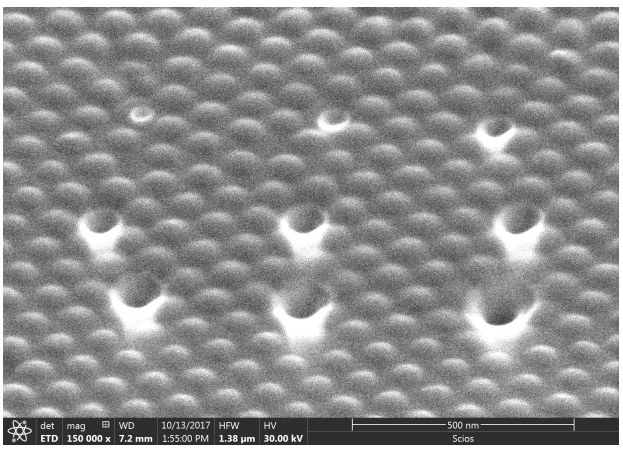

Figure 4.36: SEM image tilted view of the barrier layer surface of a nPAAM on which (FIB) milling has been used to remove selectively from each pore the barrier layer. Courtesy of: Pierre-Eugéne Coulon, Laboratoire des Solides Irradiés, École Polytechnique.

The substructure of the nPAAM can be studied further with SANS in the high q region and with neutron diffraction in different solvents, in order to understand the wetting behaviour of the nPAAM wall. When measuring the PE inside the nPAAM with SANS, the signal is covered from incoherent contributions from the solvent and from the polymer chain that are difficult to estimate. The use of D_2O can improve the signal to noise ratio, thus revealing the PE conformation.

Neutron reflectivity (NR) measurements of nPAAMs prepared on Si wafers show promising results for further use in studies of kinetics of penetration and adsorption of polyelectrolytes inside nanopores. During the thesis, the first NR experiments were made on nPAAMs immersed in NaPSS solution. The prepared nPAAM layer consisted of a duplex layer with two different pore diameters as seen in the scheme of Figure 4.37b. The reflectivity spectra of the bare nPAAM measured in D_2O and the one measured in NaPSS solution of 0.12% v\v in D_2O present a relative shift (Figure 4.37a), marking a change in the filling solution. Moreover, the theoretical reflectivity spectra, assuming that the pore channel is filled with NaPSS of the same concentration as the bulk doesn't correspond to the experimental one. The scattering length density derived from the fit of the experimental reflectivity curve is clearly lower (Figure 4.37b), marking a higher concentration of PE chains present in the channel than the theoretical one. This result needs further study to elucidate whether the measure excess PE arises due to adsorption of the PE or is related to a general increase of the concentration inside the pore.

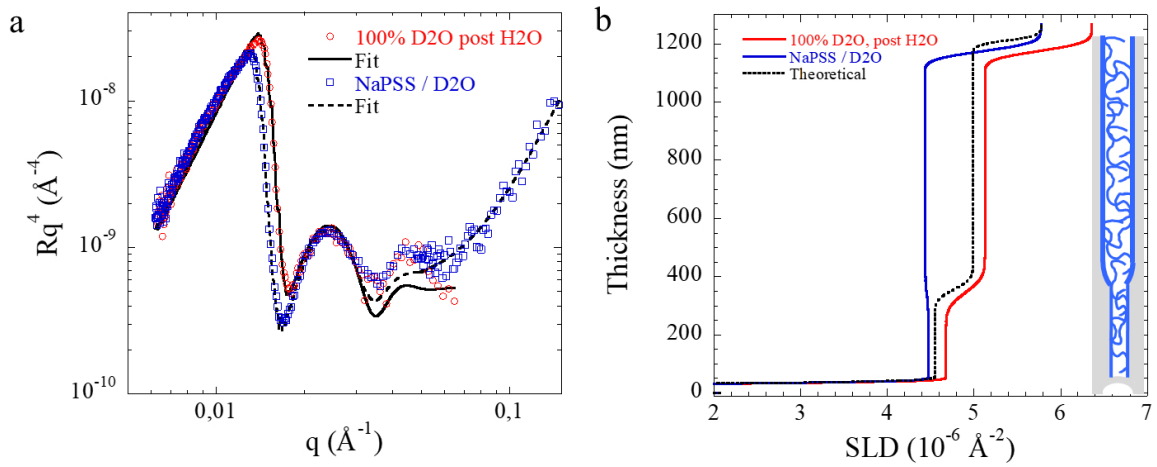

Figure 4.37: a) NR experimental spectra of a nPAAM with a duplex structure, measured bare in D_2O (red), in NaPSS solution with D_2O blue. b) SLD profiles of the bare nPAAM (red), in NaPSS solution (blue). The black line corresponds to a theoretical SLD assuming that the concentration of NaPSS inside the pore channels equals the one in the bulk solution.

The synthesis of duplex layers with different pore diameters along their length are interesting to study the effect of the reduction in the pore diameter during the adsorption of polyelectrolytes. In addition, the characteristic inverted barrier layer which may add some complexity during the fitting of the spectra can be avoided by ending the anodization at an earlier time.

ANNEXES

Appendix A

Structure characterisation by SEM

The membranes were characterised by Scanning Electron Microscopy (SEM) in order to have access to the geometrical characteristics such as the pore diameter D_p, interpore distance D_{int}, pore density n, barrier layer thickness L_b, porosity P and thickness h. From such images as in Figure A.1 and with the aid of an image analysis software (Imagej) we present the results for the three electrolytes.

The images are processed as following:

a) Set the scale by using the scale bar and crop the picture to exclude the text bar (Figure A.2)

b) Convert the image into a black and white binary image (Figure A.3)

c) Using the option "Analyse Particles", the processing software calculates the number of particles N, in our case the pores, of the image as well as, the total occupied area S_{pores}. For the calculation of the pore diameter we choose to exclude the pores at the

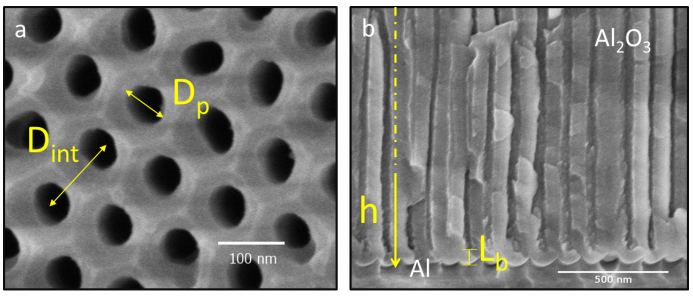

Figure A.1: SEM image of a porous alumina membrane synthesized at 40V oxalic acid 0.3M a) Top view, b) cross section.

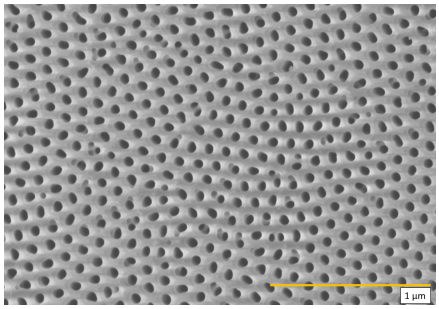

Figure A.2: Cropped SEM image.

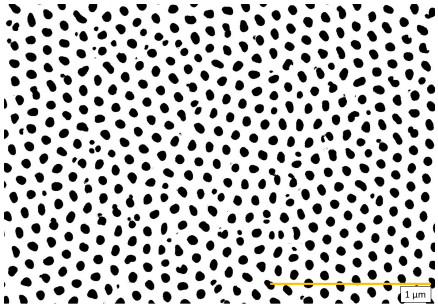

Figure A.3: Binary image.

edges because they are not complete and they contribute to the distribution of the pore diameters with different weighting factors. The average pore diameter D_p is given by:

$$D_p = \sqrt{\frac{4S_{\text{pores}}}{N\pi}} \tag{A.1}$$

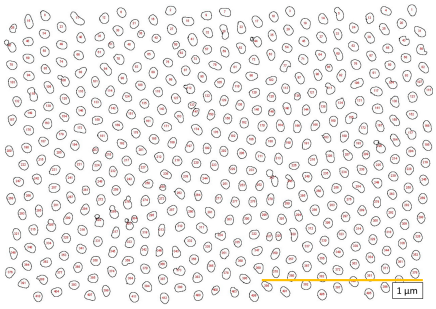

Figure A.4: Image with identified pores and exclusion them at the edges of the window.

d) For the pore density n and porosity P we include all of the pore populations both in the center and the edges (Figure A.5). The porosity is directly calculated by the software through the ratio of white to black pixels while for the pore density we use:

$$n = \frac{N}{A} \tag{A.2}$$

where A is the total window area.

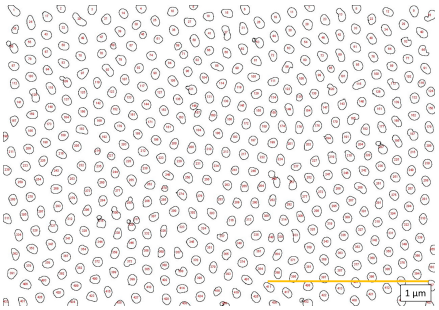

Figure A.5: Image with identified pores including those at the edges of the window.

The D_{int} was calculated with the use of an image processing software developed by Alexis Chennevière (Laboratoire Léon Brillouin). The software finds the center of each pore from the binary image as the one in Figure A.3. Then it makes a two dimensional Fast Fourier Transform(FFT) and produces a 2D plot as shown in Figure A.6. By radial integration we end up to an 1D plot of the Structure factor, S_q of the pores. The fitting of the derived S_q with an appropriate model (e.g hexagonal S(q), Figure A.7) gives access to the structural parameters such as the lattice constant (in our case is the D_{int}), the distribution in the D_{int} and the grain size of the ordered domains .

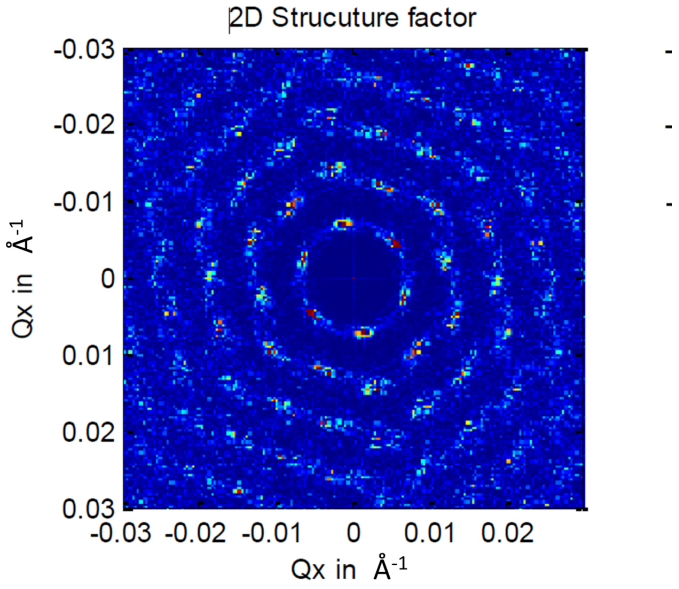

Figure A.6: 2D plot of the FFT of the pore centers image.

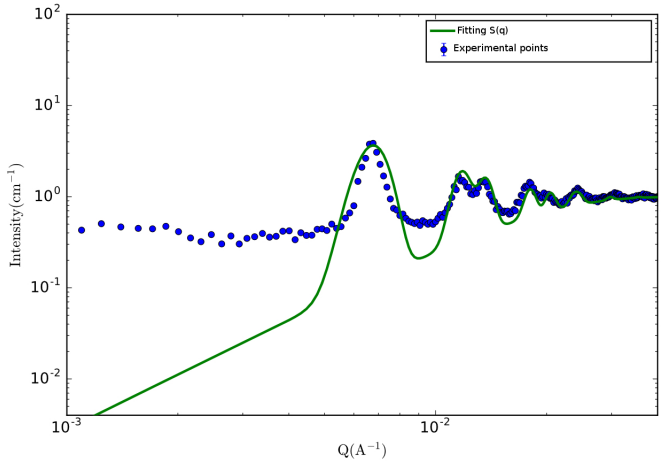

Figure A.7: 1D FFT plot and fitting with an hexagonal structure factor.

Appendix B

Small Angle neutron Scattering

Small Angle Neutron Scattering is a non destructive technique that is used to characterize the structure and composition of matter. In a typical SANS experiment, low energy neutrons of a certain wavelength λ are scattered elastically by a material and fall on a detector. Due to the dual particle-wave character of neutron an interference pattern appears on the detector plane. At the end of the experiment this pattern is analysed and related to the structure and composition of the sample under study. The following paragraphs and notation has been based on [171].

The scattering process, depicted in Figure B.1, can be viewed under the wave character of the neutrons. An incident plane wave with momentum

$$\mathbf{k_i} = \frac{\mathbf{2}\pi}{\lambda}$$

is scattered due to the presence of a central potential *V(r)*, (the scattering is isotropic and the scattered wave spherical), propagating with momentum $\mathbf{k}_d$ and diminishing as 1/r. Here, we will consider the time independent case.

The plane wave can be described as:

$$\psi = \psi_0 e^{k_i \mathbf{r}} \tag{B.1}$$

with the probability of finding the neutron over the whole space is given by:

$$\int_V \psi\psi^* = \int_V |\psi_0|^2 = 1$$

While for the scattered wave, far from the scatterer it can be considered as a plane wave:

$$\psi_d = \psi_0 \frac{b}{r} e^{i\mathbf{k_d}.\mathbf{r}} \tag{B.2}$$

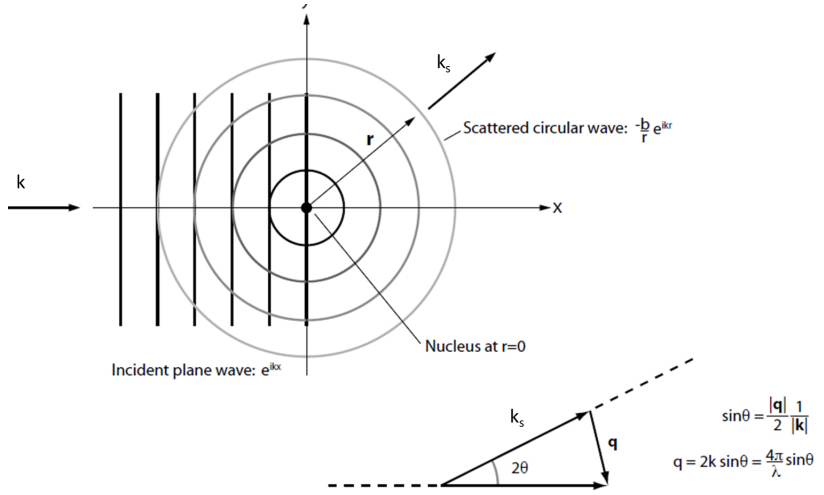

Figure B.1: The process of neutron scattering under the view of their wave character. Image taken from [171].

The quantity b is the scattering length, and it defines the extent of the neutron-nucleus interaction (Figure B.2. Each scattering length can be related to a scattering cross section σ which can be viewed as a surface of a sphere with radius the scattering length. The scattering length is an experimentally determined parameter for each isotope. For example hydrogen has $b_H = -3.74 * 10^{-5}$ Å^{-5} while deuterium has $b_D = 6.67$ Å^{-5} and it enables to tune the scattering length of the molecule by isotopic variation. Moreover, the tuning can be done in such a way that whole components of a system under study can become "invisible" to neutrons. This is the so-called method of contrast variation and the milestone of the technique.

The scattered wave for an assembly of scatterers will be the superposition of each wave corrected by a phase factor due to their relative positions:

$$\Psi_s = -\sum_n \frac{b_i}{r} e^{i\mathbf{kr}} e^{\mathbf{q}.\mathbf{r}} \tag{B.3}$$

The phase difference is:

$$\Delta\Phi = (\mathbf{k_i} - \mathbf{k_d}).\mathbf{r} = \mathbf{q}.\mathbf{r} \tag{B.4}$$

with $\mathbf{q}$ the scattering wavevector, that gives the transfer of momentum.

As the interaction is considered elastic, that is

$$|k| = |k_s| = \frac{2\pi}{\lambda}$$

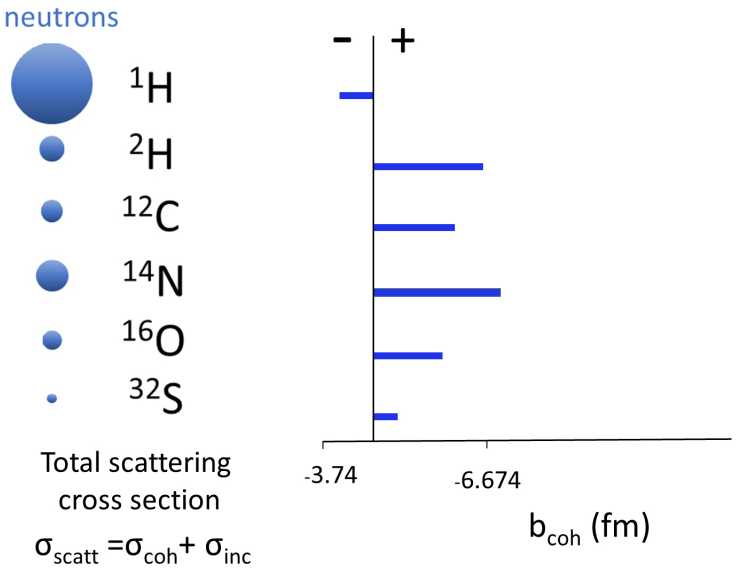

Figure B.2: Left: Neutron scattering cross section for different isotopes. Right: Scattering length density of the different isotopes.

the norm momentum transfer is given by (B.1):

$$q = \frac{4\pi}{\lambda} sin(\theta) \tag{B.5}$$

The number of neutrons scattered per second into a solid angle $d\Omega$ is given by the differential cross section $\frac{d\sigma}{d\Omega}$ which is related to the total scattering cross section of the sample:

$$\sigma_{tot} = \int \frac{d\sigma}{d\Omega} d\Omega \tag{B.6}$$

The total scattering cross section gives the total number of neutrons scattered per second in all directions. The number of scattered neutrons per second passing through an area dS will be:

$$udS|\psi_d|^2 = udS\frac{b^2}{r^2} = ub^2\frac{dS}{r^2} = ub^2 d\Omega \tag{B.7}$$

and because the incident flux is $\Phi = |\psi_0|^2 u = u$ the differential scattering cross section is given by:

$$\frac{d\sigma}{d\Omega} = b^2 \tag{B.8}$$

By integration over the whole space the total cross section σ_{tot} is:

$$\sigma_{tot} = \int_0^{4\pi} \frac{d\sigma}{d\Omega} d\Omega = 4\pi b^2 \tag{B.9}$$

Due to the fact that in reality the measured σ_{tot} values are the averaged values of elements with a distribution in their isotope fraction and spins, a contribution to the measured signal must be included that is not responsible for interference. Thus, the total cross section is divided into:

$$\sigma_{tot} = \sigma_{coh} + \sigma_{inc} \tag{B.10}$$

Correspondingly, each cross section is related to a scattering length b_{coh} and b_{inc}.

In an analogous way, for an assembly of n scatterers it can be shown that it is a function of the wavevector q:

$$\frac{d\sigma}{d\Omega} = \frac{1}{N} |\sum_i^N b_i e^{i\mathbf{q}.\mathbf{r}}|^2 \tag{B.11}$$

In the case of molecules we define the scattering length density as:

$$\rho = \frac{\sum_i^n b_i}{V} \tag{B.12}$$

where V is the molar volume of the molecule. Of course, this sum is valid at length scales where the local structure of the molecule is lost. The macroscopic cross section $\frac{d\Sigma}{d\Omega}$ will be:

$$\frac{d\Sigma}{d\Omega} = \frac{N}{V}\frac{d\sigma}{d\Omega} = \frac{1}{V} |\int_V \rho(\mathbf{r}) e^{i\mathbf{q}.\mathbf{r}}|^2 \tag{B.13}$$

For a two component system with scattering length densities ρ_1, ρ_2 it can be shown that [171]:

$$\frac{d\Sigma}{d\Omega}(q) = \frac{1}{V}(\rho_1 - \rho_2)^2 |\int_{V_1} e^{i\mathbf{q}.\mathbf{r}} d\mathbf{r_1}|^2 \tag{B.14}$$

The last term inside the integral is related to the arrangement of the scatterers inside the sample and can be described as the product of a structure factor and a form factor constituting the macroscopic scattering object. Thus, we end up in a model formalism as in:

$$\frac{d\Sigma}{d\Omega}(q) = \frac{1}{V}(\rho_1 - \rho_2)^2 V_p^2 P(q) S(q) \tag{B.15}$$

In a neutron experiment intensity is not directly the macroscopic cross section $\frac{d\Sigma}{d\Omega}(q)$ but there is a prefactor:

$$\frac{d\Sigma}{d\Omega}(q) = [\Phi AlT\Delta\Omega\epsilon t]\frac{d\Sigma}{d\Omega}(q) \tag{B.16}$$

where, Φ is the neutron flux, A is the illuminated sample area, l the beam's path length through the sample, T the transmission of the sample, $\Delta\Omega$ is the pixel size in units of solid angle, ϵ the detector efficiency and t is the counting time. The normalization of the data before proceed to the fitting has to do with this prefactor.

Appendix C

Neutron Reflectivity

Neutron Reflectivity is a technique that can probe the composition and thickness of thin layers. The measuring principle is the specular reflection of a neutron beam from an interface (C.1).

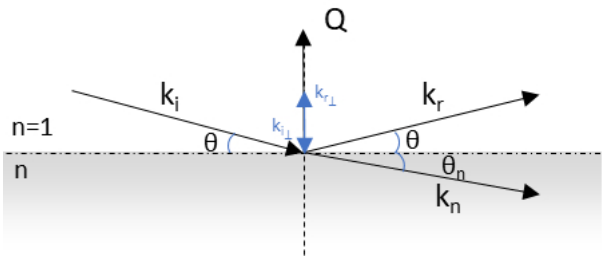

Figure C.1: Reflection of a neutron beam at vacuum/medium interface.

We will follow the analysis of [172] and [173], we consider a neutron beam of wavevector:

$$k_i = \frac{2\pi}{\lambda}$$

and of energy

$$E = \frac{\hbar}{2m}k$$

falls at a grazing angle at an inteface and is scattered elastically by a potential V(r).

The transfer in momentum takes place in the direction of the wavevector Q, thus the variation of the potential in the z direction is given by:

$$V(z) = \frac{1}{V}\int_V V(r)dr = \frac{2\pi\hbar}{m}Nb \tag{C.1}$$

Where b is the scattering length (neglecting absorption) and N the number of atoms per

unit volume. The product Nb reflects the composition of the layer and is called the coherent scattering length density.

From conservation of energy at z=0 we can calculate a refractive index for the refractive medium.

$$\frac{\hbar^2 k_i^2}{2m} = \frac{\hbar^2 k_n^2}{2m} + V(z) \tag{C.2}$$

with k_n the wavevector of the neutron beam inside the medium with refractive index n. Thus the wavevector k_n can be expressed as:

$$k_n^2 = k_i^2 - 4\pi Nb \tag{C.3}$$

And the refractive index as :

$$n^2 = \frac{k_n^2}{k_i^2} = 1 - \frac{\lambda^2}{\pi} Nb \tag{C.4}$$

With the derivation of the refractive index n, the analysis can be made as in the classical optics,

$$cos\theta = ncos\theta_n$$

At the critical angle θ_c the angle $\theta_n = 0$. For $\theta_c \leq \theta$ total external reflection occurs. The critical angle is given:

$$\cos\theta_c = n \tag{C.6}$$

Because n$\ll$1 we can write,

$$n \approx 1 - \frac{\lambda^2}{2\pi} Nb \tag{C.7}$$

In order to take into account absorption the refractive index is written as:

$$n = 1 - \frac{\lambda^2}{2\pi} Nb - i\lambda \frac{N\sigma_a}{4\pi}$$

where σ_a is the neutron absorption cross section.

Combining the last two relations, we obtain the relation of the scattering length density of the layer and the critical angle.

$$sin\theta_c = \sqrt{\frac{Nb}{\pi}}\lambda \tag{C.8}$$

Note that the transfer in momentum is given by

$$Q = \mathbf{k_r} - \mathbf{k_i}$$

and that $k_i = k_r = k$, thus:

$$Q = 2ksin\theta = \frac{4\pi}{\lambda} \tag{C.9}$$

The derivation of the refractive index enables for treating the neutron reflectivity problem as in the classical optics analysis and make use of the Fresnel equations. As an example the case of reflection at an interface of air and a substrate is given. The propagating waves at each medium are:

In air:

$$\psi_0(z) = A_0 e^{ik_{z,0}z} + B_0 e^{ik_{z,0}z} = e^{ik_{z,0}z} + re^{ik_{z,0}z}$$

In the substrate:

$$\psi_1(z) = te^{ik_{z,1}z}$$

At the interface the two wavefunctions must be continuous, thus:

$$\psi_0(0) = \psi_1(0)$$

$$\psi_0(0)^{'} = \psi_1(0)^{'}$$

Thus, the equations yield:

$$1 + r = t$$

$$k_{z,0}(1 - r) = k_1 t]$$

with r the coefficient of reflection:

$$r = |\frac{k_{z,0} - k_{z,s}}{k_{z,0} + k_{z,s}}|$$

and t, the coefficient of transmission:

$$t = \frac{2k_{z,0}}{k_{z,0} + k_{z,1}}$$

The intensities of the reflected and refracted waves (Reflectivity R and Transmission T) are given by the square of their amplitudes, thus:

$$R = |r|^2$$

and

$$T = |t|^2$$

We define the vector

$$\mathbf{q} = k_z = \frac{Q}{2}$$

and the coefficients can be expressed in terms of the momentum transfer q. Also with the use of the expression C.3 and that

$$q_c = \sqrt{16\pi N b_1}$$

we have:

$$r = |\frac{q_0 - q_1}{q_0 + q_1}|^2 = |\frac{q_0 - \sqrt{q_0^2 - q_c^2}}{q_0 + \sqrt{q_0^2 + q_1^2}}|^2 \tag{C.12}$$

For a thin film of refractive index n_1 between air and a substrate with refractive indexes n_2 we have the propagating waves:

Inside medium of n_1:

$$\psi_1(z) = A_1 e^{k_1 z} + B_1 e^{-ik_1 z}$$

Inside the medium of n_2:

$$\psi_2(z) = A_2 e^{ik_2} + B_2 e^{-ik_a z}$$

where A and B are the amplitudes of the propagating waves.

For

$$q < q_c$$

the q_1 is imaginary, the reflectivity R=1 and an evanescence wave exists in the z direction. For $q > q_c$ the reflectivity falls rapidly and for very high q, it falls as q^{-4}.

Appendix D

Emission Spectroscopy

Flame Atomic Emission Spectroscopy is a chemical analysis technique that is used to characterise the concentration of atoms in a sample. The measuring principle is based in measuring the intensity of radiation emitted from an atom at a characteristic wavelength. The sample is usually dissolved in an appropriate solvent that keeps the element well dissolved. The sample is brought inside a flame by a vaporiser. The solvent is vaporized and the chemical compounds dissociate due to heat, resulting in a gas of free atoms. Through collisions, the electrons of each atom are excited to higher bands and when they come back to the ground state, they emit photons of specific wavelength. The radiation is recorded by a detector and its intensity is proportional to the atomic concentration in the sample.

Instead of a flame, the free atoms can be produced by a plasma. This technique is called ICP (Induced Coupled Plasma) Emission spectroscopy. The advantage of using plasma is that it is more efficient in the dissociation of compounds and the excitation of more atoms as it can reach a higher temperature. Compared to flame spectroscopy the detection limit is lower in the case of ICP. For example, for aluminum for ICP is 0.2 µg per mL while for flame spectroscopy the detection limit is 3 µg.

Bibliography

[1] Patrick Huber. Soft matter in hard confinement: phase transition thermodynamics, structure, texture, diffusion and flow in nanoporous media. *Journal of Physics: Condensed Matter*, 27(10):103102, 2015.

[2] Abdul Mutalib Md Jani, Dusan Losic, and Nicolas H. Voelcker. Nanoporous anodic aluminium oxide: Advances in surface engineering and emerging applications. *Progress in Materials Science*, 58(5):636 – 704, 2013.

[3] Carole V. Cerclier, Makha Ndao, Rémi Busselez, Ronan Lefort, Eric Grelet, Patrick Huber, Andriy V. Kityk, Laurence Noirez, Andreas Schönhals, and Denis Morineau. Structure and phase behavior of a discotic columnar liquid crystal confined in nanochannels. *The Journal of Physical Chemistry C*, 116(35):18990–18998, 2012.

[4] R. Lefort, J. L. Duvail, T. Corre, Y. Zhao, and D. Morineau. Phase separation of a binary liquid in anodic aluminium oxide templates. *The European Physical Journal E*, 34(7):71, Jul 2011.

[5] A. Razzak Abdel Hamid, Ramona Mhanna, Ronan Lefort, Aziz Ghoufi, Christiane Alba-Simionesco, Bernhard Frick, and Denis Morineau. Microphase separation of binary liquids confined in cylindrical pores. *The Journal of Physical Chemistry C*, 120(17):9245–9252, 2016.

[6] André Kusmin, Simon Gruener, Anke Henschel, Nicolas de Souza, Jürgen Allgaier, Dieter Richter, and Patrick Huber. Polymer dynamics in nanochannels of porous silicon: A neutron spin echo study. *Macromolecules*, 43(19):8162–8169, 2010.

[7] Stelios Alexandris, Georgios Sakellariou, Martin Steinhart, and George Floudas. Dynamics of unentangled cis-1,4-polyisoprene confined to nanoporous alumina. *Macromolecules*, 47(12):3895–3900, 2014.

[8] Fabienne Barroso-Bujans, Pablo Palomino, Felix Fernandez-Alonso, Svemir Rudić, Angel Alegría, Juan Colmenero, and Eduardo Enciso. Intercalation and confinement

of poly(ethylene oxide) in porous carbon nanoparticles with controlled morphologies. *Macromolecules*, 47(24):8729–8737, 2014.

[9] Linling Li, Dongshan Zhou, Dinghai Huang, and Gi Xue. Double glass transition temperatures of poly(methyl methacrylate) confined in alumina nanotube templates. *Macromolecules*, 47(1):297–303, 2014.

[10] Jon Maiz, Wei Zhao, Yu Gu, Jimmy Lawrence, Arantxa Arbe, Angel Alegría, Todd Emrick, Juan Colmenero, Thomas P. Russell, and Carmen Mijangos. Dynamic study of polystyrene-block-poly(4-vinylpyridine) copolymer in bulk and confined in cylindrical nanopores. *Polymer*, 55(16):4057 – 4066, 2014.

[11] Leili Javidpour, M. Reza Rahimi Tabar, and Muhammad Sahimi. Molecular simulation of protein dynamics in nanopores. ii. diffusion. *The Journal of Chemical Physics*, 130(8):085105, 2009.

[12] E. P. Gilbert, L. Auvray, and J. Lal. Structure of polyelectrolyte chains confined in nanoporous glass. *Macromolecules*, 34(14):4942–4948, 2001.

[13] William M. Deen and Frank G. Smith. Hindered diffusion of synthetic polyelectrolytes in charged microporous membranes. *Journal of Membrane Science*, 12(2):217 – 237, 1982.

[14] Jie Ren Ku and Pieter Stroeve. Protein diffusion in charged nanotubes: "on-off" behavior of molecular transport. *Langmuir*, 20(5):2030–2032, 2004.

[15] G. Oukhaled, L. Bacri, J. Mathé, J. Pelta, and L. Auvray. Effect of screening on the transport of polyelectrolytes through nanopores. *EPL (Europhysics Letters)*, 82(4):48003, 2008.

[16] Mubarak Ali, Basit Yameen, Javier Cervera, Patricio Ramírez, Reinhard Neumann, Wolfgang Ensinger, Wolfgang Knoll, and Omar Azzaroni. Layer-by-layer assembly of polyelectrolytes into ionic current rectifying solid-state nanopores: Insights from theory and experiment. *Journal of the American Chemical Society*, 132(24):8338–8348, 2010.

[17] Thomas D. Lazzara, K. H. Aaron Lau, Ahmed I Abou-Kandil, Anne-Marie Caminade, Jean-Pierre Majoral, and Wolfgang Knoll. Polyelectrolyte layer-by-layer deposition in cylindrical nanopores. *ACS Nano*, 4(7):3909–3920, 2010.

[18] Hideki Masuda and Kenji Fukuda. Ordered metal nanohole arrays made by a two-step replication of honeycomb structures of anodic alumina. *Science*, 268(5216):1466–1468, 1995.

[19] Xiao Kai, Wen Liping, and Jiang Lei. Biomimetic solid-state nanochannels: From fundamental research to practical applications. *Small*, 12(21):2810–2831.

[20] Woo Lee and Sang-Joon Park. Porous anodic aluminum oxide: Anodization and templated synthesis of functional nanostructures. *Chemical Reviews*, 114(15):7487–7556, 2014.

[21] C. T. Sousa, D. C. Leitao, M. P. Proenca, J. Ventura, A. M. Pereira, and J. P. Araujo. Nanoporous alumina as templates for multifunctional applications. *Applied Physics Reviews*, 1(3):031102, 2014.

[22] V. Romero, M.I. Vázquez, S. Cañete, V. Vega, J. García, V.M. Prida, B. Hernando, and J. Benavente. Frictional and electrical effects involved in the diffusive transport through a nanoporous alumina membrane. *The Journal of Physical Chemistry C*, 117(48):25513–25518, 2013.

[23] A. Mozalev, S. Magaino, and H. Imai. The formation of nanoporous membranes from anodically oxidized aluminium and their application to li rechargeable batteries. *Electrochimica Acta*, 46(18):2825 – 2834, 2001.

[24] F. Boué, J. P. Cotton, A. Lapp, and G. Jannink. A direct measurement of the polyion conformation in aqueous solutions at different temperatures. small angle neutron scattering of PSSNa using zero average and full contrast. *The Journal of Chemical Physics*, 101(3):2562–2568, 1994.

[25] M. N. Spiteri, F. Boué, A. Lapp, and J. P. Cotton. Persistence length for a PSSNa polyion in semidilute solution as a function of the ionic strength. *Phys. Rev. Lett.*, 77:5218–5220, Dec 1996.

[26] E. Dubois and F. Boué. Conformation of poly(styrenesulfonate) polyions in the presence of multivalent ions :â small-angle neutron scattering experiments. *Macromolecules*, 34(11):3684–3697, 2001.

[27] Jérôme Combet, François Isel, Michel Rawiso, and François Boué. Scattering functions of flexible polyelectrolytes in the presence of mixed valence counterions : condensation and scaling. *Macromolecules*, 38(17):7456–7469, 2005.

[28] Ralph H. Colby. Structure and linear viscoelasticity of flexible polymer solutions: comparison of polyelectrolyte and neutral polymer solutions. *Rheologica Acta*, 49(5):425–442, May 2010.

[29] Jan-Michael Y. Carrillo and Andrey V. Dobrynin. Detailed molecular dynamics simulations of a model napss in water. *The Journal of Physical Chemistry B*, 114(29):9391–9399, 2010.

[30] Qingtao Wang, Yunze Long, and Bin Sun. Fabrication of highly ordered porous anodic alumina membrane with ultra-large pore intervals in ethylene glycol-modified citric acid solution. *Journal of Porous Materials*, 20(4):785–788, Aug 2013.

[31] Osamu Nishinaga, Tatsuya Kikuchi, Shungo Natsui, and Ryosuke O. Suzuki. Rapid fabrication of self-ordered porous alumina with 10-/sub-10-nm-scale nanostructures by selenic acid anodizing. *Scientific Reports*, 3:2748.

[32] Hideki Masuda and Kenji Fukuda. Ordered Metal Nanohole Arrays Made by a Two-Step Replication of Honeycomb Structures of Anodic Alumina. *Science*, 268(5216):1466–1468, 1995.

[33] K. Nielsch, F. Müller, A.P. Li, and U. Gösele. Uniform nickel deposition into ordered alumina pores by pulsed electrodeposition. *Advanced Materials*, 12(8):582–586, 2000.

[34] Abel Santos, Tushar Kumeria, and Dusan Losic. Nanoporous anodic aluminum oxide for chemical sensing and biosensors. *TrAC Trends in Analytical Chemistry*, 44:25–38, 2013.

[35] Alexandros G. Koutsioubas, Nikolaos Spiliopoulos, Dimitris Anastassopoulos, Alexandros A. Vradis, and George D. Priftis. Nanoporous alumina enhanced surface plasmon resonance sensors. *Journal of Applied Physics*, 103(9):094521, 2008.

[36] E. M. Sevick. Shear swelling of polymer brushes grafted onto convex and concave surfaces. *Macromolecules*, 29(21):6952–6958, 1996.

[37] E. P. Gilbert, L. Auvray, and J. Lal. Structure of polyelectrolyte chains confined in nanoporous glass. *Macromolecules*, 34(14):4942–4948, 2001.

[38] K. Lagrené and J.-M. Zanotti. Anodic aluminium oxide: Concurrent SEM and SANS characterisation. influence of AAO confinement on PEO mean-square displacement. *The European Physical Journal Special Topics*, 141(1):261–265, 2007.

[39] Karine Lagrené, Jean-Marc Zanotti, Mohamed Daoud, Bela Farago, and Patrick Judeinstein. Large-scale dynamics of a single polymer chain under severe confinement. *Physical Review E*, 81(6):060801, 2010-06-24.

[40] Frank Lange, Patrick Judeinstein, Cornelius Franz, Brigitte Hartmann-Azanza, Salim Ok, Martin Steinhart, and Kay SaalwÃ¤chter. Large-scale diffusion of entangled polymers along nanochannels. *ACS Macro Letters*, 4(5):561–565, 2015.

[41] F. Keller, M. S. Hunter, and D. L. Robinson. Structural Features of Oxide Coatings on Aluminum. *Journal of The Electrochemical Society*, 100(9):411–419, September 1953.

[42] Hideki Masuda and Masahiro Satoh. Fabrication of gold nanodot array using anodic porous alumina as an evaporation mask. *Japanese Journal of Applied Physics*, 35(1B):L126, 1996.

[43] Woo Lee, Ran Ji, Ulrich Gösele, and Kornelius Nielsch. Fast fabrication of long range ordered porous alumina membranes by hard anodization. *Nature Materials*, 5:741, 2006.

[44] Woo Lee and Sang-Joon Park. Porous anodic aluminum oxide: Anodization and templated synthesis of functional nanostructures. *Chemical Reviews*, 114(15):7487–7556, 2014.

[45] Begoña Abad, Jon Maiz, and Marisol Martin-Gonzalez. Rules to determine thermal conductivity and density of anodic aluminum oxide (aao) membranes. *The Journal of Physical Chemistry C*, 120(10):5361–5370, 2016.

[46] Karine Lagrene. *ÉTUDE DYNAMIQUE DE POLYMÈRES SOUS CONFINEMENT QUASI-UNIAXIAL*. Theses, Université Paris Sud - Paris XI, October 2008.

[47] S. Förster, A. Timmann, M. Konrad, C. Schellbach, A. Meyer, S. S. Funari, P. Mulvaney, and R. Knott. Scattering curves of ordered mesoscopic materials. *The Journal of Physical Chemistry B*, 109(4):1347–1360, 2005.

[48] Andreas Sundblom, Cristiano L. P. Oliveira, Anders E. C. Palmqvist, and Jan Skov Pedersen. Modeling in situ small-angle x-ray scattering measurements following the formation of mesostructured silica. *The Journal of Physical Chemistry C*, 113(18):7706–7713, 2009.

[49] Ilya V. Roslyakov, Elena O. Gordeeva, and Kirill S. Napolskii. Role of electrode reaction kinetics in self-ordering of porous anodic alumina. *Electrochimica Acta*, 241:362 – 369, 2017.

[50] Osamu Nishinaga, Tatsuya Kikuchi, Shungo Natsui, and Ryosuke O. Suzuki. Rapid fabrication of self-ordered porous alumina with 10-/sub-10-nm-scale nanostructures by selenic acid anodizing. *Scientific Reports*, 3:2748, 2013.

[51] Hideki Masuda, Fumio Hasegwa, and Sachiko Ono. Selfâordering of cell arrangement of anodic porous alumina formed in sulfuric acid solution. *Journal of The Electrochemical Society*, 144(5):L127–L130, 1997.

[52] Myungjun Kim, Hyunchul Kim, Changdeuck Bae, Joobong Lee, Hyunjun Yoo, Josep M. Montero Moreno, and Hyunjung Shin. Initial self-ordering of porous anodic alumina: Transition from polydispersity to monodispersity. *The Journal of Physical Chemistry C*, 118(46):26789–26795, 2014.

[53] Nikolay A. Vinogradov, Gary S. Harlow, Francesco Carlá, Jonas Evertsson, Lisa Rullik, Weronica Linpé, Roberto Felici, and Edvin Lundgren. Observation of pore growth and self-organization in anodic alumina by time-resolved x-ray scattering. *ACS Applied Nano Materials*, 1(3):1265–1271, 2018.

[54] Jude Mary Runge. *A Brief History of Anodizing Aluminum*, pages 65–148. Springer International Publishing, Cham, 2018.

[55] Feiyue Li, Lan Zhang, and Robert M. Metzger. On the growth of highly ordered pores in anodized aluminum oxide. *Chemistry of Materials*, 10(9):2470–2480, 1998.

[56] Mikhail Pashchanka and Jörg J. Schneider. Origin of self-organisation in porous anodic alumina films derived from analogy with rayleighâbénard convection cells. *J. Mater. Chem.*, 21:18761–18767, 2011.

[57] Mikhail Pashchanka and Jörg J. Schneider. Formation of alumina under unstable electroconvection flow regimes: A case study of tartronic acid electrolyte. *The Journal of Physical Chemistry C*, 121(42):23683–23692, 2017.

[58] Mikhail Pashchanka and Jörg J. Schneider. Self-ordering regimes of porous anodic alumina layers formed in highly diluted sulfuric acid electrolytes. *The Journal of Physical Chemistry C*, 120(27):14590–14596, 2016.

[59] J. Siejka and C. Ortega. An O18 Study of Field Assisted Pore Formation in Compact Anodic Oxide Films on Aluminum. *Journal of The Electrochemical Society*, 124(6):883–891, June 1977.

[60] C. Cherki and J. Siejka. Study by Nuclear Microanalysis and O18 Tracer Techniques of the Oxygen Transport Processes and the Growth Laws for Porous Anodic Oxide Layers on Aluminum. *Journal of The Electrochemical Society*, 120(6):784–791, June 1973.

[61] A. Baron-Wiecheć, M. G. Burke, T. Hashimoto, H. Liu, P. Skeldon, G. E. Thompson, H. Habazaki, J.-J. Ganem, and I. C. Vickridge. Tracer study of pore initiation in anodic alumina formed in phosphoric acid. *Electrochimica Acta*, 113:302 – 312, 2013.

[62] Jihun Oh and Carl V. Thompson. The role of electric field in pore formation during aluminum anodization. *Electrochimica Acta*, 56(11):4044 – 4051, 2011.

[63] F. Brown and W. D. Mackintosh. The use of rutherford backscattering to study the behavior of ionâimplanted atoms during anodic oxidation of aluminum: Ar, kr, xe, k, rb, cs, cl, br, and l. 120(8):1096–1102, 1973.

[64] S. J. Garcia-Vergara, P. Skeldon, G. E. Thompson, and H. Habazaki. A flow model of porous anodic film growth on aluminium. *Electrochimica Acta*, 52(2):681 – 687, 2006.

[65] Jerrod E. Houser and Kurt R. Hebert. The role of viscous flow of oxide in the growth of self-ordered porous anodic alumina films. *Nature Materials*, 8(5):415–420, May 2009.

[66] Stress induced by electrolyte anion incorporation in porous anodic aluminum oxide. *Electrochimica Acta*, 238:368 – 374, 2017.

[67] Qi Dou, Quentin van Overmeere, Pranav Shrotriya, Wenfang Li, and Kurt R. Hebert. Stress induced by incorporation of sulfate ions into aluminum oxide films. *Electrochemistry Communications*, 88:39 – 42, 2018.

[68] Xufei Zhu, Lin Liu, Ye Song, Hongbing Jia, Huadong Yu, Xuemei Xiao, and Xiuli Yang. Oxygen evolution and porous anodic alumina formation. *Materials Letters*, 62(24):4038 – 4040, 2008.

[69] Yang Ruiquan, Jiang Longfei, Zhu Xufei, Song Ye, Yu Dongliang, and Han Aijun. Theoretical derivation of ionic current and electronic current and comparison between fitting curves and measured curves. *RSC Adv.*, 2:12474–12481, 2012.

[70] Xu-Fei Zhu, Ye Song, Lin Liu, Chen-Yu Wang, Jie Zheng, Hong-Bing Jia, and Xin-Long Wang. Electronic currents and the formation of nanopores in porous anodic alumina. *Nanotechnology*, 20(47):475303, 2009.

[71] D. Mercier, Q. Van Overmeere, R. Santoro, and J. Proost. In-situ optical emission spectrometry during galvanostatic aluminum anodising. *Electrochimica Acta*, 56(3):1329 – 1336, 2011.

[72] Mikhail Pashchanka and Jörg J. Schneider. Experimental validation of the novel theory explaining self-organization in porous anodic alumina films. *Phys. Chem. Chem. Phys.*, 15:7070–7074, 2013.

[73] Malgorzata Norek, Dariusz Zasada, and Dariusz Siemiaszko. Systematic study on morphology of anodic alumina produced by hard anodization in the electrolytes modified with ethylene glycol. *Journal of Nano Research*, 46:165–178, 4 2017.

[74] Jaime Martín, Cristina V. Manzano, Olga Caballero-Calero, and Marisol Martín-González. High-aspect-ratio and highly ordered 15-nm porous alumina templates. *ACS Applied Materials & Interfaces*, 5(1):72–79, 2013.

[75] Wojciech J. Stęniowski, Dominika Forbot, Małgorzata Norek, Marta Michalska-Domanska, and Artur Król. The impact of viscosity of the electrolyte on the formation of nanoporous anodic aluminum oxide. *Electrochimica Acta*, 133:57 – 64, 2014.

[76] Xiufang Qin, Jinqiong Zhang, Xiaojuan Meng, Lanfang Wang, Chenhua Deng, Guqiao Ding, Hao Zeng, and Xiaohong Xu. Effect of ethanol on the fabrication of porous anodic alumina in sulfuric acid. *Surface and Coatings Technology*, 254:398 – 401, 2014.

[77] Marco Salerno, Niranjan Patra, Romeo Losso, and Roberto Cingolani. Increased growth rate of anodic porous alumina by use of ionic liquid as electrolyte additive. *Materials Letters*, 63(21):1826 – 1829, 2009.

[78] G. A. Dorsey. The characterization of anodic aluminas: Iii . barrier layer composition and structure. *Journal of The Electrochemical Society*, 113(3):284–286, 1966.

[79] Pei Hsuan Doris Lu, Hartmuth Strutzberg, Stuart Wenham, and Alison Lennon. Hydrogen incorporation during aluminium anodisation on silicon wafer surfaces. *Electrochimica Acta*, 133:153 – 160, 2014.

[80] Artur Krezel and Wojciech Bal. A formula for correlating pka values determined in D_2O and H_2O. *Journal of inorganic biochemistry*, 98(1):161â166, January 2004.

[81] Mikhail Pashchanka and Jörg J. Schneider. Experimental validation of the novel theory explaining self-organization in porous anodic alumina films. *Phys. Chem. Chem. Phys.*, 15:7070–7074, 2013.

[82] G. E. Thompson and G. C. Wood. Porous anodic film formation on aluminium. *Nature*, 290:230, 1981.

[83] I. Mínguez-Bacho, S. Rodríguez-López, A. Climent, D. Fichou, M. Vázquez, and M. Hernández-Vélez. Influence of sulfur incorporation into nanoporous anodic alumina on the volume expansion and self-ordering degree. *The Journal of Physical Chemistry C*, 119(49):27392–27400, 2015.

[84] Catherine Y. Han, Gerold A. Willing, Zhili Xiao, and H. Hau Wang. Control of the anodic aluminum oxide barrier layer opening process by wet chemical etching. *Langmuir*, 23(3):1564–1568, 2007.

[85] Xue Hua Wang, Cheng Yong Li, Gui Chen, Lei He, and Hong Cao. Preparation and thermal stability of porous alumina membranes with nano-pore arrays. *Applied Physics A*, 98(4):745–749, Mar 2010.

[86] Yi Chang, Zhiyuan Ling, Yisen Liu, Xing Hu, and Yi Li. A simple method for fabrication of highly ordered porous α-alumina ceramic membranes. *J. Mater. Chem.*, 22:7445–7448, 2012.

[87] Tatsuya MASUDA, Hidetaka ASOH, Satoshi HARAGUCHI, and Sachiko ONO. Nanoporous alpha;-alumina membrane prepared by anodizing and heat treatment. *Electrochemistry*, 82(6):448–455, 2014.

[88] Levin Igor and Brandon David. Metastable alumina polymorphs: Crystal structures and transition sequences. *Journal of the American Ceramic Society*, 81(8):1995–2012, 2005.

[89] Shiyong Zhao, Karen Chan, Arthur Yelon, and Teodor Veres. Preparation of open-through anodized aluminium oxide films with a clean method. *Nanotechnology*, 18(24):245304, 2007.

[90] Takashi Yanagishita and Hideki Masuda. High-throughput fabrication process for highly ordered through-hole porous alumina membranes using two-layer anodization. *Electrochimica Acta*, 184:80 – 85, 2015.

[91] Cousin, Fabrice and Menelle, Alain. Neutron reflectivity. *EPJ Web of Conferences*, 104:01005, 2015.

[92] Tetyana Lebyedyeva, Serhii Kryvyi, Petro Lytvyn, Mykola Skoryk, and Pavlo Shpylovyy. Formation of Nanoporous Anodic Alumina by Anodization of Aluminum Films on Glass Substrates. *Nanoscale Research Letters*, 11, April 2016.

[93] Ottone C, Laurenti M, Bejtka K, Sanginario A, and Cauda V. The effects of the film thickness and roughness in the anodization process of very thin aluminum films. *Journal of Materials Science and Nanotechnology*, 1(1):1.

[94] M. Kokonou, A. G. Nassiopoulou, and K. P. Giannakopoulos. Ultra-thin porous anodic alumina films with self-ordered cylindrical vertical pores on a p-type silicon substrate. *Nanotechnology*, 16(1):103, 2005.

[95] Jerome K. Percus and George J. Yevick. Analysis of classical statistical mechanics by means of collective coordinates. *Phys. Rev.*, 110:1–13, Apr 1958.

[96] M. T. Wu, I. C. Leu, and M. H. Hon. Anodization behavior of al film on si substrate with different interlayers for preparing si-based nanoporous alumina template. *Journal of Materials Research*, 19(3):888–895, 2004.

[97] Andrew Nelson. Co-refinement of multiple-contrast neutron/X-ray reflectivity data using *MOTOFIT*. *Journal of Applied Crystallography*, 39(2):273–276, April 2006.

[98] I. Vrublevsky, K. Chernyakova, A. Bund, A. Ispas, and U. Schmidt. Effect of anodizing voltage on the sorption of water molecules on porous alumina. *Applied Surface Science*, 258(14):5394 – 5398, 2012.

[99] M.E. Mata-Zamora and J.M. Saniger. Thermal evolution of porous anodic aluminas: a comparative study. *Revista mexicana de física*, 51:502 – 509, 00 2005.

[100] J. P. O'Sullivan, J. A. Hockey, and G. C. Wood. Infra-red spectroscopic study of anodic alumina films. *Trans. Faraday Soc.*, 65:535–541, 1969.

[101] I. Mínguez-Bacho, S. Rodríguez-López, A. Climent-Font, D. Fichou, M. Vázquez, and M. Hernández-Vélez. Variation of the refractive index by means of sulfate anion incorporation into nanoporous anodic aluminum oxide films. *Microporous and Mesoporous Materials*, 225:192–197, May 2016.

[102] François Le Coz, Laurent Arurault, and Lucien Datas. Chemical analysis of a single basic cell of porous anodic aluminium oxide templates. *Materials Characterization*, 6(3):283–288, March 2010.

[103] A. Kirchner, K.J.D. MacKenzie, I.W.M. Brown, T. Kemmitt, and M.E. Bowden. Structural characterisation of heat-treated anodic alumina membranes prepared using a simplified fabrication process. *Journal of Membrane Science*, 287(2):264 – 270, 2007.

[104] Peter P. Mardilovich, Alexander N. Govyadinoy, Nadezhda I. Mazurenko, and Russell Paterson. New and modified anodic alumina membranes part II. Comparison of solubility of amorphous (normal) and polycrystalline anodic alumina membranes. *Journal of Membrane Science*, 98(1):143 – 155, 1995.

[105] François Le Coz, Laurent Arurault, and Lucien Datas. Chemical analysis of a single basic cell of porous anodic aluminium oxide templates. *Materials Characterization*, 61(3):283 – 288, 2010.

[106] Porous anodic film formation on aluminium. 290.

[107] Y. Xu, G. E. Thompson, G. C. Wood, and B. Bethune. Anion incorporation and migration during barrier film formation on aluminium. *Corrosion Science*, 27(1):83 – 102, 1987.

[108] D. H. Fan, G. Q. Ding, W. Z. Shen, and M. J. Zheng. Anion impurities in porous alumina membranes: Existence and functionality. *Microporous and Mesoporous Materials*, 100(1):154 – 159, 2007.

[109] Sachiko Ono, Hideki Ichinose, and Noboru Masuko. The high resolution observation of porous anodic films formed on aluminum in phosphoric acid solution. *Corrosion Science*, 33(6):841 – 850, 1992.

[110] Peter P. Mardilovich, Alexander N. Govyadinov, Nikolai I. Mukhurov, Alexander M. Rzhevskii, and Russell Paterson. New and modified anodic alumina membranes part i. thermotreatment of anodic alumina membranes. *Journal of Membrane Science*, 98(1):131 – 142, 1995.

[111] KINGO ITAYA, SHIZUO SUGAWARA, KUNIO ARAI, and SHOZABURO SAITO. Properties of porous anodic aluminum oxide films as membranes. *Journal of Chemical Engineering of Japan*, 17(5):514–520, 1984.

[112] Xavier Carrier, Eric Marceau, Jean-François Lambert, and Michel Che. Transformations of γ-alumina in aqueous suspensions: 1. alumina chemical weathering studied as a function of ph. *Journal of Colloid and Interface Science*, 308(2):429 – 437, 2007.

[113] Shunta Akiya, Tatsuya Kikuchi, Shungo Natsui, and Ryosuke O. Suzuki. Nanostructural characterization of large-scale porous alumina fabricated via anodizing in arsenic acid solution. *Applied Surface Science*, 403:652 – 661, 2017.

[114] Chang-Woo Lee, Hyun-Seop Kang, Yoon-Ho Chang, and Yeong-Min Hahm. Thermo-treatment and chemical resistance of porous alumina membrane prepared by anodic oxidation. *Korean Journal of Chemical Engineering*, 17(3):266–272, May 2000.

[115] Dmitrii I Petukhov, Dmitrii A Buldakov, Alexey A Tishkin, Alexey V Lukashin, and Andrei A Eliseev. Liquid permeation and chemical stability of anodic alumina membranes. *Beilstein Journal of Nanotechnology*, 8:561–570, 2017.

[116] Napolskii Kirill S., Roslyakov Ilya V., Eliseev Andrey A., Petukhov Andrei V., Byelov Dmytro V., Grigoryeva Natalia A., Bouwman Wim G., Lukashin Alexey V., Kvashnina Kristina O., Chumakov Andrey P., and Grigoriev Sergey V. Long-range ordering in anodic alumina films: a microradian xâray diffraction study. *Journal of Applied Crystallography*, 43(3):531–538.

[117] Ilya V. Roslyakov, Andrey A. Eliseev, Ekaterina V. Yakovenko, Alexander V. Zabelin, and Kirill S. Napolskii. Longitudinal pore alignment in anodic alumina films grown on polycrystalline metal substrates. *Journal of Applied Crystallography*, 46(6):1705–1710, Dec 2013.

[118] Ilya V. Roslyakov, Dmitry S. Koshkodaev, Andrei A. Eliseev, Daniel Hermida-Merino, Vladimir K. Ivanov, Andrei V. Petukhov, and Kirill S. Napolskii. Growth of porous anodic alumina on low-index surfaces of al single crystals. *The Journal of Physical Chemistry C*, 121(49):27511–27520, 2017.

[119] Abdul Waheed, Mazhar Mehmood, Robert Benfield, Jamil Ahmad, Heinz Amenitsch, Muhammad Aslam, Abdur Rauf, and Mujtabaul Hassan. Small-angle x-ray scattering (SAXS) study of porous anodic aluminaâa new approach. *Materials Chemistry and Physics*, 131(1):362–369, 2011.

[120] Martin Engel, Bernd Stühn, Jörg J. Schneider, Thomas Cornelius, and Maike Naumann. Small-angle x-ray scattering (*saxs*) off parallel, cylindrical, well-defined nanopores: from random pore distribution to highly ordered samples. *Applied Physics A*, 97(1):99–108, Oct 2009.

[121] Ivan Turkevych, Vasyl Ryukhtin, Vasyl Garamus, Seiichi Kato, Tadashi Takamasu, Giyuu Kido, and Michio Kondo. Studies of self-organization processes in nanoporous alumina membranes by small-angle neutron scattering. *Nanotechnology*, 23(32):325606, 2012.

[122] S. V. Grigoryev, N. A. Grigoryeva, A. V. Syromyatnikov, K. S. Napolskii, A. A. Eliseev, A. V. Lukashin, Yu. D. Tretyakov, and H. Eckerlebe. Two-dimensional spatially ordered Al_2O_3 systems: small-angle neutron scattering investigation. *JETP Letters*, 85(9):549–554, 2007.

[123] Damien Marchal and Bruno Demé. Small-angle neutron scattering by porous alumina membranes made of aligned cylindrical channels. *Journal of Applied Crystallography*, 36(3 Part 1):713–717, Jun 2003.

[124] Karine Lagrené and Jean-Marc Zanotti. Evidence of bayerite clusters within the AAO amorphous bulk alumina. Consequence for AAO SANS matching properties. *MRS Online Proceedings Library Archive*, 1074, 2008.

[125] R. Lefort, J.-L. Duvail, T. Corre, Y. Zhao, and D. Morineau. Phase separation of a binary liquid in anodic aluminium oxide templates. *The European Physical Journal E*, 34(7):71, July 2011.

[126] Damien Marchal, Christian Bourdillon, and Bruno Demé. Small-angle neutron scattering by highly oriented hybrid bilayer membranes confined in anisotropic porous alumina. *Langmuir*, 17(26):8313–8320, 2001.

[127] Yuyan Han, Liang Cao, Faqiang Xu, Tiexin Chen, Zhiyuan Zheng, Kun Qian, and Weixin Huang. Quantitative investigation in the influence of oxalic impurities on photoluminescence properties of porous aaos. *Materials Chemistry and Physics*, 129(3):1247 – 1251, 2011.

[128] Kyusoon Shin, Sergei Obukhov, Jiun-Tai Chen, June Huh, Yoontae Hwang, Soonchun Mok, Priyanka Dobriyal, Pappannan Thiyagarajan, and Thomas P. Russell. Enhanced mobility of confined polymers. 6:961.

[129] M. Krutyeva, A. Wischnewski, M. Monkenbusch, L. Willner, J. Maiz, C. Mijangos, A. Arbe, J. Colmenero, A. Radulescu, O. Holderer, M. Ohl, and D. Richter. Effect of nanoconfinement on polymer dynamics: Surface layers and interphases. *Phys. Rev. Lett.*, 110:108303, Mar 2013.

[130] R. Syed, D. Sen, K.V. Mani Krishna, and S.K. Ghosh. Fabrication of highly ordered nanoporous alumina membranes: Probing microstructures by saxs, fesem and afm. *Microporous and Mesoporous Materials*, 264:13 – 21, 2018.

[131] I. Grillo. *Small-Angle Neutron Scattering and Applications in Soft Condensed Matter*, pages 723–782. Springer Netherlands, Dordrecht, 2008.

[132] M.E. Mata-Zamora and J.M. Saniger. Thermal evolution of porous anodic aluminas: a comparative study. *Revista mexicana de física*, 51:502 – 509, 00 2005.

[133] I. Vrublevsky, K. Chernyakova, A. Bund, A. Ispas, and U. Schmidt. Effect of anodizing voltage on the sorption of water molecules on porous alumina. *Applied Surface Science*, 258(14):5394 – 5398, 2012.

[134] Andreas Sundblom, Cristiano L. P. Oliveira, Anders E. C. Palmqvist, and Jan Skov Pedersen. Modeling in situ small-angle x-ray scattering measurements following the formation of mesostructured silica. *The Journal of Physical Chemistry C*, 113(18):7706–7713, 2009.

[135] I. Vrublevsky, A. Jagminas, S. Hemeltjen, and W.A. Goedel. Effect of heat treatment on the structure of incorporated oxalate species and photoluminescent properties of porous alumina films formed in oxalic acid. *Applied Surface Science*, 254(22):7326 – 7330, 2008.

[136] D. Peak and D. L. Sparks. Mechanisms of selenate adsorption on iron oxides and hydroxides. *Environmental Science & Technology*, 36(7):1460–1466, 2002.

[137] Gordon E. Brown, Victor E. Henrich, William H. Casey, David L. Clark, Carrick Eggleston, Andrew Felmy, D. Wayne Goodman, Michael GrÃ¤tzel, Gary Maciel, Maureen I. McCarthy, Kenneth H. Nealson, Dimitri A. Sverjensky, Michael F. Toney, and John M. Zachara. Metal oxide surfaces and their interactions with aqueous solutions and microbial organisms. *Chemical Reviews*, 99(1):77–174, 1999.

[138] George A. Parks. The isoelectric points of solid oxides, solid hydroxides, and aqueous hydroxo complex systems. *Chemical Reviews*, 65(2):177–198, 1965.

[139] Reto B. Schoch, Jongyoon Han, and Philippe Renaud. Transport phenomena in nanofluidics. *Reviews of Modern Physics*, 80(3):839–883, 2008.

[140] Tennyson L. Doane, Chi-Hung Chuang, Reghan J. Hill, and Clemens Burda. Nanoparticle ζ -potentials. *Accounts of Chemical Research*, 45(3):317–326, 2012.

[141] Wei Chen, Jin-Hua Yuan, and Xing-Hua Xia. Characterization and manipulation of the electroosmotic flow in porous anodic alumina membranes. *Analytical Chemistry*, 77(24):8102–8108, 2005.

[142] Elizabeth A. Bluhm, Eve Bauer, Rebecca M. Chamberlin, Kent D. Abney, Jennifer S. Young, and Gordon D. Jarvinen. Surface effects on cation transport across porous alumina membranes. *Langmuir*, 15(25):8668–8672, 1999.

[143] Benjamin H. Winkler and Ruth E. Baltus. Modification of the surface characteristics of anodic alumina membranes using solâgel precursor chemistry. *Journal of Membrane Science*, 226(1):75 – 84, 2003.

[144] Birgit Joana Pedimonte, Tobias Moest, Thomas Luxbacher, Cornelius von Wilmowsky, Tobias Fey, Karl Andreas Schlegel, and Peter Greil. Morphological zeta-potential variation of nanoporous anodic alumina layers and cell adherence. *Acta Biomaterialia*, 10(2):968 – 974, 2014.

[145] Francesca Bragheri, Rebeca Martinez Vazquez, and Roberto Osellame. Chapter 12.3 - microfluidics. In Tommaso Baldacchini, editor, *Three-Dimensional Microfabrication Using Two-photon Polymerization*, Micro and Nano Technologies, pages 310 – 334. William Andrew Publishing, Oxford, 2016.

[146] Christophe Tasserit. *Transport d'ions et d'objets dans des nanopores*. PhD thesis, 2011. Thése de doctorat dirigé par Lairez, Didier Physique Palaiseau, Ecole polytechnique 2011.

[147] Tomokazu Fukutsuka, Kohei Koyamada, Shohei Maruyama, Kohei Miyazaki, and Takeshi Abe. Ion transport in organic electrolyte solution through the pore channels of anodic nanoporous alumina membranes. *Electrochimica Acta*, 199:380 – 387, 2016.

[148] A. Gadaleta, C. Sempere, S. Gravelle, A. Siria, R. Fulcrand, C. Ybert, and L. Bocquet. Sub-additive ionic transport across arrays of solid-state nanopores. *Physics of Fluids*, 26(1):012005, 2014.

[149] N.A. Lange and J.A. Dean. *Lange's Handbook of chemistry*. Number v. 12 in Lange's Handbook of Chemistry. McGraw-Hill, 1979.

[150] M. Kosmulski. *Chemical Properties of Material Surfaces*. Surfactant Science. Taylor & Francis, 2001.

[151] A. Hernández, J. I. Calvo, P. Prádanos, L. Palacio, M. L. Rodríguez, and J. A. de Saja. Surface structure of microporous membranes by computerized SEM image analysis applied to Anopore filters. *Journal of Membrane Science*, 137(1):89 – 97, 1997.

[152] Wei Shi, Yuqing Shen, Dongtao Ge, Maoqiang Xue, Huihui Cao, Sanqing Huang, Jixiao Wang, Guoliang Zhang, and Fengbao Zhang. Functionalized anodic aluminum oxide (AAO) membranes for affinity protein separation. *Journal of Membrane Science*, 325(2):801 – 808, 2008.

[153] M. Muthukumar. 50th anniversary perspective: A perspective on polyelectrolyte solutions. *Macromolecules*, 50(24):9528–9560, 2017.

[154] Andrey V. Dobrynin, Ralph H. Colby, and Michael Rubinstein. Scaling theory of polyelectrolyte solutions. *Macromolecules*, 28(6):1859–1871, 1995.

[155] Damien Baigl, Thomas A. P. Seery, and Claudine E. Williams. Preparation and characterization of hydrosoluble, partially charged poly(styrenesulfonate)s of various controlled charge fractions and chain lengths. *Macromolecules*, 35(6):2318–2326, 2002.

[156] Gerald S. Manning. Limiting laws and counterion condensation in polyelectrolyte solutions i. colligative properties. *The Journal of Chemical Physics*, 51(3):924–933, 1969.

[157] F. Oosawa. *Polyelectrolytes*. M. Dekker, 1971.

[158] Andrey V. Dobrynin and Michael Rubinstein. *Progress in Polymer Science*, 30(11):1049–1118, 11 2005.

[159] I. Borukhov, D. Andelman, and H. Orland. Steric effects in electrolytes: A modified poisson-boltzmann equation. 79(3):435–438, 1997.

[160] David D. Jiang, Q. Yao, Michael A. McKinney, and Charles A. Wilkie. Tga/ftir studies on the thermal degradation of some polymeric sulfonic and phosphonic acids and their sodium salts. *Polymer Degradation and Stability*, 63(3):423 – 434, 1999.

[161] David C. Boris and Ralph H. Colby. Rheology of sulfonated polystyrene solutions. *Macromolecules*, 31(17):5746–5755, 1998.

[162] I. Mínguez-Bacho, S. Rodríguez-López, A. Climent-Font, D. Fichou, M. Vázquez, and M. Hernández-Vélez. Variation of the refractive index by means of sulfate anion incorporation into nanoporous anodic aluminum oxide films. *Microporous and Mesoporous Materials*, 225:192 – 197, 2016.

[163] Sandeep K. Dalvie and Ruth E. Baltus. Transport studies with porous alumina membranes. *Journal of Membrane Science*, 71(3):247 – 255, 1992.

[164] Anastasia Christoulaki Dimitrios Anastassopoulos Nikolaos Spiliopoulos Alexandros Vradis Chris Toprakcioglu Christos Kostaras, Spilios Dellis and George Priftis. Flow through polydisperse pores in an anodic alumina membrane; a new method to measure the mean pore diameter. Manuscript submitted for publication.

[165] IAPWS 2008. Viscosity of water, 1999.

[166] Benjamin J. Rogers, Bingchuan Wei, and Mary J. Wirth. Ultra high efficiency protein separations with submicrometer silica using slip flow. 30(10):890–897.

[167] Kah Peng Lee, Hannah Leese, and Davide Mattia. Water flow enhancement in hydrophilic nanochannels. *Nanoscale*, 4:2621–2627, 2012.

[168] V. M. Prabhu, M. Muthukumar, G. D. Wignall, and Y. B. Melnichenko. Polyelectrolyte chain dimensions and concentration fluctuations near phase boundaries. *The Journal of Chemical Physics*, 119(7):4085–4098, 2003.

[169] C. Tasserit, A. Koutsioubas, D. Lairez, G. Zalczer, and M.-C. Clochard. Pink noise of ionic conductance through single artificial nanopores revisited. *Phys. Rev. Lett.*, 105:260602, Dec 2010.

[170] Mickael Lillo and Dusan Losic. Ion-beam pore opening of porous anodic alumina: The formation of single nanopore and nanopore arrays. *Materials Letters*, 63(3):457 – 460, 2009.

[171] Andrew J Jackson. Introduction to small-angle neutron scattering and neutron reflectometry. 2008.

[172] Cousin, Fabrice and Menelle, Alain. Neutron reflectivity. *EPJ Web of Conferences*, 104:01005, 2015.

[173] Frédéric Ott. *Study of magnetic thin fims by polarized neutron reflectometry. Off-specular scattering on periodic structures.* Theses, Université Paris Sud - Paris XI, November 1998.

Abstract

Experimental approaches in studying polyelectrolytes inside a porous matrix: The case of nanoporous alumina membranes

The confinement of condensed matter in nanoporous medium can induce at the nanoscale drastic structural or dynamical changes that ultimately lead to original properties. Of a specific interest is the confinement of polyelectrolytes that are polymers carrying an electrical charge. In this project, self-ordered nanoporous alumina membranes (nPAAMs), whose structural parameters are tuned through the synthesis, have been chosen as a confining medium and experimental approaches have been proposed to study the confinement of a strong polyelectrolyte (PE), sodium polystyrene-sulfonate . An important part of this work has been devoted to the structural and surface charge characterization of nPAAMs. The nPAAMâs structure and composition are characterized by combining scanning electron microscopy and small angle neutron scattering (SANS). A detail strategy is proposed for measuring the nPAAMs under optimal conditions due to their anisotropic shape and high scattering power and information on their chemical composition. The membraneâs surface charge has been determined by streaming potential measurements. The poreâs wall charge can be adjusted to positive or negative charge and the extent of the electrostatic interactions can be tuned, tailoring the medium for electrostatic confinement studies. The permeation behavior and the adsorption of the polyelectrolyte inside the pores is studied by SANS combined with flow measurements. The kinetics of the adsorption is accessed by streaming potential and the possibility to use of neutron reflectivity for such studies is proposed. This work provides experimental approaches insight into the characterization of PE under confinement.

Keywords: nanoporous alumina, anodization, polyelectrolyte, confinement, small angle neutron scattering, streaming potential